The Hamlyn Symposium
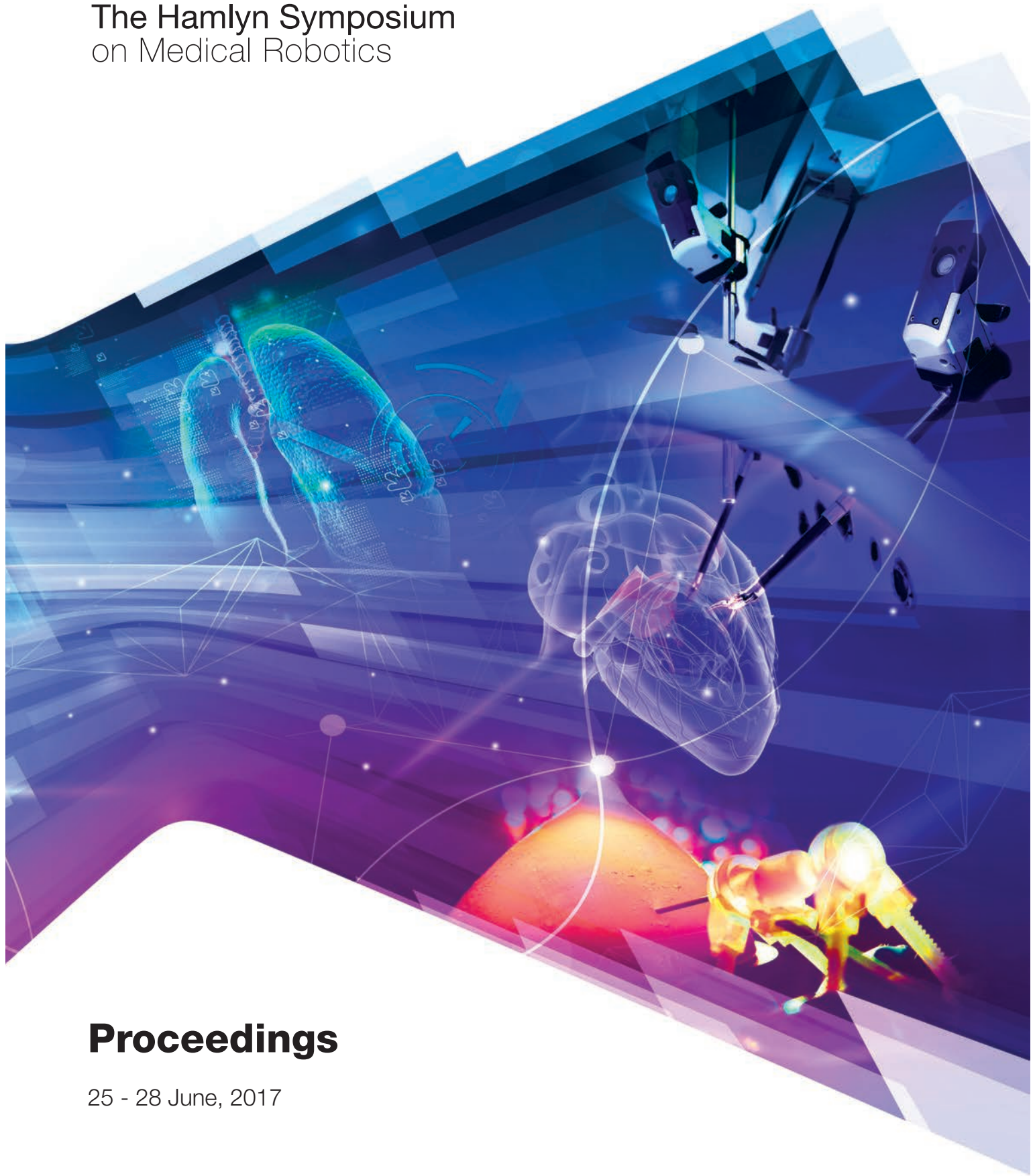## on Medical Robotics

10 YEARS

Proceedings

25 - 28 June, 2017

Proceedings

Guang-Zhong Yang and Ara Darzi (Eds.)

The Hamlyn Symposium on Medical Robotics

25–28 June 2017
Imperial College London, UK

Preface

This year marks the 10th anniversary of the Hamlyn Symposium on Medical Robotics, which was held at the Royal Geographical Society from 25th to 28th June 2017. On this special occasion, we set the theme of this year's symposium as 'The Next 10 Years: Challenges, Innovation and Diffusion of Medical Robotics.' We had the honour of an impressive line-up of leading scientists and engineers in medical robotics, covering intra-operative imaging and sensing, smart surgical instruments, soft and continuum robotics, micro-nano robots, surgical workflow analysis, surgical vision, clinical highlights and first-in-human studies. This year's Storz-Hopkins lecture was delivered by Professor Joseph Sung, The University of Hong Kong. The keynote speakers include Professor Dong-Soo Kwon, Korea Advanced Institute of Science and Technology (KAIST), Dr Catherine Mohr, Vice President of Strategy at Intuitive Surgical, and Professor Andrew Turberfield, University of Oxford.

We also hosted, for the first time, a Leader's Forum chaired by Professor Russ Taylor, John Hopkins University with panel members including: Rick Satava, University of Washington; Howie Choset, Carnegie Mellon School of Computing Science; Nikolay Vasilyev, Boston Children's Hospital; and Bradley Nelson, ETH Zurich. Discussion was focused on this year's symposium theme in terms of the opportunities, expectations and challenges that are facing the medical robotics community now and in the coming years.

A total of 79 papers were submitted from 17 countries, and after systematic peer review, 48 papers were selected for presentation at the Symposium. The topics covered ranged from autonomous and co-operative robots to continuum robots, simulation and training, neurosurgery, orthopaedics and soft robotics.

We were delighted to see our workshop programs continue to grow and flourish. Topics focused on some of the following areas: robotic catheters, soft robotics, continuum robotics, robotically assisted paediatric interventions, surgical workflow to cognitive surgery, image guided therapies, microrobotics and microfabrication, human-robot interaction and first-in-human studies.

As with last year, two of the workshops were organised in conjunction with the EPSRC-NIHR Healthcare Technology Co-operatives (HTC) Partnership Award on Devices for Surgery and Rehabilitation. In collaboration with the Trauma HTC at University Hospital Birmingham NHS Foundation Trust, the Rehabilitation and Assistive Technologies workshop had an impressive line-up of international leaders in the field in an area of growing importance. The Human-Robot Interactions Applied to Health workshop was supported by the Enteric HTC at Barts Health NHS Trust and Queen Mary University of London.

We were particularly excited to host the third Surgical Robot Challenge following on the open platforms for medical robots in partnership with Intuitive Surgical, Kuka Robotics and Applied Dexterity. A large number of submissions were received, with 10 finalists bringing their kit to London to compete over a 3-day competition, starting in the lab, followed by presentations to an esteemed judging panel and cumulating in the short-listed finalists presenting to the Hamlyn Symposium wider audience.

We would like to thank the International and Local Programme Committees, the Workshop Organising Committee and the Local Organising Committee for giving up their valuable time to ensure timely review of the submitted papers, to shape an excellent symposium programme. We are also grateful to the team who have worked behind the scenes and for their continuous effort in managing all aspects of the Symposium organisation. In particular, thanks go to Karen Kerr, Charence Wong, Robert Merrified, Raphaele Raupp, Ulrika Wernmark, Jo Seed, Nikita Rathod, Stephen Godfrey, Melissa Berthelot and Marina Hall.

We would like to thank the Science Museum for hosting our 10th Anniversary Celebration in their fabulous exhibition halls. Lastly, special thanks go to Lady Hamlyn. This would not be possible without the generous philanthropic support from both the Helen Hamlyn Trust and Lady Hamlyn herself.

It was our great pleasure to welcome attendees to the 10th Hamlyn Symposium in London.

June 2017, London
Guang-Zhong Yang, Ara Darzi

Organisation

General and Programme Co-Chairs
Guang-Zhong Yang
Ara Darzi

Conference Organisers
Karen Kerr
Charence Wong
Robert Merrifield
Ulrika Wernmark

Proceedings Associate Editors
Charence Wong
Karen Kerr
Melissa Berthelot

International Programme Committee

Darwin Caldwell	IIT, Italy
Philip Chiu	The Chinese University of Hong Kong, China
Howie Choset	Carnegie Mellon University, USA
Kevin Cleary	The Sheikh Zayed Institute, Washington, USA
Paolo Dario	Scuola Superiore Sant'Anna, Pisa, Italy
Simon DiMaio	Intuitive Surgical Inc, USA
Pierre Dupont	Children's Hospital Boston, USA
Giancarlo Ferrigno	Politecnico Milan, Italy
Hubertus Feussner	Technical University Munich, Germany
Gabor Fichtinger	Queen's University, Canada
Paolo Fiorini	University of Verona, Italy
Dennis Fowler	Titan Medical Inc., USA
Toshio Fukuda	Nagoya University/Meijo University, Japan
Blake Hannaford	University of Washington, USA
Koji Ikuta	University of Tokyo, Japan
Leo Joskowicz	The Hebrew University of Jerusalem, Israel
Peter Kazanzides	Johns Hopkins University, USA
Thomas Looi	Sick Kids, Toronto, Canada
Jacques Marescaux	University Hospital Strasbourg, France
Arianna Menciassi	Scuola Superiore Sant'Anna, Pisa, Italy
Leonardo Mattos	IIT, Italy
Azad Najmaldin	St James University Hospital, UK
Bradley Nelson	ETH Zürich, Switzerland
Rajni Patel	The University of Western Ontario, Canada
Vipul Patel	Global Robotics Institute, USA
Christopher Payne	Harvard University, USA
Cameron Riviere	Carnegie Mellon University, USA
Ichiro Sakuma	University of Tokyo, Japan
Rick Satava	University of Washington, USA
Lee Swanstrom	University of Oregon, USA
Mark Talamini	University of California, San Diego, USA
Russ Taylor	Johns Hopkins University, USA
Ashutosh Tewari	Mount Sinai School of Medicine, USA
Chris Thompson	Harvard Medical School, USA
Joe Wang	UCSD, USA
Robert Webster III	Vanderbilt University, USA
Steve Wexner	Cleveland Clinic Florida, USA

Local Programme Committee

Kaspar Althoefer	Queen Mary University of London, UK
Thanos Athanasiou	Imperial College London, UK
Christos Bergeles	University College London, UK
Colin Bicknell	Imperial College London, UK
Nick Cheshire	Imperial College London, UK
Brian Davies	Imperial College London, UK
Kamal Deep	Glasgow University, UK
Sanja Dogramadzi	UWE Bristol/University of Bristol, UK
Daniel Elson	Imperial College London, UK
Leonard Fass	Imperial College London, UK
Mohamad Hamady	Imperial College London, UK
Su-Lin Lee	Imperial College London, UK
Daniel Leff	Imperial College London, UK
Hani Marcus	Imperial College London, UK
Erik Mayer	Imperial College London, UK
Andreas Melzer	Dundee University, UK
George Mylonas	Imperial College London, UK
Dinesh Nathwani	Imperial College London, UK
Geoff Pegman	RU Robotics, UK
Philip Pratt	Imperial College London, UK
Kawal Rhode	King's College London, UK
Ferdinando Rodriguez y Baena	Imperial College London, UK
Pallav Shah	Imperial College London, UK
Paulo Stanga	Manchester Royal Eye Hospital, UK
Julian Teare	Imperial College London, UK
Justin Vale	Imperial College London, UK

Webmaster
Charence Wong

Media Coordinator
Jo Seed

v

Contents

Development of an Endoscopic Surgical Robotic System – from Bench to Animal Studies

K.C. Lau[2], E. Leung[2], C.C.Y. Poon[1], J.Y.W. Lau[1,3], Y. Yam[2,3], P.W.Y. Chiu[1, 3]

[1]Department of Surgery, Faculty of Medicine; [2]Department of Mechanical and Automated Engineering, Faculty of Engineering; and [3]Chow Yuk Ho Technology Centre for Innovative Medicine, The Chinese University of Hong Kong

INTRODUCTION

Over the past two decades, development in novel technologies broadens the horizon of therapeutic endoscopy. From researches at the Chinese University of Hong Kong, we have established endoscopic treatment to replace surgery as primary treatment of bleeding peptic ulcers [1]. We also pioneered endoscopic resection with the technique of endoscopic submucosal dissection (ESD) for treatment of early GI cancers [2,3]. Peroral Endoscopic Myotomy extended the arena of therapeutic endoscopy from endoluminal to submucosal treatments [4]. Although ESD was shown to achieve similar oncological clearance as compared to conventional surgery, the performance of ESD is technically challenging [5]. Unlike minimal invasive surgery, ESD is carried out through single instrumental dissection along a single axis without retraction. The concept of Natural Orifices Transluminal Endoscopic Surgery (NOTES) further challenged the performance of conventional flexible endoscope and triggered researches to redesigning the endoscope and the therapeutic tools [6]. Our group first developed a prototype endoscopic suturing device – Eagle Claw [7]. From preclinical researches, Eagle Claw was found to be safe and effective in achieving hemostasis for massively bleeding ulcers as well as closure of a gastrotomy [8]. The design of endoscopic suturing device cannot provide adequate degree of freedom to achieve secure suturing. Suturing is considered to be one of the most sophisticated surgical procedures. Since it requires 6 degree-of-freedom (DOF) of motion to complete the procedure, current endoscopic suturing protocols that are designed based on conventional endoscopic tools with 1 to 2 DOF are non-intuitive and extremely difficult to use. To overcome the above inadequacy, we proposed to use the latest endoscope technology, which is only 5 mm in diameter, and coupled with a hollow overtube as the basic working platform. Without going through the endoscope and with the freed space, it is possible to design two robotic arms with more DOF to satisfy the requirements of complex procedure such as suturing.

MATERIALS AND METHODS

This project aims to develop enabling technologies for flexible robot-assisted endoscopic surgery. From 2014 to 2016, basing on a commercially available platform – the USGI Transport, we developed a prototype with 9-degree-of-freedoms (DOFs) robotic arms (Fig 1 and 2). From bench studies, the robotic arms has been test to be able to complete simpler surgical task including tissue retraction and dissection. The system consisted of two robotic arms mounted with different end effectors for tissue retraction and dissection respectively (Fig 2). We developed an advanced and intelligent control scheme for intuitive manipulation of the robotic arms within the confined gastrointestinal lumen. Through the process of development, we have conducted multiple experiments using this prototype robotic endoscope for performance of ESD in ex-planted porcine stomach (Fig 3). After serval trials, we moved forward to conduct live porcine model experiment.
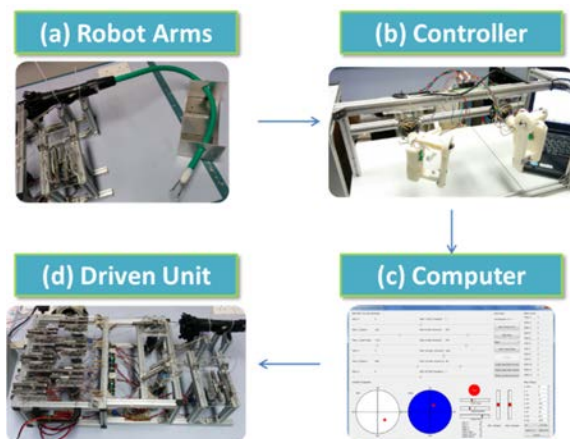
Fig. 1. Schematic diagram of the endoscopic robotic system. (a) Robotic arms; (b) Controller; (c) Driven Unit; (d) Computer
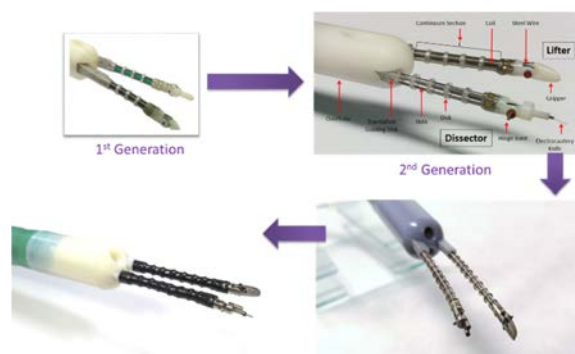
Fig. 2. Revolution of the design and development of Robotic Arms

RESULTS

From 2014 to 2016, a novel robotic endoscopic system was developed upon USGI transport [9]. The two robotic arms could be retracted within the working channels during insertion of the transport into the porcine stomach. In the first ex-planted porcine stomach model, we successfully performed gastric ESD in size of 40mm using the robotic system. A total of four robotic ESDs were performed in ex-planted porcine model with an average specimen size of 35mm. The mean operative time was 35 minutes, and there was no perforation. Gastric ESD was performed in two live porcine models with our surgical robotic system (CU Robotic Endoscope) under general anesthesia. Figure 4 shows the experimental setup in the second trial. Figure 5 shows a typical endoscopic view during this trial. The mean operative time was 50 minutes, and the mean size of specimen was 30mm. There was no perforation or intraprocedural bleeding, and the speed of dissection per specimen area was 1.9mm2/minutes. The efficiency of the robotic system, especially in dissection, surpass the ordinary ESD procedure, mainly due to strong tissue retraction ability of the robotic system. This prevented the target area being blocked by the dissected tissue which increase the difficulties of dissection.
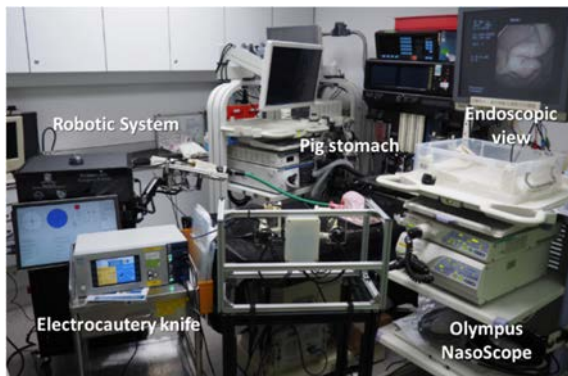
Fig 3 – Ex-vivo porcine stomach model for ESD experiments using the prototype robotic endoscope
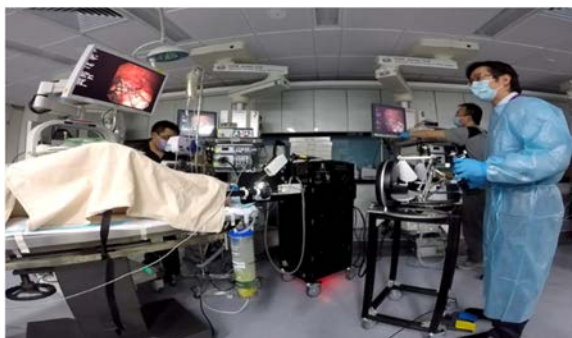
Fig 4 - Experimental setup of second trial of live porcine model. Two robotic arms were being inserted into pig stomach. The endoscopic view on the top-left showed two robotic arms were cooperating which the tissue was being retracted and dissected. Surgeon on the right was using master-console to perform ESD through our system.
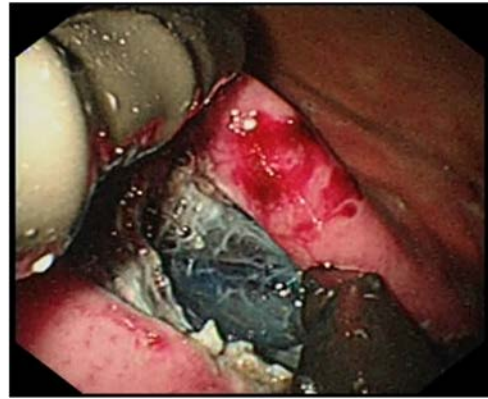
Fig. 5 – Endoscopic view during the second trial of live porcine model. This typical moment showed the two robotic arms were cooperating which the retractor on the left lifting up the mucosa and the dissector on the right dissecting the submucosa.

DISCUSSION

The current study confirmed the efficacy and safety of a newly designed robotic endoscope building on a commercially available platform for performance of gastric ESD. Future prospective clinical study will focus on performance of gastric and rectal ESD using this system.

REFERENCES

1. Lau J, Sung JJ. From endoscopic hemostasis to bleeding peptic ulcers: strategies to prevent and treat recurrent bleeding. Gastroenterology. 2010 Apr;138(4):1252-4, 1254.e1
2. Chiu PW, Chan KF, Lee YT, Sung JY, Lau JY, Ng EK. Endoscopic submucosal dissection (ESD) for treatment of early neoplasia of the foregut using combination of knives. Surgical Endoscopy 2008; 22(3):777-83.
3. Chiu PW, Teoh AY, To KF, Wong SK, Liu SY, Lam CC, Yung MY, Chan FK, Lau JY, Ng EK. Endoscopic submucosal dissection (ESD) compared with gastrectomy for treatment of early gastric neoplasia: a retrospective cohort study. Surg Endosc. 2012 Dec;26(12):3584-91.
4. Chiu PW, Wu JC, Teoh AY, Chan Y, Wong SK, Liu SY, Yung MY, Lam CC, Sung JJ, Chan FK, Lau JY, Ng EK. Peroral endoscopic myotomy for treatment of achalasia: from bench to bedside (with video). Gastrointest Endosc. 2013 Jan;77(1):29-38.
5. Teoh AY, Chiu PW, Wong SK, Sung JJ, Lau JY, Ng EK. Difficulties and outcomes in starting endoscopic submucosal dissection. Surgical Endoscopy 2009; 24(5):1049-54.
6. Spaun GO, Zheng B, Swanstrom LL. A Multitasking platform for natural orifice translumenal endoscopic surgery (NOTES): a benchtop comparison of a new device for flexible endoscopic surgery and a standard dual-channel endoscope. Surgical Endoscopy 2009;23(12):2720-7.
7. Chiu PW, Lau JY, Ng EK, Lam CC, Hui M, To KF, Sung JJ, Chung SC. Closure of a gastrotomy after transgastric tubal ligation by using the Eagle Claw VII: a survival experiment in a porcine model. Gastrointestinal Endoscopy 2008; 68(3):554-559.
8. PWY Chiu, Bing Hu, JYW Lau, LCL Sun, T Yamamoto, JJY Sung, SCS Chung. Endoscopic plication of massively bleeding peptic ulcer by using Eagle Claw VII device: a feasibility study in a porcine model. Gastrointestinal Endoscopy 2006; 63(4): 681-685
9. Lau, Ka Chun, Esther Yun Yee Leung, Philip Wai Yan Chiu, Yeung Yam, James Yun Wong Lau, and Carmen Chung Yan Poon. "A Flexible Surgical Robotic System for Removal of Early-Stage Gastrointestinal Cancers by Endoscopic Submucosal Dissection." IEEE Transactions on Industrial Informatics 12, no. 6 (2016): 2365-2374.

SAID: A Semi-Autonomous Intravenous access Device for Paediatric Peripheral Intravenous Catheterisation

Z. Cheng[1], B.L. Davies[1,2], D.G. Caldwell[1], L.S. Mattos[1]

[1]Department of Advanced Robotics, Istituto Italiano di Tecnologia, Genova, Italy,

[2]Department of Mechanical Engineering, Imperial College London, London, UK
zhuoqi.cheng@iit.it

INTRODUCTION

Peripheral IntraVenous Catheterization (PIVC) on pediatric patients is consistently one of the most challenging operations in hospitals. Since their veins are small, fragile and readily ruptured, the success rates of this operation are found to be commonly low. Extravasation injuries often occur which can potentially cause very critical issues such as skin necrosis.

Robotic technology has been the focus of research for improving the first-stick accuracy and shortening the time required for the PIVC procedure. The earlier designs [2,3] include several grounded robots, which are placed on a desk for operation. These robots aimed at a fully autonomous PIVC, and thus resulted in bulky and complex designs. Even so, they can only do PIVC on specific insertion areas, e.g., forearm Basilic vein. In addition, these robots normally require the patients to keep their forearms static during the whole operation, which is not easy for children.

Compared to such autonomous surgical robots, a 'handheld' robotic device has several benefits such as lower cost, lower complexity, allowing flexible insertion sites and keeping surgeons in control for safety. So far, several auxiliary devices have been developed. However, few devices were proposed for gauging the needle insertion to enter the vein, which is actually difficult on pediatric patients and often fails.

MATERIALS AND METHODS

Semi-Autonomous Intravenous access Device

In this study, a smart hand-held device named **Semi-Autonomous Intravenous access Device (SAID)**, is proposed. This constitutes a collaborative robot-assisted surgery, one in which the clinician is responsible for establishing the position and orientation of the catheter for insertion, and the device takes care of the delicate forward insertion. The device is designed with only one DOF for the insertion depth control as the other operations were reported to be relatively easy for medics. By measuring the electrical impedance at the needle tip, SAID identifies the type of tissue contacting the needle tip and controls the insertion.

The system configuration of SAID is shown in Fig. 1. A central controller reads the electrical impedance measurement from an impedance converter and controls a stepper motor for inserting the catheter. The Nanotec LSP2575 stepper motor is selected because it can provide enough insertion force (10 N) and displacement (30 mm) for this application. The electrical impedance is measured through a concentric electrode needle between the end of its center core and its outer shaft. The excitation frequency for the electrical impedance measurement is set to 80 kHz and the sampling rate is optimized to about 300 Hz. The cannula part of a 26G catheter is placed over the needle. In addition, two IR position sensors are included as limit sensors to aid in device positioning. A footswitch is used for the insertion control. The motor inserts the catheter when the footswitch is activated, and stops the insertion if it is released. During the insertion, if the acquired impedance value corresponds to that of blood, the insertion is stopped immediately regardless of the footswitch status. More technical specifications of SAID are listed in Table. 1.

Table 1 Technical specifications of SAID.

Design specifications	Parameter
Insertion force	10 N
Maximum displacement	30 mm
Step resolution	8.3 μm/step
Insertion speed	1 mm/s
Sensor sampling rate	300 Hz
Sensor excitation frequency	80 kHz
Weight	90 g
Other	Ergonomic shape
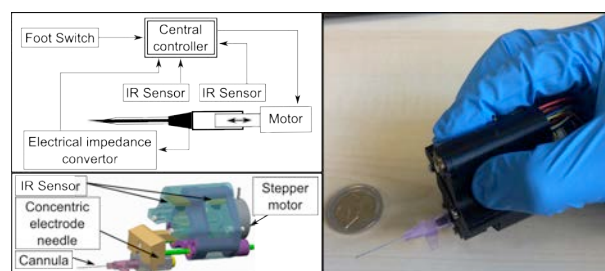
Fig. 1 Left top: The system configuration of SAID; Left bottom: 3D modeling of SAID; Right: a prototype of SAID.

RESULTS

Device characterization

SAID was firstly clamped to a 4-axes motion stage for characterization. Therefore, potential disturbances related to an user's performance could be removed.
Firstly, SAID was evaluated to ensure it provides a fast response for venous entry detection by measuring the overshoot distance. The orientation of the position stage was adjusted to make SAID point downwards to the surface of a saline solution. The height of the catheter was finely monitored until its tip just touched the liquid

surface. This position was set as the origin. Then SAID was retracted by 2 mm, and subsequently activated to insert the catheter downwards. It was automatically stopped when the saline solution was detected. The number of executed motor steps relative to the origin, corresponding to the overshoot distance, was collected. This test was repeated 5 times. The response time was found to be 21.6 ms and the average overshoot distance was found to be 0.7 mm, which is smaller than the mean diameter of veins for young children.

Secondly, the effectiveness of venipuncture detection of SAID was validated. A realistic PIVC phantom was designed and used for this test. It was made by a small latex tube (Ø = 1.5 mm) which was wrapped in a layer of pig skin including epidermis, dermis and fat layers. A circulation pump was included for circulating a 0.5% saline solution, which presents a similar electrical impedance to that of blood, inside the tube. The drawback of the phantom may be that the pig skin is too thick and visually occludes the tube. This issue, in reality, can be solved by trans-illumination technologies. During the tests, SAID was carefully positioned to target the phantom vein, perform the insertion and stop automatically when blood was detected. The insertion tests were repeated 10 times and 5 trials were failed because the insertion completely missed the vein and passed alongside it. These reuslts demonstrate that online correction of the needle insertion direction were very necessary and this reinforces the idea of human-robot cooperation and points to a clear benefit of the proposed hand-held robotic device configuration.
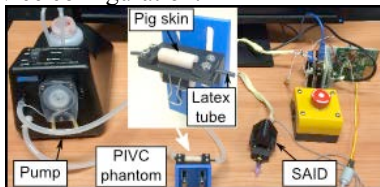
Fig. 2 Experimental setup for evaluating SAID.

PIVC performance assessment experiments

A series of experiments were designed and conducted to evaluate SAID on the PIVC phantom as shown in Fig. 2. 10 naïve subjects (8 males and 2 females, average age 29 years old) were involved in the experiment. None of them had previous experience with PIVC. The subjects were divided in two groups: 5 in the Experimental group and 5 in the Control group. During the experiments, the subjects were required to select an insertion site about the center of the PIVC phantom, align the catheter along the vein, and try their best to insert the catheter into the latex tube of the phantom with an insertion angle about 30°. For subjects in the Experimental group, the insertion was done by stepping on the foot switch when they were ready. They were instructed to hold the device steadily during the insertion and adjust the catheter orientation whilst targeting the tube. Subjects in the Control group were required to perform the catheterization by hand with an ordinary 26G IV catheter, and judge the venipuncture moment to stop the insertion.

For each subject, the number of successful operations over all 5 experimental trials was collected. And for failed attempts, we also recorded the possible reasons, which were categorized qualitatively in terms of: Miss-target (catheter passed by along side the vein), Prior-to-puncture (catheter did not puncture through the skin) and Puncture-through (catheter punctured completely through the vein).

The experimental results in Fig. 3 demonstrate a significant difference ($p < 0.01$) of scores between 2 groups. Subjects who used SAID had a much higher success rate (88%) than those who didn't (12%). In addition, the failed reasons between the Experimental group and the Control group were also compared. From the results of the Control group, the common reasons were: stopping the insertion either too early before reaching the tube (48%), or too late after puncturing the distal wall (18%). In addition, 1 'miss-target' failure (4%) was found in the Control group and 2 cases (8%) were found in the Experimental group. This result implies that motorizing the insertion motion changes the way of insertion direction control, which requires the user to make some effort to learn. In addition, one case of 'puncture-through' was noted in the Experimental group. The reason was found that the catheter penetrated a point very close to the vein edge, and caused the vein compressed during the insertion. Vessel deformation during the insertion was considered in the study but found not to be significant in practice.

Furthermore, a questionnaire investigation was submitted to the subjects for acquiring feedbacks on the usability of SAID. According to the results of the questionnaire, SAID was highly appreciated by the subjects under all dimensions of usability.
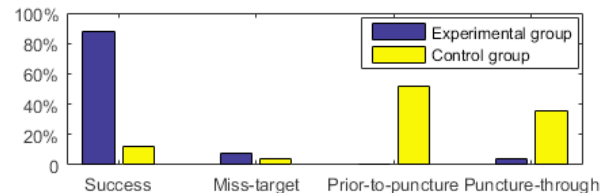
Fig. 3 Comparing the experimental results of the Experimental group and the Control group.

DISCUSSION

This study introduces and evaluates a hand-held robotic device for assisting in pediatric PIVC. The obtained experimental results demonstrate a significant improvement of the PIVC performance on small veins when this device is used, compared to the control group.

REFERENCES

[1] Z. Cheng, *et al.* A venipuncture detection system for robot-assisted intravenous catheterization. BioRob'2016.
[2] R. Brewer, Improving peripheral iv catheterization through robotics: From simple assistive devices to a fully-autonomous system. Thesis (Ph.D.), Stanford University, 2015.
[3] A. Zivanovic & B. Davies. A robotic system for blood sampling. IEEE Transactions on Information Technology in Biomedicine. Vol: 4, Pages: 8-14, ISSN: 1089-7771. 2000.

Image-Guided Robot-Assisted Fracture Surgery: a Cadaveric Study

G. Dagnino[1], I. Georgilas[1], S. Morad[1], P.Gibbons[1], P. Tarassoli[2], R. Atkins[2], S. Dogramadzi[1]

[1]Bristol Robotics Laboratory, Bristol, UK,

[2]University Hospitals Bristol, Bristol, UK
giulio.dagnino@uwe.ac.uk

INTRODUCTION

Reduction is a crucial step for the treatment of lower limb fractures, including joint fractures [1]. This involves manipulating bone fragments to reconstruct the fracture as precisely as possible. Percutaneous techniques have been developed to mitigate the problems related to open surgery (i.e. extensive soft tissue damage, slow bone healing, increased risk of infection [2]), involving fragment manipulation using two (or more) pins inserted in the fragments through small incisions in the patient's flesh. Such techniques are associated with a faster recovery and a lower risk of infection compared to open surgical techniques [3]. However, their application to joint fractures is limited by the current sub-optimal 2D intra-operative imaging (fluoroscopy) and by the high forces involved in the procedure. Earlier research by the authors of this paper toward improving percutaneous reduction of intra-articular fractures has resulted in the creation of a robotic system prototype, i.e. RAFS (Robot-Assisted Fracture Surgery) system [4]. This is an image-based robotic system which allows the surgeon to intraoperatively pre-plan the reduction of distal femur fractures (DFFs), by virtually manipulating 3D models of the fracture generated by pre-operative CT data. This prototype was demonstrated to be able to successfully reduce 2-fragments DFFs on bone phantoms [4], [5]. Although the incidence of DFFs has been found to be ten times less frequent than proximal femur fractures [7], their mismanagement can result in abnormalities of alignment of the load-bearing axis of the lower limb and/or rotational deformities with catastrophic biomechanical consequences. The simultaneous manipulation of 3 fragments is necessary in order to achieve the reduction of complex intra-articular fractures such as 33-C1 (Fig.1c,d) [7]. The aim of this paper is to introduce a new prototype of the RAFS system able to manipulate complex 3-fragments DFFs, and to demonstrate its applicability to a real surgical environment through a cadaveric study.

MATERIALS AND METHODS

The RAFS system (Fig.1a,b) is made up of: two robotic fracture manipulators [4] (RFM1 and RFM2, 6DOF) attached to the bone fragments through orthopaedic manipulation pins; two carrier platforms [4] (CP1, CP2, 4DOF) used to position the RFMs close to the orthopaedic pins; one automated traction table
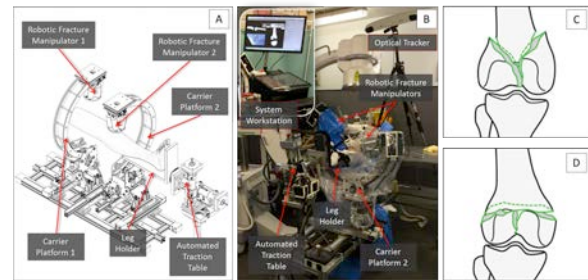
Fig. 1 The RAFS surgical system (A, B). 33-C1 DDFs: Y-shape (C) and T-shape (D).

(ATT, 4DOF) which, connected to the tibia through an orthopaedic boot, allows the application of a constant and adjustable traction force to the lower limb through the tibia; a system workstation to operate the robot [4], and a navigation system consisting of reduction software, optical tracking system (Polaris Spectra, NDI Inc.), and contact-less user controller (Leap Motion) [6]. The navigation system allows the surgeon to interact with CT-generated 3D models of the fracture using the user controller for pre-operative planning of fracture reduction, i.e. virtually reduces the fracture [5]. It also provides real-time update of the 3D models through the optical tools placed on the orthopaedic pins inserted into the bone fragments (see [5]). We have tested the RAFS system on 9 fresh frozen human cadaveric specimens. An orthopaedic surgeon fractured the distal part of each femur creating Y-shape 33-C1 fractures in 5 specimens and T-shape 33-C1 in 4 specimens [7]. Each fracture consisted of three fragments: F1 (condyle), F2 (condyle), and FEM (rest of the femur). The following clinical workflow was applied to each specimen to reduce the fracture. Pre-operative operations: 3D models of each bone fragment were generated by the segmentation of pre-operative CT data of the fracture. The same surgeon virtually reduced the fracture using the GUI [5] by manipulating the models, i.e. F1 and F2 to match FEM. This generated the desired pose of fragments F1 ($^{F1}P_d$) and F2 ($^{F2}P_d$) with respect to FEM, in order to achieve the anatomical reduction of the fracture. Intra-operative operations: 3 orthopaedic pins were inserted into the bone fragments F1, F2, and FEM. The relative position of each pin with respect to the bone fragment in which it is inserted was calculated performing 2D/3D registration between two 2D intra-operative fluoroscopic images of each pin+fragment and the relative 3D models (CT model of fragment, CAD

TABLE I. CADAVERIC STUDY RESULTS

Specimen [a]		#1 – T,R	#2 – Y,R	#3 – T,L	#4 – Y,L	#5 – T,L	#6 – T,R	#7 – Y,L	#8 – Y,L	#9 – Y,R
F1 ΔT (RMSE)	mm	1.41±0.30	1.83±0.10	1.00±0.40	0.69±0.26	0.51±0.12	0.79±0.11	1.04±0.25	7.13±3.63	3.44±0.82
F1 $\Delta\vartheta$ (RMSE)	deg	3.12±0.40	2.40±0.30	2.40±0.20	1.75±0.10	2.72±0.01	3.43±0.22	0.12±0.05	20.7±0.81	1.14±0.16
F2 ΔT (RMSE)	mm	0.93±0.20	0.85±0.30	1.38±0.40	2.83±1.94	0.82±0.39	1.15±0.60	1.13±0.01	0.95±0.37	12.1±1.54
F2 $\Delta\vartheta$ (RMSE)	deg	3.30±0.50	2.20±0.10	2.40±0.60	4.88±3.10	2.01±0.58	7.24±0.56	0.69±0.04	3.28±0.18	12.9±7.42
Force	N	69.9±4.4	113.1±5.4	18.0±0.5	94.6±5.1	147±10	82.7±7.5	25.9±7.4	55.9±11.9	74.5±8.1
Torque	Nm	4.8±0.4	3.2±0.3	1.60±0.1	6.83±0.6	6.31±0.2	1.96±0.3	3.24±0.6	1.91±0.4	2.12±0.5
Surgical Time	min	119	131	132	119	117	127	123	119	107

[a] T = T-shape 33-C1 fracture; Y = Y-shape 33-C1 fracture; R = right limb; L = left limb

model of the pin) pre-operatively generated, as described in [8]. Optical tools were placed on the pins enabling the intra-operative real-time image guidance [5]. The surgeon's assistant connected the ATT to the patient's foot, and RFM1 and RFM2 to F1 and F2, respectively through the inserted pins. The surgeon applied the desired traction to the joint through the external robot to restore the appropriate length and rotation of the joint. Results of the pre-operative planning $^{F1}P_d$ and $^{F2}P_d$, i.e. the virtual reduction parameters, were uploaded into the intra-operative procedure, and the corresponding poses in the task space for the RFMs $^{RFM1}P_d$ and $^{RFM2}P_d$ calculated as described in [5]. The RFMs executed the desired movements for F1 and F2 to achieve the physical reduction of the fracture, while FEM remained fixed. The intra-operative imaging updated the actual pose of the fragments in real time, and the surgeon checked the reduction in 2D and 3D views. When the reduction was acceptable, the surgeon fixated the fracture.

RESULTS

The metrics chosen for the RAFS system evaluation were: the fracture reduction accuracy expressed as the root-mean-squared-error (RMSE) measured after the physical reductions; the force/torque applied by the RFM_S during the physical reduction measured through 6DOF load cells mounted on the RFM; and the surgical procedure time. The assessment of reduction was completed by a surgeon by measuring the residual translational and rotational errors on post-operative fluoroscopic images of the reduced fractures. Translational error was expressed as the separation of two points between one fragment and the femur (reference). For each fragment, 12 data points were taken from two different fluoroscopic images (lateral and coronal plane) to determine the average translational error ΔT (RMSE). Rotational error was measured as the difference between the axis defined by the femur (reference) and the axis defined by the fragment. For each fragment, 2 data points were taken from two different fluoroscopic images (lateral and coronal plane) to determine the average rotational error $\Delta\vartheta$ (RMSE). Results are reported in Table I.

DISCUSSION

The RAFS system showed clinically acceptable reduction values (1mm, 5°) on both Y- and T-shape 33-C1 fractures in 5 specimens, namely #1, #2, #3, #5, and #7. For these specimens, average residual reduction errors of only 1.1±0.3mm/2.13±0.9° were achieved. Specimens #4 and #6 presented average residual error of

1.36±0.8mm/4.35±2°, resulting in sub-optimal albeit acceptable reduction. Reduction accuracy for specimens #8 and #9 can't be considered acceptable with the average residual error of up to 5.9±4.1mm/9.5±7.8°. This is related with the failure of the gripping system connecting the RFMs and to the pin. The average surgical time to reduce a fracture with the RAFS system was 123±7 minutes, slightly higher than the open-procedure (≈100 minutes). Pins insertion took 33±3min; 2D/3D registration 52±6min; robot setup 27±3min; intra-operative virtual reduction 2±1min; and physical reduction 9±3min. Cadaveric trials demonstrated the accuracy and effectiveness of the RAFS system, and its applicability in surgical environment. This study provided valuable data for future improvements. The gripper system has to provide a more stable gripping to avoid displacements between pins and RFMs that can cause sub-optimal reductions. The 2D/3D registration is currently overly time consuming and should be improved to make the whole surgical procedure quicker.

ACKNOWLEDGMENT

REFERENCES

[1] G. Mathew and B. P. Hanson, "Global burden of trauma: Need for effective fracture therapies," *Indian J. Orthop.*, vol. 43, no. 2, pp. 111–116, 2009.

[2] J.L. Marsh, *Rockwood And Green's Fractures In Adults*, 8th ed., vol. 2. Wolters Kluwer, 2015.

[3] P. Gaston *et al.*, "Recovery of knee function following fracture of the tibial plateau," *J Bone Joint Surg Br*, vol. 87, no. 9, pp. 1233–6, 2005.

[4] G. Dagnino *et al.*, "Image-based robotic system for enhanced minimally invasive intra-articular fracture surgeries," *ICRA16*, Stockholm, Sweden, 2016.

[5] G. Dagnino *et al.*, "Navigation system for robot-assisted intra-articular lower-limb fracture surgery," *Int. J. Comput. Assist. Radiol. Surg.*, May 2016.

[6] G. Dagnino *et al.*, "Surgical Pre-Planning for Robot-Assisted Fracture Surgery," *Hamlyn Symposium on Medical Robotics*, London, UK, 2016.

[7] "Distal Femur Fracture - Reduction and Fixation," *AO Foundation*. 2015.

[8] G. Dagnino *et al.*, "Intra-Operative Fiducial-Based CT/Fluoroscope Image Registration Framework for Image-Guided Robot-Assisted Joint Fracture Surgery," *CARS17*, Barcelona, Spain, 2017.

A Variable Stiffness Mechanism for Minimally Invasive Surgical Needles

C. Culmone[1*], I. De Falco[2*], A. Menciassi[2], J. Dankelman[1], J. J. van den Dobbelsteen[1]

[1]Department of BioMechanical Engineering, Delft University of Technology, The Netherlands

c.culmone@tudelft.nl

[2]The BioRobotics Institute, Scuola Superiore Sant'Anna, Italy

* equal contribution

INTRODUCTION

Needles are instruments frequently employed in Minimally Invasive Surgery (MIS), and are especially requested in percutaneous diagnosis and in local therapies [1]. During procedures, tissue inhomogeneity, tissue deformation, and thus needle deflection can cause tip misplacement resulting in inaccurate anesthesia, re-puncturing with additional damages of the tissue or false negative detection [2]. Previous studies focused on needle-tissue interaction and possibilities to improve the needle steerability [3]. The proposed work is aimed to design a new concept of needle based on variable stiffness able both to balance tissue inhomogeneity and to guarantee needle steering during the insertion. The structure of the Variable Stiffness Mechanism (VSM) allows the needle to adjust the deflection when passing through tissues, while the omnidirectional steering of the tip facilitates the achievement of the target.

MATERIALS AND METHODS

The steerable needle is shown in Fig.1. The prototype has an outer diameter of 3 mm, which approximately corresponds to an 11-needle gauge, appropriate for breast procedures [4]. The needle is composed of a tip, a VSM, a cannula, and four cables for driving the needle and tuning its stiffness. The tip is fabricated in aluminum with a bevel shape in order to have a predictable trend of the deflection during the test phase. The VSM is 11 mm long, in which rigid and compliant segments alternate. Four rigid plates, 0.5 mm long, were manufactured by aluminum, while three compliant cylindrical segments, 3 mm long, were made by compliant material (Smooth-Sil 940 Silicone, Smooth-On). Compliant and rigid parts are fixed by silicone glue (Momentive, 127374). The cannula is a steerable hallowed tube in PEEK plastic (IDEX® Health & Science), which includes four holes in the wall for cables passage. Cables are Dyneema wires with 0.08 mm in diameter. They are placed at 90 degrees from each other and pass through the rigid plates, the compliant parts, and the cannula, due to dedicated grooves. The tensioning of the cables allows having different configurations of the needle, permits the omnidirectional steering of the tip and the control of the stiffness. If two cables placed at 180 degrees from each other are tensioned simultaneously with the same

tension, the compliant parts are slightly compressed producing a stiffness increasing of the VSM, thus of the overall needle. If just one cable is tensioned, the tip of the needle bends towards the opposite cable.
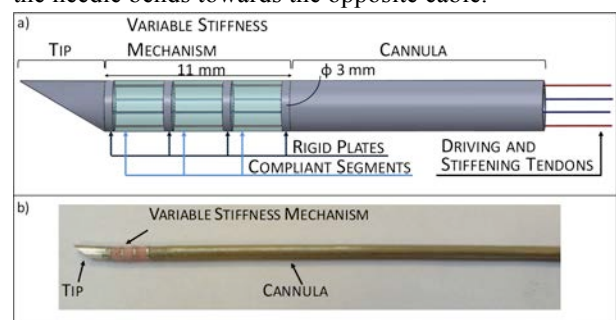
Fig. 1 a) Overall sketch of the needle, b) final prototype.

As reported in [5], the VSM was individually tested in order to evaluate its properties in terms of stiffness. Two stiffening tendons were pulled by loads in the range 0-17 N and the generated force was measured. Experiments demonstrated that when the tension increases, also the force exerted by the prototype increases with an almost linear trend. In particular, if there is no tension, the exerted force is lower than 0.5 N, while at 17 N it is 3.6 N. It is worth mentioning that for 9 N of tension, the force exerted by the prototype is 1.3 N, which is a value compatible with many tissue puncturing.
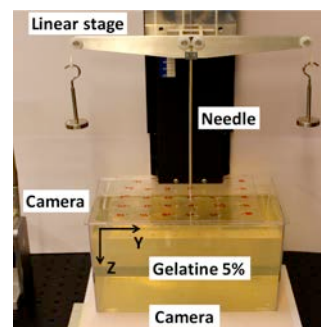
Fig. 2 The experimental set-up of the needle tests.

Once assessed the working principle, the needle prototype was tested in gelatin phantom for analyzing how the deflection changes with respect to the VSM activation. The set-up used to test the needle is shown in Fig. 2. The needle was rigidly linked with a support to a linear vertical stage. The support was constituted of two lateral arms, on which two pulleys for each arm were

fixed. The linear vertical stage gave translation in vertical direction at a constant speed of 3 mm/s [6]. Two cables at 180 degrees from each other, slid on the pulleys, and loads were laterally attached for tensioning the cables. The remaining two cables were left free and considered as the driving cables. The images acquisition of the needle motion during the tests, was done using two cameras (iShight Camera 8MPX, 30 frames per second). The phantom, used to reproduce a biological tissue, was made with 5% (in weight) gelatin-water mixture at 70 °C, and stored at 2 °C until the use. The elastic modulus of the phantom was 21 kPa, which is similar to the elastic modulus of the breast [7]. The cables were pulled with the same tension in the range 0-10 N with steps of 1 N. For each different tensioning state, the needle was inserted into the gelatin for a displacement of 100 mm. Three tests were performed for each applied tension. At 100 mm in depth of each insertion, images of the needle were acquired, and the deflection (k in the inset of Fig. 3) was calculated as distance between the tip and the ideal straight trajectory (red line in the inset of Fig. 3).

RESULTS

Fig. 3 shows the results of the deflection in the gelatin phantom for different applied tensions. In the inset, the configuration of the needle when tensioned with 10 N is shown.
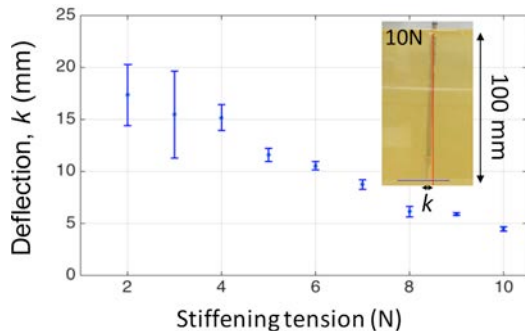
Fig. 3 Deflection of the needle in 5% gelatin phantom and the tensioned needle at 10 N. k indicates the average of measured deflection after three repetitions.

The deflection decreased when the tension on the cables increased. The maximum deflection of 17.34 mm was measured when the needle was tensioned with 2 N, and it reached 4.4 mm when the needle was tensioned with 10 N. For tensions in the range 2-4 N, the tip and the cannula seemed to move independently, due to the fact that tip displaced more than cannula. Moreover, the high value of the standard deviation, calculated after three repetitions of each increment in tension, indicated a big variability of the deflection. At 5 N, the tip and the cannula started to move together, and the standard deviation significantly decreased. Hence, 5 N tension can be assumed as the first working value of the proposed needle. For tensions higher than 5 N, the deflection decreases and the standard deviation is acceptable [8].

DISCUSSION

In this work a new concept of a needle with a variable stiffness mechanism for minimally invasive procedures was presented. The VSM consists of rigid plates that alternate with cylindrical compliant parts. Pulling the cables placed through the mechanism allows tuning the stiffness of the needle. Force tests demonstrated that the mechanism is able to exert up to 3.6 N when tensioned with 17 N. Therefore, the integration of the VSM in the needle gave the possibility to investigate how the deflection of the needle varies when the VSM is activated. The deflection decreased from 11.6 mm to 4.4 mm between 5-10 N pulled tensions demonstrating how the variable stiffness represents a possible solution to control needle deflection in tissues. Future studies will focus on the optimization of the VSM in terms of geometry and functionality in order to reduce the forces on the cables and minimize geometric variations. Manufacturing process and materials will be improved making the needle usable in a really working scenario. Moreover, combined studies of steering and variable stiffness will be developed in order to improve the target approach and avoid needle tip displacement.

REFERENCES

[1] N. J. van de Berg, D. J. van Gerwen, et al., "Design choices in needle steering—a review," *IEEE/ASME Transactions on Mechatronics,* vol. 20, no. 5, pp. 2172-2183, 2015.

[2] N. Abolhassani, and R. Patel, "Deflection of a flexible needle during insertion into soft tissue," in Engineering in Medicine and Biology Society, 2006. EMBS'06. 28th Annual International Conference of the IEEE, 2006.

[3] A. Majewicz, J. J. Siegel, et al., "Design and evaluation of duty-cycling steering algorithms for robotically-driven steerable needles," in Robotics and Automation (ICRA), 2014 IEEE International Conference on, 2014.

[4] S. Huber, M. Wagner, et al., "Benign Breast Lesions: Minimally Invasive Vacuum-assisted Biopsy with 11-Gauge Needles—Patient Acceptance and Effect on Follow-up Imaging Findings 1," *Radiology,* vol. 226, no. 3, pp. 783-790, 2003.

[5] I. De Falco, and J. J. van den Dobbelsteen, "Variable stiffness mechanism for needles: preliminary study," in Design of Medical Devices Conference (DMD), Vienna, 2015.

[6] A. M. Okamura, C. Simone, at al., "Force modeling for needle insertion into soft tissue," *IEEE transactions on biomedical engineering,* vol. 51, no. 10, pp. 1707-1716, 2004.

[7] M. Tanter, J. Bercoff, et al., "Quantitative assessment of breast lesion viscoelasticity: initial clinical results using supersonic shear imaging," *Ultrasound in medicine & biology,* vol. 34, no. 9, pp. 1373-1386, 2008.

[8] I. De Falco, C. Culmone, et al., "A variable stiffness mechanism for minimally invasive instruments and its integration in a surgical needle," *Medical engineering & physics*, under review, 2016.

Nintendo for Neurointerventionists: Technology for Remote Neurovascular Navigation

T.C. Gopesh[1], B. Yan[4], A.M. Norbash[2], A.A. Khalessi[3], J.R. Friend[1]

[1]*Center for Medical Devices and Instrumentation, Dept. of Mechanical and Aerospace Engineering;* [2]*Dept. of Radiology; and* [3]*Dept. of Neurosurgery; UC San Diego, USA*

[4]*Neurointernvention Unit, Royal Melbourne Hospital, Melbourne, Australia*
jfriend@eng.uscd.edu

INTRODUCTION

Treatment of saccular cerebral aneurysms was limited to surgical clipping until the advent and broad clinical adoption of endovascular coiling, now a preferred, relatively inexpensive, and statistically more successful option [1]. However, it is hampered by an absence of effective actuation methods for navigation and precise tip positioning. Magnetic [2], piezoelectric ultrasonic [3], and wire-pulley [4] devices have been proposed in the past, but have not found broad acceptance. The existing panoply of passive guidewires, catheters, balloons, stents, and flow diverters for the treatment of cerebral aneurysms cannot be steered *in vivo*. As a conequence, endovascular coiling is precluded for 17-25% of patients due to the location of the aneurysm in tortuous cerebrovasculature [5,6]. For those aneurysms judged to be treatable, coiling attempts fail 8-32% of the time [7,8,9]. Typically, in these cases the microcatheter cannot be steered into the dome of the aneurysm because it is simply pointing in the wrong direction. Worse, the coil deployment can shift the microcatheter tip out of the aneurysm or into an unfavorable direction, causing further coil deployment to be impossible.

In this project, we design and fabricate a prototype navigable microcatheter with a steerable tip and integrate it with a hand controller to control it. Combining soft robotics and hydraulically-actuated microchannels, it provides the neurointerventionist with a means to rapidly steer the tip in the desired direction *in vivo*. This inherently safe method uses saline as the working fluid, offering simplicity, ease of use, and design flexibility absent in previous approaches.

MATERIALS AND METHODS

The limiting outer diameter for a microcatheter to navigate to the most tortuous cerebral aneurysms is 1 mm. These typically have a 500 μm diameter inner lumen to provide a passage for the guidewire and detachable coils; the smallest guidewires are 360 μm in diameter, and are easily pushed through the 500-μm lumen. In the present work a novel meso-scale injection casting process was used to make steerable tips for guidewires and catheters. Starting with semi-circular glass rods and a flat glass slide, a two-part mold was created using a high hardness resin. Silicone rubber was pumped into the mold and an assembly of microtubes were used to blow compressed air to make microchannels within. Upon curing, steerable tips for the microguidewire and microcatheter with outer diameters of 400 μm and 750 μm respectively were obtained. Both enclose 50 μm diameter channels for hydraulically-actuated steering. Additionally, the microcather tip has a 500 μm diameter central lumen. Cross-sections of the microguidewire and microcatheter are shown in Fig. 1(c and d), respectively. In each case the 50 μm diameter channels were tethered to a handheld controller through microtubing to luer lock connectors. The risk of air embolism or arterial puncture possible in other actuator technologies is eliminated here by using saline as the working fluid.

The performance of the steerable tip was quantified through measurements of the tip bending angle versus input pressure over time, combining high speed imagery (Photron®), microfluidics pressure sensor (Elveflow®), custom image post-processing in MATLAB, and Gent's model for the strain induced in hyperelastic tubes by inflation [9]. The pressure is analytically represented by

$$P = \frac{2wC_1\left(\nu^2 - 1\right)}{r}\left[\frac{2\nu}{\left(\nu^2 + 1\right)^{1/3}}\right]$$

where P is the pressure, w is the wall thickness, r is the radius of the hydraulic channel, C_1 is the first hyperelastic constant, and $\nu = \lambda_1^2\lambda_2$; λ_1 and λ_2 are the principal stretch ratios in the axial and circumferential directions and C_1 was separately determined by conducting biaxial membrane tests on thin films [10].

RESULTS

Inflating one of the 50-μm channels, an axial differential strain is induced in the structure about its midplane – the axis of symmetry along the length of the tip – causing bending of the tip away from the inflated channel as shown in Fig. 1 (e-h). The bending angle is dependent on the inflation pressure; a C-shaped tip can be formed at only 20 psi. The tip may be steered in any direction by inflating only one or two of the three channels. Using four channels permits finer control of the deflection.

Avoiding radial expansion in this application is crucial, unlike the typical use of saline injection in a neurointerventional balloon inflation. The nonlinear stress-strain relationship of the hyperelastic media was tailored such that the initial inflation quickly strains the tip ~10 μm in increasing the tip diameter, while the axial expansion of the tip responsible for bending occurs over a far longer length scale, causing substantial

bending with insignificant radial expansion. Placing a fluorescent marker at the tip, and imaging it end-on as illuminated with a UV lamp, the crude prototype's precise control is illustrated in Fig. 1 (i-l).
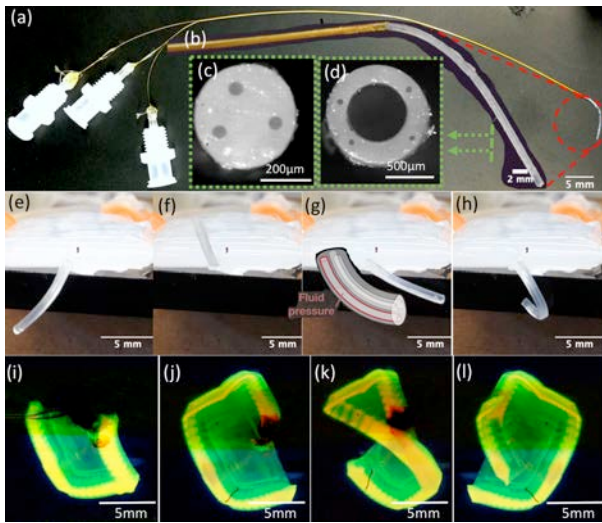
Fig. 1 Top row: a 400 μm diameter tip (enlarged, b) tethered to 15cm tubing incorporating connections to each of the 50μm (c) channels shown in the cross-sections. A lumen (d) can be incorporated for a 750 μm microcatheter tip. Pressurising the 50 μm channels with saline, the tip can be steered in multiple directions (e-h), with sufficient precision to crudely write UCSD (i-l). The inset in (g) shows how the device works: with a sealed tip, the structure is steered by imposing a fluid pressure from the attached tubing through the base into one or more channels.

Comparison of the experimentally obtained pressures reasonably fits the Gent model in Figure 2, validating the experimental results. The strains never exceed 10%, indicating a complex model for hyperelastic materials is unnecessary.
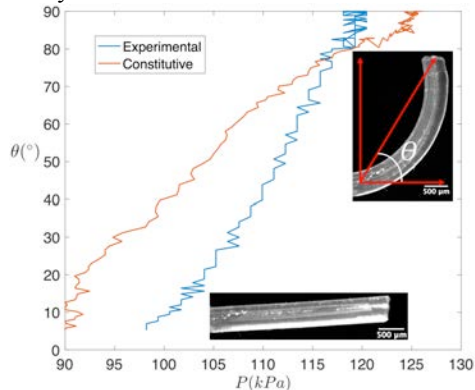
Fig. 1 Comparison of the experimental results with those obtained by the analytical Gent model.

DISCUSSION

We use a novel injection mold-casting method to fabricate circular steerable tubing encapsulating hydraulically actuated microchannels for neurointerventional manipulation. The outer diameter of the devices is 400 μm for the guidewire to 750 μm for the microcatheter. Using saline as the driving fluid, we demonstrated multi degree of freedom control of the tip deflection. Application of 20 psi (137 kPa) of pressure,

representing a light squeeze of the surgeon's hand using the handheld controller, causes bending of the tip in the respective direction, thus giving the user direct control of the steerable tip.

Our ongoing research involves testing of the steerable tip microcatheter in *ex vivo* models of currently inaccessible saccular aneurysms with collaborating neurointerventionists. The models are made from MRI scans of patients with saccular aneurysms in inaccessibly tortuous locations. Results and feedback from the testing will be used to develop refined prototypes paving the way for animal trials to come.

REFERENCES

[1] Molyneux, A.J., et al. The durability of endovascular coiling versus neurosurgical clipping of ruptured cerebral aneurysms: 18 year follow-up of the UK cohort of the International Subarachnoid Aneurysm Trial (ISAT). The Lancet. 385.9969 (2015): 691-697.

[2] Hetts, S. W., et al. Magnetically assisted remote controlled microcatheter tip deflection under magnetic resonance imaging. JoVE (Journal of visualized experiments). 74 (2013): e50299-e50299.

[3] Yun, C.H., et al. Multi-degree-of-freedom ultrasonic micromotor for guidewire and catheter navigation: The Neuroglide actuator. Applied Physics Letters. 100.16(2012): 164101.

[4] Feng W. X., et al. Highly precise catheter driving mechanism for intravascular neurosurgery. Mechatronics and Automation, Proceedings of the 2006 IEEE International Conference on. IEEE, 2006.

[5] Moon, K., et al. Treatment of ruptured anterior communicating artery aneurysms: equipoise in the endovascular era?. Neurosurgery. 77.4 (2015): 565-571.

[6] Raftopoulos, C., et al. Prospective analysis of aneurysm treatment in a series of 103 consecutive patients when endovascular embolization is considered first option. Journal of Neurosurgery. 93.2 (2000): 175-182.

[7] Suzuki, S., et al. Endovascular treatment of middle cerebral artery aneurysms with detachable coils: angiographic and clinical outcomes in 115 consecutive patients. Neurosurgery. 64.5 (2009): 876-889.

[8] Khatri, R., et al. Frequency and factors associated with unsuccessful lead (first) coil placement in patients undergoing coil embolization of intracranial aneurysms. Neurosurgery. 72.3 (2013): 452-458.

[9] Regli, L., et al. Endovascular coil placement compared with surgical clipping for the treatment of unruptured middle cerebral artery aneurysms: a consecutive series. Journal of Neurosurgery. 90.6 (1999): 1025-1030.

[10] Gent, A.N. Elastic instabilities in rubber. International Journal of Non-Linear Mechanics. 40.2 (2005): 165-175.

[11] Feng, W. W. Viscoelastic behavior of elastomeric membranes. Journal of applied mechanics. 59 (1992): S29-S34.

Exploring Reflected Light Intensity to Estimate Depth of the Basal Turn in Cochlear Implant Surgery

R. Yasin, G. Aiello, N. Simaan

Mechanical Engineering, Vanderbilt University,
rashid.m.yasin@vanderbilt.edu

INTRODUCTION

Cochlear implants (CIs) are the standard-of-care for treating severe to profound sensorineural hearing loss. As of 2011, there were only 70,000 Americans using cochlear implants out of a population of 1.5 million deaf individuals. An important improvement that will help bridge the gap between current and potential users is improved surgical guidance and feedback. This includes the creation of tools and techniques that enable safe and efficient electrode array (EA) insertion to maximize hearing preservation. Such soft insertion techniques would increase adoption of CIs for patients with residual hearing, where it is important to insert the EA atraumatically in order to retain inner ear function [1].

Regarldess of EA type, correct orientation and trajectory of the EA relative to the internal anatomy of the scala tympani is key to atraumatic technique. This work focused on perimodiolar EAs (e.g. Contour Advance® or Slim Modiolar [CI532] by Cochlear Corporation). These pre-curled arrays assume their contoured shape when a stylet is withdrawn from their body. Using an electrode holder, the EA is inserted to a depth marker before holding the stylet and advancing the array off the stylet (AOS technique).

During EA insertion, surgical perception may be hampered by three factors: interaction forces are small [2]; the exact internal geometry of sensitive and easily-damaged inner ear anatomy is not well-determined by examination of external anatomy [3]; even though the EA has markers to indicate the insertion depth at which AOS technique should be initiated, the cochleostomy location and anatomical variability introduce uncertainty in the insertion process.

To assist surgeons in proper EA orientation and depth for initiating AOS, we developed a visualization tool to assist in the CI insertion process and a light-intensity based estimation framework that will allow better estimation of depth of the basal turn to inform surgeons when to begin AOS. Previous work has shown that intracochlear visualization may be clinically useful [4] and that OCT may be used for registration to internal anatomy within the cochlea [5]. We are combining the simplicity of low-cost visual techniques with optical tool tracking and simple light intensity measurements to work towards a guided surgery techique that allows surgeons to better view the anatomy and use sofware-based visual feedback to guide the surgeon to more repeatably execute CI insertion with proper alignment and accurate insertion depth for initiation of AOS.

MATERIALS AND METHODS

We have developed a 3D printed Cochlear Inspection Tool (CIT) that clamps around a Medit 1mm fiberscope with 10,000 fibers. Weighing only 32 g, it fits comfortably in a surgeon's hand, Fig. 1. The fiberscope fits into the cochlea without contacting the walls of the scala tympani. The CIT is outfitted with optical tracking markers so that the location and orientation of the tool can be tracked and recorded during the procedure. After the CIT is used to determine the location and orientation of relevant anatomy, these measurements can be used to guide surgeons' hand movements while inserting the CI through the use of visual and audio cues generated by custom software we have created. In these experiments, a Claron Technology MicronTracker 2 was used to track the tool position and orientation.

In addition to using the CIT for increased surgical awareness, we wanted to characterize the distance to the basal turn from the cochleostomy site to increase accuracy in choosing the right depth to initiate AOS. Early experiments using optical flow and monocular imaging with automatic image segmentation were unreliable due to the feature-poor intra-cochlear environment. Therefore, we opted for a simple image-intensity method. When approaching the wall, more of the light from the fiber is reflected back into the image and image intensity increases – this intensity can be thresholded to determine proximity to the basal turn which can inform when to initiate AOS technique.
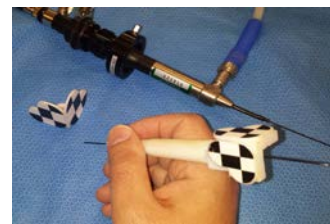
Fig. 1 Cochlear inspection tool with optical tracking markers on a fiberscope for low-cost inspection of cochlear anatomy to enhance surgeon knowledge and performance.

The method was tested on human temporal bones prepared with a lateral round window mastoidectomy mounted on an ATI Nano43 force-torque transducer. Repeated insertions were carried out using the bone holder setup and cartesian robot seen in Fig. 2a, 2b.

The CIT was mounted on a 3-axis Cartesian robot and aligned to have clear access through a cochleostomy into the cochlea. The robot was used to slowly insert the fiber into the cochlea vertically until its tip made contact with the wall of the basal turn. Contact with the wall

was determined by manually segmenting a rise in the force measurements indicating wall contact – this manual process is one source of potential error. After wall contact, the fiber was retracted 5mm to set a home point. From this point, repeated insertions were carried out in steps of 0.2 mm until reaching the original home point. An image was taken at each step to characterize the intensity vs depth relationship, Fig. 2c. The force sensor was unbiased at the start of each insertion into the cochlea and force data was filtered by a moving-window averaging filter with a length of 10 samples at 5kHz sampling frequency. Intensity was reported as the mean of all pixels in the image, normalized between 0 and 1.
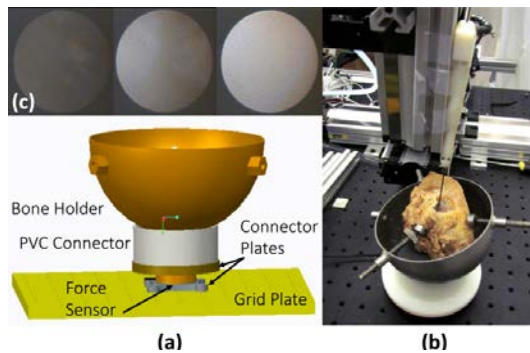
Fig. 2 (a, b) Experimental setup for controlled insertion of CIT into temporal bone specimen with force measurements and fiberscopic visualization (c) example intensity images as the fiberscope approaches the

We carried out 36 insertions in 3 temporal bones. Originally, 5 bones were analyzed using the experimental setup, however 2 bones were removed from analysis due to discoloration from mold/bacteria not representative of living anatomy due to long storage time. The 36 insertion experiments were divided into 3 groups of 4 insertions per bone. For each insertion group, the bone was removed and affixed to the setup in a new orientation to capture changes in approach angle and rotation of the endoscope relative to the bone.

RESULTS

Figure 3 shows the intensity-measurement results across 36 insertion in 3 temporal bones. The solid line is the average intensity, the error bars are the 95% confidence interval on the mean, the dotted lines are the 95% data intervals (two standard deviations from the mean), and the gray bounds represent the maximum and minimum intensities. In two insertion groups, the fiber was deflected away from the wall, reducing intensity measurements. Since a surgeon would know to reorient when seeing such a deflection, these were dropped from analysis in Fig. 3b. With this exclusion, a threshold of mean normalized intensity of 0.33 can estimate the basal turn depth in 95% of cases with an uncertainty of 1.2 mm without touching the wall of the basal turn.

DISCUSSION

This work shows the viability of using fiberscopic visualization of cochlear anatomy and the usefulness of

light-intensity-based methods for characterizing distance to the basal turn. This exploratory work presented a naïve approach to estimate the distance to the basal turn based on 95% of expected normalized intensity across bones. Future work should investigate Bayesian filtering considering measurement history for a given bone and a statistical prior across many bones to improve the distance estimation robustness and accuracy. We believe the intensity rise near the turn should be more prominent in a clinical setting where the surgeon can manually re-orient the fiber, and in living specimens where there will be less drying out of the bone which, even after re-wetting, contributed to decreased light reflectivity. The tools in this paper will be used in future experiments with trained surgeons to validate the usefulness of guided surgery in CI insertion in controlled user-study trials.
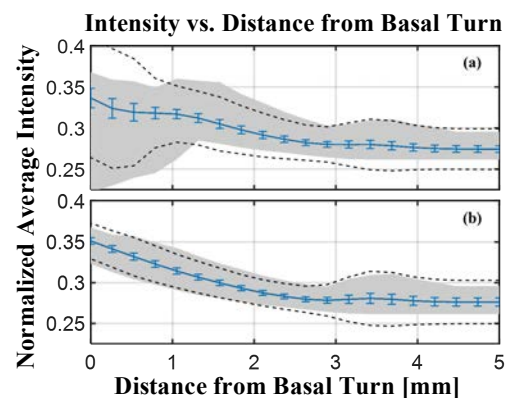
Fig. 3 Intensity vs wall distance results: mean intensity (solid line), 95% CI error bars oft he mean, 95% of expected data (dotted line), max and min bounds (gray area) ofr behaviour in (a) all insertions (b) insertions without fiber deflection.

REFERENCES

[1] T. J. Balkany, S. S. Connell, A. V Hodges, S. L. Payne, F. F. Telischi, A. A. Eshraghi, S. I. Angeli, R. Germani, S. Messiah, and K. L. Arheart, "Conservation of residual acoustic hearing after cochlear implantation.," *Otol. Neurotol.*, vol. 27, no. 8, pp. 1083–8, Dec. 2006.

[2] P. Rohani, J. Pile, L. a Kahrs, R. Balachandran, G. S. Blachon, N. Simaan, and R. F. Labadie, "Forces and trauma associated with minimally invasive image-guided cochlear implantation.," *Otolaryngol. Head. Neck Surg.*, vol. 150, no. 4, pp. 638–45, Apr. 2014.

[3] J. H. Noble, R. B. Rutherford, R. F. Labadie, O. Majdani, and B. M. Dawant, "Modeling and segmentation of intra-cochlear anatomy in conventional CT," in *Proc. SPIE 7623*, 2010, pp. 762302-762302–9.

[4] D.-I. A. Lueder Kahrs, R. Fellow, T. R. McRackan, and R. F. Labadie, "Intracochlear visualization -comparing established and novel endoscopy techniques."

[5] S. S. Gurbani, P. Wilkening, M. Zhao, B. Gonenc, G. W. Cheon, I. I. Iordachita, W. Chien, R. H. Taylor, J. K. Niparko, and J. U. Kang, "Robot-assisted three-dimensional registration for cochlear implant surgery using a common-path swept-source optical coherence tomography probe," *J. Biomed. Opt.*, vol. 19, no. 5, p. 57004, May 2014.

Neuromonitoring during Robotic Cochlear Implantation – First Clinical Experience

J. Ansó[1], O. Scheidegger[2], W. Wimmer[1], D. Schneider[1], J. Hermann[1], C. Rathgeb[1], N. Gerber[1], M. Stebinger[1], K. Gavaghan[1], G. Mantokoudis[3], M. Caversaccio[3], S. Weber[1]

[1]ARTORG Center for Biomedical Engineering, University of Bern, Switzerland

[2]Department of Neurology, ENMG-Station, University Hospital Bern, Switzerland

[3]Department of Head and Neck Surgery, University Hospital Bern, Switzerland
juan.anso@artorg.unibe.ch

INTRODUCTION

The first clinical application of image-guided cochlear implantation (CI) ([1]) lacked facial nerve monitoring (NM) as part of the clinical approach. At Bern (Switzerland), a robotic cochlear implantation (RCI) approach (Fig. 1) has been proposed incorporating integrated NM ([2]). The aim of the NM approach is to monitor function and preserve the facial nerve (FN) anatomy in case of navigation system error. The NM approach is based on multipolar stimulation through the facial recess (Ø 2.5 mm space between the FN and chorda tympani, Fig. 2). The aim of NM during RCI is to monitor facial nerve (FN) function and estimate trajectory-to-nerve distance during the procedure. The NM approach is designed threefold: 1) *Positive control*: a positive stimulating channel is used to have direct feedback of FN sensitivity at any time during surgery. 2) *Free-running EMG* ([3]): facial muscle activity is continuously monitored and presented to the surgeon to track the nerve status during drilling. 3) *Drill-FN safety distance assessment*: a discretized protocol is used to discriminate *safe* and *unsafe* trajectory passages ([4]). Herein, we present the first patient experiences using the proposed NM approach during RCI. We hypothesize that stimulus-triggered EMG via multipolar stimulation through the facial recess enables sensitive and specific (>95 %) drill-to-FN distance assessment during RCI.

MATERIALS AND METHODS

With approval of the local ethics commission (IRB Bern, Switzerland, KEK-BE Nr.156/13) a first-in-man RCI clinical is currently underway at the university hospital of Bern [5]. Prior to start the RCI procedure four fiducial screws (2.2mm × 5mm, M-5243.05, Medartis) are implanted in the mastoid of the patient. Then, a CT scan is acquired (SOMATOM, Siemens) and a trajectory planned to the entrance of the cochlea (Fig. 2). With the patient back in the operating room, the patient's head is accommodated into a non-invasive head-rest and electromyogram (EMG) electrodes are located in the facial (orbicularis oris and oculi) muscles. A pair of surface stimulating electrodes are positioned on the superficial branch of the FN serving as *positive control* stimulating channel. Then, a reference optical marker is fixed in the patient's mastoid to enable tracking of head movements during the procedure. After physical registration of the mastoid to the preoperative plan, RCI drilling is started (1000 RPM, 0.5 mm/s, 2 mm pecking steps, Ø 1.8 mm). At 3 mm before the FN, radiologic safety confirmation of the drilled axis is achieved via intraoperative CT imagery (xCAT, Xoran, USA) [5]. Consequently, an optimized drilling protocol (0.5 mm pecking steps, rest of drilling parameters the same as before) is initiated through the critical drilling phase (the facial recess segment) to reduce temperature.

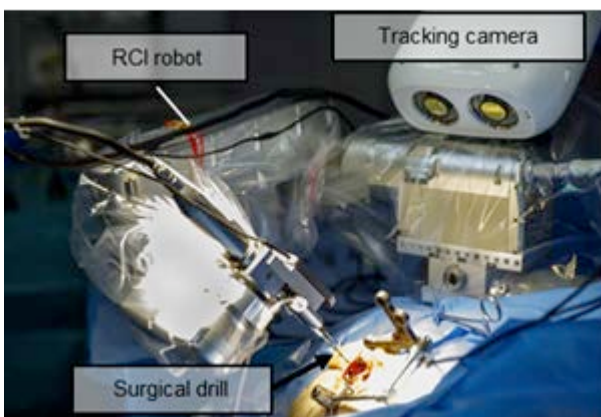**Fig. 1** RCI robot (arm, tracking camera, surgical drill and optical markers) performing drilling through the facial recess.

Fig. 2 The drill trajectory relative to the facial nerve the chorda tympani and the nerve monitoring measurement points

Drill-to-FN distance assessment based on NM is then achieved at five measurement points equally spaced (0.5 mm) through the facial recess: NMP_1: 1.2 mm in front of the FN center; NMP_5: 0.9 mm passed the FN center; NM_{1-5} axial distance = 0.5 mm. In each NM point, a series of monophasic stimulating pulses (0.2 to 2.5 mA, 250 µs) are applied per each of four stimulating channels of a multipolar probe ([4]). The minimum stimulating intensity that elicits an EMG response above threshold (> 100 µV) is determined as stimulus threshold. The stimulus threshold capable of discriminating *safe* and *unsafe* drill-to-FN distance margins was defined as 0.3 mA from previous in-vivo experimental studies ([4]). Bipolar (B_{1-2}) stimulus thresholds above 0.35 mA are used as indication of sufficient drill-FN distance above 0.4 mm (*safe passage)*. Bipolar stimulus thresholds below 0.35 indicate an *unsafe* (<0.1 mm, B1) or an uncertain drill-to-FN distance margin (0.1-0.4 mm, B2) ([2]). A manual NM stimulation modules is then used to verify threshold stimulation values from the automatic NM protocol. If the NM assessment confirms sufficient safety margins, RCI drilling is finalized to the entrance of the cochlea and CI electrode insertion is carried out.
Data analysis: NM data (EMG, stimulating signals and electrode-tissue contact impedances) were recorded for postoperative analysis. Drill-to-FN distance assessment was determined from postoperative CT images co-registered to the preoperatively segmented facial nerves. For each measurement point, the Euclidian distance from the drill to the FN surface was defined as closest distance (CD).

RESULTS

Up to date the RCI approach has been applied in n = 4 patients. In all cases, NM was able to determine drill-to-FN distance margins above 0.4 mm. The drill-to-FN distance (CD_{min}) were determined to be within the suggested margins (± 0.1 mm) (Table 1). This results in 100% sensitivity and specificity to discriminate drill-FN distance above 0.6 mm. In Figure 3, a representative facial recess trajectory (subject 2) showing a typical monopolar threshold pattern: decrease of stimulus thresholds as the drill approaches the FN center, and subsequent increase of values as the drill passes the FN. The bipolar thresholds were relatively large (>2 mA) for subjects 1-3, and above 0.5 mA in subject 4.

Table 1 Stimulus threshold and distance data (n = 4 subjects)

Subject	Min. stimulus threshold (mA)				FN-NM distance (mm)	CD_{min} (mm)
	B1	B2	B3	Mo.		
1	NR	NR	NM	2	> 0.7	0.82
2	NR	2.5	2.5	1.5	> 0.7	0.67
3	NR	NR	NM	2	> 0.7	0.78
4	1.25	0.5	0.5	0.4	> 0.7	0.61

NR: no EMG response; NM: not measured (Z > 22 KΩ)

Fig. 3 Postoperative co-registered stimulus thresholds (subject 2) relative to each of the 5 axial NM measurement points.

DISCUSSION

The proposed NM approach was capable of determining *safe* drill-to-FN proximity ranges during the first-in-man RCI cases (n=4). The NM results were consistent with in-vivo (sheep) experimental data at drill-to-facial nerve distance ranges above 0.6 mm ([4]). However, the robustness of the NM approach at the critical FN distance range (<0.3 mm) remains undetermined.

To minimize nerve risk in case of unexpected system error during the first RCI clinical trial, trajectories are planned at drill-to-FN distances above 0.4 mm. Therefore acquisition of NM data at the critical distance range (<0.3 mm) may become challenging. We propose to use our navigated NM probe (monopolar) during middle ear surgeries to validate stimulus threshold at dehiscent facial nerves (no bony covering, expected $ST_{mono} \leq 0.2$ mA) and directly above the facial nerve canal (thin bony covering, $ST_{mono} > 0.2$ mA).

ACKNOWLEDGEMENTS

REFERENCES

[1] Labadie RF, Balachandran R, Noble JH et al. Minimally invasive image-guided cochlear implantation surgery: first report of clinical implementation. Laryngoscope. 2014 August;124(8):1915–22

[2] Weber S, Gavaghan K, Wimmer W et al. Instrument flight to the inner ear. Science Robot. 2017 Mar; 2(4).

[3] Holland NR. Intraoperative electromyography. J. Clin. Neurophysiol. 2002;19(5):444–453.

[4] Ansó J, Dür C, Gavaghan K et al. A Neuromonitoring Approach to Facial Nerve Preservation During Image-guided Robotic Cochlear Implantation. Otol Neurotol. 2016; 37(1):89–98.

[5] Caversaccio M, Gavaghan K, Wimmer W et al. Robotic cochlear implantation: surgical procedure and first clinical experience. Acta Otolaryngol. 2017 Apr; 137(4):447–454.

Toward Safer Neurosurgery with an Active Handheld Instrument

F. Prudente[1], S. Moccia[1,2], A. Perin[3], R. F. Sekula[4], L. S. Mattos[2],
J. R. Balzer[4], W. Fellows-Mayle[4], E. De Momi[1], C. N. Riviere[5]

[1]*Dept. of Electronics, Information and Bioengineering, Politecnico di Milano, Milan, Italy*
[2]*Department of Advanced Robotics, Istituto Italiano di Tecnologia, Genoa, Italy*
[3]*Besta NeuroSim Center, IRCCS Istituto Neurologico C. Besta, Milan, Italy*
[4]*Department of Neurological Surgery, University of Pittsburgh, Pittsburgh, USA*
[5]*Robotics Institute, Carnegie Mellon University, Pittsburgh, USA*
francesca.prudente@mail.polimi.it, sara.moccia@polimi.it

INTRODUCTION

Improvements in microsurgical dissection techniques, skull base approaches, imaging modalities, and intraoperative neurophysiologic monitoring have led to a reduction in surgical morbidity and mortality for deep-seated brain tumors and cerebrovascular lesions. Despite these improvements, however, postoperative rates of cerebral infarction and cranial nerve deficits remain high and dramatically reduce quality of life in patients with a variety of brain disorders [1], [2]. In the case of petroclival meningioma, for example, the incidence of permanent cranial nerve deficits is between 20% to 76% while gross total resection is achieved in only 20% to 85% of patients [3]. An assist device that would allow the surgeon to reduce larger unintended movements, automatically avoiding sensitive tissues, may result in reduced morbidity for patients [4].

MATERIALS AND METHODS

This work consists of three main steps: (i) vessel segmentation, (ii) 3D reconstruction and (iii) implementation of the forbidden-region VF framework.

Segmentation Algorithm

A Geometrical Deformable Model (GDM)-based approach is used to perform vessel segmentation [5]. The vessel segmentation algorithm requires as initialization the manual selection of a starting point p_1 and an ending point p_2, which are then automatically connected with a minimal-cost path algorithm. The resulting path is used as initialization of the GDM algorithm. The deformation of the GDM is guided by intensity-based external forces, which are retrieved from the *vesselness* measures defined in [6].

3D Reconstruction Algorithm

The 3D reconstruction is performed in order to extract the 3D position of the segmented vessel surface in the Micron control reference system. Micron is a 6-DOF handheld instrument equipped with piezoelectric actuators so that its tip can move semi-independently of the hand motion (range of motion: Ø4.0 × 4.0 mm) [7]. The Micron system setup (Fig. 1) includes (i) an optical tracker (Apparatus to Sense Accuracy of Position (ASAP)) for tracking Micron tip position, and (ii) a stereo operating microscope (Zeiss OPMI, Carl Zeiss,

AG, Germany) equipped with two CCD cameras (*f*=30 Hz, 800x600 pixels). Since the controller of Micron works in the ASAP reference system while the target is detected by the stereo-cameras, calibration mappings are mandatory. A laser probe integrated into Micron is used to scan the surface, since the camera calibration must match a set of 3D tip positions measured by the ASAP with a set of 2D locations detected in the camera images [8]. For the 3D reconstruction, the Speeded Up Robust Features (SURF) detection algorithm is used [9]. The point cloud relative to the vessel position is retrieved by applying the sum-of-squared-distance-ray tracing method to corresponding point pairs. The vessel surface is reconstructed exploiting the convex hull, a triangular mesh that encompasses the retrieved point cloud.

Forbidden-Region Virtual Fixtures

The forbidden-region VF implements the vessel collision avoidance task, preventing the manipulator to enter into a predefined avoidance zone, representing the segmented vessel and a cylindrical safety zone surrounding it.

The control command is triggered as soon as the distance d between the tool tip and the vessel surface becomes lower than the cylindrical radius. Each time a new tip position sample is detected by ASAP, the algorithm finds the closest point p_s belonging to the vessel surface and computes d. The *Micron* tip is driven to reach a point distant d_{safety} (i.e. the cylindrical radius) from p_s if d is less than d_{safety}.
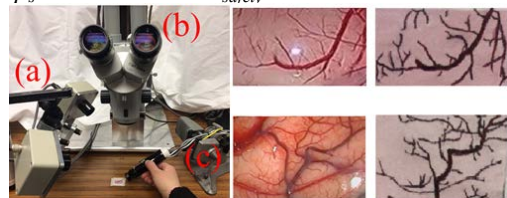

Fig. 1 On the left the system set-up: (a) ASAP tracking system; (b) Zeiss stereo operating microscope; (c) Micron manipulator. On the right orginal video frames and examples of printed pattern.

Experimental Protocol

The vessel segmentation algorithm was tested on fifty microscopy video frames acquired during two neurosurgical interventions at Istituto Neurologico Carlo Besta. The segmentation algorithm was evaluated

in terms of accuracy, sensitivity, specificity and Dice similarity coefficient, computed with respect to gold-standard manual segmentation performed by an expert.

For the VF performance evaluation, an experimental setup was developed to simulate the surgical environment and let Micron interact with phantom vessels. Three flat patterns that reproduce the vessels to avoid were printed (Fig.1). Twenty-one images of these patterns (seven of each pattern) with different orientations were captured by the left and the right camera of the Micron microscope (4× magnification). The accuracy of the 3D reconstruction was evaluated in terms of reprojection errors of the point cloud.

The vessel avoidance algorithm was tested in real time by operating Micron above an image of the vascular pattern and making repeated attempts to cross the blood vessel while in contact with the surface.

RESULTS

Vessel segmentation performance values are reported in Table 1. The reprojection error statistics computed for the 21 phantom images are shown in Table 2.

Table 1. Segmentation algorithm performance

	q_1	$\tilde{x}$	q_2	IQR
Acc	0.999	0.999	0.999	4.0e-04
Se	0.701	0.761	0.819	0.119
Sp	0.999	0.999	0.999	2.0e-04
DSC	0.796	0.8329	0.849	0.053

Acc=Accuracy; Se=Sensitivity; Sp=Specificity; DSC=Dice Similarity Coefficient; q_1= 1st quartile; $\tilde{x}$=median; q_3= 3rd quartile; IQR=Interquartile Range

Table 2. Reprojection error distribution for 21 phantom images

images	q_1	$\tilde{x}$	q_2	IQR
left	0.6791	0.8890	1.4158	0.7367
right	0.6901	0.8992	1.4276	0.7375

q_1= 1st quartile; $\tilde{x}$=median; q_3= 3rd quartile; IQR=Interquartile Range

Using the VF algorithm, the Micron tip was forced to lift over the vessel (green trajectory in Fig. 2) when the null position of the manipulator (red trajectory in Fig. 2) was within d_{safety} = 1.6 mm. The d measure over time when the VF is active (green) is plotted in Fig. 3 against what the distance would have been if the VF were inactive (red).
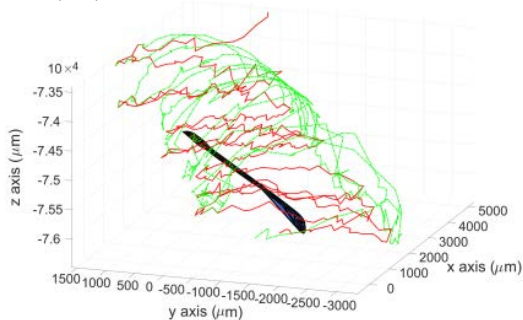

Fig. 2 Automatic avoidance of vessel (black). The Micron tip trajectories are shown for when the Virtual Fixtures are on (green) and off (red).
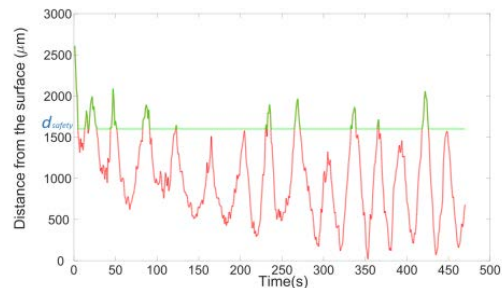

Fig. 3 Distance, d, of the Micron tip from the vessel surface over time when the Virtual Fixture is on (green) vs. what it would have been if the fixture were off (red). d_{safety} is the chosen safety distance (1600 μm).

DISCUSSION

In this paper, we presented a new approach to vessel avoidance for safe robotic assisted neurosurgery, which exploits an actuated handheld tool to reliably constrain penetration into predefined forbidden zones. Future work will aim at implementing a tracking algorithm for real-time applications in order to take into account also tissue deformation and the presence of surgical tools in the scene, which can eventually occlude the vessel to be avoided. A 3D phantom that reproduces a more truthful surgical scenario will be further developed for testing.

ACKNOWLEDGMENTS

REFERENCES

[1] Lawrence JD et al. An investigation into quality of life improvement in patients undergoing microvascular decompression for hemifacial spasm. Journal of Neurosurgery. 2017; 1-9.

[2] Sekula RF et al. Microvascular decompression for hemifacial spasm in patients> 65 years of age: an analysis of outcomes and complications. Muscle & nerve. 2013; 48(5): 770-776.

[3] Xu F et al. Petroclival meningiomas: an update on surgical approaches, decision making, and treatment results. Neurosurgical focus. 2013; 35(6): E11.

[4] Trope M et al. The role of automatic computer-aided surgical trajectory planning in improving the expected safety of stereotactic neurosurgery. Int J Comput Assist Radiol Surg. 2015;10(7):1127-40.

[5] Moccia S et al. Safety enhancement in robotic neurosurgery through vessel tracking. Proc 6th Joint Workshop on New Technologies for Computer/Robot Assisted Surgery. 2016.

[6] Frangi AF et al. Multiscale vessel enhancement filtering. Med Image Comput Comput Assist Interv. 1998;130-7.

[7] Yang S et al. Manipulator design and operation for a six-degree-of-freedom handheld tremor-canceling microsurgical instrument. IEEE/ASME Trans Mechatron. 2015; 20(2):761-72.

[8] Yang, S. Handheld micromanipulator for robot-assisted microsurgery. Ph.D. dissertation, Carnegie Mellon Univ. 2015.

[9] Bay H et al. Speeded-up robust features (SURF). Comput Vis Image Understanding. 2008;110:346-59.

Image-based Contact Stabilisation Inside the Beating Heart

B. Rosa[1,2], G. Fagogenis[1], J. Ha[1], P.E. Dupont[1]

[1]*Cardiac Surgery Department, Boston Children's Hospital, Boston, MA, USA*

[2]*ICube, CNRS, University of Strasbourg, Strasbourg, France*

b.rosa@unistra.fr

INTRODUCTION

While catheters have enabled a variety of beating-heart intracardiac procedures, the range of procedures has been limited by the inability to provide detailed visualization of the tissue at the catheter tip and by a lack of dexterity for tissue manipulation. Recent work has demonstrated that incorporating a tip-mounted camera (cardioscopy) can provide excellent imaging during tissue contact [1]. Furthermore, robotic control can provide additional dexterity. A fundamental challenge to implementing a robotic solution, however, is to provide the capability to stabilize the robot tip on a tissue structure inside the beating heart while ensuring that the applied forces are not excessive. While current solutions employ a combination of ultrasound imaging and force sensors [2], this paper proposes an image-based contact stabilization algorithm.

Cardioscopic images are acquired by pressing an optical window containing a chip-based camera and LED against the intracardiac tissue such that the blood is displaced. Exploiting the fact that images during contact with tissue are distinctly different from noncontact images of blood, it is possible to estimate the contact state and design a controller to drive robot position so that contact is maintained over a desired fraction of the cardiac cycle. This contact ratio acts as a proxy for mean contact force over the cardiac cycle. This low-bandwidth "force" control is relatively safe since it slowly adjusts robot tip position in response to the higher frequency heart motion. This paper describes the image-based controller together with initial validation results.

IMAGE-BASED CONTACT STABILIZATION

Our contact state estimator uses the Bag of Features (BoF) algorithm [3], a supervised machine learning algorithm usually used for high-level content retrieval in images. This approach uses a set of image descriptors as an input. In this study, we used the FAST feature detector [4] and LUCID descriptor [5], for a good balance between performance and computational burden. After training on a set of manually labeled examples, the algorithm is used for predicting the contact state c of a given input image,

$$c(t) = \begin{cases} 1, \text{contact} \\ 0, \text{no contact} \end{cases} \qquad (1)$$

Thanks to low computational burden in the feature detection and prediction steps, the estimation executes at video rate.

Using the contact state estimator, we wish to derive a controller that will stabilize the robot tip at a position which produces tissue contact for a specified fraction, r^d, of the cardiac cycle. Since the motion of certain heart structures is predominantly uniaxial, the contact ratio, r, can be expressed as a function of robot tip position, $x(t)$, and heart position, $x_h(t)$, along the direction of motion. This is illustrated in Fig. 1 for a valve annulus.
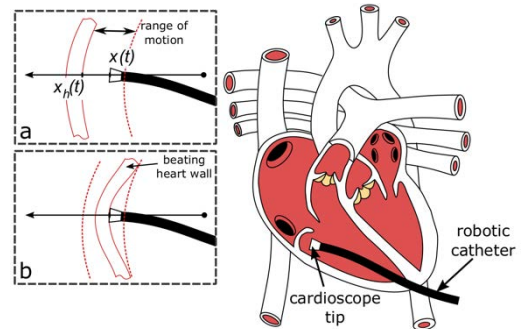

Fig. 1 Example of a transapically-inserted catheter approaching the pulmonary valve annulus to perform intracardiac surgery. (a, b) show the contact between the catheter at position $x(t)$ and the heart for two extremes of the wall movement $x_h(t)$.

Assuming that the measured heart rate, $1/T_c$, is slowly varying, the contact ratio can be computed from

$$r(t) = \frac{1}{T_c} \int_{t-T_c}^{t} c\left(x(u), x_h(u)\right) du \qquad (2)$$

Stabilizing the contact can then be achieved by regulating the value of r to a desired value r^d using proportional derivative control:

$$\dot{x} = K_p(r^d - r) - K_d \dot{r} \qquad (3)$$

Using this controller, robot tip position adjusts to regulate r to the desired value r^d. Under the assumptions that heart rate remains stable or slowly varying and that the contact ratio does not saturate, $r(t)<1$, controller stability can be demonstrated using the candidate Lyapunov function:

$$V(r) = \frac{1}{2}(r^d - r)^2 \qquad (4)$$

This 1 DOF controller can be used during teleoperation as part of a hybrid position-"force" control scheme. In this scenario, the operator controls tip orientation as well as tip position in the plane of contact while the contact stabilizer controls position normal to the plane of contact.

EXPERIMENTAL VALIDATION

To validate the approach, the contact state estimator was first trained and evaluated. Subsequently, the controller was tested in bench experiments. Each experiment is described below. The behavior of the

contact estimation algorithm was validated on cardioscopic images taken from six *in vivo* experimental surgeries, performed using five different cardioscopes (Fig. 2). A total of 1540 images were selected to build a balanced dataset, which was divided into three subsets: 70% for training; 15% for tuning algorithm parameters; and 15% for validation. The trained contact state estimator exhibited a specificity of 95.4% and a sensitivity of 95.4%. The average computational time (core i7 CPU) was 2.63msec per image.
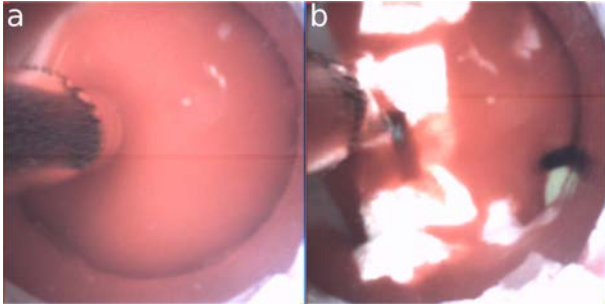

Fig. 2 Sample cardioscopic images. (a) No contact; (b) Contact.

To prepare for in vivo testing, the contact stabilization controller was evaluated in bench experiments as shown in Fig. 3. A concentric tube robot with a cardioscope camera at its tip was used together with a target oscillating at 75 "beats per minute." The *z*-direction of the robot was aligned under teleoperation to be approximately collinear with the direction of target motion and at a distance of several centimeters from the target. The contact controller was then turned on such that the robot approached the target and attempted to stabilize at the desired contact ratio. The controller gains were adjusted using a desired ratio of $r^d = 0.5$ to obtain an overdamped response. The final gain values were $K_p = 8$, $K_d = 3$.

Fig. 4 depicts the step response of the controller as it moves, initially from non-contact, to set points of $r^d = \{0.2, 0.4, 0.6, 0.8\}$. It is observed that robot displacement is smooth and the desired contact ratios achieved without overshoot. These tests will be repeated *in vivo* during the next few months.

DISCUSSION

The need for force sensing and haptics has long been debated in the robotics community. Despite general agreement on the benefits of force sensing, their cost, size and reliability have remained impediments to their general use. Furthermore, in medical applications, surgeons performing minimally invasive procedures have learned to substitute visual cues of tissue deformation for haptic feedback. Extending this visual approach to intracardiac surgery is difficult, however, owing to the opacity of blood, the poor resolution of ultrasound and the inability to directly image tissue with fluoroscopy.

The proposed technique combining cardioscopy and image-based contact stabilization provides a means for overcoming these challenges that does not rely on force sensing nor on high-bandwidth catheter motion.

Furthermore, since it is designed specifically around the expectation of a changing contact state, it does not suffer the usual stability problems associated with robot controllers making and breaking contact.
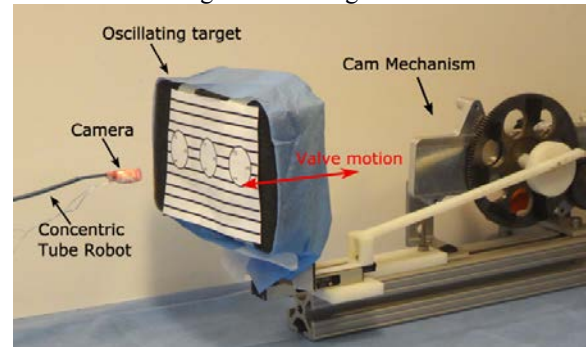

Fig. 3. Test set up for evaluation of contact controller. Cardioscope mounted on the tip of a concentric tube robot advances to press against oscillating paper target.
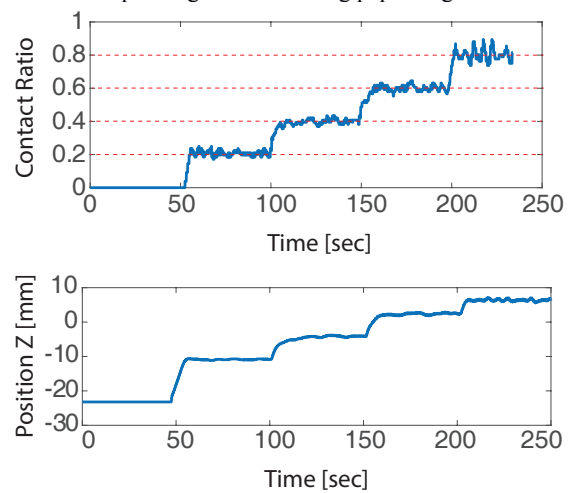

Fig. 4. Step response of contact ratio controller for a sequence of set points using the test set up of Fig. 3.

REFERENCES

[1] A. Ataollahi, I. Berra, N.V. Vasilyev, Z. Machaidze, P. E. Dupont, "Cardioscopic Tool-delivery Instrument for Beating-heart Surgery", *IEEE/ASME Trans. Mechatronics*, vol. 21, no. 1, pp. 584-590, 2016

[2] S. B. Kesner and R. D. Howe, "Robotic catheter cardiac ablation combining ultrasound guidance and force control," The International Journal of Robotics Research, vol. 33, no. 4, pp. 631–644, 2014.

[3] Fei-Fei, Li, and Pietro Perona. "A bayesian hierarchical model for learning natural scene categories." *Computer Vision and Pattern Recognition, 2005. CVPR 2005. IEEE Computer Society Conference on.* Vol. 2. IEEE, 2005.

[4] E. Rosten and T. Drummond, "Fusing points and lines for high performance tracking." in IEEE International Conference on Computer Vision, vol. 2, October 2005, pp. 1508–1511.

[5] A. Ziegler, E. Christiansen, D. Kriegman, and S. J. Belongie, "Locally uniform comparison image descriptor," in Advances in Neural Information Processing Systems, 2012, pp. 1–9.

Controlling Virtual Views in Navigated Breast Conserving Surgery using Tracked Instrument

T. Vaughan[1], T. Ungi[1,2], A. Lasso[2] , G. Gauvin[2], C.J. Engel[2], J. Rudan[1,2], G. Fichtinger[1,2]

[1]School of Computing, Queen's University, Kingston, Ontario, Canada

[2]Department of Surgery, Queen's University, Kingston, Ontario, Canada
gabor@cs.queensu.ca

INTRODUCTION

Virtual views are commonly used in computer-assisted surgical systems to show the positions of instruments relative to target anatomy. In a typical case, a technician uses keyboard and mouse interfaces to align the view to the surgeon's perspective. Technicians need to be highly trained in the surgical workflow and they are a costly presence in the already busy operating room. Reliance on technicians continues to pose an obstacle to wide-spread commercialization and clincial use of computer-assisted surgical systems.

We are accutely aware of this obstacle in our NaviKnife breast conserving surgery navigation system [1]. The NaviKnife features electromagnetic position sensors to track an eletrosurgery cautery device relative to a needle hooked in the target tumor. In the navigation display, the needle, tumor and cautery are shown to the surgeon (Fig. 1). This view needs to be aligned with the patient's anatomical directions and also adjusted to the position and view angle of the surgeon. When multiple surgeons operate, the view may need to alternate between them.
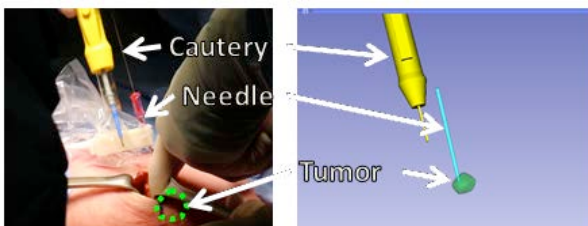

Fig. 1: Photograph of a bnigated breast conserving surgery and a virtual view aligned to the photograph's perspective

Our objective is to remove reliance on the technician by giving the surgeon direct and easy to use control of the virtual view. We demonstrate the concept in navigated breast conserving surgery, but it is readily applicable in computer-assisted surgical systems in general.

MATERIALS AND METHODS

We propose using the cautery device as a view-aiming pointer. The key concept is that objects in the navigation system are represented using coordinate systems that can be expressed relative to one another (Fig. 2a). Each electromagnetic position sensor defines a coordinate system updated in real-time. The virtual view is also considered as a coordinate system, so we can turn the tracked surgical cautery tool into a view-aiming pointer by temporarily aligning the view to the tool (Fig. 2b).
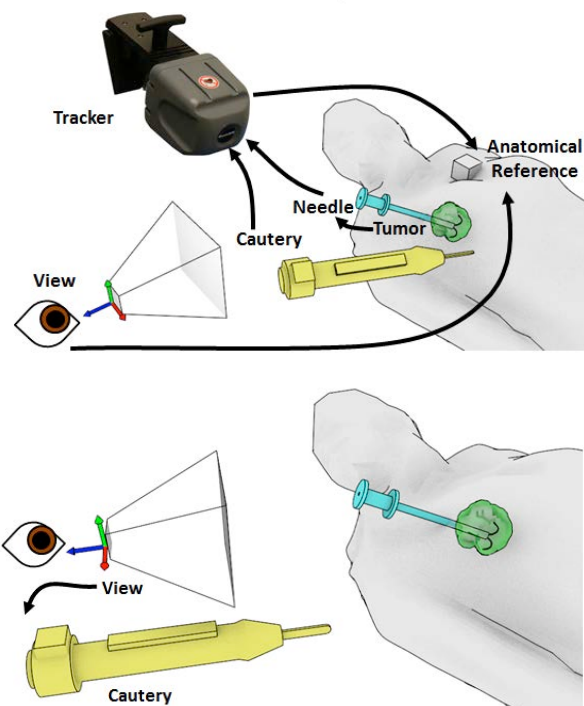

Fig. 2: Top, coordinate systems used in navigated breast conserving surgery. Bottom, the view is itself a coordinate system, and can be temporarily tracked relative to the cautery tool. Arrows indicate how coordinate systems are tracked relative to one another.

Setting the view proceeds in three steps: the surgeon associates the view to the cautery, the view is updated in real-time, the surgeon dissociates the view from the cautery when the view is satisfactory. The view setting process is started and stopped by a button click on a touchscreen (see Fig. 3), pressing on a foot pedal or by delegation to another individual in the operating room.

Based on our experience in the operating room, we also found that the technician frequently needed to adjust the view so that the tumor was in the center of the computer screen. The reason for this was that the tumor and view were both tracked relative to an anatomical reference (Fig 2a). The breast is a mobile organ, so it is easy for the tumor to move relative to the anatomical reference, while the view would remain stationary.
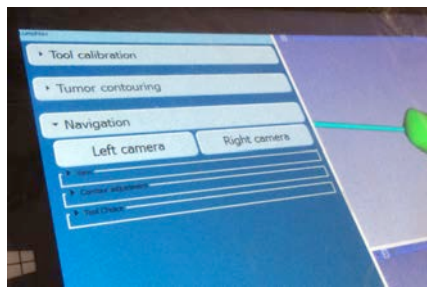
Fig. 3: The buttons on the touch-screen used to enable or disable instrument-control of the view.

To circumvent this issue, we developed an auto-center feature. Using this feature, we track the position of the tumor in the view. If the tumor moves outside a defined "safe zone", then the view translates such that the tumor is once again centered in the view (Fig. 4).
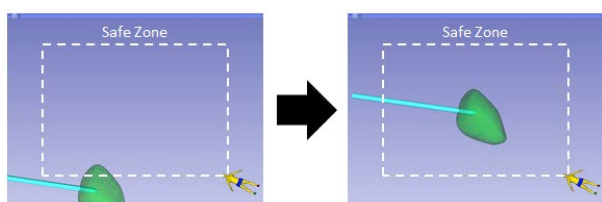

Fig. 4: Left, the tumor is outside the defined safe zone (dashed white box). Right, the view is moved such that the tumor is centered again.

We implemented view control methods in a simple plugin to NaviKnife based on open source platforms. We used the PLUS toolkit [2] to read sensor information, which was then relayed to 3D Slicer [3] for processing. The view control was implemented as plug-in to SlicerIGT (www.SlicerIGT.org). All of these platforms are open-source to foster collaboration and reproducible research.

RESULTS

The view control module has been incorporated into the NaviKnife breast conserving surgery system (Fig. 5).
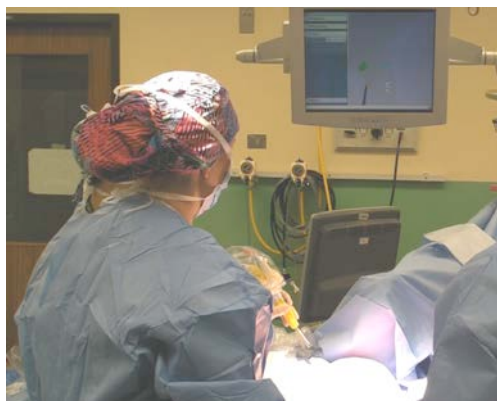

Fig. 5: Surgeon creating a virtual view using the cauterizer as a pointing device.

The cautery has been used as a view pointing device on 15 and the auto-centering feature on 12 patients. The technician who regularly runs the navigation system reported that the average number of manual interactions per procedure was reduced from 65 to 15, showing that over 75% of manual interactions were eliminated.

DISCUSSION

We have eliminated the majority of manual interactions required by the technician throughout navigated breast conserving surgery. This was accomplished by giving surgeons a mechanism to control the view directly and automating the task of centering the view on the tumor. Together these mark an important milestone in the translation of the NaviKnife breast conserving surgery navigation system.

The remaining manual interactions involve button clicks on the surgeon's behalf. Automatic view zooming is the next area for improvement. If the tumor is small or far from the cautery during the view set-up, it can appear too small on the computer screen (Fig. 6). The technician manually sets the zoom so the tumor will appear in a nominal size. We will automate this zooming procedure for the surgeon.
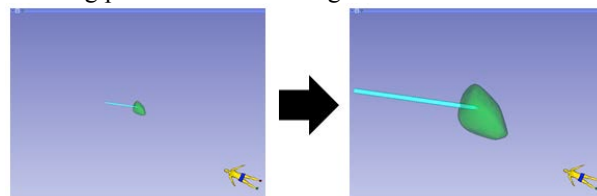

Fig. 6: Left, the tumor appears small because it is far from the initial view. Right, the view zooms in on the tumor.

Altogether, setting the view angle, center and zoom will eliminate nearly all interactions required from surgical navigation system technician. The remaining few button clicks can be executed by the two surgeons who are well-accustomed to using a tablet computer (Fig. 3). The tablet is conveniently placed for them in a sterile plastic bag over the patient' abdomen.

REFERENCES

[1] T Ungi *et al.*, Navigated breast tumor excision using electromagnetically tracked ultrasound and surgical instruments, IEEE Trans Biomed Eng, 63(3):600-6, 2016

[2] Lasso *et al.*, PLUS: open-source toolkit for ultrasound-guided intervention systems. IEEE Trans Biomed Eng., 61(10):2527-37, 2014

[3] Fedorov *et al.*, 3D Slicer as an Image Computing Platform for the Quantitative Imaging Network. Magnetic Resonance Imaging 30(9), 1323-41, 2012

Positioning and Stabilisation of a Minimally Invasive Laser Osteotome

M. Eugster[1], P. Weber[1], P. Cattin[2], A. Zam[3], G. Kosa[1], G. Rauter[1]

{1BIROMED, 2CIAN, 3BLOG}, Dep. of Biomedical Engineering, University of Basel, CH

manuela.eugster@unibas.ch

INTRODUCTION

Robot-assisted surgery allows surgeons to surpass limitations of human performance. In particular, surgical robots increase the surgeon's performance by functionalities like movement scaling and tremor suppression. Surgical robots also allow transferring preoperatively planned interventions precisely into practice. Particularly for frequent orthopedic interventions such as hip and knee surgeries, surgical robots can produce cuts with high fit accuracy. Commercially available systems for robotic and robot-assisted hip and knee replacement surgeries include the ROBODOC (THINK Surgical, Inc., Fremont, CA, USA), the Mako (Stryker Corporation, Kalamazoo, MI, USA), the NAVIO Surgical System (Smith and Nephew, London, UK) and iBlock (OMNIlife Science, East Taunton, MA, USA). Until today, the standards for cutting bone in surgical interventions are oscillating bone saws and drills. This is also true for cutting bone with robots. However, using a laser to cut bone offers multiple advantages. These advantages are: i) higher flexibility in the ablation geometry, ii) smaller cut width compared to mechanical tools, iii) high accuracy, and iv) faster healing of the bone ([1],[2]). The CARLO system is the first medical robot that can cut bone in open surgery without contact due to cold laser ablation technology [3].

Currently, we are developing a computer-aided laser osteotome which aims at combining the advantages of robot-assisted laser osteotomy and minimally invasive surgery (MIS). The final system will consist of a serial robot which manipulates a robotic endoscope. The end-effector at the tip of the endoscope will contain the laser optics as well as additional devices for laser ablation such as irrigation and vision (see Fig. 1). As a first application, we focus on uni-compartmental knee arthroplasty (UKA). We consider UKA as a benchmark application for MIS laser osteotomy since it involves cutting of thick bones such as the femur. UKA also allows testing any other functionality required for endoscopes in MIS laser surgery such as irrigation, laser ablation, endoscope manipulation, visual feedback, planning and execution of pre-planned movements, registration and tissue characterization.

One main challenge from the robotics point of view is the positioning and stabilization of the end-effector at the intervention site. Since the end-effector is far away from the robot's base, many sources of disturbance can influence the pose of the end-effector. This way, disturbances can prevent the irrigation device and the narrow laser beam from precise targeting. Thus, carbonization, unprecise cuts, or undesired tissue damage could be the result. To prevent disturbances from influencing the laser osteotome's performance, this paper presents for the first time a stabilization mechanism for a laser osteotome.

MATERIALS AND METHODS

Based on a preceding evaluation, we have decided to stabilize the end-effector of the laser osteotome using a bone mounted mechanism. This mechanism first attaches the end-effector to the bone. In a second step the endoscope's shaft is decoupled from the end-effector by decreasing the stiffness of the endoscope's flexible shaft. In this way, disturbances on the robot's side that holds the endoscope are not transferred to the end-effector.
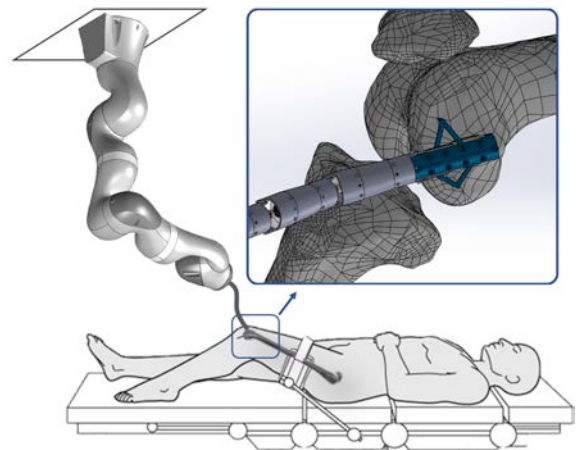

Fig. 1 Laser osteotome consisting of a serial robot that holds a robotic endoscope (Ø 15 mm). The end-effector (blue) of the robotic endoscope consists of a parallel robot which carries the laser optics and can be fixed to the bone which is to be cut. Figure adapted with permission from [4] and [5] (Copyright by AO Foundation, Switzerland).

More importantly, movements of the patient's bone are directly transferred to the endoscope's end-effector that will move together with the bone. Hence, the relative pose of the end-effector with respect to the bone can be maintained. A key component of the stabilization mechanism is a planar parallel manipulator integrated into the end-effector. This manipulator (six bar mechanism) is connected to the bone at two anchoring points. For example by means of suction. To position the laser, the mechanism has three planar active degrees of freedom (DoF) (see Fig. 2). In addition, the laser optics will have a long depth of focus that allows us to adjust the ablation location in vertical direction.
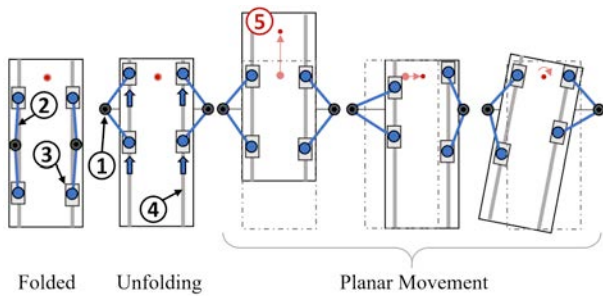
Fig. 2 Schematic illustration of the mechanism's DoF. From left to right; Folded during insertion, unfolding and attaching by moving the four sliders accordingly, planar movement in two translations and a rotation. The mechanism's parts are: Two fixed anchoring points (1) and four legs (2) mounted on actuated sliders (3) that can move on linear rails (4) (designated by grey lines). The laser (5) operates orthogonal to the end-effector.

The main components of the six bar mechanism are: the base, the body of the end-effector, and two legs on each side. Each of the four legs is mounted on one side on a separate slider which can glide on a separate linear rail (see Fig. 3). The other side of each leg can pivot about the corresponding anchoring point. All four sliders are actuated from outside the endoscope using cables with pre-tension springs controlled by motors. During insertion and extraction of the endoscope into and out of the patient, the legs can be folded away, making the mechanism suitable for MIS.
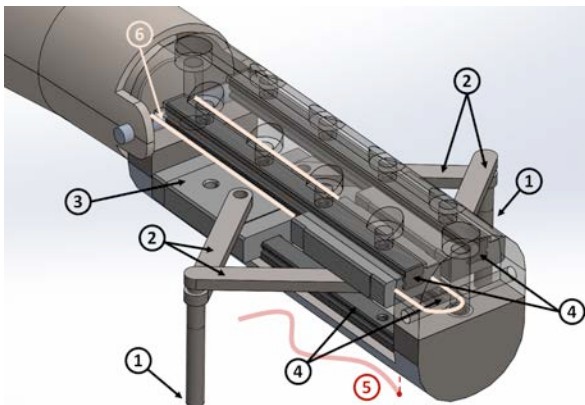

Fig. 3 CAD-model of the mechanism mounted on the robotic endoscope. (6) illustrates the cable actuator of the upper right leg. The other part numbers are described in Fig. 2.

One crucial characteristic of the mechanism is the space in which the end-effector can place the laser optics when the anchoring points are set. The shape and size of this workspace depends on four mechanical parameters of the mechanism, namely the length of the legs, the length of the linear rails, the distance between the anchoring points, and the distance between the linear rails on the right and left side of the mechanism. In order to maximize the workspace of the laser, the respective optimal set of parameters needs to be found. This is known as "the synthesis problem" in parallel robotics [6]. We used a custom written search algorithm in MATLAB to find the four parameters which result in a maximal workspace in terms of the covered area by the laser.

RESULTS

From all the parameter sets investigated, the largest workspace calculated has a size of 762 mm^2. It is obtained with the largest considered rail length of 35 mm, a leg length of 7 mm, the minimal considered rail distance of 5 mm and an anchoring distance of 18 mm. The resulting workspace is shown in Fig. 4. The simulation results also showed that the shape of the workspace is symmetric and has a similar form for all parameter sets which lead to large workspaces.
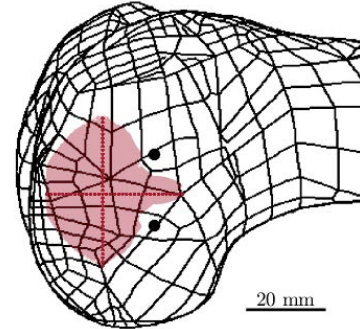

Fig. 4 Illustration of the largest obtained planar workspace of the mechanism (in red) projected onto the femur for size relation. The anchoring points are marked by black dots. The dotted lines represent the maximal straight cuts parallel (39 mm) and orthogonal (35 mm) to the virtual line that connects the two anchor points.

DISCUSSION

This paper describes the design of a parallel robot that is connected to the surface of bone and provides a stable platform for minimally invasive laser osteotomy. The mechanism enables up to 35 mm long straight line cuts parallel and 39 mm orthogonal to the base of the robot as illustrated in Fig. 4. It enables a workspace which is approximately 1.5 times larger than the footprint of the mechanism.

ACKNOWLEDGMENT

REFERENCES

[1] Baek, Kyung-won, et al. A comparative investigation of bone surface after cutting with mechanical tools and Er: YAG laser. Lasers in surgery and medicine 47.5 (2015): 426-432.

[2] Rajitha Gunaratne, G. D., et al. A review of the physiological and histological effects of laser osteotomy. Journal of Medical Engineering & Technology 41.1 (2017): 1-12.

[3] Bruno, Alfredo E., Hans-Florian Zeilhofer, and Philipp Jürgens. Carlo-computer assisted and robot guided laser-osteotome. U.S. Patent Application No. 13/497,520.

[4] Selic, Mario, et al. Robot. U.S. Patent No. D692,041. 22 Oct. 2013.

[5] AO Surgery Reference, Aosurgery.org, 2017. [Online]. Available: http://www.aosurgery.org. [Accessed: 20-Mar- 2017].

[6] Merlet, Jean-Pierre. Parallel robots. Vol. 128. Springer Science & Business Media, 2006.

Robotic-assisted Platform for USgFUS Treatment of Moving Organs

A. Diodato[1], A. Schiappacasse[2], A. Cafarelli[1], S. Tognarelli[1], G. Ciuti[1], A. Menciassi[1]

[1]*The BioRobotics Institute, Scuola Superiore Sant'Anna, Pisa, Italy,*

[2] *Camelot Biomedical Systems S.r.l.*
a.diodato@sssup.it

INTRODUCTION

Focused Ultrasound Surgery (FUS), also referred as High Intensity Focused Ultrasound (HIFU), is a non-invasive therapeutic technology that enables the treatment of several pathologies. FUS delivers ultrasound energy onto the human tissue for treating tumours by causing thermal or mechanical necrosis into the target area without harming surrounding tissues. Although Ultrasound guided FUS (USgFUS) has some limitations, *e.g.* thermal mapping, it offers major advantages, such as lower cost and platform encumbrance, and the possibility to monitor the treatment with a higher frame rate that allows real-time therapy monitoring and compensation of physiological movements. The use of a robotic-assisted approach for USgFUS may relieve the problems related to the predictability and repeatability of the current procedures by enhancing accuracy, safety and flexibility of the treatment. Indeed, there are already some platforms for extracorporeal USgFUS that operate in clinical setting, such as the HAIFU JC (Chongqing Haifu Medical Technology Co. Ltd, Chongqing, China), EchoPulse (Theraclion, Malakoff, France) and Alpius 9000 (ALPINION Medical Systems, Seoul, Korea). However, these platforms are not able to compensate organs motion during sonication. This limitation is partially solved in some research platforms by exploiting a Pulse Width Modulation (PWM) signal for the HIFU transducer. In Chanel *et al.*, an all-in-one robotized FUS system was developed for real-time intra-abdominal organ motion compensation through US visual servoing [1]. Seo *et al.* developed a visual US-based servoing system for ablating moving medical target [2]. Exploiting a sophisticated timeline schedule, the authors are able to interlace two US sources thus achieving a motion compensation accuracy of 1.7 mm (RMS) on average with a sonication duty cycle of 50%.

In this framework, the FUTURA (Focused Ultrasound Therapy Using Robotic Approaches) project (*www.futura-project.eu*) proposes a robotic-assisted platform for flexible HIFU treatment. The control of two independent anthropomorphic manipulators (one equipped with a HIFU transducer and with an US confocal imaging probe and the other one with a 3D US imaging probe) provides to the FUTURA platform a high flexibility in terms of operating workspace and maneuverability. The FUTURA platform is able to treat

moving target areas during HIFU sonication and in this paper the authors report the performance of the system in terms of treatment precision.
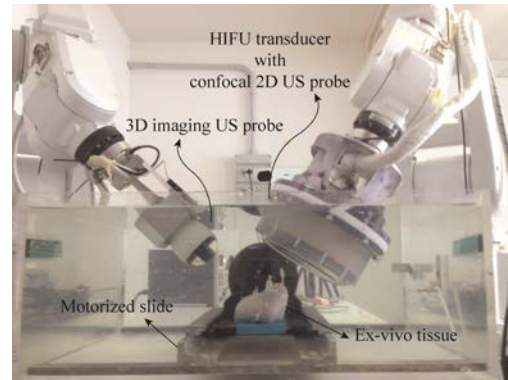

Fig. 1 – Experimental setup of the FUTURA platform with the robotic, monitoring and therapeutic modules. An *ex-vivo* porcine kidney is placed on a 1 DoF motorized slide for simulating the organ motion.

MATERIALS AND METHODS

The FUTURA platform is composed by different modules (Fig. 1): i) a robotic module including two 6 DoFs anthropomorphic manipulators (monitoring and therapeutic manipulators - ABB IRB 120); ii) a therapeutic module with a dedicated broadband 16 channels wave generator with power output capability of 20W/channel and a 16 channels annular array HIFU transducer; iii) a monitoring module composed of two different US probes (a 2D imaging US probe - Analogic Ultrasound PA7-4/12 - confocal to the HIFU transducer mounted on the therapeutic manipulator; and a motorized 3D imaging US probe - Analogic Ultrasound 4DC7-3/40 - mounted on the monitoring manipulator), both connected to a US machine (Analogic Ultrasound SonixTablet) The platform control architecture (based on Robot Operating System – ROS) allows controlling all components (i.e., robotic, monitoring and therapeutic modules) involved in FUS treatments through a dedicated Human Machine Interface (HMI) with an accurate real-time visualization of the working environment.

The FUTURA platform treats moving target area using machine learning and computer vision techniques and exploiting a PWM signal for the HIFU transducer. More precisely, our strategy is the combination of three different modules: i) a tracking and detection module; ii) a trajectory prediction module; and iii) a safety check module. The tracking and detection module estimates the motion of a Region of Interest (ROI) selected by the users through the HMI. This module is based on the ap-

proach named Tracking-Learning-Detection (TLD) described in [3], which decomposes the long-term tracking task into tracking, detection, and learning. The tracker follows the selected ROI in the US image stream using optical flow. The detector localizes similar patches in the image via a template matching approach using the Normalized Correlation Coefficient (NCC) as the main similarity measure. A variance filter and a random fern classifier are employed in the specific detector implementation as a pre-filtering stage to reduce computational costs. The learning task combines the tracker and the detector information in order to: *i)* correct and re-initialize the tracker when the detector is more confident, and *ii)* update the internal model of the detector when the tracker is more confident.

The trajectory prediction module learns the trajectory estimated by the tracking and detection module, and it drives the therapeutic manipulator during HIFU sonication even when the US images are completely distorted. Namely, the prediction module learns the organ motion using a Gaussian process model with a periodic kernel (solving a uni-dimensional regression problem). When the organ motion is learned, the therapeutic manipulator starts to follow the predicted motion of the currently tracked area. Before shooting, the safety check module computes the distance between the current target position in the US image and its predicted position, thus allowing to sonicate only if this distance is smaller than a settable threshold (*e.g.*, 1 mm). Therefore, if a deviation is detected between the tracked trajectory and the learned trajectory, the HIFU sonication is disabled until the new target trajectory is learned or the target area starts following again the estimated trajectory.

In order to assess the performance of the FUTURA platform, an experimental setup has been designed (Fig. 1). To simulate the organ motion, an *ex-vivo* porcine kidney is placed on a motorized slide and its motion is set as a sine function with amplitude 200 mm and frequency 0.2 Hz (12 breaths per minute). Three tests have been performed in dynamic condition. The first test aimed to evaluate the precision of the compensation motion method. The target area has been set on the US image provided by the 3D probe mounted on the monitoring manipulator. Then, the therapeutic module was activated following the learned trajectory without sonicating. The procedure has been performed 10 times on different kidney target areas and all the data have been recorded to evaluate the vector error between the target and the nominal HIFU focal spot. The second test evaluated the time needed to satisfy the safety check before and between HIFU irradiations. We planned a sonication composed by 100 time slots of 1 s which are executed only if the safety check is satisfied. The values of frequency and acoustic power of the sonication are 1200 kHz and 115 Watts respectively (able to perform a thermal lesion on chicken breast), while the 3D monitoring probe acquires images at 15 Hz. Finally, two lesions in static and dynamic conditions have been performed, displaced 10 mm on the chicken breast. These lesions have been performed through a sonication composed of 20 time slots of 0.9 s with the aforementioned values of acoustic power and frequency.

RESULTS

Fig. 2 illustrates the results of the first test performed without sonication. The box and whiskers plot shows that the motion compensation error norm is always lower than 1 mm. The achieved accuracy is less than the accuracy reported in Seo *at al.* [2]. The second test evaluates the time needed to satisfy the safety check before and between HIFU irradiations. The needed time is 0.07±0.04 s with a maximum value of 0.17 s. The result of the third test is shown in Fig. 3 where two lesions are performed in static and dynamic conditions, which were found to be similar.
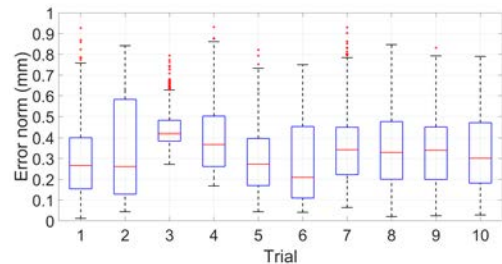

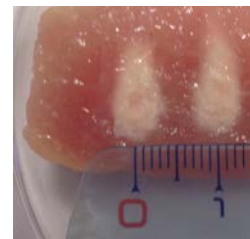**Fig. 2** – Boxplot of the error between the target area and the HIFU focal spot.

Fig. 3 – Lesions on chicken breast performed in static (0 mm) and dynamic conditions (10 mm).

DISCUSSION

This work assesses the ability of a novel USgFUS robotic platform to perform sonication and lesion on moving organs. The platform employs machine learning and computer vision techniques to track, learn and follow organ motion. Namely, FUTURA follows periodic motion trajectory with accuracy better than 1 mm. The HIFU irradiation is performed only if the distance of tracked and learned trajectories is lower than 1 mm for a time slot that can be chosen accordingly to the desired duty cycle. Indeed, the duty cycle is the duration of the time slot divided by the sum of this duration and the time needed to satisfy the safety check. Therefore, the lesions on chicken breast were performed with a duty cycle of about 90%. Future works aim to extend the FUTURA compensation method on 3D moving organs.

REFERENCES

[1] L. A. Chanel, *et al.*, "Robotized High Intensity Focused Ultrasound (HIFU) system for treatment of mobile organs using motion tracking by ultrasound imaging: An in vitro study," EMBC (2015).

[2] J. Seo, *et al.*, "Ultrasound image based visual servoing for moving target ablation by high intensity focused ultrasound." Int. J. Med. Robot (2016).

[3] Z. Kalal, *et al.* "Tracking-learning-detection." IEEE Trans. Pattern Anal. Mach. Intell. (2012).

Augmented 3D Catheter Navigation using Constrained Shape from Template

R. Trivisonne[1], E. Kerrien[1], S. Cotin[1]

[1]*Inria, France*
raffaella.trivisonne@inria.fr

INTRODUCTION

Endovascular surgery is a medical specialty of minimally invasive procedures, which relies on the use of catheters, guide-wires and other endovascular devices, to reach and treat a variety of pathologies. During the intervention, fluoroscopic images provide the clinician with live feedback on the anatomy of the patient, and the position and shape of the catheter. In conventional 2D fluoroscopic guidance, the complexity of the procedure, the radiation exposure and the loss of depth perception in X-ray images, are reasons why improved means of visualization have been investigated Commercial systems are already available [5], fusing live X-ray images with pre-acquired 3D MRI or CT images. This can be further improved by reproducing the 3D navigation of the catheter, which would otherwise remain 2D. Several approaches have been proposed, based on computer vision, numerical simulations, or the use of physical sensors ([8], [1], [7]). In [6] the authors present a method to retrieve the 3D position of the catheter combining the 2D fluoroscopic view with pre-operative models of the vasculature. In this context of augmented endovascular procedures, we propose a method to retrieve the 3D navigation of the catheter from a single view scenario, without the use of external sensor. Using a combination of visual features extracted from the fluoroscopic image, and the registered pre-operative 3D vessel surface, we drive a constraint-based numerical simulation, which allows us to retrieve the 3D catheter shape from fluoroscopic images. This will allow clinicians to virtually explore different angles of view without moving the imaging equipment.

MATERIALS AND METHODS

To reconstruct the 3D shape of a flexible device, we perform a real-time physics-based simulation of the flexible tool constrained by information extracted from the live fluoroscopic data and boundary conditions arising from the pre-operative vascular surface. The mechanical consistency provided by the physics-based model of the flexible tool avoids ambiguous situations and provides a complete and accurate 3D visualization of the catheter. The model of the surgical tool is based on Timosenko beam theory, solved using an efficient finite element method and a co-rotational approach [4]; it is represented as a series of serially-linked beam elements, where each node has 6 degrees of freedom [2] and the mechanical parameters are coherent with the reality. Currently image-features are easily extracted and tracked using OpenCV; we used a catheter with radiopaque tags every 1cm in order to have a higher

gradient variation. We impose that the projection of each 3D node should coincide with its corresponding point onto the image; to do that, we allow each 3D nodes to slide along the line of sight, defined between its corresponding 2D point detected in the image and the optical center of the camera. Nevertheless, 2D image features alone are not sufficient to retrieve the 3D shape of the device. Assuming that the position of the point through which the catheter is inserted, is known in 3D (for instance, obtained thanks to makers located on the catheter sheath), we define a further geometrical constraint enforcing the catheter to slide along a direction which reproduces the orientation of the insertion valve. A set of unilateral constraints are applied along the shaft of catheter to prevent crossing the surface of the 3D anatomy. Each of these constraints applies 1 dof unilateral contact force along the normal of the triangulated vessel surface, in order to enforce Signorini conditions i.e. A contact force is applied if and only if a (set of) point(s) of the device model move(s) outside of vessel geometry (see [9] for instance). As all of these are linear constraints (i.e. sliding constraints on a line), they allow to solve the problem with a Lagrangian approach for FE models [4] where the global equation is expressed with a static formulation.

$$\begin{pmatrix} \mathbf{K} & \mathbf{J^T} \\ \mathbf{J} & \alpha\mathbf{I} \end{pmatrix}\begin{pmatrix} \Delta\mathbf{X} \\ \lambda \end{pmatrix} = \begin{pmatrix} \mathbf{0} \\ \delta \end{pmatrix}$$

Where for each iteration, $\mathbf{K}$ is the stiffness matrix of the FE model, $\Delta\mathbf{X}$ is the equilibrium state of the 3D positions of the catheter, δ is the violation of the constraints and $\mathbf{J}$ is the Jacobian of the constraints.

RESULTS

We performed catheter insertion on a rigid phantom. Two data-set have been acquired through a 3D capable angiography C-arm at low and high fluoroscopy frequency, performing some 3D acquisitions (CBCT) to retrieve the real 3D position of the catheter and validate our simulation; 3D and 2D images are registered through calibration [3]. Beside the catheter navigation under 2D fluoroscopy and 3D scans to validate the reconstructed shape at times, we acquired some fluoroscopic images while shifting the table downwards, orthogonally to the direction of insertion, to simulate movement deriving from patient's breathing motion or machinery adjustment, showing the robustness of our method to important motion. We exploited the temporal coherence of the detected markers to bind the 2D markers with the corresponding 3D nodes of the catheter. To validate our registration, we computed the Euclidean distance between the simulated catheter and

the real one, previously retrieved from segmentation. For the first data-set, we had an average error of 2.7±0.7mm, corresponding to 11% of vessel diameter; for the data-set at 7.5pps, the higher acquisition rate produced more noisy and blurred images, entailing a higher error in the registration process (4.8±0.8mm). Within this second data set (Fig.1), we wanted to test as well the robustness of our method to potential table movement or breathing motion of the patient, i.e. any potential movement in a direction different from the direction of insertion. For that, we shifted the table 50mm downwards, under the assumption that the camera stays fixed. In this second phase, the registration error uniformly increases during the downwards shift (8±0.6mm average deviation) due to the reprojection error of the calibration matrix that is not uniform along the image. The surface's constraint was not active.
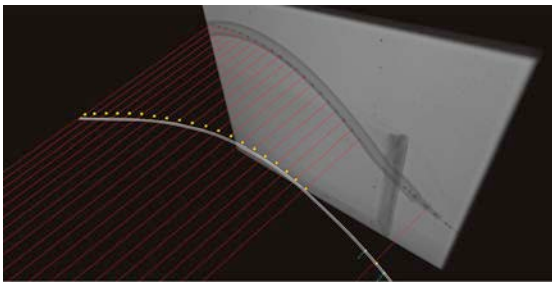

Fig. 1 3D catheter reconstruction for Real Dataset at the end of the insertion. Red lines represent the line of sight of projective constraints; yellow points represent the real catheter, obtained from segmentation of 3D medical images.

In any case, this kind of error can be easily compensated since the movement of the table can be known from the set-up parameters. Moreover, typical breathing motion of a patient reaches an amplitude of at most 2cm, i.e. inferior to the displacement imposed in this test. In order to evaluate our registration within a less trivial anatomy, we created a synthetic data-set simulating a catheter insertion. We recorded the images of the insertion, as under fluoroscopic guidance, and we used it as ground truth for the following registration. An average error of 0.8±0.07mm, corresponding to the 4% of the total diameter of the vessel, is registered (Fig.2). Detection errors and calibration errors, are compensated through empirical parameters α applied on the constraints.

Fig. 2 Different views of 3D catheter reconstruction for Synthetic dataset; blue and red catheter are respectively the real and the simulated one.

DISCUSSION

In this work, we presented a single view reconstruction method to retrieve the 3D navigation of the catheter. Dealing with a rigid registration, this could be potentially applicable to neuro interventional radiology procedures, where brain's movement is limited. In order to progress towards different clinical application, we will investigate other detection methods to deal with guidewires or untagged catheters, and automatic calibration to deal with deformations and breathing motions. Eventually, we will exploit this simulation to reduce the acquisition frequency, where the information between two images will be provided by the simulation itself.

REFERENCES

[1] Condino, S., Ferrari, V., Freschi, C., Alberti, A., Berchiolli, R., Mosca, F., Ferrari, M.: Electromagnetic navigation platform for endovascular surgery: how to develop sensorized catheters and guidewires. The international journal of medical robotics + computer assisted surgery : MRCAS 8(3), 300–10 (2012).

[2] Cotin, S., Duriez, C., Lenoir, J., Neumann, P., Dawson, S.: New approaches to catheter navigation for interventional radiology simulation. MICCAI 8(Pt 2), 534–42 (2005).

[3] Gorges, S., Kerrien, E., Berger, M.O., Trousset, Y., Pescatore, J., Anxionnat, R., Picard, L., Bracard, S.: 3D Augmented Fluoroscopy in Interventional Neuroradiology: Precision Assessment and First Evaluation on Clinical Cases (2006).

[4] Felippa, C.A., Haugen, B.: A unified formulation of small-strain corotational finite elements: I. Theory (2005).

[5] VesselNavigator by Philips.

[6] Groher, M., Bender, F., Khamene, A., Wein, W., Heibel, T.H., Navab, N.: 3D Guide Wire Navigation from Single Plane Fluoroscopic Images in Abdominal Catheterizations. pp. 356–360.

[7] Pujol, S., Pecher, M., Magne, J.L., Cinquin, P.: A virtual reality based navigation system for endovascular surgery. Studies in health technology and informatics 98, 310–2 (2004).

[8] Schwein, A., Kramer, B., Chinna Durai, P., Walker, S., O'Malley, M., Lumsden, A., Bismuth, J.: Flexible Robotics With Electromagnetic Tracking Improve Safety and Efficiency During In Vitro Endovascular Navigation. Journal of Vascular Surgery 63(1), 285–286 (2016).

[9] Courtecuisse, H., Allard, J., Kerfriden, P., Bordas, S.P.A., Cotin, S., Duriez, C.:Real Time simulation of contact and cutting of heterogeneous soft-tissue. Med. Image Anal. **18**(2) (2014) 394-410.

Self-Supervised Siamese Learning on Stereo Image Pairs for Depth Estimation in Robotic Surgery

M. Ye[1], E. Johns[2], A. Handa[3], L. Zhang[1], P. Pratt[4], G.-Z. Yang[1]

[1]The Hamlyn Centre for Robotic Surgery, IGHI, Imperial College London, UK
[2]Dyson Robotics Laboratory, Imperial College London, UK
[3]OpenAI, USA
[4]Department of Surgery and Cancer, Imperial College London, UK
{menglong.ye, e.johns}@imperial.ac.uk, ankur@openai.com

INTRODUCTION

Robotic surgery has become a powerful tool for performing minimally invasive procedures, providing advantages in dexterity, precision, and 3D vision, over traditional surgery. One popular robotic system is the da Vinci surgical platform, which allows preoperative information to be incorporated into live procedures using Augmented Reality (AR). Scene depth estimation is a prerequisite for AR, as accurate registration requires 3D correspondences between preoperative and intraoperative organ models. In the past decade, there has been much progress on depth estimation for surgical scenes, such as using monocular or binocular laparoscopes [1,2]. More recently, advances in deep learning have enabled depth estimation via Convolutional Neural Networks (CNNs) [3], but training requires a large image dataset with ground truth depths. Inspired by [4], we propose a deep learning framework for surgical scene depth estimation using self-supervision for scalable data acquisition. Our framework consists of an autoencoder for depth prediction, and a differentiable spatial transformer for training the autoencoder on stereo image pairs without ground truth depths. Validation was conducted on stereo videos collected in robotic partial nephrectomy.

MATERIALS AND METHODS

In this work, depth estimation is addressed by training a non-linear function in the form of an autoencoder, outputting per-pixel "inverse depth" (disparity) from a single RGB image. Given stereo image pairs along with intrinsic and extrinsic camera parameters, we formulate a self-supervised deep learning framework as shown in Fig.1. The autoencoder estimates the disparity map D_l from image $\mathbf{I}_l$. This map is then transformed using a Spatial Transformer ST [5], along with image $\mathbf{I}_r$ (counter-part of $\mathbf{I}_l$), to reconstruct $\mathbf{I}_l^*$ via bilinear interpolation. Training the network then requires minimising the reconstruction errors between $\mathbf{I}_l$ and $\mathbf{I}_l^*$.

In this paper, two network architectures for depth estimation are investigated. The first (Fig.1a) is a basic depth estimation network, similar to [4], but modified using, DeConvNet [6] for the autoencoder. For efficient training, we keep the convolutional and deconvolutional layers of DeConvNet, and remove the fully connected
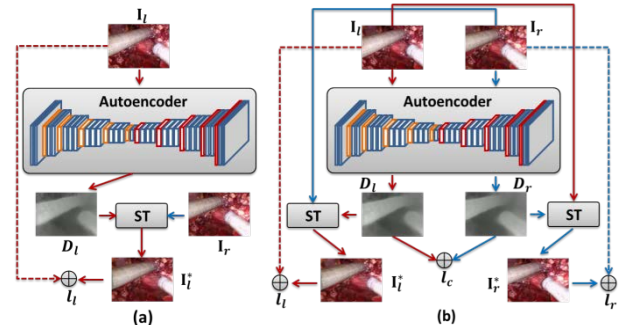

Fig. 1 Self-supervised depth learning networks. (a) Basic architecture. (b) Siamese architecture.

Table 1 Autoencoder architecture. Conv: convolution; Deconv: deconvolution; Pool: max pooling; Unpool: max unpooling; In: input channels; Out: output channels; K: kernel size; S: stride.

Encoder		Decoder	
Layer	**In/Out/K/S**	**Layer**	**In/Out/K/S**
conv1_1	3/64/3/1	unpool5	-/-/2/2
conv1_2	64/64/3/1	deconv5_1	512/512/3/1
pool1	-/-/2/2	deconv5_2	512/512/3/1
conv2_1	64/128/3/1	deconv5_3	512/512/3/1
conv2_2	128/128/3/1	unpool4	-/-/2/2
pool2	-/-/2/2	deconv4_1	512/512/3/1
conv3_1	128/256/3/1	deconv4_2	512/512/3/1
conv_3_2	256/256/3/1	deconv4_3	512/256/3/1
conv_3_3	256/256/3/1	unpool3	-/-/2/2
pool3	-/-/2/2	deconv3_1	256/256/3/1
conv4_1	256/512/3/1	deconv3_2	256/256/3/1
conv4_2	512/512/3/1	deconv3_3	256/128/3/1
conv4_3	512/512/3/1	unpool2	-/-/2/2
pool4	-/-/2/2	deconv2_1	128/128/3/1
conv5_1	512/512/3/1	deconv2_2	128/64/3/1
conv5_2	512/512/3/1	unpool1	-/-/2/2
conv5_3	512/512/3/1	deconv1_1	64/64/3/1
pool5	-/-/2/2	deconv1_2	64/3/3/1
conv6	512/512/3/1	conv0	3/1/3/1

layers to reduce the number of parameters in the network. Batch normalisation and rectified linear units are added after each convolutional/deconvolutional layer, and a convolutional layer is included in the last layer to produce the per-pixel disparity map for a total of approximately 31,800,000 parameters (see Table 1). The loss function used for this basic architecture is based on the L1 reconstruction error:

$$l_l = \frac{1}{N}\sum_{i,j}|\mathbf{I}_l(i,j) - \mathbf{I}_l^*(i,j)|. \tag{1}$$

The second architecture is a Siamese network that performs depth estimation on both $\mathbf{I}_l$ and $\mathbf{I}_r$ images (Fig.1b). The two autoencoders have the same structure as the first architecture, but share the same weights during training. This architecture enables us to fully utilise the image dataset, and generalise the network model for both left and right cameras. The loss now is a combination of the outputs from an image pair, and includes the left-right disparity consistency:

$$loss = \alpha_l l_l + \alpha_r l_r + \alpha_c l_c. \qquad (2)$$

Here, l_r is derived similarly as in Eq. 1. $\alpha_l = \alpha_r = 0.5$, and $\alpha_c = 1.0$ weight the individual losses, and l_c is the disparity consistency loss:

$$l_c = \frac{1}{N}\sum_{i,j}|D_l(i,j) - D_r(i + D_l(i,j),j)|. \qquad (3)$$

RESULTS

Our depth learning networks were implemented using the Torch library on an HP 840 workstation (12 GB NVidia Titan X GPU). We trained both architectures on an *in vivo* dataset collected in a partial nephrectomy procedure performed using a da Vinci Si surgical system. Our dataset includes 20,000 stereo pairs of rectified images, which are randomly sampled over 11 video sequences. The images are resized to 192×96-pixel for efficient training on a GPU.

The Adam optimiser [7] is adopted for loss minimisation. We trained both architectures with 40 epochs on our training dataset. The learning rate was initialised to 10^{-4}, and reduced by half for every 5 epochs. The batch sizes were 25 (for basic) and 16 (for Siamese), and the total training time were approximately 8 hours and 18 hours, respectively. The trained frameworks only require single image as the input, and take approximately 7ms in depth estimation on a 192×96-pixel image.

For testing, we used a separate video sequence of 3000 stereo pairs of images. We compared our Siamese architecture to the basic architecture, as well as two popular stereo matching approaches, ELAS [8] and SPS [9]. As ground truth depth labels are not available for our *in vivo* surgical data, we evaluate estimated disparity maps using Structural Similarity Index (SSI) [10] (instead of L1 for fair comparisons). For all approaches, SSIs (range of [0.0,1.0]) are calculated between every pair of $\mathbf{I}_l$ and $\mathbf{I}_l^*$, and $\mathbf{I}_r$ and $\mathbf{I}_r^*$ in the testing dataset. Table 2 lists the mean SSI accuracies of all approaches, which shows that the deep learning based approaches outperform the others, with the Siamese architecture achieving the best performance. Finally, example qualitative results of the basic and Siamese networks are presented in Fig. 2, which shows the Siamese network providing more consistent depth estimation than the basic network.

DISCUSSION

In this work, we have presented self-supervised learning frameworks for depth estimation in surgical images. We introduced a basic depth estimation network which
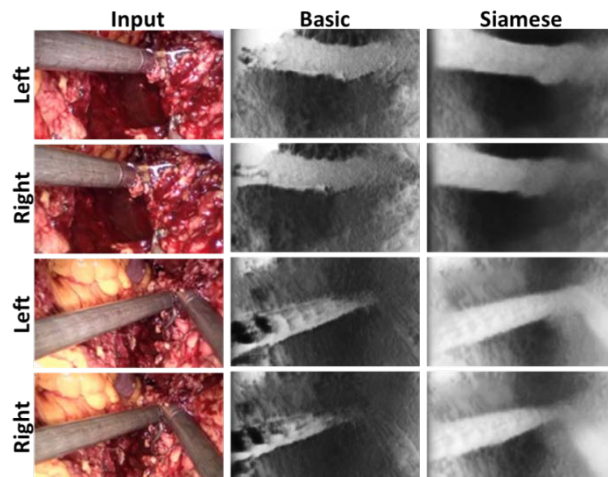

Fig. 2 Example pairs of image results of the basic and Siamese network architectures. High intensity values indicate close distances to cameras.

Table 2 SSI measures on image reconstruction quality based on estimated disparity maps. Higher means indicate better performance.

Methods	ELAS [8]	SPS [9]	Basic	Siamese
Mean SSI	0.473	0.547	0.555	**0.604**
Std. SSI	0.079	0.092	0.106	**0.066**

includes an autoencoder and a spatial transformer, and then extended this to a Siamese network which improves the model generalisability. Experiments conducted on *in vivo* videos collected during robotic surgery, showed that our approach performs accurate depth estimation, and outperforms standard stereo matching approaches. Our framework does not require known depth labels during training, and thus provides superior applicability to large-scale *in vivo* video processing where known depths are not available.

REFERENCES

[1] Mountney P., Yang G.Z. Motion compensated SLAM for image guided surgery. MICCAI. 2010; 496-504.

[2] Chang P.L., et al. Robust real-time visual odometry for stereo endoscopy using dense quadrifocal tracking. IPCAI. 2014; 11-20.

[3] Eigen D., et al. Depth map prediction from a single image using a multi-scale deep network. NIPS. 2014; 2366-2374.

[4] Garg G., et al. Unsupervised CNN for single view depth estimation: Geometry to rescue. ECCV. 2016; 740-756.

[5] Handa A., et al. gvnn: Neural network library for geometric computer vision. ECCV. 2016 Workshops; 67-82.

[6] Noh H., et al. Learning deconvolution network for semantic segmentation. ICCV. 2015; 1520-1528.

[7] Kingma D., Ba J. Adam: A method for stochastic optimizatoin. arXiv preprint. 2014; 1412.6980.

[8] Geiger A., et al. Efficient large-scale stereo matching. ACCV. 2010; 25-38.

[9] Yamaguchi K., et al. Efficient joint segmentation occlusion labelling, stereo and flow estimation. ECCV. 2014; 756-771.

[10] Wang Z., et al. Image quality assessment: from error visibility to structural similarity. IEEE Trans. Image Process. 2004; 14(4) 600-612.

A Wirelessly Actuated Robotic Arm for Endoscopy

T. Qiu[1], S. Palagi[1], F. Adams[1,2], U. Wetterauer[2], A. Miernik[2], P. Fischer[1,3]

¹Max Planck Institute for Intelligent Systems, Stuttgart, Germany

²Department of Urology, University Medical Centre Freiburg

³Institute of Physical Chemistry, University of Stuttgart

fischer@is.mpg.de

INTRODUCTION

Endoscopy enables a number of important minimally invasive medical procedures. Current commercial flexible endoscopes with small diameter often have only one bending section near the tip with only one degree of freedom (DoF). This strongly limits the area that can be reached by the endoscope. Researchers have made many efforts to develop multi-DoF miniaturized robotic endoscopes that can be controlled in multiple bending sections and that still possess an overall size small enough to enter the body through a single-port [1]. Robotic endoscopes are normally actuated by tendons [2], pneumatics [3] or the rotation of concentric tubes [4]. In comparison to these tethered approaches, wireless actuation allows for more flexibility and easier miniaturization.

Ultrasound is a promising way to transfer power wirelessly *in vivo*. Recently, we reported an active surface actuator that directly converts ultrasound power into mechanical work via acoustic streaming from an array of micro-bubbles [5]. Here, we apply such wireless actuators to a miniaturized robotic arm, which works as an endoscopic tip (Fig. 1). The active surfaces consisting of arrays of micro-bubbles are attached to the arm and generate streaming of the adjacent fluid under ultrasound excitation. The recoil force actuates the arm. Different bubble sizes are addressed by different ultrasound frequencies, thus multiple DoFs are realized by the arm and require only one tunable ultrasound source.

MATERIALS AND METHODS

The active surfaces were fabricated by photolithography, as described previously [5]. Briefly, the micro-cavity arrays were made of SU-8 photoresist (MicroChem) with the desired dimensions. Here, two kinds of cavity sizes with the same depth of 120 μm, but different diameters 30 μm and 50 μm are used (Fig. 2(b) and 2(c)). The surfaces were diced into suitable dimensions to fit on the robotic arms.

A miniaturized robotic arm onto which the active surfaces were affixed was printed with VeroBlack material using a 3D printer (Objet 260 Connex, Stratasys). As shown in Fig. 2(a), the 3D-printed arm consists of three sections (with a cross-section of 2 mm × 2 mm and a length of ~5 mm) connected in series with two passive steel hinges (ϕ0.8 mm) in orthogonal direction. Active surfaces (2 mm × 4 mm) with different micro-cavity sizes were glued to two orthogonal surfaces onto the 1st arm section.

The arm was tested in a customized ultrasound excitation apparatus (a water tank of 50 × 50 × 50 mm³ with a piezoelectric disk ϕ50 mm × 3 mm). Two ultrasound frequencies, *i.e.* 52 kHz and 44 kHz, were used to address the two active surfaces with different bubble sizes (and bubble resonance frequencies), respectively.
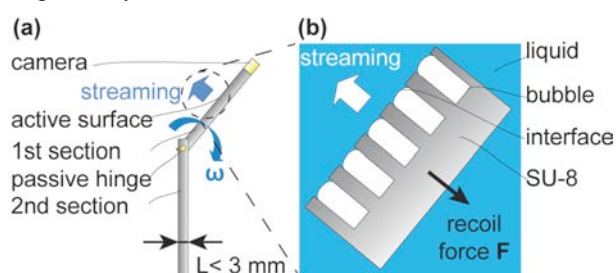

Fig. 1 Scheme of the miniaturized robotic arm. (a) The rotation of the 1st section of the arm is actuated by an "active surface" wireless actuator attached to the surface. (b) An enlarged view of the active surface, which consists of an array of microbubbles with controlled size. Under ultrasound excitation, the oscillation of the bubbles generates streaming in the fluid and the recoil force actuates the arm.
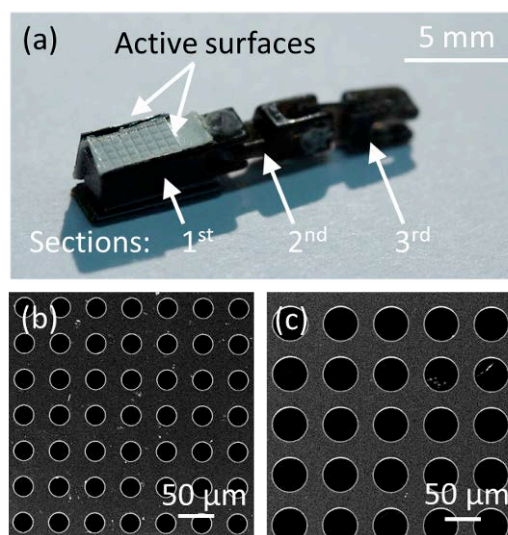

Fig. 2 A 3D-printed miniaturized robotic arm, which consists of three sections connected by passive hinges. Active surfaces are attached to the surfaces on the 1st section to achieve two DoFs (a). Two SEM pictures of the active surfaces are shown. They consist of micro-holes with the same height 120 μm, but different diameters 30 μm (b) and 50 μm (c), respectively.

RESULTS

As shown in Fig. 3, the 3D-printed mini-arm can achieve two rotational DoFs thanks to the two active surfaces. Fig. 3 shows the wireless actuation of the arm, which is held under water by tweezers through which no power is transmitted. The arm is powered wirelessly by ultrasound, and the piezoelectric transducer is at a distance of 30 mm from the arm. Once the mini-arm is submerged in water, air bubbles are sealed in the micro-cavities on the active surfaces, as the surface is hydrophobic. The size of the micro-bubbles is determined by the cavity size, and corresponds to different acoustic resonant frequency, as we showed previously [5]. First, an ultrasound field of 44 kHz is applied and excites the bubbles of 50 µm in diameter, which causes ultrasonic streaming and thus propels both the 1st and 2nd sections causing a rotating to the left (shown as rotation ω in Fig. 3 (b)). When the ultrasound frequency is changed to 52 kHz, the second active surface with 30 µm bubble in diameter is activated, which results in the rotation φ of the 1st section (Fig. 3 (c)). In this way, two rotational DoFs are realized with the arm. With more active surfaces attached on all four sides of the arm, it is in principle possible to achieve bidirectional rotations in two DoFs.
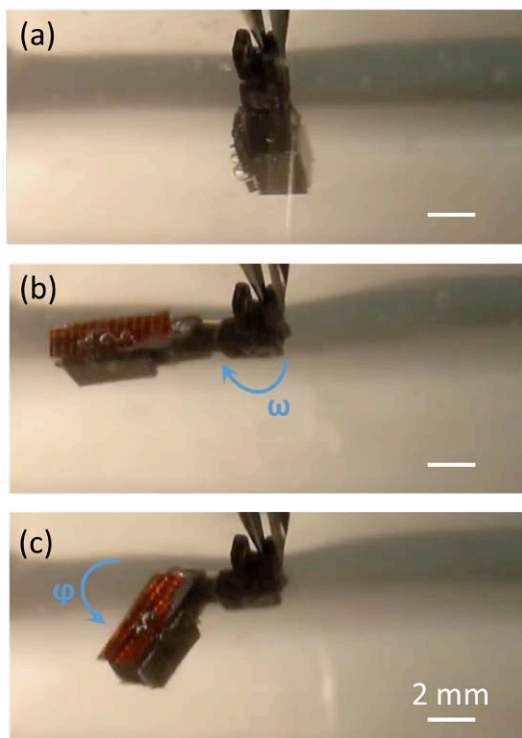

Fig. 3 Snapshots from a video showing the 2 DoF wireless actuation of the 3D-printed miniaturized robotic arm. (a) The arm is held under water by tweezers and stays still without ultrasound. (b) Ultrasound excitation at 44 kHz excites the active surface for the 2nd section and causes a rotation ω, due to fluidic streaming. (c) Changing the ultrasound frequency to 52 kHz results in the rotation φ of the 1st section.

DISCUSSION

We report a novel miniaturized robotic arm, which achieves two controlled DOFs under wireless actuation by ultrasound. The novel actuation mechanism reported herein is compatible with medical ultrasound, thus it has the potential to power miniaturized medical robots and endoscopes. Indeed, in addition to the demonstrated 3D-printed mini-arm, a second arm consisting of two aluminum sections was implemented and provided with a miniaturized camera (1 mm × 1 mm × 1.85 mm, Naneye 2D sensor, Awaiba). Comparing this second arm with a commercial flexible endoscope, although the sealing and illumination have not yet been included in the system, the arm has an overall smaller size in both the lateral size and the bending radius (Fig. 4). These advantages will allow better coverage of the endoscope to hard-to-reach positions in the body as well as minimize the potential side-effect of the procedure. Future work will address these both *in vitro* and *ex vivo*.
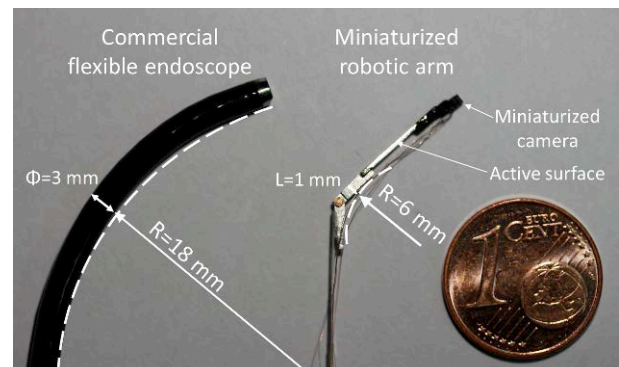

Fig. 4 Comparison of a commercial flexible endoscope with the miniaturized robotic arm based endoscope constructed here. Both the lateral dimension of the endoscope and the bending radius are smaller in the constructed system. A miniaturized camera is attached to the tip of the active surface on the 1st section.

REFERENCES

[1] J. Shang, K. Leibrandt, P. Giataganas, *et al.* A Single-Port Robotic System for Transanal Microsurgery—Design and Validation. IEEE Robotics and Automation Letters. 2017; 2(3): 1510-7.

[2] L. Fichera, N.P. Dillon, D. Zhang, *et al.* Through the Eustachian Tube and Beyond: A New Miniature Robotic Endoscope to See Into the Middle Ear. IEEE Robotics and Automation Letters, 2017; 2(3): 1488-94.

[3] F. Maghooa, A. Stilli, Y. Noh, *et al.* Tendon and Pressure Actuation for a Bio-inspired Manipulator based on an Antagonistic Principle. IEEE ICRA, 2015; 2556-61.

[4] P.E. Dupont, J. Lock, B. Itkowitz, *et al.* Design and Control of Concentric-Tube Robots. IEEE Transactions on Robotics. 2010; 26(2): 209-25.

[5] T. Qiu, S. Palagi, A.G. Mark, *et al.* Wireless Actuation with Functional Acoustic Surfaces. Applied Physics Letters. 2016; 109: 191602.

Disposable Force Sensing Clip for Robotic Surgical Instruments

C. A. Seneci, S. Anastasova, G. Z. Yang

Hamlyn Centre for Robotic Surgery, Imperial College London, UK

INTRODUCTION

Force feedback in robotic Minimally Invasive Surgery (MIS) plays a very important role to increase the level of immersion that surgeons experience during surgical procedures. On the other hand, at present, there is no viable solution to produce cost-effective force sensors that could be mounted on surgical instruments before the surgical procedure and disposed of at the end of it. Furthermore, force sensors are generally not sufficiently robust to be reusable. In fact, the solutions proposed in literature often are featured with permanent sensors that could be damaged during the sterilization in the autoclave. For instance a high-resolution tactile sensor for surgical tweezers was developed in [1]. The sensor is fixed to the jaw and cannot be inserted or removed. Therefore, building a sensor is an additional cost that furthermore limits the instrument's life. The aim of this work is to design a simple disposable force sensor that can be mounted on the tip of the surgical graspers of the surgical system presented in [2] and that can be produced with reduced cost and consequently disposed. Therefore the optimal sensor for the robotic instruments presented in this work would be an insert that clips onto the instrument's jaws.

MATERIALS AND METHODS

The grasper's jaw component is featured with a sensor slot and it is produced with Selective Laser Melting (SLM) of Stainless Steel (SS) 316, according to the findings in [3]. The force-sensing clips are built with Additive Manufacturing (AM) of plastic. This choice is based on the freedom of design and the high speed for the production of small components. In addition to this, a broad selection of prototyping materials is available and several of them are biocompatible. With regard to the sensing element, the requirement of reduced cost and simplicity led to the use of strain gauges; these also happen to be broadly used and covered abundantly in literature. Figure 1 shows the sensor clip mounted on the surgical grasper's jaw and the main dimensions of the sensor clip and its strain gauge. As depicted in Figure 1, the sensor clip has a thickness of 0.8mm where the strain gauge is applied and can fit a 2 x 5mm strain gauge with value at rest. The sensor is glued to the top face of the plastic insert, which is inserted from the side of the jaw. When fully inserted, it reaches a hard limit and it is locked in position through a tight fit. The top part of the jaw is open, to allow the passage of the soldered wires to the sensor. After soldering, the wires are covered in epoxy glue to reinforce the connection and make it more durable once the glue hardened.
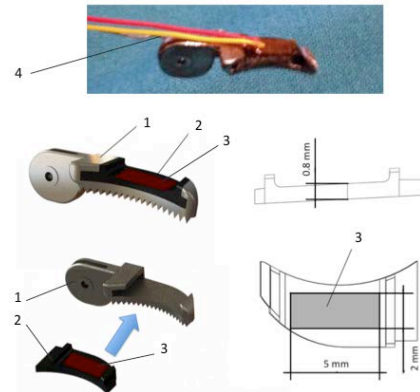

Fig. 1: Above: picture of the force sensor mounted on a grasper's jaw. Left: sensor clip disconnected and mounted on curved grasper's jaws. Right: Main dimensions of the strain gauge and the clip. Elements: 1) jaw with sensor slot, 2) sensor clip, 3) strain gauge and 4) connection wires.

The overall length of the sensor clip is 9mm and it is 4mm wide at the largest point, which makes it a very compact and cost-effective component. FEM simulations were carried out for the optimization of the design of the clip sensor and the instrument's jaw. The objective was to obtain a jaw that is robust enough to be used multiple times and sterilised, without hindering the resolution of the sensor when measuring limited forces. Simulations were carried out using a parametric solver to identify the optimal thickness for the jaw and for the plastic clip. The chosen thickness was 0.8mm for the plastic sensor clip and 0.6mm for the metal jaw. Figure 2 shows the result for a 5N load applied at the tip of the jaw, with the load normal to the jaw's grasping surface. To reduce the complexity of the simulation, some details like the grasping-teeth or the tendon holes were neglected. The inner surface of the hinge hole was used as fixed constraint, while the load was applied normally to the grasper position at about 9mm from the flat face of the jaw. Figure 2(a) shows the computed Von Mises Stress with the maximum value of about 40MPa generated in the thin wall of the jaw. Since this value is lower than the fatigue limit SS 316L, considered to be in the range 60-90 MPa, the jaw component should be robust enough for multiple uses. With regards to Figure 2(b), the image displays the 3rd principal strain and its direction. The maximum value of the strain is about $4 \cdot 10^{-3}$, which in relation to 120 Ohm at rest, it implies that under compression the final resistance value would be about 119.52 Ohm when a force of 5N is applied to the tip. If we plot the average value of the strain on the top surface of the clip for loads varying from 0 to 5N, we obtain the following curve shown in Fig. 3, which

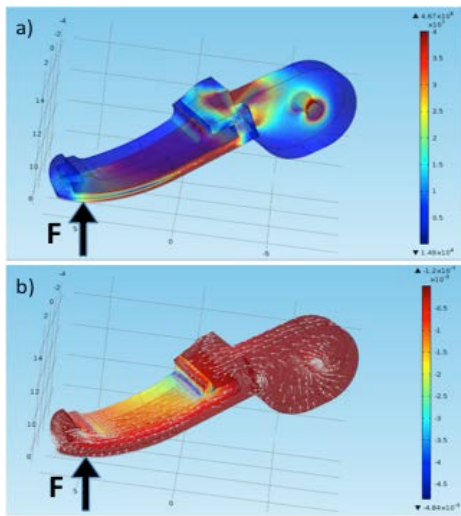can then also be related to the theoretical change in the strain gauge resistance value.

Fig. 2: a) Graph of the Von Mises Stress results for a grasping force of 5N. b) Graph of the 3rd principal strain with arrows to indicate the direction of the strain.

RESULTS AND DISCUSSION

For the validation experiment, one jaw of the instrument, provided with sensing clip, was clamped in a vice. The resistance value of the strain gauge was measured for each load applied. Figure 3 shows the response measured for a tip load in the range of 0 to 5N. The response resulted to be closely approximated with a parabolic curve. The relative error between the averaged data measured and the parabolic reconstruction is shown to be within ±0.2N, with hysteresis about 5%, which could be sufficient for general tissue manipulation in most of the cases done with robotic MIS. On other hand this level of error probably would not be suitable for more delicate applications such as brain surgery, which would require an adaptation of the proposed design. The theoretical response of the sensor was obtained using the maximum strain from the FEM simulations to calculate the variation of resistance of the strain gauge, assuming that the same value was applied to the whole gauge surface. The curve was offset by 0.4 Ohm, since the initial point of the theoretical curve is 120 Ohm. The theoretical and the measured curves are fairly similar, with the difference that the prototype's performance shows a parabolic behaviour, while the theoretical curve has a predominantly linear distribution, with a change of slope due to the interaction of two materials with different properties (Figure 3). One of the problems encountered during usage was that when connecting the sensor to the amplification circuit it was noticed that the sensor was affected with some drift and therefore it required to be reset when no load was present. This could be resolved by improving the overall quality of the manufacturing process, to achieve more repeatable properties, through the use of conductive ink printing directly on the sensor's top surface and by compensating for thermal drift.
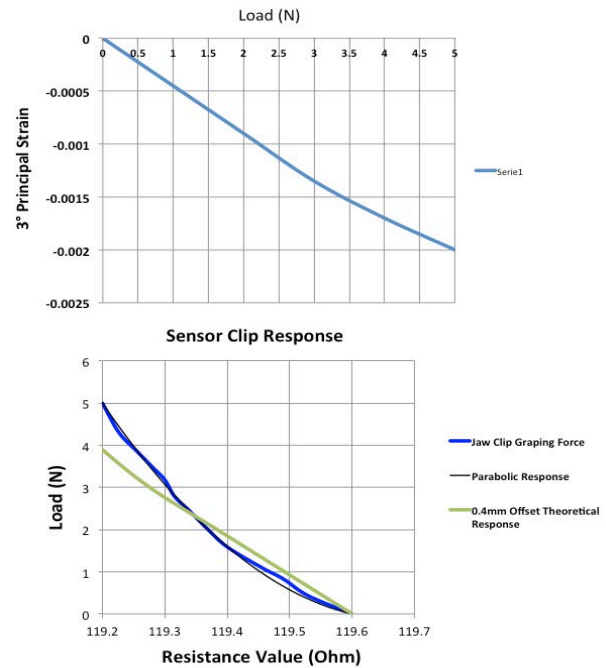

Fig. 3: *Top:* Theoretical strain values for grasping loads in the range 0 to 5N. *Bottom:* Response of the force clip sensor with its parabolic response.

Another limit of this design is that below 0.2N it is not possible to reconstruct the measured value, making this solution not viable for highly delicate procedures. One possible way to increase the resolution is to increase the sensing surface area. Furthermore, this would also sensibly reduce the assembly time while improving the resolution of the sensor. Another possibility is to prepare preformed structures that include carbon-based materials, such as nanoparticles, evenly distributed through the polymer matrix [4], to embed in the design to measure compressive forces to achieve force feedback.

REFERENCES

[1] Hammond, Frank L., Rebecca K. Kramer, Qian Wan, Robert D. Howe, and Robert J. Wood. "Soft tactile sensor arrays for force feedback in micromanipulation." IEEE Sensors Journal 14, no. 5 (2014): 1443-1452.
[2] Shang, Jianzhong, Konrad Leibrandt, Petros Giataganas, Valentina Vitiello, Carlo A. Seneci, Piyamate Wisanuvej, Jindong Liu et al. "A Single-Port Robotic System for Transanal Microsurgery—Design and Validation." IEEE Robotics and Automation Letters 2, no. 3 (2017): 1510-1517.
[3] C. A. Seneci, Jianzhong Shang, A. Darzi and Guang-Zhong Yang, "Rapid manufacturing with selective laser melting for robotic surgical tools: Design and process considerations," 2015 IEEE/RSJ International Conference on Intelligent Robots and Systems (IROS), Hamburg, 2015, pp. 824-830.
[4] Bergmann, Jeroen HM, Salzitsa Anastasova-Ivanova, Irina Spulber, Vivek Gulati, Pantelis Georgiou, and Alison McGregor. "An attachable clothing sensor system for measuring knee joint angles." IEEE Sensors Journal 13, no. 10 (2013): 4090-4097.

Closed-loop Autonomous Needle Steering during Cooperatively Controlled Needle Insertions for MRI-guided Pelvic Interventions

M. Wartenberg[1], J. Schornak[1], P. Carvalho[1], N. Patel[1], I. Iordachita[2],
C. Tempany[3], N. Hata[3], J. Tokuda[3], G.S. Fischer[1]

[1]*Automation and Interventional Medicine Lab, WPI, Worcester, MA, USA*
[2]*Laboratory for Computational Sensing and Robotics, JHU, Baltimore, MD, USA*
[3]*Surgical Navigation and Robotics Laboratory, BWH Radiology, Boston, MA, USA.*
marek.wartenberg@wpi.edu

INTRODUCTION

Multiple insertion attempts are often required to reach sufficient targeting accuracy in needle based percutaneous pelvic interventions. Although intraoperative imaging is used to assist in these procedures, preplanned open-loop trajectories do not account for unmodeled needle deflection or target shift due to tissue deformation. For instance in prostate biopsy, excessive number of insertions per target leads to lengthened procedure time, increased cost, and unnecessary discomfort to the patient.

Limiting the number of erroneous insertions can be accomplished through actuated compensation from the deviated insertion path. One approach to actively control needle path is by rotating a bevel-tipped needle during insertion. An overview of bevel tipped needle steering can be found in [1]. Coupled with real-time needle tracking, closed-loop steering can increase targeting accuracy by continuously updating bevel tip position. Our group has previously reported real-time scan plane control for closed-loop needle steering under multiplanar MR imaging [2], while another group demonstrated similar results using ultrasound [3].

Using a robot to actuate needle insertion typically distances the clinician from patient interaction through teleoperation. Instead, a cooperatively controlled robotic system would require them to be at the procedure site, maintaining ultimate control while adding robotic accuracy to the final placement of the needle tip. In our case cooperative control is referred to as the direct robotic guidance of a tool that is also held and controlled by a user [4, 5].

We introduce a robotic system configured for autonomous closed-loop needle steering during hands-on cooperatively controlled robotic needle insertion. Needle placement is performed using a 6-DOF robotic system suitable for the MR environment.

MATERIALS AND METHODS

The experimental setup shown in Fig. 1 was built to demonstrate image-guided autonomous needle steering under cooperative control. The robot was fixed to an optical table along with a camera stage to serve as a proxy for multiplanar MR imaging. The 4-DOF base is a clinical system which aligns the needle guide in the 2D insertion plane and has been used in clinical trials of MRI guided robot assisted prostate biopsy [7].
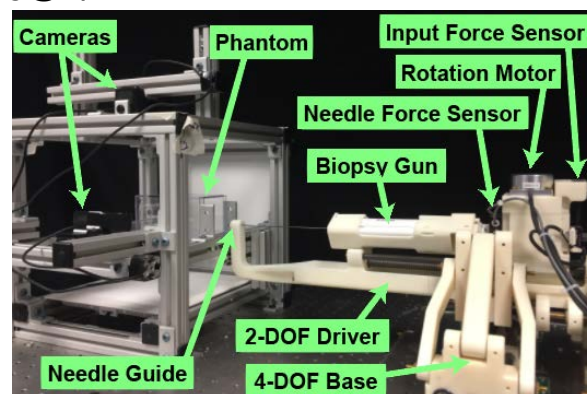

Fig. 1 Experimental setup. The rotation motor spins the clinical biopsy gun to position the bevel tip of the needle for closed-loop autonomous needle steering. The user applies an input force and forces on the needle are collected for continuous cooperatively controlled insertion. The cameras provide image feedback of needle tip position to track the needle tip in real-time.

The 2-DOF needle driver collects user input and needle force, where the insertion velocity is a function of the two. This architecture was developed to target specific locations within a phantom, track the needle tip and continuously update rotational bevel location during cooperative needle insertion to steer towards the target. Regardless of imaging modality, the robotic system steers the needle based on closed-loop feedback of continuously updated target error. Coordinates of the moving needle tip are detected using the Farneback dense optical flow algorithm [8]. This calculation compares sequential video frames to find the magnitude and direction of motion for objects moving in a particular search region. The 3D needle tip position is calculated through stereo triangulation using paired 2D needle tip coordinates from each camera and projection matrices computed during initial camera calibration. Position error from the needle tip to target was calculated and transferred to the robot control system using OpenIGTLink (http://openigtlink.org/), an open network interface for image-guided therapy. Steering direction was determined by calculating the arctangent of the 2D insertion plane error. Once the robot reaches the target plane the 2D in-plane error is the metric by which targeting accuracy is assessed.
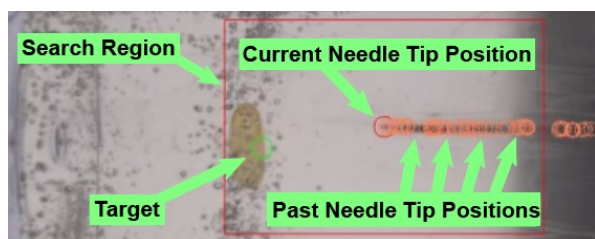
Fig. 2 An annotated still image from the side view camera during a targeted phantom insertion trial. Paired 2D tracking coordinates from the side and top view cameras are combined to continuously update the 3D angle and magnitude of position error from the needle tip to the target.

RESULTS

First we evaluated the accuracy of camera tracking with insertions into homogeneous transparent phantoms made from Versagel (Penreco, Karns City, PA, USA). A series of insertions of various known depths were performed and camera tracking of the needle tip was found to be within one pixel of camera resolution. Figure 2 shows a 2D still of the needle being tracked during an insertion trial from the side view camera, with phantom and camera location described in Fig. 1.

Phantoms also made from Versagel were used in hands-on cooperatively controlled needle insertions with an MR visible Vitamin-E capsule molded in as a target, also seen in Fig. 2. Two needles were used for insertions, a clinical biopsy gun, Full-Auto Bx Gun 18G 175mm from Invivo (Best, Netherlands), and a solid core 22 AWG bevel tipped nitinol needle. Figure 3 shows two representative insertion trajectories using each needle: 1) target aligned insertion point trajectories using the biopsy gun typical in clinical cases, with no obstacles between the insertion and target points and 2) target misaligned insertion point trajectories showing the system is capable of reaching a target if there is an obstacle to avoid between the insertion and target points.

DISCUSSION

Insufficient targeting accuracy during percutaneous needle-based pelvic interventions results in multiple insertion attempts to reach a single target. Robotic needle placement using image-feedback can improve targeting accuracy, but often these devices employ teleoperation which removes the physician from the procedure site.
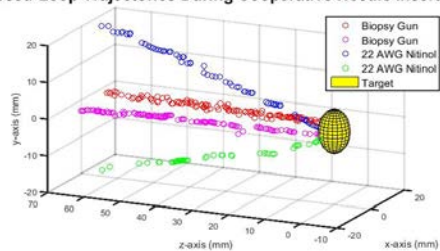

Fig. 3 Hands-on cooperatively controlled needle tip insertion trajectories with autonomous closed-loop steering. The red and magenta trajectories correspond to aligned insertions with the biopsy gun while the green and blue trajectories correspond to misaligned insertions with the nitinol needle.

Instead, sharing the workspace through hands-on cooperative insertion preserves the physician's point of presence, maintains the traditional manual insertion surgical workflow and adds robotic accuracy.

This 6-DOF robotic system is suitable for the MR environment and has previously performed cooperative controlled open-loop trajectory insertions inside the MR bore while showing an acceptable level of signal-to-noise ratio. The autonomous closed-loop needle steering developed herein is based on a continuously updated target error accounting for both change in target position due to tissue deformation and unmodeled needle deflection, regardless of imaging modality. Furthermore, although a homogeneous phantom was used, the closed-loop control is robust to unmodeled error which would come from a layered phantom. As the needle passes through separate layers and deflects during transition, the system tracks the tip and repositions the bevel location to compensate for it.

Trajectories using different sized needles were performed to demonstrate the broader capabilities of the system. In a clinical biopsy procedure the insertion point would be set to create a straight-line trajectory and active compensation could correct for deviations from this path. This is a realistic scenario for the 18 gauge needle on the biopsy gun, where the slotted needle and outer sheath have a limited radius of curvature. In the case of an enlarged prostate a suspicious lesion may lie behind the pubic arch where a straight-line trajectory cannot reach. Here a flexible needle capable of more aggressive steering is an option and the 22 gauge needle was used to show the system's capability of reaching these targets.

REFERENCES

[1] Webster III R, Kim J, Cowan N, Chirikjian G, Okamura A. Nonholonomic modeling of needle steering. Inter. J. of Robotics Research. 2006; 25(5-6): 509-525.
[2] Patel N, Katwijk T, Moreira P, Shang W, Misra S, Fischer GS. Closed-loop asymmetric-tip needle steering under continuous intraoperative MRI guidance. IEEE Int Conference on EMBC. 2015; 4869-4874.
[3] Vrooikink G, Abayazid M, Patil D, Alterovitz R, Misra S. Needle path planning and steering in a three-dimensional non-static environment using two-dimensional ultrasound images. Int. J. of Robotics Research. 2014; 33(10): 1361-1374.
[4] Troccaz J, Peshkin M, Davies B. Guiding systems for computer aided surgery: introducing synergistic devices and discussing different approaches. Medical Image Analysis. 1998; 2(2): 101-119.
[5] Taylor R, Jensen P, Whitcomb L, Barnes A, Kumar R, Stoianovici D, Gupta P, Wang Z, deJuan E, Kavoussi L. A Steady-Hand Robotic System for Microsurgical Augmentation. Int. J. of Robotic Research. 1999; 18(12) 1201-1210.
[6] Tokuda J, Tuncali K, Li G, Patel N, Heffter T, Fischer GS, Iordachita I. In-bore MRI-guided transperineal prostate biopsy using 4-dof needle-guide manipulator. Int. Soc. For Magnetic Resonance in Medicine Annual Meeting. 2016.
[7] Farneback G. Two-Frame Motion Estimation Based on Polynomial Expansion. Scandinavian Conference on Image Analysis. 2003; 363-370.

More Ports = Less Invasive? A Multi-Needle Robot for Lung Ablation

A. W. Mahoney[1,3], P. L. Anderson[1,3], F. Maldonado[2,3], R. J. Webster III[1,3]

[1]*Department of Mechanical Engineering, Vanderbilt University*
[2]*Division of Allergy, Pulmonary & Critical Care Medicine, Vanderbilt University Medical Center*
[3]*Vanderbilt Institute for Surgery and Engineering*
{art.mahoney, robert.webster}@vanderbilt.edu

INTRODUCTION

There has been a great deal of interest in single-port robot surgical systems based on their promise to reduce invasiveness by reducing the number of incisions needed to perform a surgical procedure. While reducing the number of incisions is a worthy goal, invasiveness is also a function of incision size. Some surgeons use needlescopic (< 3mm diameter) instruments to eliminate incisions and sutures all together. However, the approach is limited by the low stiffness of small-diameter tools [1].

In this paper, we present a system that addresses this problem by using needle-diameter tools, yet enabling them to grasp one another within the patient's body to form parallel structures for greater stiffness (Fig. 1). The needles and flexible instruments (e.g., thin endoscopes, ablation probes, and other interventional instruments) grasp one another within a body cavity with snares as shown in Fig. 2. The parallel structure formed by the needles can be maneuvered inside the body via coordinated motion of the needles' bases outside the body using robot manipulators (Fig. 1). The snares can be released and retightened to reconfigure the needle structure into different topologies inside the body to satisfy changing task requirements. This reconfigurable robotic multi-needle concept was first introduced in [2] with the motivating example of diagnostic palpation.

Here, we address therapy delivery for the first time, performing a feasibility study on percutaneous thermal ablation of a partially deflated lung from within the pleural cavity. This is motivated by the high incidence of lung cancer, which kills more than 158,000 Americans each year [3]. Percutaneous thermal ablation is a useful tool for treating inoperable lung tumors, but challenges remain with targeting, particularly in the typical case where multiple overlapping ablation zones are needed to fully cover the tumor. Accurately targeting a lung tumor with needles is challenging due to needles' tendency to unpredictably deflect along the insertion path. Small aiming misalignments can cause an ablation needle to entirely miss the desired target [4]. These issues are compounded when attempting to overlap ablation zones since repositioning typically requires new transthoracic needle insertions. To address this, we propose a thoracoscopic paradigm in which the lung is partially deflated to create an open cavity (i.e., the pleural space) for tools. In this context, the multi-needle concept can be viewed as a platform for dexterously maneuvering and re-aiming ablation needles from within the pleural space that facilitates
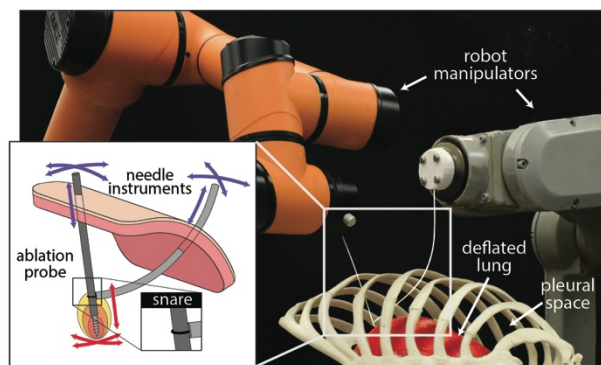

Fig. 1: A multi-needle system is assembled inside a body cavity and is maneuvered by manipulating the needles outside the body using robot manipulators. The needles bend each other to produce coordinated motion inside the body.
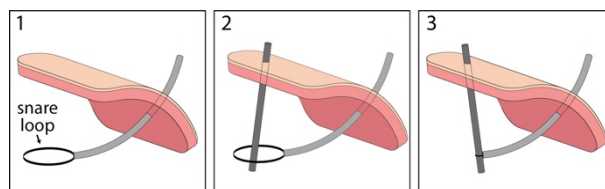

Fig. 2: A multi-needle structure is assembled inside a body cavity using snares that form structural grasps when tightened. The assembly of a two-needle structure is shown in three steps.

greater ablator placement accuracy through a single set of thoracic entry points.

This paper investigates the aiming dexterity and needle insertion stiffness of the multi-needle concept in this thoracoscopic setting. We demonstrate dexterity with a mechanics-based simulation that directs an ablation probe through a trajectory in a patient's chest. We experimentally demonstrate the ability of a multi-needle structure to aim and insert a radiofrequency ablation probe into ex vivo chicken tissue. This provides the first feasibility study of interventional capability in our new robotic paradigm that focuses on minimizing the size of individual ports rather than the number of ports.

MATERIALS AND METHODS

We fabricated a benchtop multi-needle system using superelastic Nitinol tubing (OD 1.78mm, ID 1.20mm). Through one of the needles, we inserted a snare made of braided Dyneema line. Through the other needle, we inserted a prototype RF ablation needle (OD 0.82mm). The ablation needle was created out of Nitinol and a Smith & Nephew Vulcan RF Generator was used for ablation experiments. The system was placed in static configurations using Noga articulated holders that will be replaced by robot manipulators in future work.
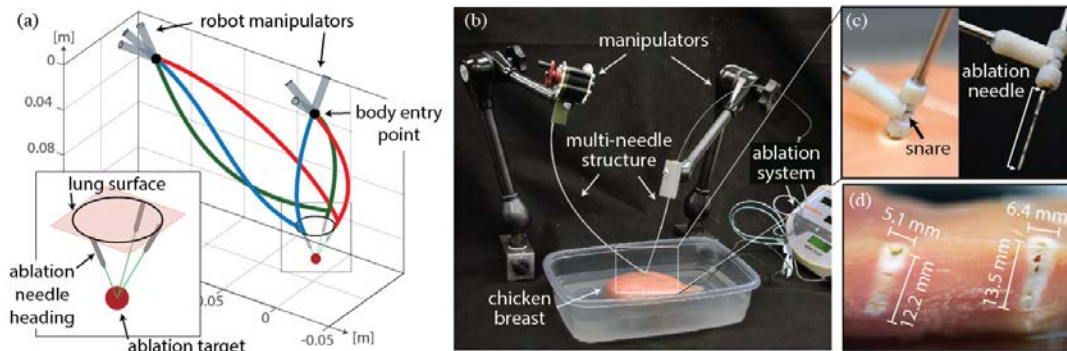
Fig. 3: (a) Simulation experiments demonstrate aiming dexterity by illustrating how the tip of the prototype multi-needle system can be maneuvered along a circular trajectory on a simulated lung surface while keeping it aimed at a subsurface lung nodule. (b) The prototype multi-needle structure is sufficiently stiff to insert an ablation needle (c) into chicken breast for ablation tasks (d).

Assembly and Therapy Delivery: The multi-needle system was assembled by (1) inserting a snare needle with an open snare, (2) inserting a guide needle for the ablation probe and directing its tip into the open snare, (3) closing the snare, (4) delivering the ablator through the guide needle and into tissue, and (5) applying ablative energy. The assembly process is illustrated in Fig. 2.

Modeling: We investigate the dexterity of a two-needle prototype in simulation using a mechanics-based model. The model inputs are the needles' entry points into the body r_i, their quaternion orientations q_i at the entry points, and their insertion lengths L_i into the body (the subscript $i \in \{1,2\}$ describes the needle in question). The model outputs are the needles' shape inside the body.

The constituent needles of a multi-needle structure can be modeled as Cosserat rods with a state vector x_i that propagates along the needles' backbones in arc length s_i according to the arc length derivative x_i' as

$$x_i = \begin{bmatrix} p_i^T & q_i^T & m_i^T & n_i^T \end{bmatrix}^T \quad \text{and} \quad x_i' = f(x_i, s_i),$$

respectively. The needles' states are also functions of arc length s_i and describe their position p_i, quaternion orientation q_i, internal moment m_i, and internal force n_i. The arc length derivatives of the states are formulated into a multi-point boundary value problem that can be solved numerically to produce the structure's shape [2].

RESULTS

To illustrated the aiming dexterity of the benchtop multi-needle system, we used the model to simulate a trajectory where the tip of an ablation probe is commanded to follow a circular trajectory on the surface of a simulated lung while always pointing at a simulated lung tumor beneath the lung's surface. Three configurations from this trajectory are shown in Fig. 3(a). Such a trajectory could be useful for guiding an ablation needle to a lung nodule from multiple angles but through only two insertion points in the chest wall. This would be impossible with a single ablation needle on its own.

To demonstrate tissue ablation, we constructed a benchtop experiment where an ablation needle was deployed through one of the parallel structure's needles into a chicken breast, which is qualitatively comparable to the density of lung parenchyma (Fig. 3(b)). Two insertions and ablations were performed with the multi-needle structure arranged in two different configurations (one is shown in Fig. 3(b)). This experiment indicates the feasibility of therapy delivery using a multi-needle system for the first time.

DISCUSSION & CONCLUSION

There is evidence that a thoracoscopic approach where the lung is deflated will enhance ablation effectiveness. For example, lung ablation is hindered by blood flow that convectively cools the ablation zone – this is reduced in deflated lung and results in larger ablation volumes [5]. Deflating lung can also increase safety. For example, ablating peripheral lung tumors risks incidental ablation of the sensitive mediastinum and chest wall. Deflating the lung displaces nodules away from these areas, creating safe space for ablation [5]. Further safety improvements are enabled by the multi-needle concept's potential for targeting multiple ablation sites through a single set of thoracic entry points, reducing the risk of painful damage to intercostal nerves. Future work will investigate these potential benefits in animal models.

As a platform for percutaneously delivering needles through open cavities like the pleural space, the multi-needle concept offers the potential for better aiming dexterity and enhanced stiffness over a single ablation needle on its own. We anticipate these benefits will open the door to more effective ablation in the lung.

REFERENCES

[1] D. M. Krpata and T. A. Ponsky, "Needlescopic surgery: what's in the toolbox?" *Surg. Endosc*, vol. 27, no. 3, pp. 1040–1044, 2013.

[2] A. W. Mahoney, et al., "Reconfigurable Parallel Continuum Robots for Incisionless Surgery," *Proc. IEEE/RSJ Int. Conf. on Intelligent Robots and Systems*, 2016, pp. 4330-4336.

[3] R. L. Siegel, K. D. Jemal, and A. Miller, "Cancer statistics, 2016," *CA Cancer J. Clin.*, vol. 66, no. 1, pp. 7-30, 2016.

[4] R. Bale, et al., "Stereotaxy: Breaking the limits of current radiofrequency ablation techniques," *Interventional Radiology*, vol. 75, no. 1, pp. 32-36, 2010.

[5] R. S. Santos et al., "Microwave ablation of lung tissue: impact of single-lung ventilation on ablation size," *Annals of Thoracic Surgery*, vol. 90, no. 4, pp. 1116-1119, 2010.

Wearable Soft Robotic Device Supports the Failing Heart *in vivo*

C.J. Payne[1], I. Wamala[2], C. Abah[1], T. Thalhofer[1], M. Saeed[2],
D. Bautista-Salinas[2], M.A. Horvath[1], N.V. Vasilyev[2], E.T. Roche[1],
F.A. Pigula[2], C.J. Walsh[1*]

[1]Wyss Institute for Biologically Inspired Engineering and School of Engineering and Applied Sciences, Harvard University

[2]Boston Children's Hospital, Harvard Medical School
*walsh@seas.harvard.edu

INTRODUCTION

Soft robots fabricated from low modulus, compliant materials hold significant potential for medical device applications that warrant safe, synergistic interaction with humans. We have recently applied this technology to develop ventricular assistive devices (VADs) that can externally massage the failing heart [1][2]. In heart failure (HF), the heart cannot provide sufficient pumping support to meet the metabolic needs of the body. For patients in end-stage HF, impeller-based VADs can be implanted to supplement heart function. However, these devices are associated with complications including bleeding and thromboembolism as a result of blood clots that form on the non-biologic surfaces of the device. Direct cardiac compression devices are an alternative form of VAD which use an inflatable cuff positioned around the ventricles to apply compressive forces during systole. This allows augmentation of cardiac pumping function without the need to contact the blood directly [3]. Based on this principle, we developed a soft robotic sleeve that fits around the heart and emulates the native cardiac muscle motion in order to restore function to the failing heart [1]. Subsequently, we developed a wearable soft robotic device which could be mechanically coupled to the ventricles [2]. This work demonstrated that actuator synchronization and mechanical coupling to the heart are significant factors for augmenting cardiac output. Here, we report the use of this wearable soft robotic device [2] with additional *in vivo* data to demonstrate repeatable performance.

MATERIALS AND METHODS

Two pairs of soft actuators are wrapped around ventricles and contract when pressurized with air so as to apply compressive forces to the heart during systole (Fig. 1). The actuators can then be depressurized to relax in synchrony with the diastolic phase of the cardiac cycle. Our system makes use of the McKibben actuator design in which an inflatable bladder is placed within a braid to create an artificial muscle which contracts when pressurized. We designed the soft actuators to store elastic energy when contracting in systole. The actuators can then recoil back to an elongated state when depressurized during diastole. This function is achieved by placing an elastic rubber sleeve around the actuator braid. We mechanically couple the soft actuators to the heart using elasticated bands that are directly sutured around both ventricles. Since the actuators are coupled to the ventricles, they can apply traction forces during diastole which we hypothesize augments blood inflow.
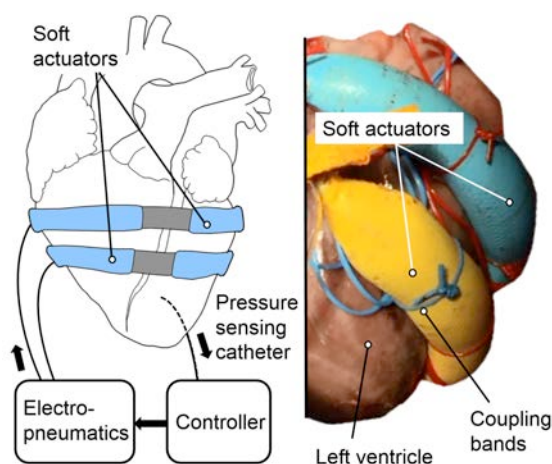

Fig. 1. The proposed soft robotic device: control schematic (left) and *in vivo* deployment showing the contracted actuator state during systole (right).

Triggering of the device is achieved through a pressure-sensing catheter (Scisense, Transonics. Inc) placed in the left ventricle (LV) which detects the end of diastole. By placing the native heart hemodynamics in to the control loop, the soft robotic device can effectively react to fluctuations in heart rate (Fig. 1). This approach also forgoes the need for a pacemaker which can further diminish cardiac output. A real-time control system (cRIO, NI) and electro-pneumatic assembly is used to supply air and vacuum to the actuators in sync with the native cardiac cycle. Further details of our system are reported in [2]. We performed *in vivo* studies (n=2) to demonstrate repeatable performance of the soft robotic device with respect to aortic flow output and LV pressure. Studies were conducted with ethical approval from the Institutional Animal Care and Use Committee at Boston Children's Hospital. Swine (75kg) were instrumented with an aortic flow probe and pressure catheter within the left ventricle (LV). We measured LV pressure and aortic
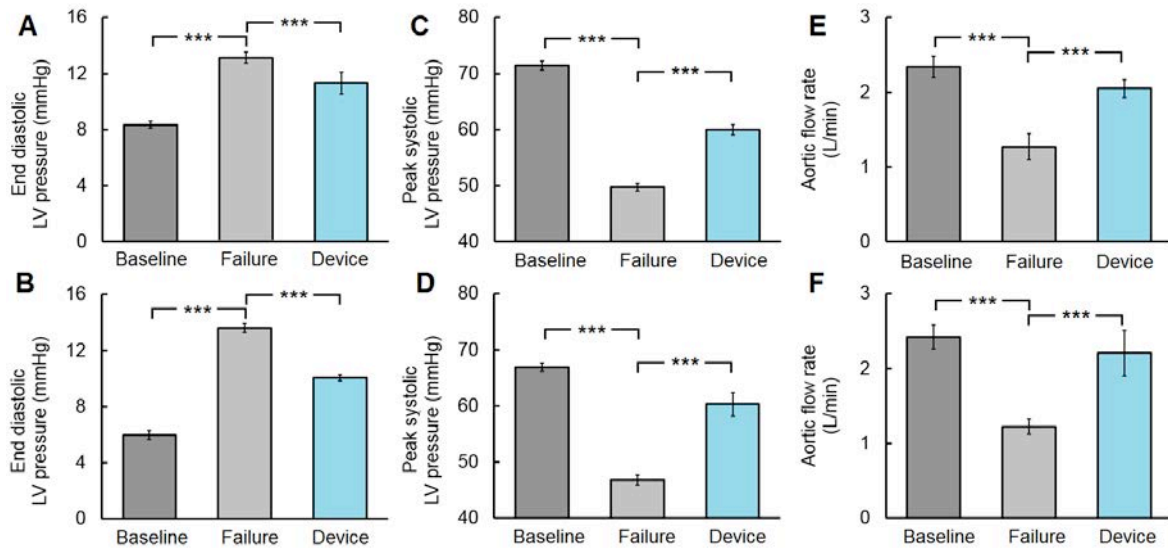
Fig. 2. (A, B) end diastolic LV pressures for animals 1 and 2, respectively. (C, D) peak systolic LV pressures for animals 1 and 2, respectively. (E, F) aortic flow outputs for animals 1 and 2, respectively. *** denotes $p<0.001$ (ANOVA). Error bars are +/- standard deviation.

flow at a baseline state before inducing acute HF. Esmolol, a cardio-selective beta blocker was then administered to reduce heart contractility and simulate HF conditions. We actuate the soft robotic device at 10PSI and for a systolic duration of 45% of the cardiac cycle since our previous work [2] demonstrated greater cardi   ac output at longer actuation periods during systole. We measured 10 consecutive cycles of end diastolic LV pressure, peak systolic LV pressure and aortic flow rate in each condition (baseline, HF, device actuating). A one-way ANOVA was used to assess significance between the conditions for each measured variable, with $p<0.05$ being considered statistically significant.

RESULTS

In acute HF, aortic flow rate and LV peak pressure were significantly reduced whilst end diastolic LV pressure increased, relative to the baseline readings. During device actuation, aortic flow rate and LV peak pressure significantly increased whereas end diastolic pressure reduced relative to HF conditions (all results are summarized in Table 1. and Fig. 2). Fig. 3. shows LV pressure profiles of animal 2 in each condition.
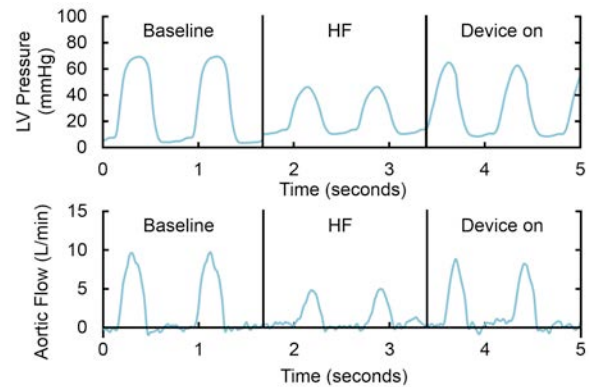

Fig. 3. LV pressure and aortic flow profiles at baseline, HF and with the device assisting the heart, for animal 2.

DISCUSSION

The results indicate that the wearable soft robotic device consistently improved cardiac function of the heart for both animals. In particular, the reduction in end diastolic LV pressure implies improved refilling of the ventricles which is important for sustaining long term cardiac output. The results are consistent with the augmentation in systolic and diastolic function from our previously reported *in vivo* data [2]. Future work will optimize the soft actuator design and coupling of the device to the ventricle walls to enable higher pressures to be generated during systole and further augmentation to ventricle refilling during diastole.

	Baseline	HF	Device
Animal 1 (Means)			
Aortic flow (L/min)	2.3	1.3	2.1
LVP peak (mmHg)	71.4	49.8	60.0
LVP end diastole (mmHg)	8.4	13.1	11.3
Animal 2 (Means)			
Aortic flow (L/min)	2.4	1.2	2.2
LVP peak (mmHg)	66.9	46.8	60.3
LVP end diastole (mmHg)	6.0	13.6	10.1

Table 1. The measured cardiac output variables for animals 1 and 2 at baseline, HF and with device support.

REFERENCES

[1] E.T. Roche *et al.* "Soft robotic sleeve supports the failing heart," in *Sci. Trans Med.* vol. 9, p. eaaf3925, 2017.
[2] C.J. Payne *et al.* "An implantable extracardiac soft robotic device for the failing heart: mechanical coupling and synchronization," in *Soft Robotics,* 2017 (in press).
[3] M. C. Oz, J. H. Artrip, and D. Burkhoff, "Direct cardiac compression devices," in *Journ. Heart. Lung Trans.* vol. 21, ed, 2002, pp. 1049-1055.

Endoscopic Transsphenoidal Surgical Robot
With Optical Tracking Control

J. Suthakorn[1*], S. Chumnanvej M.D.[1,2]

[1]Center for Biomedical and Robotics Technology (BART LAB), Faculty of Engineering, Mahidol University, Thailand.

[2]Neurosurgery Division, Department of Surgery, Faculty of Medicine Ramathibodi Hospital, Mahidol University, Thailand.
*jackrit.sut@mahidol.ac.th

INTRODUCTION

Endoscopic transsphenoidal surgery (EETS) is a minimal invasive surgery for treating a pituitary tumor [1]. In EETS it is needed to insert the sinus surgical tool together with an endoscope through nasal cavity enlarging and passing nasal openings before removing the adenoma and it requires a skillful surgeon [1]. To remove the tissues and the soft bone in the surgical pathway surgeon normally uses an endoscopic visual feedback. During the EETS procedures, the surgeon requires a high skill of knowledge about anatomical structure but the conventional endoscope provides only 2-D images. Determining the positions and orientation of surgical tools is depended only on surgeon's experience. Fatigue from long-time surgery is also a reason for hand quiver and tiredness in surgeon [1],[2]. This research presents a new robotic system to assist in normal procedure of EETS as shown in fig.1. A real-time 3D navigation system is used in this proposed system, which is based on imaging technique with optical tracking occurring in the period before a surgical operation. The tracking system is used to develop a virtual endoscopy along with the surgical tool and provides a 3D model of the bone structure. The bone anatomy 3D model in the workspace is created by using CT pre-operative images [3]. The real-time surgical tool navigation along with virtual endoscope is provided by the optical tracking system along with the 3D model.
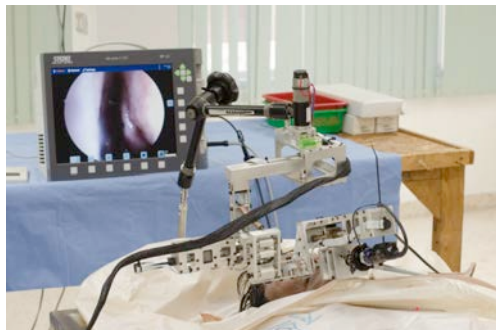

Fig. 1 BART LAB EETS robotic platform in cadaveric experiment.

MATERIALS AND METHODS

Motion analysis of a surgical tool is to a great extent in all the type Minimal Invasive Surgery. To design and develop a new robotic system for supporting in a surgery and also for a surgical tool navigation system study on tool motion is valuable [2]. During EETS the surgical tool motion data are collected using an optical tracking system. To estimate and collect the position of the markers during surgery, optical markers are attached with the surgical tools and computed using MATLAB program. The workspace and the motion behavior of surgical tools can be easily calculated using the collected motion data. Using a homogeneous transformation the tool's position can be calculated from the marker to the tool tip [4]. The difference of patterns in markers can be identified using a set of passive markers and stereo camera. The position and orientation data of the object attached with the optical marker is recorded in 3-dimension. The commercial optical tracking system, Polaris® Vicra® system from Northern Digital Inc. is used during the experiment shown in fig. 2 [1] [4]. To estimate the motion of robot to deliver remote center of motion for the EETS procedures, a robot motion analysis experiment is carried out and to evaluate the robot system a commercial optical tracking system from NDI is used [1].

Fig. 2 Medical tool attached with optical marker.

There are numerous tools used during the EETS procedures. The main objective of this research is to develop a robotic surgical support system to hold an endoscope and a medical anatomize, guiding tools along the path of a planned surgery [4]. Perceiving the limitations and motion analysis of the surgical tools is important because it is needed for the design of a robot for its purpose. The position and orientation relationship between the tools attached to optical markers are

represented by using the homogeneous transformation matrixes. Using the tooltip calibration method the homogeneous transformation matrix from attached marker to the tip of the tool can be attained [1]. By applying the transformation shown below the homogeneous transform from optical marker attached at the end of the tool handle can be calculated.

$$^{Marker}_{End}H = {}^{Marker}_{Tip}H\ {}^{Tip}_{End}H \qquad {}^{Tip}_{End}H = \begin{bmatrix} 1 & 0 & 0 & x_{tip}+L \\ 0 & 1 & 0 & y_{tip} \\ 0 & 0 & 1 & z_{tip} \\ 0 & 0 & 0 & 1 \end{bmatrix}$$

$$^{Marker}_{Tip}H = \begin{bmatrix} c\alpha c\beta & c\alpha s\beta s\gamma - s\alpha c\gamma & c\alpha s\beta c\gamma + s\alpha s\gamma & x_{marker}+x_{tip} \\ s\alpha c\beta & s\alpha s\beta s\gamma + c\alpha c\gamma & s\alpha s\beta c\gamma - c\alpha s\gamma & y_{marker}+y_{tip} \\ -s\beta & c\beta s\gamma & c\beta c\gamma & z_{marker}+z_{tip} \\ 0 & 0 & 0 & 1 \end{bmatrix}$$

RESULTS

An optical marker was attached to the robot to collected tool pose controlled by the robot. A phantom was used to implement in the experiment. The representative of the nostril entrance made by the plastic cylindrical tube illustrated in fig. 3.
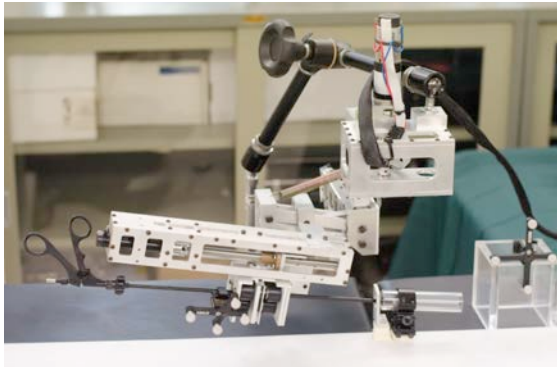

Fig. 3 Robot attached with optical marker for the experiment.

The horizontal plane was represented by another optical tracking system. Controlling algorithm is interfaced by using the joystick. MATLAB Programming was used to record instrument motion. The remote center of motion at nostril entrance must generate to create a mechanical constraint of the surgery. The experiment was executed to confirm that the tool moved with the constraint at the remote center of motion point [1] [4]. The position of the medical tool tip located at the phantom nostril entrance. The movement of the tool was controlled by a joystick and was recorded the motion during the experiment. The 3D plot in fig. 4 (a) represents the tool movement during the experiment time. While the red circle represents the medical tool tip, yellow circle perform as a center of motion point. And the color is indicating the time moment of the record. From the result, the robot can perform tool movement under the constraint at the tool tip and yield the remote center of motion movement [1]. To accumulate the tool movements during EETS a human cadaver-based experiment was conducted. The experiments were carried out in two steps the first step is to break and open the vomer bone and the surgical tool were inserted through the nostril. The second step is to open the sella bone to access pituitary and the surgical tool was inserted through sphenoid sinus. To

estimate and record the position of the nostril before the surgery the medical dissector was used.
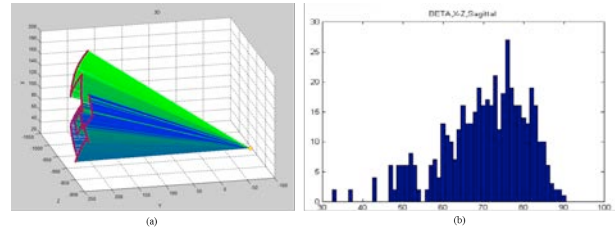

Fig. 4 Robot motion with tool tip (a) at the RCM point (b) sagittal plane.

Fig 4. (b) & fig. 5 (a) - (b) shows the tool motion angle and number of angle in each plane used during the surgery. Fig 4 (b) & fig. 5 (a) - (b) represents the range of angle in a sagittal, coronal and transverse plane for moving a surgical tool. For sagittal plane angle the minimum angle at 33.4 degrees and the maximum angle of 89.72 degrees, 89.00-degree maximum angle with the least angle at 0.15 degree for the coronal plane and in transverse plane 89.91-degree maximum angle with the minimum angle at 45.77 degrees. By using the data from surgical tool angle histograms in each plane, we can estimate the most tool angle used during the surgery to determine the initial position of the robot.
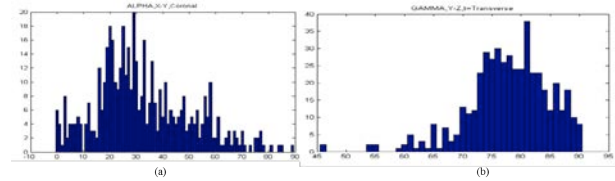

Fig. 5 Robot motion with tool tip (a) at the Coronal plane (b) Transverse plane.

DISCUSSION

The 3D model of anatomy along with the optical tracking system and surgical tool the real-time navigation system can be recorded. To use the real-time navigation applications (image guided system, virtual endoscope etc.) during the surgery, 3D model and surgical tool attached with optical marker need a proper calibration. This research did not focus more on the calibration between optical navigation and 3D model of anatomy. Presently, there are various methods used for calibrating medical images to the patient during the surgery, for example fiducial mask calibration and laser calibration methods. Effective calibration method for EETS is desirable to be further investigated.

REFERENCES

[1] Nonthachai Suratriyanont. Endoscopic Transsphenoidal Surgical Robot with Optical Tracking Control, Master Thesis, 2014, Mahidol University.
[2] Taylor R. H, and Stoianovici D. Medical Robotics in Computer-Integrated Surgery,IEEE Trans. Robotics and Automation, 2003 Oct; 19(3):765-781.
[3] Emeagwali I, Marayong P, Abbott J.J, and Allison M. Okamura. Performance Analysis of Steady-Hand Teleoperation versus Cooperative Manipulation. Proc. IEEE Virtual Reality, March 27-28, 2004.
[4] Suratriyanont N, Suthakorn J. 3D Navigation for Transsphenoidal Surgical Robotics System Based on CT - Images and Basic Geometric Approach. Proc. IEEE ROBIO. 2013 Dec; 2007-2012.

Design and Kinematic Modelling of a Miniature Compliant Wrist for the da Vinci Research Kit

P. Francis, K. W. Eastwood, V. Bodani, T. Looi, J. M. Drake

Centre for Image-Guided Innovation and Therapeutic Intervention (CIGITI),
The Hospital for Sick Children, Toronto, Canada
p.francis@mail.utoronto.ca

INTRODUCTION

To improve and extend the use of the da Vinci Surgical System to applications such as neurosurgery or pediatric surgery, smaller instruments (<5 mm) are required [1], [2]. Notch-tube compliant mechanisms are one common approach used for manipulator miniaturization because of their monolithic nature. They are constructed by removing cut-outs from nitinol tubes, creating directional compliance, and are actuated by one or more tendons. An asymmetric notch, which is a cut-out taken from one side of the tube that typically extends across the midline, has the advantage of sharper bending, lower tendon forces and is simpler to fabricate compared to symmetric notches [3]. Here, we present a new asymmetric notch wrist design capable of two degree-of-freedom (DOF) bending within a 2 mm shaft diameter, for use on the da Vinci Research Kit. The mechanism's kinematics model is discussed and compared to experimental performance.

MATERIALS AND METHODS

The new wrist design is composed of asymmetric notches helically patterned onto a nitinol tube and positioned 120° apart, as seen in Fig. 1. Three cables, aligned with each cut side, are attached at the wrist's distal end and are routed outside of the tube. These features provide decoupled articulation as each cable is positioned at the open side of one set of cuts and near the neutral bending plane of the other two cut sides. Cable-guides, made from small steel wire rings, hold the tendons in position on the tube's outer wall. Table 1 summarizes the device's dimensions. Each notch can bend up to 30° and twelve notches were used in total to ensure the wrist bends >90° in every direction. The physical specimen, seen in Fig. 2, was cut on a benchtop CNC (Minitech Machinery, USA). A 2 mm diameter steel tube is added proximally to extend the joint and an end-effector has been added to the tip.
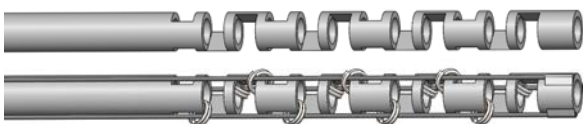

Fig. 1 Tube cut pattern shown alongside full three cable assembly with cable-guide rings.

Table 1 Tube cutting geometry and cable size

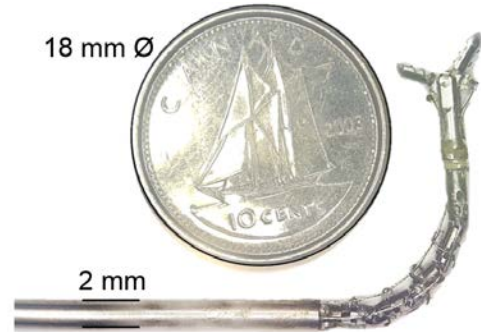|	
Tube ID, OD	0.94, 1.37 mm
Cut Width (h), Depth (g)	0.79, 1.17 mm
Width between cuts (c)	0.34 mm
Total Joint Length	13.3 mm
Cable Diameter	0.14 mm

Fig. 2 Actuated wrist assembled with end-effector.

The kinematics of the wrist is based on the technique derived by York et al. for one DOF bending in-plane [3], but extended with modifications for our three cable, 2-DOF bending mechanism, shown in Fig. 3. Here, a transformation T_{notch} for each of the asymmetric notches is calculated from a known tendon displacement Δl, where Δl can be directly mapped to a pair of constant curvature arc parameters (κ, s). Here, κ is the bending curvature of a single notch and s is its arc-length at the tube's midline. These parameters are related to the geometry of the notch, which includes the notch width h, the location of the notch's neutral bending plane $\bar{y}$, and the distance from the tube's midline to the actuation cable (in red) d. To extend the kinematics to three notches arranged in different bending planes, two additions have been made. First, the transformation T_c must account for a rotation of 120° about the z-axis as well as an offset of c, the width between each notch.
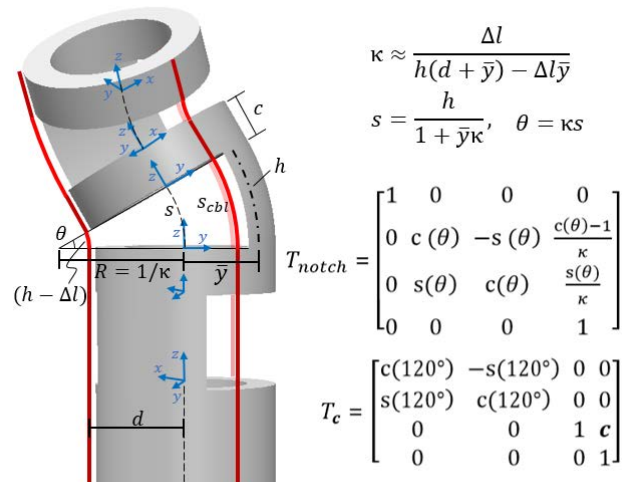

$$\kappa \approx \frac{\Delta l}{h(d + \bar{y}) - \Delta l \bar{y}}$$

$$s = \frac{h}{1 + \bar{y}\kappa}, \quad \theta = \kappa s$$

$$T_{notch} = \begin{bmatrix} 1 & 0 & 0 & 0 \\ 0 & c(\theta) & -s(\theta) & \frac{c(\theta)-1}{\kappa} \\ 0 & s(\theta) & c(\theta) & \frac{s(\theta)}{\kappa} \\ 0 & 0 & 0 & 1 \end{bmatrix}$$

$$T_c = \begin{bmatrix} c(120°) & -s(120°) & 0 & 0 \\ s(120°) & c(120°) & 0 & 0 \\ 0 & 0 & 1 & c \\ 0 & 0 & 0 & 1 \end{bmatrix}$$

Fig. 3 Parameters defining the bending of an asymmetric notch. Curvature κ is solved based on small angle approximation. s(θ)=sin(θ), c(θ)=cos(θ), s(120°)=sin(120°), c(120°)=cos(120°)

In the case of three notches stacked in three different planes, the transformation is:

$$T_{3notch} = T_1 T_c T_2 T_c T_3 T_c, \quad \text{where } T_i = T_{notch}(\Delta l_i)$$

Here, each cable is associated with a cable displacement Δl_i as well as the notch it aligns with. To calculate the mechanism's overall transformation, accounting for all of the notches on the wrist, the transformation becomes:

$$T_{wrist} = T_{3notch}{}^n$$

where n is the number of cuts in each direction. The model assumes that an overall cable displacement, $n\Delta l$, contributes equally to the closing of all aligned notches.

When the wrist is straight, all Δl are zero. When one cut side is actuated, the tube will bend with a shortening midline resulting in the other two cables becoming slack. To account for this behavior, a second addition to the kinematics model has been made. Assuming the cables follow a similar curve as the tube's midline, the "slack" Δl required before seeing any deflection can be solved as:

$$slack = n(h - s_{cbl})$$
$$s_{cbl} = s(1 + \kappa\, d \sin(30°))$$

where s_{cbl} represents the length of the cables which are not being actuated to close the notch, as shown in Fig. 3. It can be seen that the path length of the cables to the right shorten when the cable on the left is actuated to bend the notch. Without this adjustment, the cables could be shortened with the expectation that it would deflect the joint but only slack would be removed.

RESULTS

To compare the kinematics model for this joint with the physical specimen, the wrist mechanism was incorporated into a da Vinci instrument base and controlled using the da Vinci Research Kit. A 6-DOF electromagnetic tracker (NDI Aurora, Canada), with an accuracy of 0.48 mm RMS, was positioned 4.5 mm distal to the end of the wrist joint to track the tip position of the wrist. Fig. 4 shows the intended trajectory of the wrist, where the dotted lines denote single cable bending and the solid lines denote two cable bending. The experimental data is overlaid, denoted by the red markers. The RMSE for all values is 1.68 mm. Fig. 5 shows the comparative size of the tool with a grasper positioned within a brain model.

DISCUSSION

This work presents a new miniature notched tube joint design which is compact enough to articulate within the brain. An early comparison between the kinematic model and experimental data suggest reasonable agreement between the two for predicting the path of the wrist's tip. Differences in the experimental data and the model are likely caused by manufacturing errors, sensing errors and the challenge of defining the actuator position associated with a cable displacement of zero.

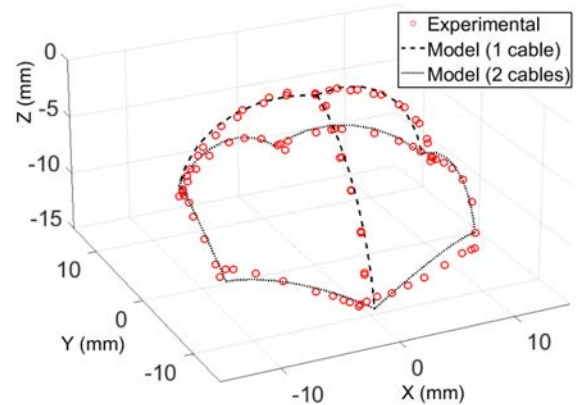As described in the kinematics model, independent control of each cable is required. From previous work,

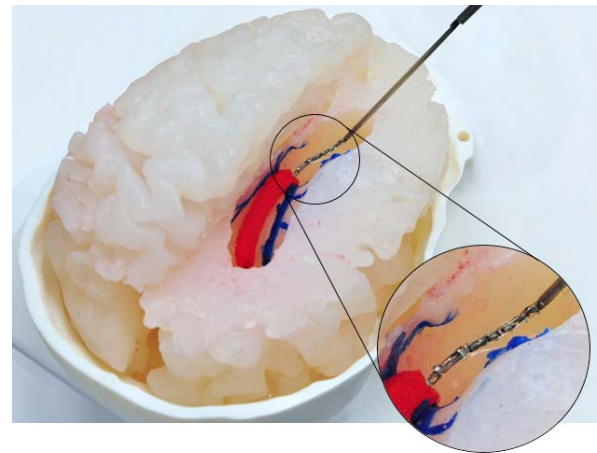**Fig. 4** Experimental wrist tip position vs. kinematics model.

Fig. 5 Tool with grasper positioned within a brain model.

we have designed a base mechanism which can drive the three cables independently with only two actuators, assuming that only two cables are being actuated at any given time [4]. The work also explores the tendon force vs. angle as well as the force output of the wrist.

Future work will involve conducting an in-depth analysis of the wrist's position and orientation accuracy after incorporating the roll of the wrist along with the tool's base mechanism. A laser-cut tube specimen will be used for this analysis. The wrist's range of motion and stiffness will also be optimized for a specific clinical task.

REFERENCES

[1] H. J. Marcus, A. Hughes-Hallett, T. P. Cundy, G.-Z. Yang, A. Darzi, and D. Nandi, "da Vinci robot-assisted keyhole neurosurgery: a cadaver study on feasibility and safety," *Neurosurg. Rev.*, vol. 38, no. 2, pp. 367–371, Apr. 2015.

[2] G. van Haasteren, S. Levine, and W. Hayes, "Pediatric robotic surgery: early assessment.," *Pediatrics*, vol. 124, no. 6, pp. 1642–9, Dec. 2009.

[3] P. A. York, P. J. Swaney, H. B. Gilbert, and R. J. Webster, "A wrist for needle-sized surgical robots," in *2015 IEEE International Conference on Robotics and Automation (ICRA)*, 2015, pp. 1776–1781.

[4] P. Francis, K. W. Eastwood, V. Bodani, K. Price, K. Upadhyaya, D. Podolsky, H. Azimian, T. Looi, and J. M. Drake, "Miniaturized Continuum Instruments for the da Vinci Research Kit," *IEEE Robot. Autom. Mag.*, 2017, *In Press*.

A Novel Variable Stiffness Mechanism for Minimally Invasive Surgery using Concentric Anisotropic Tube Structure

J. Kim[1], C. Kim[2], S. Kang[2], K.-J. Cho[1]

[1] The School of Mechanical and Aerospace Engineering, Seoul National University,

[2]Robot and Media Research Institute, Korea Institute of Science and Technology (KIST)
kimjongwoo1988@gmail.com

INTRODUCTION

Minimally invasive surgery (MIS) has become widely used due to its clinical benefits compared with conventional open surgery. MIS patients tend to have less side-effect and trauma, and shorter recovery time. One of the major challenges in MIS is that the dexterity and the choice of actuators are greatly reduced due to the smaller incisions and long and slim instruments. It therefore, motivates the development of tube-type instruments with variable stiffness that can have proper stiffness when they are introduced into the human body and when they are manipulated inside the restricted space inside the body.

A variable stiffness structure is required to adjust the perceived stiffness to meet needs imposed by a changing conditions in medical environments. Many different variable stiffness mechanisms have been studied: some mechanisms emloyed shape memory materials [1], fluidic flexible matrix composite [2], material anisotropy of structure, electro-bonded laminates [3], etc. However, the current variable stiffness mechanisms accompany complex structure which is hardly feasible under small dimension of inner body, or heat/electricity stimulus which is possibly harmful for medical usage.

This research presents a novel safe and scalable variable stiffness mechansim using concentric anisotropic tubes. The mechanism consists of two or more concentric tubes with combination of rigid and compliant segments. The stiffness of the mechanism can be varied by relative translation and rotation between the concentric tubes. The load test at the distal tip was performed to measur the variation of bending stiffness. The results show that the bending stiffness of the structure can be varied by simply sliding and rotating the two tubes. Therefore, the mechanism enhances the functionality of MIS tools without any complex actuators or bulky structures.

MATERIALS AND METHODS

The structure of the mehanism can be composed of two or more concentric tubes. The design parameters of each tube are chosen to control the anisotropic material properties of the structure. The tube can be divided into the series of arc-shape units and the parameters determine the shape of the arc. Fig. 1 shows the design parameters—l_1 and l_2 stand for the length of the unit, θ for the angle of the arc unit, n for the number of units,

and α and β for the type of material, whether rigid one or compliant one.

In this research, we fabricated two types of the structure to examine variable stiffness mechanism. Type A has anisotropy along longitudinal direction. Type B has anisotropy along both rotational and the longitudinal directions. We set the design parameters as (l_1, l_2, n, θ) = (8mm, 3mm, 6, 360°) for type A, and (l_1, l_2, n, θ) = (10mm, 4mm, 5, 180°) for type B. The material selection, α and β, were determined as Fig. 2. The white segment refers rigid 'verowhite material' while the black segment refers compliant 'tangoblack+ material.' The outer diameter of the outer tube and the inner tube were 19.0mm and 13.5mm respectively (thickness: 2.5T). The tubes were manufactured by Objet 260 Connex 3D printer (resolution: 600dpi), Stratasys, USA.
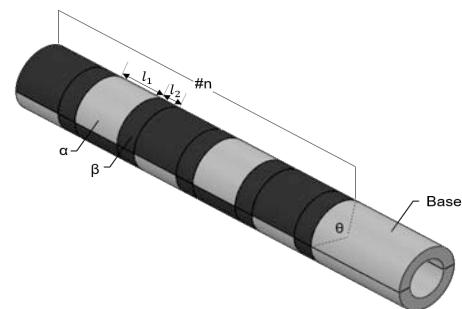

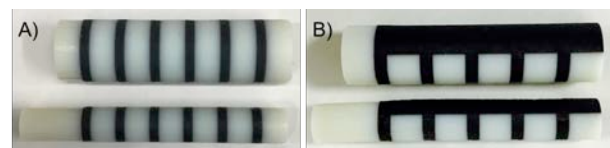**Fig. 1** Design parameters of each tube: $(l_1, l_2, n, \theta, \alpha, \beta)$

Fig. 2 Type A and B set design parameters as (l_1, l_2, n, Θ) = (8mm, 3mm, 6, 360°) and (10mm, 4mm, 5, 180°). The lower is the inner tube and the upper is the outer tube.

There are two major ways to control the stiffness of the structure: relative rotational and translational movement between the tubes. For Type A, translating one tube from the other changes the bending stiffness of the structure as shown in Table 1. At the flexible state, each flexible segment of the inner tube exactly overlapped with that of the outer tube. At the rigide state, each flexible segment of the inner tube positions at the middle of rigid segment of the outer tube. The rigid segment of the outer tube holds the flexible segment of the inner tube from bending more. To change neighboring materials is the key to achieve variable stiffness in this structure.

Table 1 Reconfiguring the longitudinal phase difference

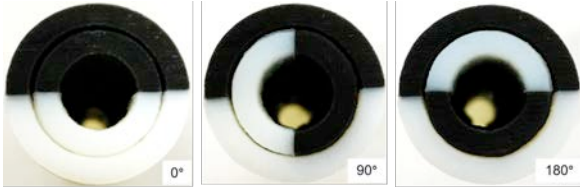| Status	Tube Configuration (by translation)
Flexible State	
Rigid State	

Fig. 3 Rotational phase difference between the inner and the outer tube: 0° (left), 90° (middle) and 180° (left) to vary the bending stiffness of the sturcture.

For Type B, rotating one tube from the other controls the stiffness, as shown in Fig. 3. —the rotational phase difference between the outer and inner tube is 0°, 90°, 180° in this study. We performed the load test to evaluate the stiffness change according to the change of tube configuration as Table 1 and Figure 3. A weight was hung at the end of the tube and we measured the change of the vertical position change at the distal tip.

RESULTS

By translating the inner tube, the structure reconfigures from flexible state to rigid state. When a 600g weight loads at the distal tip, the tip position lowers 33mm at the flexible state and 27mm at the rigid state as shown in Fig. 4. Red and black horizontal dot lines compare the distal point position each other. The result shows that the bending stiffness is 178N/m and 218N/m respectively: the bending stiffness increases by 22.2% when the inner tube translates relative to the outer tube from the flexible state to the rigid state in Fig. 4.
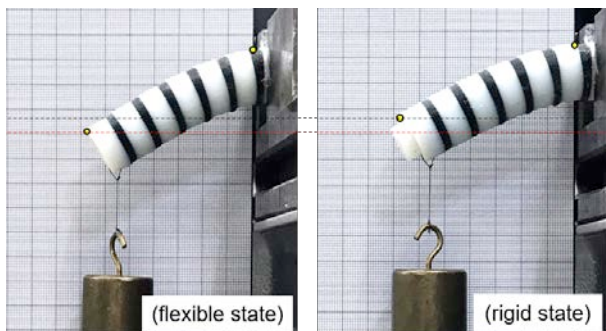

Fig. 4 Bending experiment for longitudinal phase change.

The bending stiffness also varies according to the rotational phase difference between tubes. Fig. 5 shows that the case of 0° phase is the most flexible, the case of 180° phase is middle, and the case of phase 90° is the most rigid (refer Fig. 3 for rotational phase difference). In Table 2, it compares deflections and bending stiffness when 100g and 150g loads are applied to the strucutre with different rotational phase. The bending stiffness increased from 60.7 N/m to 163.3 N/m (about 2.7 times).
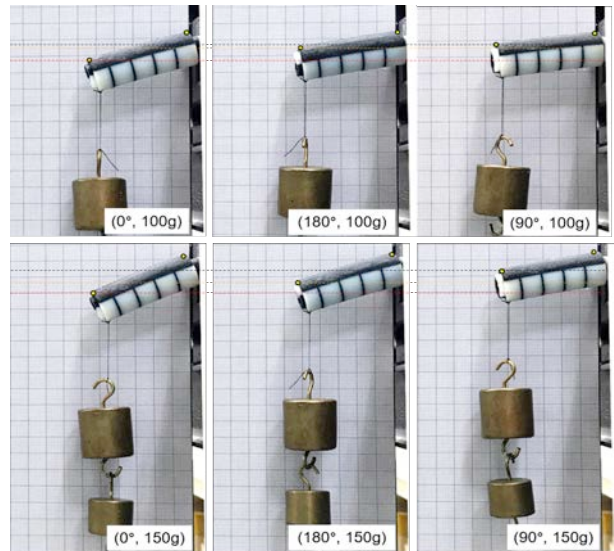

Fig. 5 Bending experiment for rotational phase change: 1st column: 0°, 2nd column: 90°, 3rd column: 180°.

Table 2 Bending stiffness as rotational phase changes.

	0°	90°	180°
100g	17 mm	6 mm	9 mm
150g	23 mm	9 mm	15 mm
Bending Stiffness	60.7 N/m	163.3 N/m	103.4 N/m
Rigidity	Flexible	Rigid	Middle

DISCUSSION

The design of the concentric anisotropic tube structure enabled the variable stiffness mechanism by the combination of relative rotational and translational movement of the tubes. The mechanism does not require any bulky or complex auxiliaries so that it suits the restricted inner body circumstances. The mechanism is also scalable to adjust small dimension. It simply approaches to the desired range of stiffness (2.7 times in the experiment) by translating and rotating tubes each other. The authors currently work on the modeling the relationship between the relative rotation/translation of the tubes and the bending stiffness of the mechanism. Based on that, we will optimize the design parameters to satisfy operating conditions and required stiffness range. The mechanism is able to adopt other materials such as nitinol by creating anisotropy by patterning slits [4] instead of combining segments with different material property. Thus, it widens the scope of the functionality of tube robot for minimally invasive surgery.

REFERENCES

[1] Chen, Y., et al. "Variable stiffness property study on shape memory polymer composite tube." Smart Materials and Structures 21.9 (2012): 094021.
[2] Shan, Y., et al. "Variable stiffness structures utilizing fluidic flexible matrix composites." Journal of Intelligent Material Systems and Structures 20.4 (2009): 443-456.
[3] Tabata, O., et al. "Micro fabricated tunable bending stiffness devices." Sensors and Actuators A: Physical 89.1 (2001): 119-123.
[4] Lee, D. Y., et al. "Anisotropic patterning to reduce instability of concentric-tube robots." IEEE Transactions on Robotics 31.6 (2015): 1311-1323.

Mining Robotic Surgery Data: Training and Modeling using the DVRK*

P. Fiorini[1], D. Dall'Alba[1], G. De Rossi[1], D. Naftalovich[2], J. W. Burdick[2]

[1] *University of Verona, Department of Computer Science, Verona, Italy*

[2] *California Institute of Technology, Mechanical and Civil Engineering, Pasadena, USA*

paolo.fiorini@univr.it

INTRODUCTION

Data systematically collected during robotic surgical interventions are not yet available for analysis, because of concerns about patients' privacy and manufacturer's trade secrets. To study what actions surgeons take during interventions, a possible approach it to simulate surgical tasks in a realistic setting. The availability of the da Vinci Research Kit (DVRK) makes this approach possible and, by addressing specific intervention steps or basic surgical actions, very rich data sets can be generated. The first step we took to analyze these data has been the evaluation of surgical skill and training progress of medical students in two specific contexts. The first was a short course to medical students who performed the same pick-and-place tasks on the DVRK and on a training simulator. The second context was training on a more complex procedure, i.e.. a micro anastomosis, carried out by a single student over many sessions. Our work follows the line of objective assessment of surgical skills [1] and aims at developing tools that will, eventually, also extract high level information, e.g. task structure and surgeon intention, from clinical data.

MATERIALS AND METHODS

Typically, data from simulations are used to assess the skill level of the person carrying out the tests. The Objective Structured Assessment of Technical Skills (OSATS) [1] is a validated tool that allows scoring the test results. The OSATS has been used in the Structured Assessment of Robotic Microsurgical Skills (SARMS) [2] and in the Fundamental of Skills of Robotic Surgery (FSRS) [3]. There also has been work on automatic estimation of OSATS scores from video data. Another useful form of information is surgical motion data. Because motion of teleoperated surgical robots reflects the motion of the operating human surgeon and because the robot senses its own kinematic variables, it is possible to acquire kinematic data from a teleoperated surgical robot that represent the motion data of the operating surgeon. However, clinical data is protected, as mentioned above, and it is not available for analysis. A sample set of laboratory data is available from Intuitive Surgical, Inc., and its academic partners at Johns Hopkins University, and is known as the JIGSAWS dataset [4]. It was acquired using the da Vinci's API software interface. Another way to acquire
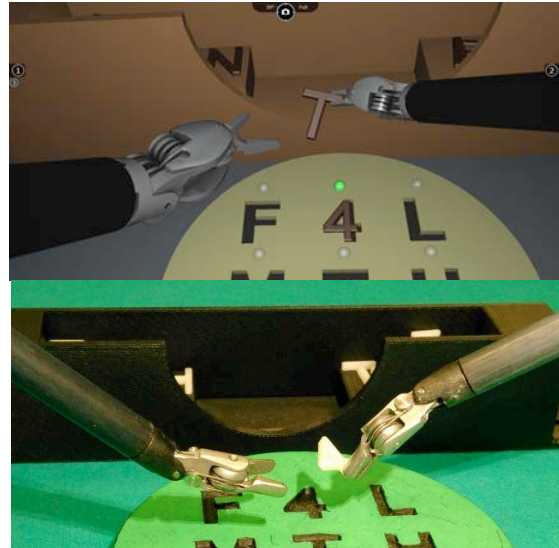
Fig. 1: The pick-and-place task: virtual simulation on top and real setup on bottom

such kinematic data is directly through the DVRK, which can be used in a laboratory setting [5]. In this paper, we use the robot data captured during training experiments at the ALTAIR laboratory in the University of Verona, Italy. The JIGSAWS dataset contains a handful of samples of a few surgical tasks and multi-class skill labels of beginner, intermediate, and expert. However, those tasks are not challenging enough to provide an ideal research environment on skill assessment. Furthermore, this data set does neither establish a correlation to training in a virtual environment, which is a more cost effective alternative to using the DVRK system, nor it allows following the learning progress of a trainee. To address the first point, we set up an experiment using the simulator developed by BBZ srl, and we involved a group of medical students taking an elective course in robotic surgery. Each student repeated a pick-and-place test on the simulator and on the DVRK. We divided the students in two groups: group A started with simulator and then moved to DVRK while group B did the inverse. The test consisted of positioning a set of letters in their correct template holes, as shown in Figure 1. To acquire a better understanding of the structure of a learning curve and its correlation within the temporal sequence of tests, our second experiment consisted of a complex training sequence carried out on the DVRK. The surgical procedure utilized was an end-to-end microvascular anastomosis performed on the Konnyaku/Shirataki phantom laboratory model [6]. This task consisted of surgically joining small (2.5 mm diameter) hollowed Japanese noodles using microsuture with robotic-

assistance under manual teleoperated control. The procedure was performed repeatedly by a single medical student as part of a training sequence, and thus reflects sequential progression along a learning curve.
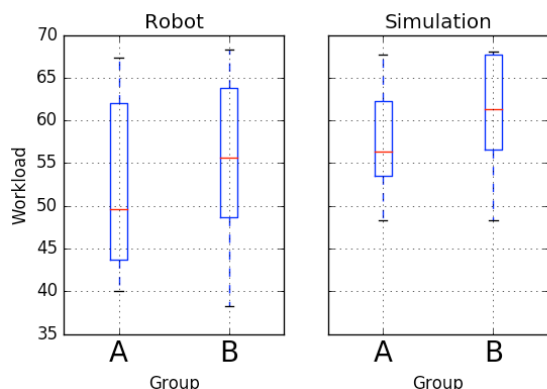

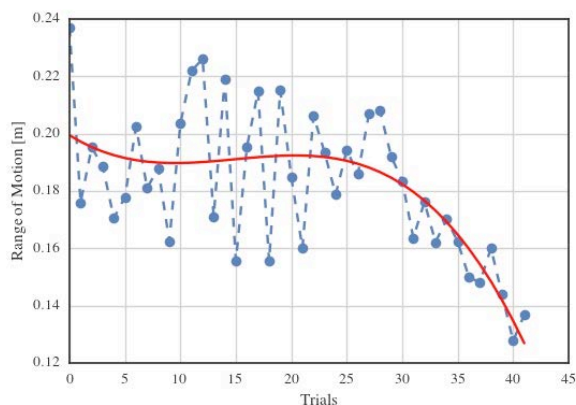**Fig. 2:** Comparison of the TLX Workload in real robotic setup (left) and in simulated environment (right).

Fig. 3: DVRK masters mean range of motions: dashed blue lines show the data, and solid red line its 3rd order poly-interp.

RESULTS

Considering the two experiments carried out, we collected nearly 75 hours of stereoscopic video at 30 frames per second and 124-dimensional kinematic data including joint angles and joint velocities of all the robotics manipulators, along with some additional data. In the first experiment, the students repeated the same test in virtual and real conditions during two one-hour sessions. The mean number of test repetitions for each student was 5.8 ± 2.2. The tests with the virtual and real surgical simulators showed the correlation between the experience with the virtual simulator and the execution of the tests with the DVRK. In Figure 2, we show the comparison of the workload for the two setups evaluated using the Nasa-TLX protocol [7]. We obtain comparable results even though the perceived workload in the simulated environment is higher than with the real robot. Group A, which performed the first test with the simulator and then with the DVRK, shows a lower workload as compared to Group B. This fact suggests that the two training have similar difficulty and that using the simulation before the real robot may ease learning, as shown also by other data collected (i.e. time required to complete the exercise, improved use of robot controls and range of motions). In the second

experiment the student performed 42 consecutive executions of a DVRK-assisted micro anastomoses task. The dataset also includes annotations on the task phases and self-reported global rating scores using the SARMS rubric. The data, as well as the subjective evaluation, shows that the student successfully learned to perform the microsurgical anastomosis procedure. For example, Figure 3, shows the metrics "mean range of motions" [3] of the master side manipulators for each trial. The data show an evident reduction of this metrics, confirming the improved robot control due to learning.

DISCUSSION

As large data sets of robot assisted procedures become available, new methods must be developed to mine these data to extract useful information on task and human performance. We started experimenting with data generation and analysis by addressing the challenges of training in robotic surgery, with intra and inter-subject tests. The availability of high quality training data allows making more precise assessments of the trainee capabilities with respect to previously available data sets.

The first test addressed training in virtual environments and with a real surgical robot, the DVRK, of a small group of medical students. This test will allow designing personalized curricula with remedial exercises to improve specific surgical skills. The large data set produced with the microsurgical training during end-to-end anastomosis tasks, consisted of motion data, video, and skill progression ratings and annotations. This data set provides a useful platform for research on automatic analysis and quantification of surgical skills. The datasets are a more realistic context than those currently available, and will support the development of automatic data segmentation and analysis methods for a possible implementation in clinical settings.

REFERENCES

[1] J.A. Martin, G. Regehr, et al., British Journal of Surgery 84(2), 273 (1997)

[2] T. Alrasheed, J. Selber, Seminars in Plastic Surgery 28(01), 005 (2014)

[3] P. Andrew, KA Stegemann, JR Syed, et al. Fundamental skills of robotic surgery: a multi-institutional randomized controlled trial for validation of a simulation-based curriculum. Urology 2013;81:767.

[4] Y. Gao, S.S. Vedula, et al. Modeling & Monitoring of Computer Assisted Interventions (M2CAI) - MICCAI Workshop 2014

[5] Kazanzides P., Chen Z., Deguet A., Fischer G. S., Taylor R. H., and DiMaio S. P. An open-source research kit for the da vinci surgical system. In Proc. of the IEEE Intl. Conf. on Robotics & Automation (ICRA), pages 6434–6439, 2014

[6] Prunières GJ, Taleb C, Hendriks S, Miyamoto H, Kuroshima N, Liverneaux PA, Facca S. Chir Main. 2014 Apr;33(2):106-11, 2014.

[7] Hart, S.G. and Staveland, L.E., 1988. Development of NASA-TLX (Task Load Index): Results of empirical and theoretical research. Advances in psychology, 52, pp.139-183

Robust Shape Recovery of Deformable Soft-tissue Based on Information from Stereo Scope for Minimal Invasive Surgery

J. Song, J. Wang, L. Zhao, S. Huang, G. Dissanayake

Centre for Autonomous Systems, University of Technology, Sydney, Australia

Jingwei.song@student.uts.edu.au

INTRODUCTION

Overcoming small field of view of scopes is an important challenge in minimal invasive surgery (MIS). Efforts have been devoted in 3D soft-tissue construction and camera localization [1-2]. This paper proposes a robust strategy for simultaneous camera localization and dense reconstruction of deformable surfaces. To boost robustness, this paper proposes three strategies: (1) using a sequence of images collected from a stereo scope by considering uncertainty map; (2) filtering images with low intensity; (3) filtering depth by normals. According to our knowledge, this is the first paper tactifully utilize the objective function value from stereo estimation process as uncertainty map to enhance performance; results show that adopting greatly reduces depth estimation parameter adjustment efforts while still achieves good performance and preserves topological details. Experiments reveal that the proposed approach is convenient for dynamically rebuilding and visualizing the latest shape of soft-tissue to mitigate unnecessary tissue damages in MIS. The supplementary video is available at https://youtu.be/ZvQBBLzgfZQ

METHODS

The map management in our simultaneous localization and mapping (SLAM) framework is colored point cloud. After initializing the model with the first depth, we implement our SLAM framework in following steps:

Raw depth estimation from stereo images. We followed previous work [2] by applying [3] to estimate raw depth from stereo scope. The difference is that no smoothing step is required because our SLAM possess the ability of fusing multiple noisy depth into a fine depth and noises resulted from depth estimation process could be compensated.

Sparse key points extraction and matching. To enhance stability and avoid drift, we applied Dense SURF (Speeded Up Robust Features) method to generate sparse registrations between last state model to current observation in the form of key control points. This idea is realized by projecting last step model to 2D RGB map and run dense SURF with current observed 2D RGB image. Value of energy function in [3] is recorded as depth quality evaluator.

Warping field estimation based on dense and sparse registration. Similar to previous work [4-6], warping field for vertex deformation is defined as:

$$\tilde{v}_i = \sum_{j=1}^{k} \omega_j(v_i)[A_j(v_i - g_j) + g_j + t_j]$$

where $\tilde{v}_i$ and v_i are the transformed and original position
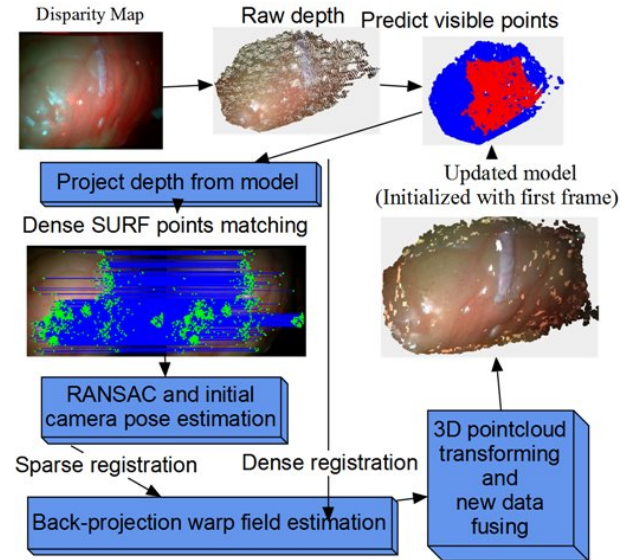

Fig. 1 Deformable soft-tissue reconstruction framework.

of the ith vertex, g_j and $\omega_j(v_i)$ are the related neighbor node position and weight. A_j and t_j are the 3x3 matrix and translation vector of the node. Each node consists of 4 neighboring nodes and these nodes are evenly downsampled. By setting distance and normal threshold to extract predicted visible points we estimate optimum A_j and t_j of the nodes by minimizing the object function:

$$\text{argmin}_{A_1,t_1 \ldots A_n,t_n} \omega_{rot}E_{rot} + \omega_{reg}E_{reg} + \omega_{dat}E_{dat} + \omega_{cor}E_{cor}$$

With four terms: Rotation (E_{rot}), Regularization (E_{reg}), back-projection data registration (E_{dat}) and correspondence (E_{cor}). E_{rot} ensures the A_j is close to SO(3) space. Term E_{reg} and E_{dat} are:

$$E_{reg} = \sum_{j=1}^{m} \sum_{k \in N(j)} \alpha_{ij} ||A_j(g_k - g_j) + g_j + t_j - (g_k + t_k)||^2$$

$$E_{dat} = \sum_{i=1}^{M} \Omega((P(\tilde{v}_i))(\hat{n}_i(P(v_i))^T(v_i - \gamma(P(v_i)))^2$$

where $N(j)$ is the neighboring node set of node j. $\hat{n}_i$ is the normal of v_i. $P(\tilde{v}_i)$ is the depth image projective function (3D point to 2D pixel) and $\gamma(\cdot)$ is the lift function (2D pixel to 3D point). $\Omega((P(\cdot))$ is the uncertainty map of depth estimated from stereo scope. E_{reg} ensures the consistency of the neighboring node and as a constraint for as rigid as possible. E_{dat} ensures the model is deformed toward target depth.

New data fusion. Deformed point cloud map is projected into 2D RGBD images and fused with new

RGBD observation if the new depth falls within the threshold of map.

$$D_{n+1}\big(P(p)\big) = \frac{\tilde{p}|_z \boldsymbol{\omega}(p) + D_n(P(p))}{\boldsymbol{\omega}(p)+1}$$

$$\boldsymbol{\omega}(p_n) = \min\left(\boldsymbol{\omega}(p_{n-1}) + 1, \boldsymbol{\omega}_{max}\right)$$

where $\tilde{p}|_z$ is the projected depth of a deformed map point $\tilde{p}$. $\boldsymbol{\omega}(p)$ is the associated weight of the map point and D_n is the current estimated depth.

RESULTS AND DISCUSSION

The proposed approach is validated by stereo video datasets provided by the Hamlyn Centre for Robotic Surgery [7]. Two Ex-vivo validation datasets with ground truth taken from associated CT scans are tested (Fig.2). Comparing with ground truth, workflow with our robust approach achieves estimation results with average errors as 0.28mm and 0.09mm, respectively, which outperforms the non-robust approach (average errors 0.35mm and 0.12mm).

We also tested the proposed approach on two in-vivo experiments (Fig. 3). More details are preserved due to our strategy of not smoothing depth map but implementing weighted average fusion for generating depth more naturally. In the initial steps the model is coarse and fragmented while model becomes smoother when fusing new depth. This is due to the fact that fusion allows more information to confirm the topology on the surface of the model.
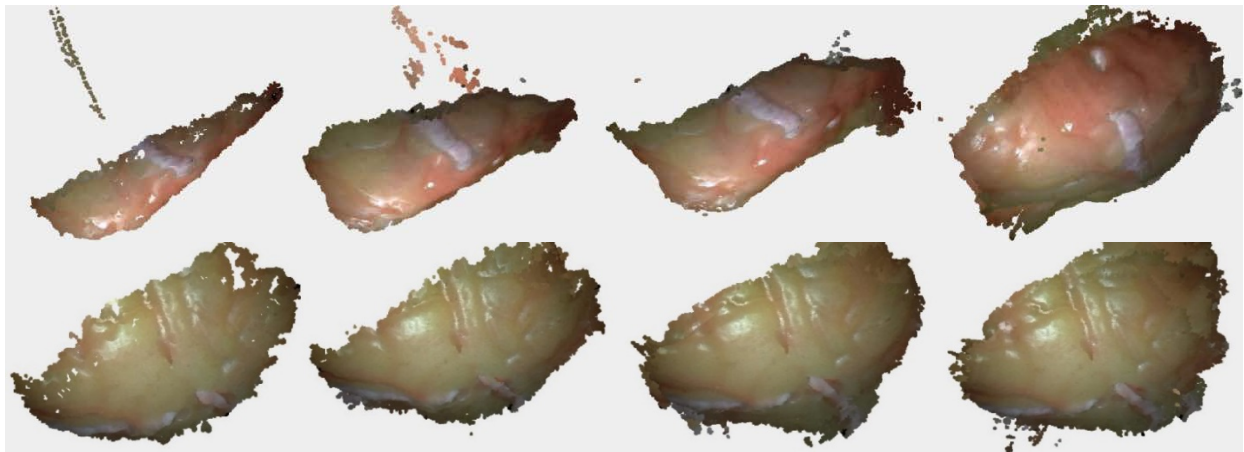

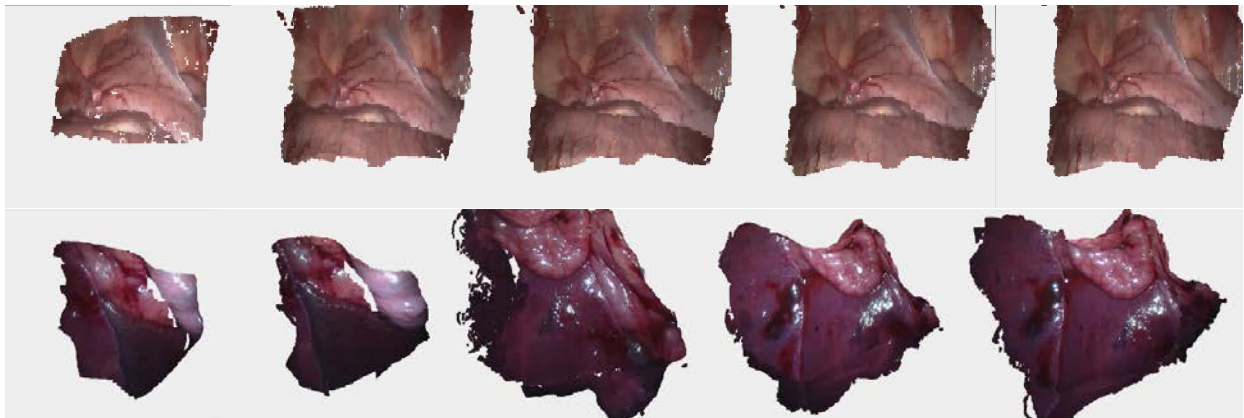**Fig. 2** Ex-vivo validation with the Hamlyn validation dataset. Frame 2, 30, 100, 200

Fig. 3 In-vivo validation with the Hamlyn validation dataset. Frame 2, 30, 100, 300, 500.

REFERENCES

[1] Chang, P. L., Handa, A., Davison, A. J., & Stoyanov, D. (2014, June). Robust real-time visual odometry for stereo endoscopy using dense quadrifocal tracking. In International Conference on Information Processing in Computer-Assisted Interventions (pp. 11-20). Springer International Publishing.

[2] Zhang L, Ye M, Giataganas P, et al. Autonomous Scanning for Endomicroscopic Mosaicing and 3D Fusion. arXiv preprint arXiv:1604.04137, 2016.

[3] Geiger, A., Roser, M., & Urtasun, R. (2010, November). Efficient large-scale stereo matching. In Proceedings of Asian conference on computer vision (pp. 25-38).

[4] Newcombe, R. A., Fox, D., & Seitz, S. M. (2015). Dynamicfusion: Reconstruction and tracking of non-rigid scenes in real-time. In Proceedings of the IEEE conference on computer vision and pattern recognition (pp. 343-352).

[5] Dou, M., Khamis, S., Degtyarev, Y., Davidson, P., Fanello, S. R., Kowdle, A., & Kohli, P. (2016). Fusion4d: Real-time performance capture of challenging scenes. ACM Transactions on Graphics (TOG), 35(4), 114.

[6] Innmann, M., Zollhöfer, M., Nießner, M., Theobalt, C., & Stamminger, M. (2016). Volumedeform: Real-time volumetric non-rigid reconstruction. In Proceedings of European Conference on Computer Vision (pp. 362-379).

[7] Giannarou, S., Visentini-Scarzanella, M., & Yang, G. Z. (2013). Probabilistic tracking of affine-invariant anisotropic regions. IEEE transactions on pattern analysis and machine intelligence, 35(1), 130-143.

A Case Study of a Passive Robotic Arm for Conventional Transanal Microsurgery

J. Liu[1], N. Penney[2], P. Wisanuvej[1], A. Darzi[2], G.-Z. Yang[1]

[1]The Hamlyn Centre, [2]Department of Surgery & Cancer, Imperial College London,

j.liu@imperial.ac.uk

INTRODUCTION

The local excision of lesions from within the rectal lumen using surgical platforms such as the Wolf 'Transanal Endoscopic Microsurgery' (TEM) system [1] offers a more stable and reliable method, as well as a much less invasive alternative for excising large benign lesions relative to radical excision of the rectum from within the pelvis via anterior or abdominoperineal excision. One challenge of the TEM surgery is to manipulate a heavy instrument set (~2kg) including a rectoscope, surgical port, endoscope and two laparoscopic instruments. The current clinical solution is to apply an articulated metal arm attached to the port that the surgeon can lock/unlock via a rotating knob. This is both inaccurate and time consuming, as the surgeon has to hold the instrument set in one hand while repeatedly loosening/tightening the lock with the other. Several endoscope holding devices have been developed, such as [2], however none of them has the payload over 2kg within a sufficient workspace. We have developed a lightweight robotic arm, named the Hamlyn Lightweight Robot Arm, for transanal microsurgery in order to help surgeons to position the port and its whole instrument set in an intuitive way. The versatile design of the arm allows it to be used for other procedures such as ENT surgery as well. Compared to the conventional supporting accessary, i.e. Martin's Arm [3], and other endoscope-holders [4], the Hamlyn arm is ergonomically intuitive to operate with larger payload, greater stiffness and weight compensation. Four human cases have been accomplished and the results show that the surgeon benefits from instant tool positioning, sufficient adjustment during lumen observation and firm tool locking.

MATERIALS AND METHODS

Figure 1 illustrates the mechanical structure of the Hamlyn Arm and its intuitive operation set up. The arm comprises of a mechanical support arm designed to clamp onto a compatible operating table. The Wolf™ TEM Port or other instruments can be fitted to the end of the device for use with conventional transanal surgery tools such as Wolf™ TEM tools with associated endoscopic equipment. It is designed with six joints to provide a large range of positioning movement.

The arm is electrically powered from a mains outlet through a 24V AC/DC power adaptor. The power supply controls electro-magnets at each of the device's joints, locking the joints in place when the control

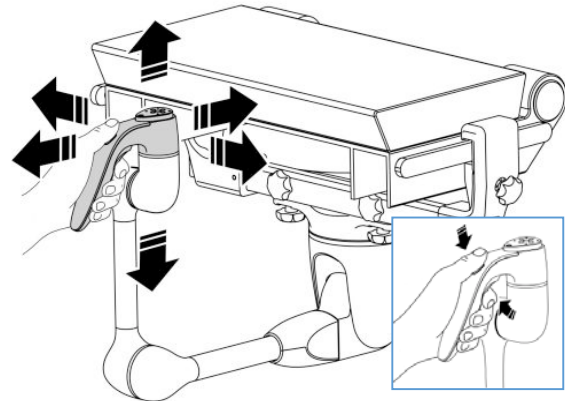handle is released. For safety, two buttons are designed on the handle and the arm is activated only if

Figure 1: Overview and operation of a Hamlyn Lightweight Robot Arm.

both buttons are pressed. A counter balance weight is used so that the weight of the port and the arm is not a burden to the surgeon when manipulating the arm. The arm is passively controlled and has no power consumption when it is locked so that it is safe to power-failure. The maximum payload of arm is 5kg and the stiffness is 0.4mm/kg in normal TEM configuration as shown in Figure 1. The arm has been fully tested to comply EN 60601-1 standard and is granted as a CE-marked Class-I medical device in 2015.

Prior to each procedure, the arm is mounted on the end of the operating table. During the procedure, the surgeon first mounts the Wolf™ TEM Port and an endoscopic camera on the arm and then inserts them into the patient's rectal lumen by manipulating the support arm and observing through the endoscope. During the insertion, the surgeon can pause and observe from time to time by locking the arm. When the port is in place, the surgeon can then insert the TEM instrument tools to perform the operation as required. The arm can be repositioned at any time during the surgery in order to obtain a better view of the lumen or to adjust the port's orientation for a convenient tissue manipulation. The transit time between locking and unlocking the arm is instant and less than 7ms. Due to the instant locking and high stiffness of the arm, the surgeon can achieve a "what you see is what you get (WYSIWYG)" result from positioning the port.

To assess the performance of the robotic arm, several factors including setup and procedure time were measured. During the operation, videos of the operating

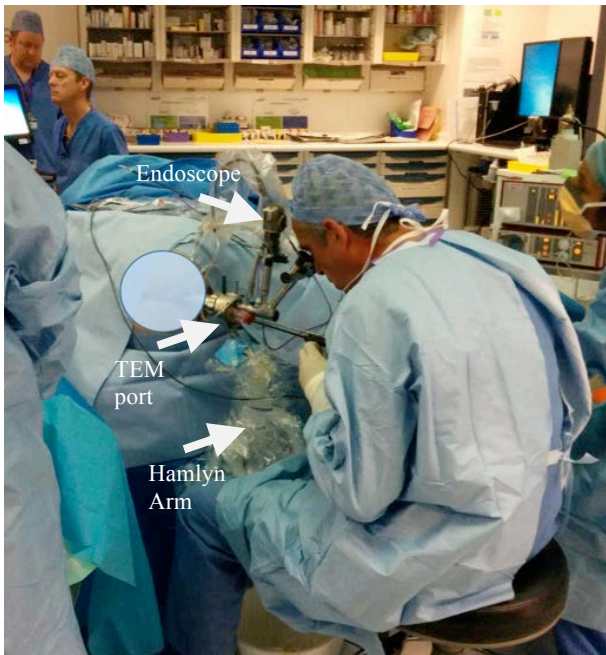theatre and the endoscope feed were recorded. A feedback form was completed by the surgeon after the operation.

Figure 2: *In vivo* **human trial of the Hamlyn Robot Arm.**

RESULTS

Table 1 provides the results from the four human studies in chronological order. One was a full TEM case including visual rectal examination, polyp excision and cloure via suturing. Two included visual rectal examinations and biopsy for potential TEM operations. One was a visual rectal examination only to judge whether a TEM procedure or a abdominoperineal procedure was suitable for the patient.

The setup of the robot arm was timed from its unboxing until securely mounting to the operating table. The mounting time included docking the TEM port on the arm, connecting the endoscope and the camera system, and draping the whole arm. The adjustment time was measured covering a brief arm test and checking all connections prior the insertion. The activation time was the total manipulating time of the arm during the entire operation from the port insertion until finishing the operation. It only counted the time when the arm was activated. The activation count was the total manipulation number during the entire operation.

The whole operation was divided into three stages, i.e. Stage I, examination, from inserting the port into the rectum to start the examination until starting the main procedure; Stage II, main procedure such as the biopsy or excision; and Stage III, post-procedure assessment, i.e. to check the outcome of the main procedure. These stages were timed and the activation of the arm was counted.

The average setup of the arm was 58s and the average mounting time was 55s. The adjustment period was long in the first trial (82s) but decreased quickly in the

following trials. The mean time was 34s. The arm's activation time was over 120s with an average of about 20s per activation in the 1st and 4th trial. The main reason was that the arm helped in Stage I for examination and choosing the optimal place for a biopsy. In the 2nd and 3rd trial, the arm was activated briefly each time with average of 7s per activation. In Stage II of both biopsy cases, there was no arm activation as the operation was straightforward. In contrast, the arm was moved 5 times in Stage II of 2nd trial in which the surgeon had to adjust the arm for a more complex operation including excision and suturing.

Table 1: Statistics of the Hamlyn Robot Arm in human trials

Trial No.	Procedure	Setup/mounting/ Adjustment/activation time,/activation count	*Duration in Operation I/II/III (count of arm activation)
1	Examination and Biopsy	56s/62s/82s/124s/5	150(5)/201/7s
2	TEM, excision of polyp	61s/55s/22s/44s/7	187(2)/2061(5)/5s
3	Examination before laparoscopy	60s/52s/15s/22s/3	195s(3)/NA/NA
4	Examination and biopsy	55s/50s/17s/191s/9	753(8)/248/6(1)s

Notes: *Duration: I, visual rectal examination; II, main procedure; III, post-procedure assessment.

DISCUSSION

The human studies show the performance advantage for the surgeon to position the port or adjust the endoscope both intuitively and instantly. Regarding the written feedback, the surgeon regard the arm as "steady, resilient and intuitive" compared to the Martin's arm. The WYSIWYG is the most salient feature as the robot arm can achieve submillimeter pointing accuracy between activating and locking stage, while the Martin's arm can drift over 10mm even when locked. All these features demonstrate the practical value of the device in routine surgical environments.

REFERENCES

[1] Kunitake, et.al. "Transanal endoscopic microsurgery for rectal tumors: a review." Perm J 16.2 (2012): 45-50.

[2] A. N. Mamelak, et al, "Single-surgeon fully endoscopic endonasal transsphenoidal surgery: outcomes in three-hundred consecutive cases," Pituitary, vol. 16, pp. 393-401, 2013.

[3] Y. Qi, D. Stoddard, et.al. "Indications and techniques of transanal endoscopic microsurgery (TEMS)," Journal of Gastrointestinal Surgery, vol. 15, no. 8, p. 1306, 2011

[4] Morita, Akio, et al. "Development of hybrid integrated endoscope-holder system for endoscopic microneurosurgery." Neurosurgery 55.4 (2004): 926-932.

Safety Enhancement Framework for Robotic Minimally Invasive Surgery

V. Penza[1,2], E. De Momi[2], N. Enayati[2], T. Chupin[2], J. Ortiz[1], L. S. Mattos[1]

[1] Department of Advanced Robotics, Istituto Italiano di Tecnologia, Genoa, Italy
[2] Department of Electronics, Information and Bioengineering, Politecnico di Milano, Italy
veronica.penza@polimi.it

INTRODUCTION

In abdominal surgery, intra-operative bleeding is one of the major complications that affect the outcome of minimally invasive surgical procedures, even when performed with a robotic system. One of the causes is attributed to accidental damages to vessels, and one of the possible risk factors falls on surgeon's skills [1].

Computer-assisted technologies coupled with surgical robotic systems can enhance surgeons' capabilities by providing additional information regarding the surgical gestures. The intra-operative identification of vessels to be preserved has been explored using pre-operative information registered on the patient and visualized by means of Augmented Reality (AR) [2]. However, this approach has to deal with dynamic changes of the anatomy between the data acquisition phase and the surgical procedure. In order to update the pre-operative/intra-operative registration at run-time, image-based stereo reconstruction and tracking algorithms can be exploited to describe the tissue deformations [3]. Although such computer vision algorithms have achieved considerable performance, what is still missing is their integration into a surgical robotic system, providing (i) high accuracy, (ii) long-term robustness in difficult circumstances (field of view occlusion, presence of blood or smoke, sudden camera movements), (iii) adaptation to various changes of the environment or of the object itself and (iv) real-time processing.

This paper presents an Enhanced Vision System to Improve Safety in Robotic Surgery (EnViSoRS) by warning the surgeon in case an instrument is approaching a delicate area to be protected. This area, also defined Safety Area (SA), can be intra-operatively identified by the surgeon on the image. A tracking algorithm is used to robustly track the SA, and consequently, the tissue surface is reconstructed. The 3D information is used to identify a Safety Volume (SV) fitted around the reconstructed tissue surface. AR is used to visualize at run-time the SV projected on the image and to display the tissue-instrument distance. The system has been integrated into the da Vinci Research Kit (dVRK, provided by WPI and Johns Hopkins University) to validate its usability under realistic conditions.

MATERIALS AND METHODS

An overview of EnViSoRS integrated in the dVRK is shown in Fig. 1. The framework consists of five main steps, which are described in the following paragraphs.
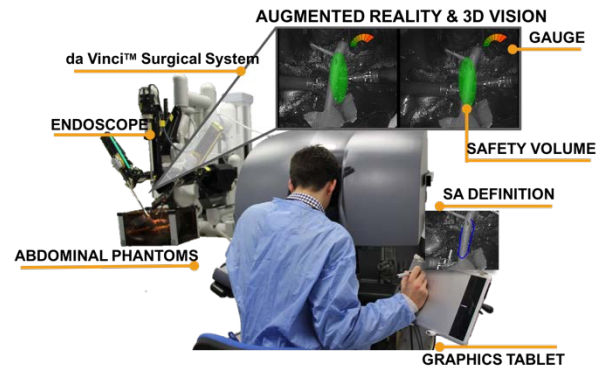

Fig. 1 EnViSoRS system: Enhanced Vision System to improve Safety in Robotic Surgery integrated into dVRK system (WPI and Johns Hopkins University). From the console the surgeon can (i) select the SA using a stylus and a graphics tablet, (ii) see the SV overlaid on the images, and (iii) see a graphical gauge warning about the tissue-instruments distance.

Step 1: Read Images

In this state, image left and right are captured, the distortion is corrected and the images are rectified in order to facilitate the search for stereo correspondence of the 3D reconstruction method. Specular highlights are also identified as bright regions with low saturation and high intensity to prevent errors in feature tracking and 3D reconstruction computation.

Step 2: Safety Area Definition

The SA is a 2D polygon that can be defined by the surgeon on the image at any moment of the surgery. A digital drawing tablet with stylus (WACOM Bamboo Pen and Touch Tablet) was placed on one side of the da Vinci[TM] master console, allowing the surgeons to perform this operation while they are seated, viewing the images from the stereo-endoscope.

Step 3: Tissue Tracking

The Long-Term Safety Area Tracking (LT-SAT) algorithm [4] is used to robustly track the SA when (i) the endoscopic camera is moved by the surgeon to navigate the operating field, (ii) the tissues are moving or deforming, or (iii) the field of view is occluded by instruments or smoke. The algorithm combines an optical flow technique with a tracking-by-detection approach to improve the robustness against failures. A Bayesian inference-based approach is used to detect tracking failures and a Model Update Strategy (MUpS) is exploited to improve the SA redetection after a failure.

Step 4: Tissue 3D Reconstruction

A dense soft tissue stereo-reconstruction algorithm [5] is used to retrieve the 3D surface of the tissue contained in the SA. To reduce the computational time, the tracked SA is used as a prior for the coarse identification of the area of the image to reconstruct. A pixel-based foreground-background segmentation is used to discard the 3D points laying on the background. The algorithm is based on a block matching approach, exploiting a non-parametric Census transform to make the stereo-matching robust to illumination variations. The density of the reconstructed surface is improved by using Simple Linear Iterative Clustering (SLIC) super pixel during the disparity refinement. With respect to the previous implementation, a novel strategy is proposed to smooth the point cloud. The disparity image is considered as a 2D Laplace equation problem. The disparity values on the super pixel contours are considered as the Dirichlet boundary conditions and the remaining as the initial conditions. The Gauss-Seidel method with red and black ordering is used to solve the equations.

Step 5: Safety Augmentation

The aim of this state is (i) to visualize the projection of the SV fitting the reconstructed surface of the SA, and (ii) to warn the surgeon when the robotic instruments are approaching the tissue surface. The SV is computed as an ellipsoid fitted on the point cloud and its 2D projection is displayed on the image by means of AR. In order to know the distance between the end-effector of the instruments and the reconstructed surface, spatial neighbor search based on octree structure is used. If the distance is inside the range Δ_{dist}, the surgeon is visually warned through a gauge located in the top-right corner of the image, as shown in Fig. 2.

RESULTS

To validate the *robustness* and *usability* of EnViSoRS, experimental trials were performed involving 14 subjects and 3 surgeons specialized in robotic surgery in urology. The task they performed consisted in tele-operating the da Vinci arms to move a piece of tissue from one side of a liver phantom to another and then moving it back, paying attention to keep a certain distance from a vessel positioned in the middle of the operating field, as shown in Fig. 2. Each subject performed 2 sessions, respectively with and without EnViSoRS; for each session the task was repeated 2 times. The operating field used was a previously developed phantom of human abdomen [6].

The *robustness* of the system was evaluated verifying the overlap between the SV projected on the image as AR and the SA visible in the image. The precision and recall curves, computed varying the overlap ratio threshold, gave an Area Under the Curve (AUC) of 0.898 and 0.932, respectively. The *usability* of EnViSoRS was evaluated asking the subjects to fill the System Usability Scale (SUS) questionnaire, which allows the evaluation of surgical technology in terms of general usability. Results showed a higher global score

Fig. 2 Example of AR visualization. From left to right, three different situations showing (i) the instruments performing the surgery in the safe green range, (i) the right instrument approaching the delicate area, (iii) the left instrument almost touching the vessel surface and the gauge completely red.

using EnViSoRS w.r.t. using the standard da Vinci system without AR feedback (79.21 vs 74.74 in the range $0 - 100$). The performance in terms of computational time showed an average frame rate between 2.5fps to 4fps.

DISCUSSION

This paper demonstrates the high robustness, usability and interactive frame rate of EnViSoRS, a computer vision framework aimed at improving the safety during robotic minimally invasive surgery. The added value of this work is the integration of EnViSoRS with dVRK system, showing the application into a state-of-the art robotic surgical system, thus shortening the distance to a future real clinical application of the technology. Future work will aim at improving the system under different aspects: (i) defining active constraints by using haptic feedback to guide the surgical gesture, (ii) exploring different modalities to define the SA and represent the AR information, and (iii) speeding up the computation time, exploiting CPU-GPU processing.

REFERENCES

[1] I. Opitz, W. Gantert, U. Giger, T. Kocher, L. Krähenbühl, et al. Bleeding remains a major complication during laparoscopic surgery: analysis of the salts database. Langenbeck's Archives of Surgery. 2005; 390:128–133.

[2] S. Onda, T. Okamoto, M. Kanehira, F. Suzuki, R. Ito, S. Fujioka, et al. Identification of inferior pancreaticoduodenal artery during pancreaticoduodenectomy using augmented reality-based navigation system. Journal of hepato-biliary-pancreatic sciences. 2014; 21:281–287.

[3] D. Stoyanov, D. Surgical vision. Annals of biomedical engineering. 2012; 40:332–345.

[4] V. Penza, X. Du, D. Stoyanov, A. Forgione, L. Mattos, and E. De Momi. Long term safety area tracking (LT-SAT) with online failure detection and recovery for robotic minimally invasive surgery. Medical Image Analysis (under review).

[5] V. Penza, J. Ortiz, L. Mattos, A. Forgione E. and De Momi. Dense soft tissue 3D reconstruction refined with super-pixel segmentation for robotic abdominal surgery. International journal of computer assisted radiology and surgery. 2015:11: 197–206.

[6] A. Ciullo, V. Penza, L. Mattos, and E. De Momi. Development of a surgical stereo endoscopic image dataset for validating 3d stereo reconstruction algorithms. 6th Joint Workshop on New Technologies for Computer/Robot Assisted Surgery. 2016.

Toward a Low-Cost Soft Robotic Manipulator based on Fluid-Actuated Bellows for Gastric Cancer Screening

N. Garbin[1], A. Stilli[2], A. Shiva[2], J. Fras[3], P.R. Slawinski[1], K.L. Obstein[4], K. Althoefer[3], H.A. Wurdemann[5], P. Valdastri[6]

[1] *Department of Mechanical Engineering, Vanderbilt University, USA*

[2] *Department of Informatics, King's College London, UK*

[3] *School of Engineering and Materials Science, Queen Mary University of London, UK*

[4] *Division of Gastroenterology, Hepatology, and Nutrition, Vanderbilt University Medical Center, USA*

[5] *Department of Mechanical Engineering, University College London, UK*

[6] *School of Electronic and Electrical Engineering, University of Leeds, UK*
nicolo.garbin.1@vanderbilt.edu

INTRODUCTION

Gastric cancer is the second highest cause of cancer related death in low- and middle-income countries (LMIC). Rural areas of LMIC lack in screening capabilities due to the high cost associated to maintain an endoscopy unit or similar specialized department.

The early diagnosis of gastric cancer is proved to increase the probability of survival [1].

Upper endoscopy (UE) is the preferred screening method, where detection of asymptomatic gastric cancer or premalignant lesions is possible by using a flexible endoscope with a steerable tip.

In order to facilitate the screening procedure in LMIC, a disposable endoscope could provide a more convenient and accessible screening option.

Soft continuum robotic solutions are getting attention in the medical field thanks to their ability to pan and tilt -yielding visualization similar to traditional endoscope– while being more compliant, hence reducing the risk of traumatic tissue interaction [2].

In this abstract, we evaluate the performance in terms of stiffness and range of motion of a parallel bellow actuated (PBA) manipulator [3] with two different diameters: PBA_14 and PBA_28. The former (14 mm diameter) is suitable for endoscopic application while the latter (28 mm diameter) has been chosen for scalability consideration of PBA and comparison to a silicon moulded soft continuum robot (STIFF FLOP) [4], which at its current stage, has similar dimensions.

MATERIALS AND METHODS

By using inexpensive material (3D printed parts, Objet30, Stratasys, Israel) and off-the-shelf bellows (Rubberstore, USA), PBA_28 and PBA_14 are assembled within minutes by arranging the three bellows at the vertex of an equilateral triangle (Fig. 1). The PBA diameter is dictated by the bellow outside diameter. The system is actuated using air by manually operating a set of syringes and locking them once a desired configuration is achieved. In order to test the stiffness of the manipulator, we tested both PBAs in 4 different configurations, as represented in Fig. 2.
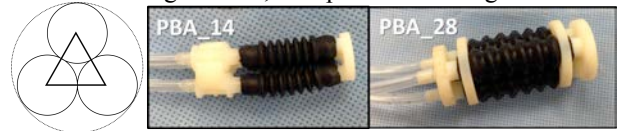

Fig. 1 (left) Schematic cross section of the PBA. **(centre)** PBA_14 assembled: bellow BC 2305 (Nitrile; $E\_1 = 3$ MPA, $4.58 each) and 3D printed tip and base ($1.36). **(right)** PBA_28 assembled: bellow BS 5070 (EPDM; $E\_2 = 16.49$ Mpa, $1.97 each) and 3D printed tip and base ($3.11).

In all the scenarios, the PBA under investigation was anchored against gravity and a load cell (ATI Nano17, ATI Industrial Automation, USA), mounted on a robotic manipulator (Mitsubishi RV-6S, Japan), was moved linearly along the x axis (see Fig. 2) in a range 0-9.5 mm (with a 0.5 mm increment step) 3 times per test.
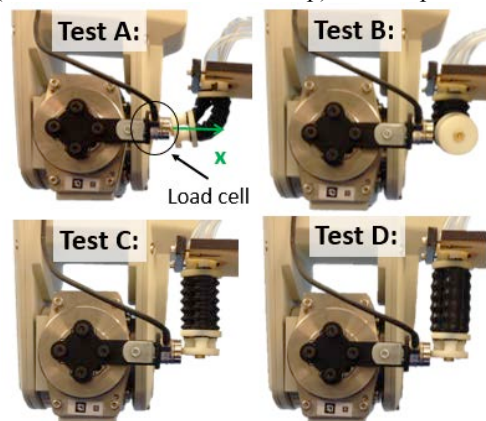

Fig. 2: Experimental set up for stiffness analysis of PBA_28. Test A: axial stiffness test when bent by 90°, Test B refers to the lateral stiffness when bent by 90°, Test C refers to the lateral stiffness when straight and depressurized, and Test D refers to lateral stiffness when straight and pressurized.

The range of motion analysis of both PBAs was instead performed tracking base and tip positions while recording the pressure in each bellow (p_1, p_2, p_3). The position was acquired using a magnetic tracker (Aurora,

NDI, Canada) and placing one 6 DoF sensor at the base and one at the tip of the bellow.

Pressures were acquired via dry pressure sensors (24PCCFB6G, Honeywell, USA) along each bellow's line. Three scenarios were investigated starting from a fully retracted configuration (Home in Fig. 3, initial -13 kPa pressure in each bellow). In each scenario, the motion – gradual increase and decrease in pressure – was performed for five times.
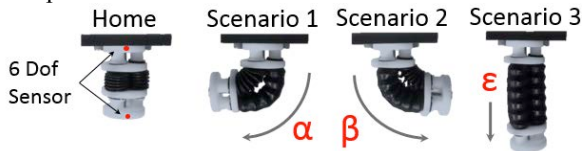

Fig 3. Range of motion analysis set up with PBA_28. Scenario 1: Single-bellow actuation to describe the tilting angle $\alpha = f(p_1)$; Scenario 2: Two-bellow actuation to determine the tilting angle $\beta = g(p_1,p_2)$ s.t. $p_1=p_2$; Scenario 3: Three-bellow actuation to obtain the base-to-tip distance $\varepsilon = h(p_1,p_2,p_3)$ s.t. $p_1 = p_2 = p_3$.

RESULTS

We define σ as the ratio between the two experimental stiffness values ($K_{\_PBA\_14}/K_{\_PBA\_28}$) of the manipulators and compare it to Σ defined as the ratio between the young moduli of the two bellow materials (E_1/E_2). For each trial, we calculated average stiffness [N/cm] and the relative hysteresis (as ratio between the area defined by the loading and unloading curve over the area identified by the loading curve only), shown in parenthesis [%].

Table 1: Stiffness experimental results

Test	$K_{\_PBA\_14}$	$K_{\_PBA\_28}$	σ	Σ
A	0.8103 (25.84)	1.869 (49.53)	0.433	0.181
B	0.3741 (50.41)	0.4505(56.11)	0.830	0.181
C	0.0631 (18.55)	0.3125(32.03)	0.202	0.181
D	0.1815 (24.90)	0.9737(33.03)	0.186	0.181

The relationships between pressure to tilt angles (α, β) and base-to-tip distance (ε), as depicted in Fig. 4, are non linear and, for negative pressures, they are less repeatable (higher standard deviation) due to bellows' contraction and subsequent vibration. PBA_14's motion occurs mainly with positive input pressure, while PBA_28 tilts and elongates more within the negative pressure range. PBA_14 is able to exceed 90° in both tilting directions ($\alpha_{max} = 107°$; $\beta_{max} = 94°$), while PBA_28 is not ($\alpha_{max} = 87°$; $\beta_{max} = 81°$). It is worth mentioning that PBA_14, undergoes ballooning (radial and axial expansion) at high-pressure due to a softer rubber. This allows it to reach a wider workspace. PBA_14 almost double its length when equally pressurized while PBA_28 elongates 10 mm. The two transfer functions for the angular displacement, f(p) and g(p), are not the same since pressures are not independent from each other. This relates to the fact that in scenario 2, two actuators overcome the stiffness of one bellow, while in scenario 1, the single bellow overcomes the stiffness of two other bellows. This is true for both PBA prototypes.
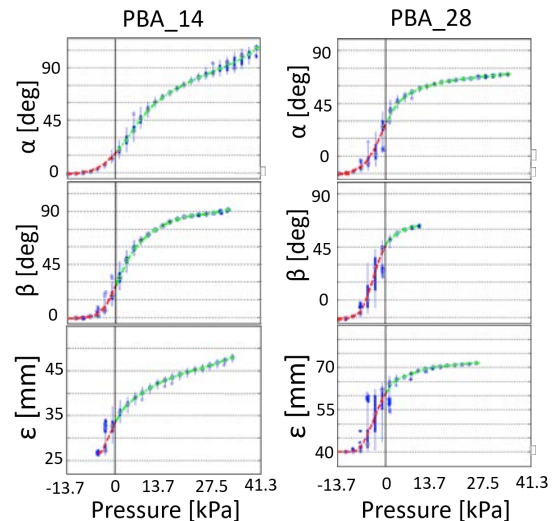

Fig. 4: Experimental results for range of motion analysis.

DISCUSSION

STIFF FLOP is a silicone (Ecoflex® 00-50, E_3 = 0.08 MPa) continuum manipulator that relies on pressurizing three couples of fiber reinforced chambers. Its size is comparable to PBA_28 and its range of motion is similar to what obtainable with the PBAs, but the pressures range from 0 kPa to 140 kPa. From a stiffness standpoint, STIFF FLOP outperform PBA_28 in test A (+30%), B (+66%), and C (+322%), but resulted -44% less stiff when elongated (Test D).

Test C and D reflect the fundamental difference of the two concepts: when all chambers are pressurized, STIFF FLOP elongates and decreases in diameter which cause reduced stiffness; PBAs elongates too, but the bellows interact with each other enhancing the manipulator ability to resist higher forces at the tip.

The large motion, compliance, ease of assembly and low cost, make PBA_14 a favourable candidate as steerable section for novel endoscopes.

Moving forward, other fluidic actuation means (water, granular material) will be investigated to increase the manipulator's stiffness.

REFERENCES

[1] H.O. Adami, N.E. Day, D. Trichopoulos, and W.C. Willett. Primary and secondary prevention in the reduction of cancer morbidity and mortality. European journal of cancer, 2001, 37, 118-127.

[2] J. Burgner-Kahrs, D.C. Rucker, and H. Choset. Continuum robots for medical applications: A survey. IEEE Trans Robotics, 2015, 31(6) 1261-1280.

[3] D. O'Brien and D.M. Lane. 3D force control system design for a hydraulic parallel bellows continuum actuator. IEEE ICRA. 2001, vol. 3, 2375-2380

[4] A. Shiva, A. Stilli, Y. Noh, A. Faragasso, I. De Falco, G. Gerbonu, M. Cianchetti, A. Menciassi, K. Althoefer, H.A. Wurdermann. Tendon based stiffening for a pneumatically actuated soft manipulator. IEEE Robotics and Automation Letter 2016, 1(2), 632-637.

"Losing Your Nerve in the Operating Room" – Prefrontal Attenuation is Associated with Performance Degradation under Temporal Demands

H. Singh*, H.N. Modi*, G.Z. Yang, A. Darzi, D.R. Leff

Hamlyn Centre for Robotic Surgery, Imperial College London
harsimrat.singh@imperial.ac.uk *Joint first author

INTRODUCTION

The ability to maintain attention and concentration when operating under high-pressure conditions is critical in order to maintain performance and protect the safety of patients.

The prefrontal cortex is integral to executive function and plays an important role in attention, concentration and performance monitoring[1]. However, literature from other fields suggests that stressful conditions leads to a loss of prefrontal activation and a deterioration in task performance[2, 3].

The aim of this study was to determine the effect of time pressure on prefrontal activation, using an autoregressive method to solve the general linear model (GLM), and technical performance during a laparoscopic suturing task.

MATERIALS & METHODS

33 general surgery trainees (ST3-Post-CCT fellow) were asked to perform a laparoscopic suturing task under (1) 'self-paced' conditions, in which subjects were permitted to take as long as require to tie each knot, and (2) 'time pressure' conditions, in which a time limit of 2 minutes per knot was imposed. Participants were required to tie 5 interrupted knots in each condition, with an inter-trial rest period of 30 seconds. Subjective workload was measured using the validated Surgical Task Load Index (SURG-TLX) questionnaire. Prefrontal activation responses were inferred from changes in cortical haemoglobin species, measured using a 24-channel functional near-infrared spectroscopy system (ETG-4000, Hitachi Medical Corp., Japan). Technical performance was assess using task progression scores (au), error scores (mm), leak volumes (ml), and knot tensile strengths (N).

Anatomical Co-registration: The geometric configuration of the probes placed bilaterally on the PFC was co-registered to a standard head volume (Colin27 MRI atlas[4]) in order to establish the approximate prefrontal regions from which data was collected. Co-registration was performed using an open source toolbox[5]. Probe coordinates were captured using a 3D digitizer and were used to project the channel locations onto a cortical surface. Sensitivity of each channel in terms of depth of brain tissue that near-infrared light could penetrate was estimated by modelling photon migration within the head volume.

General Linear Model (GLM): The haemodynamic response to the functional stimulus was analysed using a boxcar function, designed on the basis of timeline and type of stimulus events. A linear model of an evoked response is given as $Y=X\beta$, where X is the design matrix, and β is the estimate of the magnitude of brain activity. A limited number of coefficients (β) are used to enable statistical testing of differences in brain activity between different task conditions. An iteratively whitened weighted least-squares regression model along with canonical repressors of the stimulus task was employed to estimate the expected response as described by Barker et al[6].

RESULTS

Subjective Workload and Heart Rate

Subjective workload was significantly greater in the time pressure compared to the self-paced condition [mean SURG-TLX score ± SD: 136.6 ± 47.0 vs 183.4 ± 51.8; t(30) = -7.3, paired samples t-test p<0.001]. There was no significant difference between conditions in the change in heart rate from rest to task (Figure 1).

Technical Performance

Time pressure led to a significant deterioration in task progression score [median task progression score (IQR): self-paced = 6.0 (0.2) vs time pressure = 5.0 (1.6); z=-4.5, Wilcoxon Signed Ranks p<0.001], and a significant increase in error score [median error score (IQR): self-paced = 2.0 (2.2) mm vs time pressure = 3.0 (2.2) mm; z=-2.0, Wilcoxon Signed Ranks p=0.041], leak volume [mean leak volume ± SD: self-paced = 17.4 ± 2.0 ml vs time pressure = 18.8 ± 2.5 ml; t(30) = -3.1, paired samples t test p=0.004], and knot tensile strength [mean knot tensile strength ± SD: self-paced = 40.4 ± 17.3N vs time pressure = 18.5 ± 19.0N; t(30) = 5.2, paired samples t test p<0.001] (Figure 1).

Cortical Brain Function

The mixed–effect model revealed diminished prefrontal activation in the time pressure condition as compared to the self-paced condition on the group level for the cohort of surgical trainees. This is evident in Figure 2, where the colour of the channels (straight lines connecting the optodes) depicts t-values computed using

a student's t-test with a Bonferroni correction (p<0.05). The non- significant channels are shown using dotted lines.

Relative to self-paced performance, operating under time pressure, manifest as a 40% decline in activation.

DISCUSSION

Our findings suggest intra-operative temporal demands lead to performance decline and attenuation in prefrontal excitation. This implies that under pressure trainees fail to adequately recruit prefrontal resources and maintain task engagement. Future work should seek to develop training strategies and/or innovations (e.g. metacognition/mental rehearsal) that mobilise prefrontal regions, enhance task engagement and improve surgeons' performance under pressure.

REFERENCES

1. Roberts AC, Robbins TW, Weiskrantz LE. The prefrontal cortex: Executive and cognitive functions: Oxford University Press, 1998.
2. Arnsten AFT. Stress signalling pathways that impair prefrontal cortex structure and function. *Nature Reviews Neuroscience* 2009; 10(6):410-422.
3. Durantin G, Gagnon JF, Tremblay S, et al. Using near infrared spectroscopy and heart rate variability to detect mental overload. *Behavioural Brain Research* 2014; 259:16-23.
4. Collins DL, Zijdenbos AP, Kollokian V, et al. Design and construction of a realistic digital brain phantom. *IEEE Trans Med Imaging* 1998; 17(3):463-8.
5. Aasted CM, Yucel MA, Cooper RJ, et al. Anatomical guidance for functional near-infrared spectroscopy: AtlasViewer tutorial. *Neurophotonics* 2015; 2(2):020801.
6. Barker JW, Aarabi A, Huppert TJ. Autoregressive model based algorithm for correcting motion and serially correlated errors in fNIRS. *Biomedical Optics Express* 2013; 4(8):1366-1379.
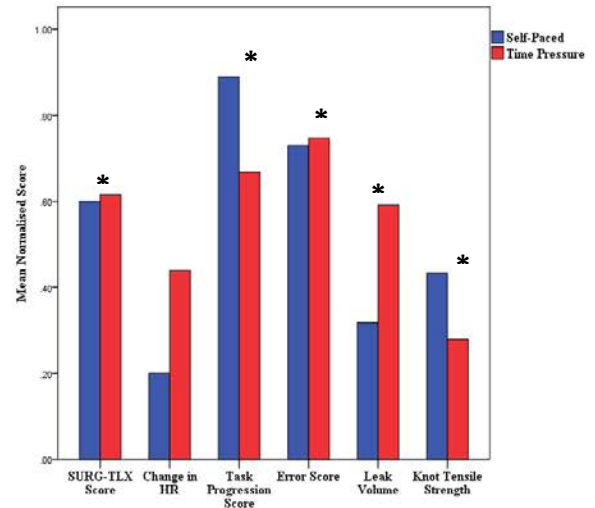
Figure 1. Normalised subjective workload, change in heart rate and performance scores in self-paced (blue bars) and time pressure (red bars) conditions. SURG-TLX: Surgical Task Load Index; HR: Heart Rate. *p<0.05.
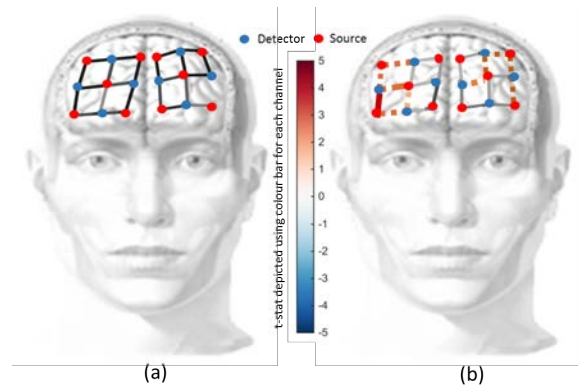

Figure 2. Whole group brain activation maps obtained using the GLM for (a) self-paced and (b) time pressure condition. Channels are highlighted using colour coded straight lines joining a source-detector pair. The colour bar is indicative of the t-values (red indicates high t-value, whilst blue indicates low t-values). Non-siginificant channels are shown as dotted lines.

Design and Evaluation of a Novel Soft MAGS Endoscope

T. Cheng[1], C.S.H. Ng[1], P.W.Y. Chiu[1, 2], Z. Li[1, 2]

[1]Department of Surgery, the Chinese University of Hong Kong,
[2]Chow Yuk Ho Technology Centre for Innovative Medicine, The Chinese University of Hong Kong

INTRODUCTION

Laparoscopes are commonly used in minimally invasive surgery (MIS) for visualizing surgical site. Along with other long shafted tools and articulated robots, these instruments crowd at access port. This limits triangulation and visualization. While there are endoscopes with articulated joints or rotatable prism to expand field of view, loss of triangulation and instruments fencing are still hurdles in MIS, particularly in laparoendoscopic single site (LESS) surgery. A potential solution is magnetic anchoring and guidance system (MAGS) proposed by Cadeduu et al [1]. Instruments are liberated from the access constraint and maneuvered in the surgical cavity via magnetic linkages. Various MAGS (retractor, cauterizer etc.) had been developed [2, 3]. Among these, MAGS endoscope had seen much research interest. However, all current MAGS endoscopes are fabricated with rigid components, and on-board motors are often required for local camera viewing direction control [4, 5]. These render the system heavier, less compact, and tedious in assembly and fabrication. Recent advances in soft robotics highlight benefits of lightweight, compactness, and safety. In light of this, we designed and fabricated a soft MAGS endoscope targeted for MIS application. Guided by permanent magnets, the endoscope can achieve anchoring, steering, and local camera maneuvering, without micromotors or articulated joints. We then proved its feasibility through *ex-vivo* tests. Some preliminary discussioin of this concept was published in [6, 7].

MATERIALS AND METHODS

The soft MAGS is composed of an internal unit, and an external controller. Internal unit contains the camera, and is inserted into surgical cavity. External controller moves outside patient's body to guide endoscope maneuver.

The internal unit is a continuous piece of silicone with two embedded internal permanent magnets (IPMs). It consists of three functional parts. A top cavity includes an upper magnet (UIPM, diameter 10mm; height 5mm), and has interior diameter greater than UIPM dimension, allowing ±4mm radial sliding of magnet. The middle joint is a compliant beam with a bending section (2mm length; 4mm diameter) connecting top cavity to lower parts. The lower suction cup has one open end. This allows insertion of a lower magnet (LIPM, diameter 15mm; height 1.5mm) and a capsule camera. Fig. 1a, b.

The external controller contains an external permanent magnet (EPM, diameter 28mm; height 10mm). A copper screw connects the EPM to a rack-pinion mechanism, mounted on a rotatable case (diameter 60mm). As such, position of EPM can be adjusted manually in radial and circular directions.
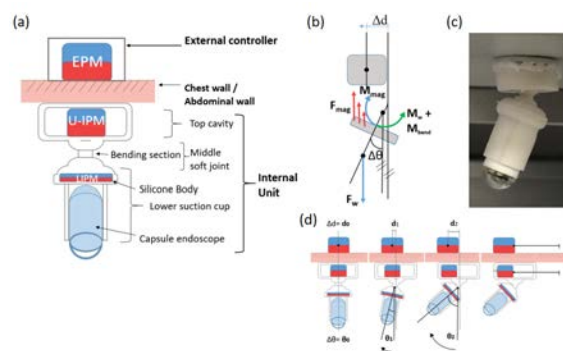

Fig. 1. (a) Schematic diagram of soft MAGS endoscope. (b) Free body diagram of IPMs. M_{mag}: Moment from magnetic force (F_{mag}); M_{bend}: middle soft joint bending moment; M_w: moment load from camera weight (F_w). (c) internal unit prototype (d) Camera pitch & locomotion sequence

While the internal unit is anchored to the external controller, UIPM follows motion of EPM. By adjusting position of EPM, UIPM moves within top cavity, attracting LIPM sideways so that their coupling force bends the middle joint. This generates pitch adjustment of camera viewing angle. (See Fig. 1c). Likewise, circular motion of EPM drives yaw of endoscope. Since LIPM is tilted to greater extend when UIPM is further from top cavity center (Δd), camera pitch angle ($\Delta \theta$) can be controlled by EPM position. As such, the middle joint bends in all directions to change endoscope viewing angle locally.

When EPM guides UIPM further ($\Delta d \geq 4mm$), UIPM eventually reaches and pushes cavity boundary. This allows magnetic driven locomotion of endoscope.
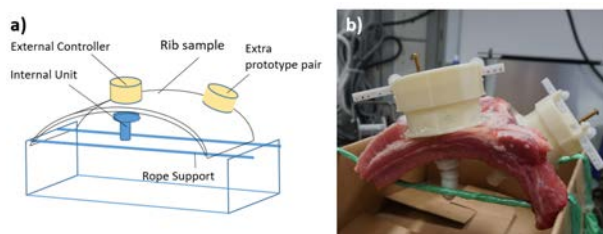

Fig. 2. (a) Schematic diagram and (b) Photograph of *ex-vivo* experiment setup

Prototypes of internal unit were fabricated by silicone casting in 3d printed mold pieces, at maximum diameter 22mm (top cavity) and weight 16.5g. Benchtop test and *ex-vivo* tests are performed to examine performances.

In Benchtop test, endsocope is anchored across 25mm thick wood plate. EPM is moved to examine the steering of the endoscope, i.e., pitch and yaw. To investigate safe operation range, internal unit locomotion (speed 20mm/s) guided by external controller is tested at increasing coupling range (20 to 50mm, 5mm increments). Maximum coupling distance without drop-off was recorded.

In *ex-vivo* test, a pig rib sample (length 18cm; width 15cm; arc height 8cm) is suspended by two parallel ropes. The sample arcs upwards, with sample membrane intact , and internal unit prototype is anchored beneath. This mimics operation environment in MIS. The experimental setup is illustrated in Fig. 2.

Two sets of *ex-vivo* tests are carried out to evaluate local view angle control and system locomotion. First, position of external controller is secured by a flexible gooseneck stand. EPM motion is controlled by rack-pinion mechanism. Bending of middle joint, and camera pitch of internal unit is observed. For the second test, external cotroller is steered manually on rib sample, guiding translation of internal unit parallel or normal to rib bone direction.
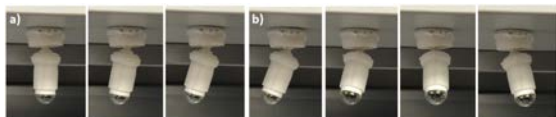
Fig. 3. Benchtop experiment snapshots. (a) Pitch (b) Yaw
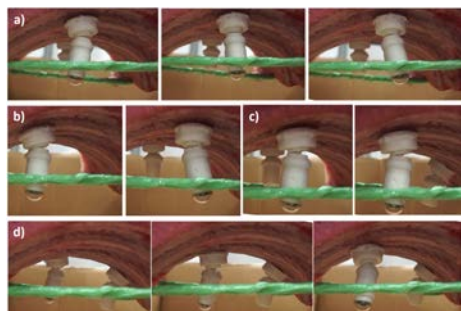
Fig. 4. Ex-vivo tests snapshots. (a) Camera pitch adjustment (b) Translation parallel to rib. Front unit; (c) Rear unit. (d) Translation normal to rib.

RESULTS

Images captured during both tests are shown in Fig. 3 and 4. In benchtop test, local control of camera view is stable at angular pitch speed 15°/s, and angular yaw speed 22.5^{o}/s. Steered at speed 20mm/s, the endoscope operates without loss of anchoring at maximum coupling range of 45mm.

For *ex-vivo* tests, stable camera pitch is observed. At tissue thickness 20-28mm, sliding parallel to rib bone direction is smooth and secure at 15mm/s. Steering normal to rib direction is secure at 20mm/s. Although compliance of medium and rib grooves introduce complexity in anchoring surface, failure of anchor did not occur. Minor wobbling of middle joint was observed, possibly due to fluctuation in coupling distance. Such instability quickly subsides (≤2s) once locomotion paused.

Placing another pair of soft MAGS prototype on the rib sample, 6 cm from tested prototype, show no crosstalk effect on system performance. This reveals the potential in using multiple soft MAGS endoscope simultaneously, thus allow exhaustive visualization of surgical targets.

Table 1. Comparison of soft MAGS endsocope to other MAGS.

Systems		On-board motor	Assembly free	Weight
	Classic MAGS camera [1]	N	Y	35g
	Modular MAGS platform [4]	Y	Y	48g Frame only
	Local magnetic actuation (LMA) camera [5]	Y	Y	20g
	Soft MAGS endoscope	N	N	16.5g

DISCUSSION

We presented a novel soft MAGS endoscope. The internal unit is a single piece of silicone embedded with two IPMs. Driven purely by magnetic linkage, the endoscope can achieve stable view direction control (local pitch and yaw), and system locomotion. Performance was evaluated in lab and *ex-vivo* environments, proving feasibility of design concept. Potential of operating multiple soft MAGS without crosstalk was also demonstrated. Compared to other MAGS endoscopes, soft MAGS is free of on-board motors, lightweight, more compact, easy to fabricate, and intrinsically safe. See table 1.

REFERENCES

[1] S. Park, R. A. Bergs, R. Eberhart, L. Baker, R. Fernandez, and J. A. Cadeddu, "Trocar-less instrumentation for laparoscopy: magnetic positioning of intra-abdominal camera and retractor," *Ann Surg,* vol. 245, pp. 379-84, Mar 2007.

[2] N. Garbin, C. Di Natali, J. Buzzi, E. De Momi, and P. Valdastri, "Laparoscopic Tissue Retractor Based on Local Magnetic Actuation," *Journal of Medical Devices,* vol. 9, pp. 011005-011005, 2015.

[3] D. J. Scott, S. J. Tang, R. Fernandez, R. Bergs, M. T. Goova, I. Zeltser*, et al.*, "Completely transvaginal NOTES cholecystectomy using magnetically anchored instruments," *Surg Endosc,* vol. 21, pp. 2308-16, Dec 2007.

[4] G. Tortora, P. Dario, and A. Menciassi, "Array of Robots Augmenting the Kinematics of Endocavitary Surgery," *IEEE/ASME Transactions on Mechatronics,* vol. 19, pp. 1821-1829, 2014.

[5] M. Simi, R. Pickens, A. Menciassi, S. D. Herrell, and P. Valdastri, "Fine tilt tuning of a laparoscopic camera by local magnetic actuation: two-port nephrectomy experience on human cadavers," *Surg Innov,* vol. 20, pp. 385-94, Aug 2013.

[6] Z. R. Zhao, Z. Li, D. R. Situ, and C. S. Ng, "Recent clinical innovations in thoracic surgery in Hong Kong," *J Thorac Dis,* vol. 8, pp. S618-26, Aug 2016.

[7] Z. Li and C. S. Ng, "Future of uniportal video-assisted thoracoscopic surgery-emerging technology," *Ann Cardiothorac Surg,* vol. 5, pp. 127-32, Mar 2016.

On-line Dexterity Maps for Guiding Redundant Surgical Robots

K. Leibrandt[1], P. Berthet-Rayne[1], G.-Z. Yang[1]

[1]Hamlyn Centre for Robotic Surgery, Imperial College London, London, United Kingdom
k.leibrandt12@imperial.ac.uk

INTRODUCTION

Deploying redundant, snake like robots enables accessing deep seated and confined surgical workspaces through natural orifices [1]. However, safe and effective navigation of these robots is a challenging task due to their increased complexity and unintuitive kinematics. Inverse kinematic solutions [2] and guidance schemes based on path plans have been introduced [3]. However, local inverse kinematic solutions, may not provide satisfactory results in complex situations due to local minima. Path-planning approaches, provide the operator with a solution to manoeuvre from an initial pose to a target pose, however the operator's influence on the shape of the trajectory is limited. This paper introduces a complementary technique to inverse kinematics and path planning. Visual cues are provided to inform the operator about the robot capabilities and to enable the user to make informed decisions on the trajectory. These cues are based on dexterity maps suitable for redundant robots and calculated on-line, and on the operator's demand.

DEXTERITY FOR REDUNDANT ROBOTS

Dexterity maps have been a common representation to determine the capabilities of robotic manipulators, with n_q degrees-of-freedom (DoF) in a n_t-DoF task-space [4]. Common measurements, such as the manipulability ($\mathcal{M}$), or the inverse conditional number ($\bar{\mathcal{C}}$), are based of the end-effector Jacobian ($\boldsymbol{J}$):

$$\mathcal{M} = \sqrt{|\boldsymbol{J}\boldsymbol{J}^T|} = \prod_{i=1}^{n_t} \sigma_i \,, \qquad (1)$$

$$\bar{\mathcal{C}} = \frac{\sigma_{\min}}{\sigma_{\max}}, \qquad (2)$$

where σ denotes the singular values obtained from a singular-value decomposition (SVD) of $\boldsymbol{J}$. However, these measurements, do not consider constraints, *e.g.* joint-limits, self-collision, obstacles, robotic systems need to account for. To account for joint limits ($q_{i,\min}$, $q_{i,\max}$) a penalization term was introduced in [5]:

$$\tilde{\mathcal{P}}^q = 1 - \exp\left\{\kappa_q \prod_{i=1}^{n_q} \frac{(q_i - q_{i,\min})(q_i - q_{i,\max})}{(q_{i,\max} - q_{i,\min})^2}\right\}, \quad (3)$$

where κ_q is scaling-factor governing the shape of the penalization function between the neutral position and the two limits. To ensure that the penalization term in (3) spans the interval [0,1] the equation was modified to $\mathcal{P}^q$ as:

$$\mathcal{P}^q = \frac{1 - \exp\left\{\kappa_q \prod_{i=1}^{n_q} \frac{4(q_i - q_{i,\min})(q_i - q_{i,\max})}{(q_{i,\max} - q_{i,\min})^2}\right\}}{1 - \exp\{\kappa_q\}}, \quad (4)$$
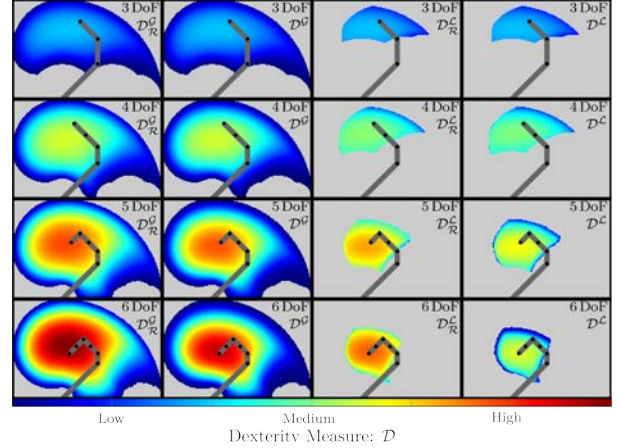

Fig. 1: Left: Comparison of global redundancy considering dexterity $\mathcal{D}_{\mathcal{R}}^{\mathcal{G}}$ and standard dexterity $\mathcal{D}^{\mathcal{G}}$. Right: local dexterity measure $\mathcal{D}_{\mathcal{R}}^{\mathcal{L}}, \mathcal{D}^{\mathcal{L}}$ for a planar robot in 3DoF task-space, in which warmer colours represent higher dexterity.

The dexterity is then calculated as:

$$\mathcal{D} = \mathcal{P}^q \, \mathcal{M} \qquad (5)$$

However, this penalization term does not account for the capabilities of redundant robots which can fully compensate with the remaining joints for a lost DoF in joint-space. To address this [4] proposed an approach in which a multitude (2^{n_t}) of local Jacobians is calculated representing possible directions of motion. The dexterity measure is evaluated by calculating the overall inverse conditional number ($\bar{\mathcal{C}}$) of all $n_t \cdot 2^{n_t}$ singular values. However, this approach is not suitable for online computation of dexterity maps since, performing 2^{n_t} SVD's is computationally expensive. Therefore, an alternative approach is presented in which the Jacobians columns ($\boldsymbol{j}_i$) are individually penalized with:

$$\wp_i^q = \frac{1 - \exp\left\{\kappa_q \frac{4(q_i - q_{i,\min})(q_i - q_{i,\max})}{(q_{i,\max} - q_{i,\min})^2}\right\}}{1 - \exp\{\kappa_q\}}, \qquad (6)$$

such that the constrained Jacobian columns are calculated as:

$$\boldsymbol{j}_i^c = \boldsymbol{j}_i \, \wp_i^q, \qquad (7)$$

which leads to the dexterity measure ($\mathcal{D}_{\mathcal{R}}$) for redundant robots:

$$\mathcal{D}_{\mathcal{R}} = \sqrt{|\boldsymbol{J}^c \boldsymbol{J}^{cT}|}, \qquad (8)$$

It is noted that further constraints can be applied to the columns as in (7). A comparison of $\mathcal{D}_{\mathcal{R}}$ and $\mathcal{D}$ is depicted in Fig. 1. The figure demonstrates how the two different measurements perform, when applied to a planar

robot with $n_q \in [3,6]$ and $n_t = 3$. The global dexterity $\mathcal{D}^{\mathcal{G}}$ is calculated by sampling over the entire joint-space, the local $\mathcal{D}^{\mathcal{L}}$ dexterity is computed by sampling a $\pm 20°$ neighbourhood for every joint based on the depicted configuration. The dexterity ($\mathcal{D}_{\mathcal{V}}$) of the respective pixel (2D) or voxel (3D) (i,j,k), with indexes i,j,k, is calculated as:

$$\mathcal{D}_{\mathcal{V}}(i,j,k) = \max_{q_m}\{\mathcal{D}(q_m)|\ x(q_m) \in v(i,j,k)\} \quad (9)$$

where $x(q_m)$ is the end-effector position of a configuration with joint values q_m. Both measures show the same result for the non-redundant manipulator in the top row of Fig. 1. With increasing redundancy the difference increases showing that high-dexterity spreads further to the edges of the workspace when using the $\mathcal{D}_{\mathcal{R}}$ measure. For local sampling the difference becomes even more apparent and $\mathcal{D}^{\mathcal{L}}$ shows uniformly low dexterity measure. In contrast $\mathcal{D}_{\mathcal{R}}^{\mathcal{L}}$ is taking the compensating capabilities of the redundant manipulator into account. To rapidly compute a dexterity map a multi-threaded Monte-Carlo sampling is performed.

IMPLEMENATION DETAILS FOR MULTI-THREADED WORKSPACE SAMPLING

The sampling is performed using multiple threads which independently generate random configurations within the joint-limits to compute the dexterity measure. In a multi-threaded environment it is necessary to synchronize access to shared resources. Here the shared resources is the dexterity workspace $\mathcal{D}_{\mathcal{V}}$ which is accessed by all threads. A standard technique is to use mutexes to lock the resource during access. However, with increasing thread-count the competition for accessing $\mathcal{D}_{\mathcal{V}}$ increases resulting in a saturation of computation speed. To avoid this issue the 3-D workspace is represented as an axis-aligned bounding box (AABB) $\mathcal{D}_{\mathcal{V}} \in \mathbb{Z}^{N_x^v \times N_y^v \times N_z^v}$. Every cell in $\mathcal{D}_{\mathcal{V}}$ could be protected by an individual mutex, which would lead to a memory overhead. Instead a smaller mutex tensor $M_x \in \mathbb{Z}^{N_x^{mx} \times N_y^{mx} \times N_z^{mx}}$ is chosen. When accessing a cell in $\mathcal{D}_{\mathcal{V}}$ at the index (i,j,k) the index to lock a mutex tensor (i^{mx}, j^{mx}, k^{mx}) is computed as:

$$\{i^{mx}, j^{mx}, k^{mx}\} = \{mod(i, N_x^{mx}), mod(j, N_y^{mx}), mod(k, N_z^{mx})\} \quad (10)$$

where mod is the modulo function. Therefore, access to the cells is synchronized and neighbouring voxels are synchronized with different mutexes. This ensures that regions in the workspace which are accessed with high frequency are protected by different mutexes.

SIMULATION RESULTS

The proposed method was applied in simulation to a surgical robotics scenario, where the surgical site would be accessed, through the oesophagus. A newly developed 7 DoF snake-like robot attached to a 5 DoF positioning system, resulting in a 12 DoF robotic mechanism, was used. The positioning system translates ± 5 mm in the plane normal to the oesophagus pathway (x, y-directions), and pivots (pitch, yaw) $\pm 5°$. Furthermore, it can translate in the z-direction with a 350mm
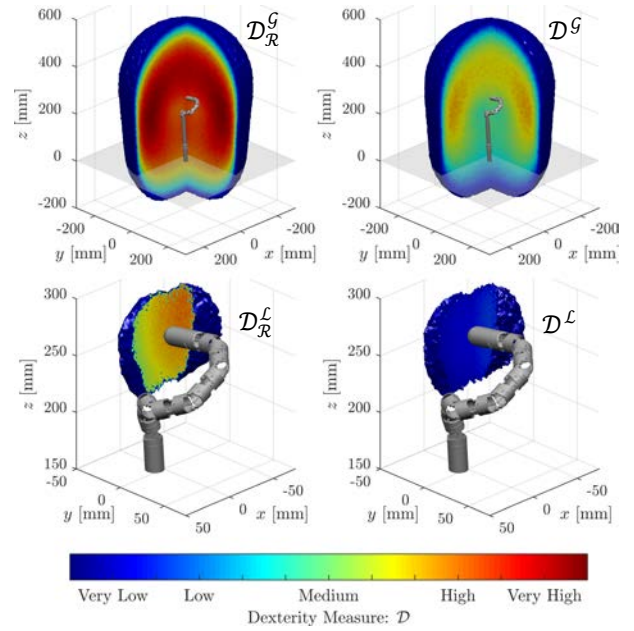
range. The 7 DoF snake- robot can roll $\pm 180°$, and has

Fig. 2: Comparison of local and global, and redundancy and conventional dexterity measures, when used with a 12 DoF surgical robot.

three sections which can pitch and yaw $\pm 70°$. Fig. 2 provides a visualization of the different dexterity measures. The global dexterity measure was generated in 738s with 10^9 different configurations. The local dexterity map was computed with 10^5 samples in 0.15s. The dexterity measure considering redundancy shows higher and more realistic dexterity values stretching closer to the edge of the workspace. The local dexterity $\mathcal{D}^{\mathcal{L}}$ shows uniformly low dexterity with little information, while $\mathcal{D}_{\mathcal{R}}^{\mathcal{L}}$ provides a better representation about the robot's capabilities.

CONCLUSION

This paper introduces on-line computation of dexterity maps for redundant manipulators to provide users with visual cues about a robots capabilities. Future work will focus on incorporating anatomical, and self-collision constraints as well as task-specific manipulability.

REFERENCES

[1] J. Burgner-Kahrs, D. C. Rucker and H. Choset, "Continuum Robots for Medical Applications: A Survey", in *IEEE Trans. Robotics*, vol. 31, no. 6, pp. 1261-1280, 2015.

[2] A. Bajo, R. B. Pickens, S. D. Herrell, and N. Simaan, "Constrained motion control of multisegment continuum robots for transurethral bladder resection and surveillance", in *IEEE Int. Conf. Robot. Autom.*, pp. 5837–5842, 2013

[3] K. Leibrandt, C. Bergeles, G.-Z. Yang. "Implicit Active Constraints for Safe and Effective Guidance of Unstable Concentric Tube", in *IEEE/RSJ Int. Conf. Intell. Robots Syst.*, pp. 1158-1163, 2016.

[4] N. Vahrenkamp and T. Asfour, "Representing the robot's workspace through constrained manipulability analysis", *Autonomous Robots*, vol. 38, no. 1, pp. 17–30, 2015.

[5] M. J. Tsai and Y. H. Chiou, "Manipulability of manipulators," *Mechanism and Machine Theory*, vol. 25, no. 5, pp. 575 – 585, 1990

Approaches to Real-Time Ventricular Wall Strain Measurement for the Control of Soft Robotic Ventricular Assist Devices

D.V. Story[1], M. Saeed[1], K. Price[1], I. Wamala[1], P.E. Hammer[1],
D. Bautista-Salinas[1], D.M. Vogt[2], C.J. Walsh[2],
R.J. Wood[2], N.V. Vasilyev[1]*

[1]Boston Children's Hospital, Harvard Medical School

[2]Wyss Institute for Biologically Inspired Engineering and Harvard John A. Paulson School of Engineering and Applied Sciences
nikolay.vasilyev@childrens.harvard.edu

INTRODUCTION

Soft robotic ventricular assist devices (SR VADs) have recently been developed for the assistance of the failing heart [1, 2]. SR VADs are actuated on the surface of the heart or inside the cardiac chamber in synchrony with the native motion of the heart. SR VADs primary function is to cause additional ejection of blood by inducing wall deformation. Current prototypes of SR VADs have relied upon blood pressure and flow measurements to assess device function, which are the secondary results of the VAD, as opposed to measuring wall deformation. Further, control inputs determining the level of deformation to apply to the heart have relied on preset parameters after optimization. Therefore, there exists a need for a continuous real time assessment of the level of strain being caused by the SR VAD both as a way to assess the local effects of the device on the heart muscle wall but also as a feedback input for the real-time optimization of device control.

While strain sensors have been extensively developed and characterized in the biological disciplines, only a handful have been optimized for function in the large strain environment of soft biological tissue [3]. Moreover, sensing strain of the heart wall has added challenges of obtaining a robust measurement in a dynamic and highly curved surface, reducing attachment area on the heart wall, measuring strains ranging 15%-35% [4], and maintaining native tissue motion. We identified two sensors corresponding with the design criteria and thus examined the accuracy and characteristics of these sensors in measuring ventricular wall strain continuously and in real time using explanted pig hearts placed on a pulsatile flow pump.

MATERIALS AND METHODS

Sensors: The first sensor is a 30mm long soft elastomer, Ecoflex 00-30 (Smooth-On Inc., PA, USA), with embedded microchannels containing liquid metal (eutectic Gallium Indium, "EGain") that change geometry when stretched resulting in a resistance change. By measuring the change in resistance it is possible to calculate strain, as previously described [5]. The liquid is encapsulated in silicone and does not contact tissue. The advantage of this sensor is its flexibility, compatible with the deformation of the heart wall, and its elastic modulus is within the range of values for passive myocardial tissue [1]. However, piesoresistive sensors are prone to drift.

The second sensor is a Hall Effect (HE) sensor composed of, a detector plate (TK2723-ND, Melexis Inc., MI, USA) and a neodymium magnet (8g). The detector plate senses magnetic field strength. These sensors do not drift but have not been commonly characterized in biological applications. The magnet's experimental size/weight would not be used clinically but was appropriate for the purpose of investigating the concept.

Voltage to strain calibration: Both sensors were calibrated to generate displacement of voltage curves upon linear deformation. The EGain sensor was calibrated using a tensile testing machine (Instron, Instron Inc., MA) that applied a controlled displacement starting from a neutral length of 20 mm in 1 mm increments to a length of 45 mm. The HE sensor was calibrated by separating the neodymium magnet and the detector plate, each attached to separate micrometer stages, in 1 mm increments from a distance of 0 mm apart to a total distance of 25 mm apart. The HE records reliably when the magnet and the detector plate are placed within a range between 6mm and 20mm and when they two components are axially aligned. The associated voltage output was recorded using an Arduino Nano (Arduino AG, Italy).

Ex-vivo comparison of the sensors on a pulsatile pig heart: Three pig hearts were placed in a pulsatile flow loop and inflated/deflated to simulate beating heart conditions. Sensors were sutured along the right ventricular (RV) wall. (Figs.1, 2).
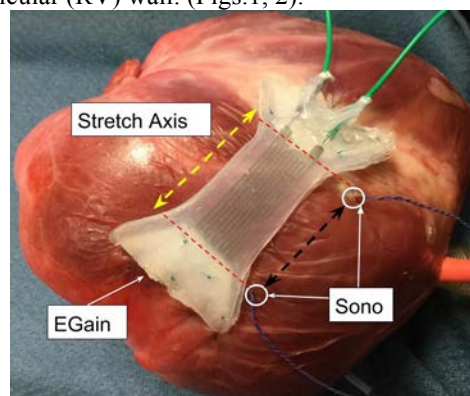

Fig. 1 - EGain sensor and sono crystals are sutured to the heart. Arrows demonsrate the axes of stretch.
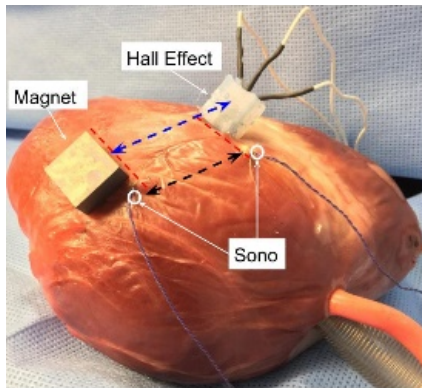
Fig. 2 - Hall Effect sensor and sono crystals are sutured to the heart. Arrows demonsrate the axes of stretch.

To validate the sensors, we implanted two 2 mm sonomicrometry (Sono) crystals (Sonometrics Corp., London ON, Canada). Sono is the accepted method of choice for detecting heart wall linear displacement in animal research studies, but is limited as an implantable device due to high operating voltages. In addition, this method is prone to noise when used in conjunction with certain perioperative monitoring equipment. The crystals were implanted such that they measured in real time the RV free wall displacement across the same wall distance as each of the sensors. Readings from the sensors and from the Sono crystals were collected. Displacement values of each sensor between inflation and deflation were converted to strain as:

$$\varepsilon = \frac{L_1 - L}{L_1} \qquad (I)$$

Where L_1 and L are segment length at peak inflation and deflation respectively [4]. A one-way ANOVA was used to assess significance between the conditions for each measured variable.

RESULTS.

EGain, HE, and Sono sensors all measured the displacement between sensor endpoints on the heart. The strain values calculated, see eqn. (I), were an average of 10 beating inflation/deflation cycles. The hearts used for each sensor had different levels of RV wall deformation between the cycles.

The EGain produced strain results with ~52% difference compared to Sono. These results were found to be statistically significant (Fig.3).
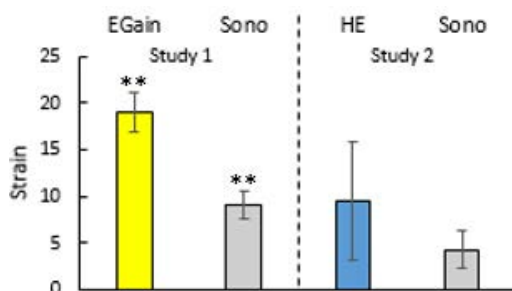
Fig. 3 - Average strain over the course of 10 beating cycles for EGain and HE compared to Sono. Error bars show +/- 1 SD; ** denotes $p<0.005$, (ANOVA). N = 3.

The HE sensor produced strain results with a ~55% difference compared to Sono. These results were not found to be statistically significant.

DISCUSSION

The purpose of this study was to examine the accuracy and characteristics of two implantable sensors in measuring RV wall strain by testing the sensors ex-vivo and comparing their strains to Sono - strain being a potential determinant of SR VAD function and control. The EGain sensor conformed to the curved surface of the heart, measuring a curved axis of strain, compared to Sono, which measures a linear strain axis (Fig. 4).
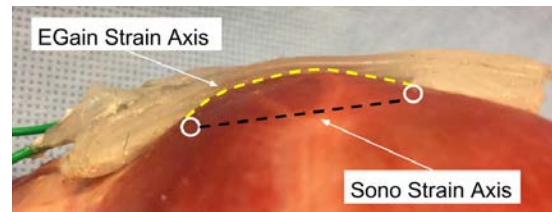

Fig. 4 - EGain and Sono axes of measurement

A discrepancy in strain between the sensors was expected - due to changing heart curvature increasing the curved axis distance versus straight axis distance – however, this may not alone explain the dissimilarity between the results. The EGain's behaviour on heart surfaces must be further characterized in order to determine its suitability as a control sensor for SR VADs.

The HE sensor showed an average accuracy of ~55% compared to Sono, but recorded large variations in strain measurement across the three experiments. The limitation of HE is that its measurement is dependent on alignment of components.

In conclusion, following further experimentation the EGain concept may become a promising solution for detecting the stain of the curved heart wall. For the HE sensor, altering the method of adherence to accommodate for the sensor's reliance on component alignment must be implemented to in order to integrate it as an SR VAD strain sensor.

REFERENCES

[1] E.T. Roche *et al.* "Soft robotic sleeve supports the failing heart." in *Sci Trans Med.* vol. 9, p. eaaf3925, 2017
[2] Horvath M. A. *et al.* "An Intracardiac Soft Robotic Device for Augmentation of Blood Ejection from the Failing Right Ventricle," in *Ann Biomed Eng,* 2017. doi: 10.1007/s10439-017-1855-z
[3] Rogers, J. *et al.* 3D multifunctional integumentary membranes for spatiotemporal cardiac measurements and stimulation across the entire epicardium. *Nat Commun.*, 5, 3329. 2014
[4] Amundsen, B. H. *et al.* Noninvasive myocardial strain measurement by speckle tracking echocardiography: Validation against sono and tagged magnetic resonance imaging. *J Am Coll Cardiol, 47*(4), 789–793. 2006
[5] Vogt, D. M. *et al.* Design and Characterization of a Soft Multi-Axis Force Sensor Using Embedded Microfluidic Channels. *IEEE Sensors Journal 13*(10),4056–4064. 2013

Strong Continuum Manipulator for Flexible Endoscopic Surgery

M. Hwang, D.S. Kwon

Department of Mechanical Engineering,

Korea Advanced Institute of Science and Technology, Korea
gkgkgk1215@kaist.ac.kr

INTRODUCTION

With its gradual curvature, continuum manipulator has widely been used for flexible endoscopic procedures. Not only removal of tissue in inner wall of organ, but it is also used for more advanced surgical procedures such as NOTES (Natural Orifice Transluminal Endoscopic Surgery), which is a newly developed surgical technique performed with a flexible endoscope passed through a natural orifice such as mouth, anus, urethra or vagina. In spite of many clinical benefits associated with scar-less operation, NOTES has not yet been become an established surgical technique due to several technical barriers, mainly originated from lack of tissue manipulation capability of the platform [1]. In order to overcome the limitations, more advanced platforms have been developed with multi-branched and articulated instrument that can make more dexterous motion on the end effector [2]. Although those platforms have highly increased performance of tissue manipulation, it seems that they still have not enough payload to perform NOTES operation.

This paper presents a novel continuum manipulator which features high payload transmission capability. The design approach differs in that the redundancy of serially connected discrete joints were mechanically constrained to prevent the joints from bending in S-shape against external force. As a result, the proposed manipulator can lift over 3(N) weight at the end effector with 3.7(mm) in outer diameter.

MATERIALS AND METHODS

This research was built upon our previously developed surgical robot system (K-NOTES) (Fig. 1a, [3]). It is a tele-operated system of which the slave robot consists of two surgical arm and a bendable endoscopic camera. Each component is modularized by its specific function and can be deployed through channel equipped in overtube. Although the robot has greatly improved manipulability of tissue, the traction force is still not enough to lift heavy organ.

Continuum manipulator shares common problem which appears in the form of S-shape or breakage of actuation wire cable when excessive external force is applied to the distal end (Fig. 1b). The phenomenon comes from the characteristics of redundancy in which the level of potential energy accumulated in the joint is minimized with distorted shape.

This problem could be mitigated by constraining the redundancy (Fig. 1c). The proposed mechanism is based on the idea that angles of all joint will be identical if the angles of any adjacent two joints are the same. In order to make adjacent angles equal, auxiliary rolling links are used to connect the centers of the rolling surfaces of two adjacent main links (Fig. 2). This is similar to operating principle of gear train.

The rolling motion of main link was implemented using the shape of gear teeth. The elastic fixture made of NiTi was used to prevent slippage between two auxiliary rolling links.
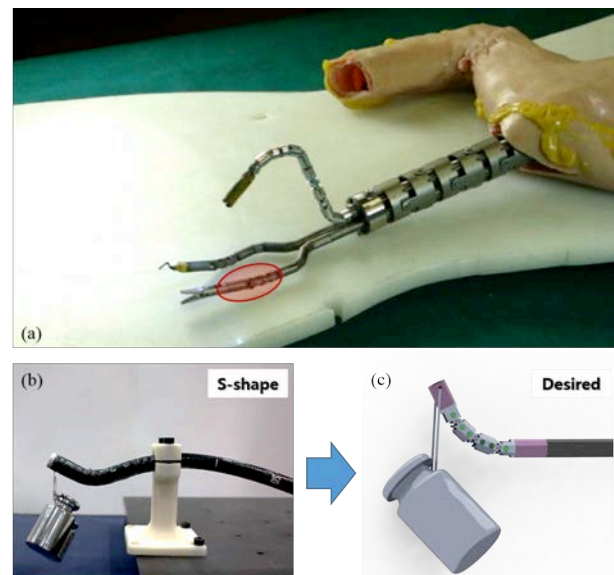

Fig. 1 (a) The previously developed platform (K-NOTES) lacks of traction force to perform flexible endoscopic surgery. (b) Shape of continuum becomes distorted with increasing payload due to its redundancy. (c) Proposed mechanism prevents the joints from bending in S-shape by mechanically constraining the redundancy.
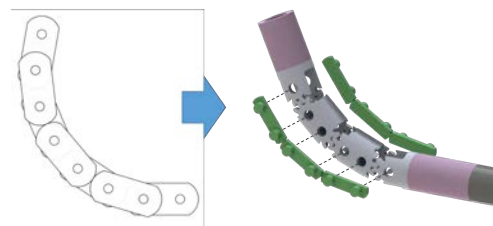

Fig. 2 Operating principle of the proposed continuum joint. Auxiliary rolling links (green) are used to connect the centers of the rolling surfaces of two adjacent main links (grey).

The Constrained Continuum (CC) manipulator was designed and fabricated to have outer diameter in 3.7(mm) in consideration of the overtube diameter of 16(mm) and the diameter of the two surgical arms and camera module. The total length was about 1 (m).

Kinematics was calculated to determine the relationship between the length of the actuation wire cable, the bending angle, and the position of the end effector. We could also obtain the trajectory of the end effector from the kinematics. Free Body Diagram (FBD) and stress analysis was performed to identify the amount of force/torque acting on each part in terms of payload at the end tip. It was predicted from the simulation that the amount of force acting tangentially on the main rolling joints at the center was calculated to be the largest. The strength of gear teeth was designed to endure the payload at the distal end up to 5 (N) in elastic limit.

RESULTS

First, trajectory of the end effector was measured with varying payloads (Fig. 3a). It can be seen from the experiment that the variance between trajectories was significantly different from the payload of 200 (g). The maximum variance was measured within 2.8 (mm). It should be noted that the weight of 250 (g) could not be fully lifted due to elongation of wire cable. However, it was confirmed that the weight of 300 (g) could be lifted when the wire cable was driven by a larger amount.

As a result of the second experiment shown in Fig. 3b, the stiffness measured in bending direction was almost similar at 30, 45, 60 (deg) of bending angle, which is 13.3 (mm/N) in average. On the other hand, the stiffness at 90 (deg) of bending angle was shown to be large enough. The deflection in all bending angles was less than 2 (mm) with loads up to 100 (g).

The pictures shown in Fig. 3c demonstrate that the CC joint is sufficient to lift up to 300 (g) weight in bending direction and 500 (g) weight in rotational direction. At this moment, the deflection at the end effector was measured within 2 (mm).
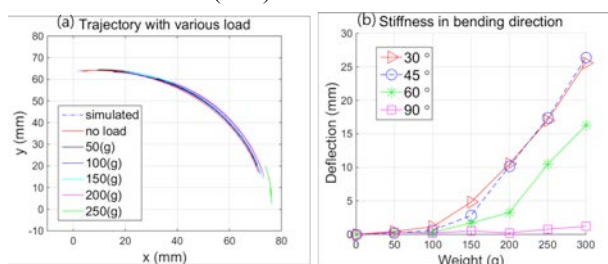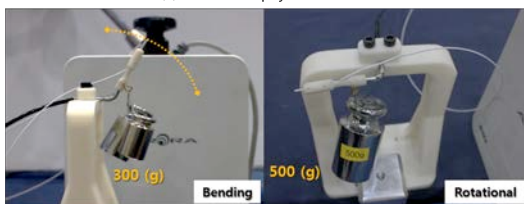

Fig. 3 (a) Maximum payload test in bending and rotational direction. (b) Stiffness measured in bending direction. (c) Trajectory with varying loads.
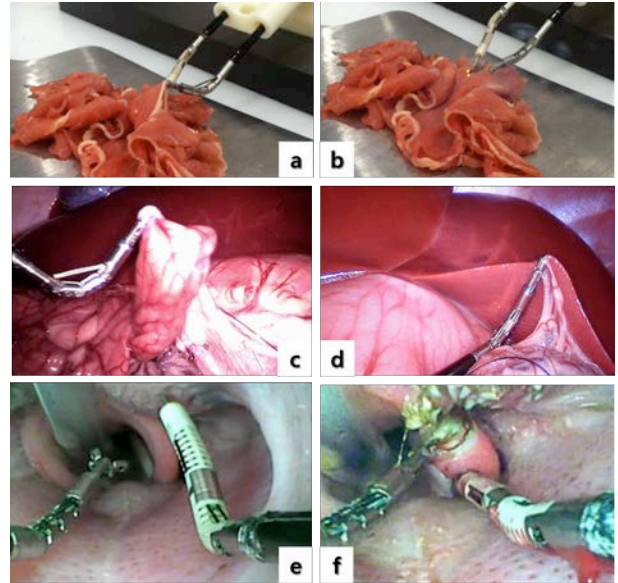

Fig. 4 Several tasks in real tissue environment have been performed as a validation process of the robot.

Several tasks in real tissue environment have been performed as a validation process of the robot. Basic operation was tested including bending, grasping, and cauterizing using sliced tissue (Fig 4, (a), (b)). The CC manipulator was inserted into abdominal cavity of in-vivo swine to verify possibility of traction of organs including intestine, liver, and gallbladder (Fig. 4, (c), (d)). Final task was performed in oral cavity of in-vivo swine. It was shown that the manipulator has sufficient manipulability and strength to resect epiglottis without the aid of assist device (Fig. 4, (e),(f)).

DISCUSSION

A novel continuum manipulator has been developed with features in high payload transmission capability. The mechanism of constraining the redundancy showed the effect to prevent the continuum joint from bending in S-shape against external force. The result of dry-lab experiment showed that the CC manipulator can lift 3(N) weight at the end effector with 3.7(mm) in outer diameter and over 90(deg) in working range of bending. It was also shown that the proposed manipulator has sufficient manipulability and strength to perform NOTES operation.

REFERENCES

[1] DW Rattner, R. Hawes, S. Schwaitzberg, M. Kochman, and L. Swanstrom. The Second SAGES/ASGE White Paper on natural orifice transluminal endoscopic surgery: 5 years of progress. Surg. Endosc. 2011;25:2441-2448.

[2] BPM Yeung, T. Gourlay. A technical review of flexible endoscopic multitasking platforms. Int. Journal of Surg. 2012;10:345-354.

[3] M. Hwang, et al. A Flexible Endoscopic Surgery Robot for NOTES and its In-vivo Animal Experiment. The 9th Asian Conf. on Comp. Aided Surg. (ACCAS). 2013.

A New Tool for Microsurgical Training and Skill Assessment

M. Berthelot[1], S. Shurey[2], C. Shurey[2], G.-Z. Yang[1], B. Lo[1]

[1]The Hamlyn Centre for Robotic Surgery, Imperial College London

[2]Northwick Park Institute for Medical Research (NPIMR), St Marks Hospital
meb14@ic.ac.uk

INTRODUCTION

Microvascular surgery requires dexterity that surgeons spend years of training to master. However, following the European working time directive, the clinical training hours in the UK have been reduced while the amount and level of skills required remain unchanged. The skills are therefore mostly acquired in the operating theatre on actual patients with supervision and each task performed is reported into their eLogBook with comments on effectiveness [1]. Although trainees gain valuable experience, the stressful operating theatre environment hinders the learning process and prolong sthe learning period [2]. Basic skills training is therefore more efficient away from the operating theatre [3]. To overcome these limitations, surgical simulators using computer vision and haptic feedback have been introduced [4]. However, they remain insufficient for microvascular surgery as it requires live subjects for the instructors to monitor and evaluate the evolution of the outcome of the microvascular task (patency and technical effectiveness). In Europe, there are only a few number of research centres established for advanced microvascular training. In addition, the strict regulations in the use of animals for training purposes along with their expense (licence to operate on animal, facilities and equipment), limit training opportunites. Although training methods have been rationalised to be more effective [3-5], microvascular skills are acquired through practice, therefore the learning curve should be taken into consideration.

This paper introduces an inexpensive miniaturised wireless device as a tool for objective microvascular skill assessment. It aims to assist the trainee in targeting technical gaps and improving dexterity.

MATERIAL AND METHOD

An inexpensive, compact, wearable, wireless, device based on optoelectronics has been developed to measure oxygen saturation in the skin (StO_2) [6] (see Fig. 1). With built-in Bluetooth low energy connectivity, the device is seamlessly integrated with any mobile device for real time data management. At any time, up to 5 devices can be connected to a smartphone or tablet. By recording the perfusion of the tissue flaps and reporting the outcomes, the device allows the trainees to view one's progress.

25 trainees (between ST3 to ST8) in microvascular surgery participated in a study which took place, in compliance with the Home Office License, during the 5-day basic microsurgical course at NPIMR [5]. The device was used to monitor the microvascular response during post-operative femoral artery and vein end-to-end anastomoses (respectively AA and VA) performed on live male Sprague Dawley rats at days 1, 2 and 5 (see Fig. 2.1, 2.2 and 2.3). A testing device was placed on the animal as depicted in Fig. 2.2 while another control device was placed symmetrically on the other lap. The device was placed on the skin on top of the downstream of the femoral blood flow. Observations were made on the duration of operating time, final blood vessel patency as judged by the instructors (see Fig. 2.3 a) and b)) and StO_2 values.

RESULTS

Results show a decrease in the operating time from 59 min in average at day 1 to 34 min at day 5 for AA (see Fig. 3.1). Considering finished tasks, the final patency of the anastomosis was marked at 0 for failure and 1 for success (see Fig. 3.2). It generally improved from 0.43 in average at day 1 to 0.74 at day 5 for AA. Considering finished tasks, using an unpaired t-test with p-value<0.01 to compare the test device values with the control device values, results show a decrease in the significant difference with h=0.71 at day 1 and h=0.50 at day 5 in average for AA.

DISCUSSION AND CONCLUSION

A wireless training tool for microvascular skill assessment is introduced. Based on optical sensing, the device measures the StO_2 level – or skin oxygen perfusion. An extensive experiment was conducted to test the feasibility and reliability of using the device for microvascular end-to-end anastomosis skill assessment. The experiment was conducted in conjunction with a 5-day training course on live rats with 25 trainees. The results show the device can accurately assess the viability of the downstream tissue and can be used as a tool to quantify microvascular training progress and assess skills. Specifically, the StO_2 level is shown to be a suitable parameter to quantify the end-to-end anastomosis effectiveness. Placed at the end of the operation, it has been found the device does not disturb the trainee's workflow and can be placed anywhere on the skin of the live animal under operation. Future work includes the monitoring of other microvascular tasks such as end-to-side anastomosis, interpositional vein graft (discrepant or same diameters) and free flap. Recording data from more trainees of different ST levels and experts performing different microvascular tasks can help providing a skill assessment index for the trainees to better improve their microvascular learning.
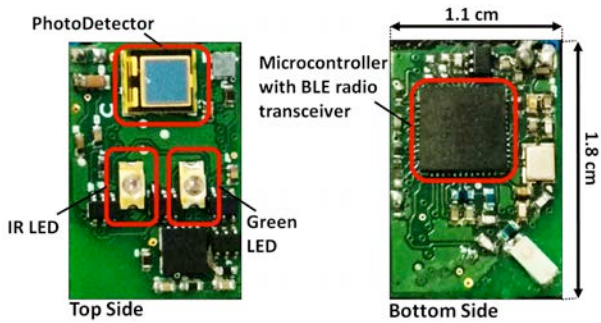
ACKNOWLEDGEMENT

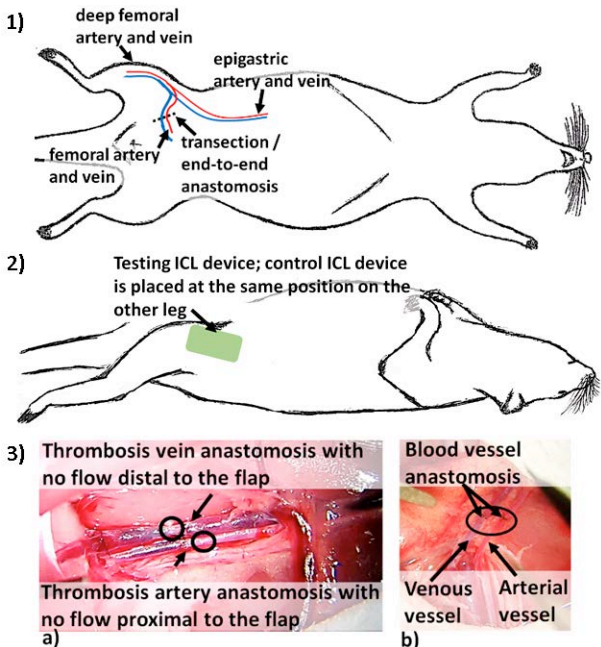**Fig. 1** top and bottom side of the device used; BLE=Bluetooth low energy.

Fig. 2 A schematic illustration of 1) an AA and VA operation, 2) the postoperative experiment set up and 3) the microscopic view of blood vessels following a failed anastomosis in a) and that of a sucessful in b).
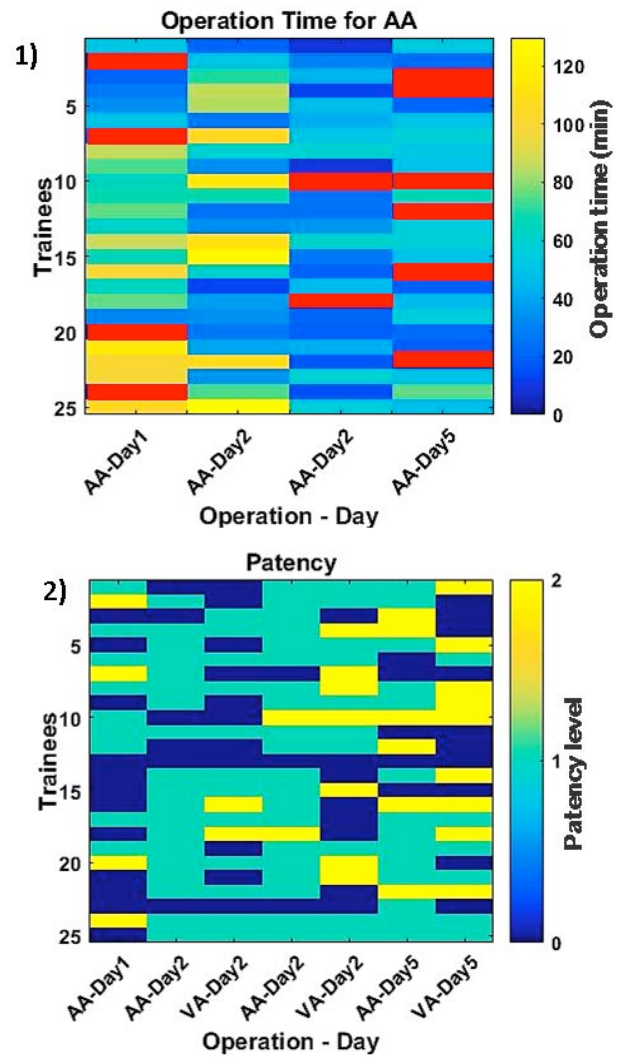

Fig. 3 1) the operating time taken of for AA in minute. For both graphs, the red cells show the not finished or not attempted tasks: the operating time was not taken into consideration.. 2) the patency result over all perfromed tasks: 0=nonpatent; 1=patent; 2=not finished or not attempted.

REFERENCES

[1] "Elogbook." www.elogbook.org. Accessed: 2017-05-16.
[2] Leff, Daniel Richard, et al. "Functional prefrontal reorganization accompanies learning-associated refinements in surgery: a manifold embedding approach." *Computer Aided Surgery* 13.6 (2008): 325-339.
[3] Kim, Eunsol, Masha Singh, Yelena Akelina, Sandra Shurey, Simon R. Myers, and Ali M. Ghanem. "Effect of Microvascular Anastomosis Technique on End Product Outcome in Simulated Training: A Prospective Blinded Randomized Controlled Trial." *Journal of reconstructive microsurgery* 32, no. 07 (2016): 556-561.
[4] Ghanem, Ali M., et al. "A systematic review of evidence for education and training interventions in microsurgery." *Archives of plastic surgery* 40.4 (2013): 312-319.
[5] Shurey, Sandra, Yelena Akelina, Josette Legagneux, Gerardo Malzone, Lucian Jiga, and Ali Mahmoud Ghanem. "The rat model in microsurgery education: classical exercises and new horizons." *Archives of plastic surgery* 41, no. 3 (2014): 201-208.
[6] Berthelot, Melissa, et al. "Wireless wearable self-calibrated sensor for perfusion assessment of myocutaneous tissue." *Wearable and Implantable Body Sensor Networks (BSN), 2016 IEEE 13th International Conference on*. IEEE, 2016

Attachable Robotic Handler to Endoscope and Instrument for Solo-Endoscopy

D.-H. Lee, B. Cheon, M. Hwang, D.-S. Kwon

Department of Mechanical Engineering, Korea Advanced Institute of Science and Technology, Korea
leedh90@kaist.ac.kr

INTRODUCTION

Flexible endoscopy is used to perform endo-luminal and trans-luminal procedures. However, it is difficult to use the endoscope and instrument in complex treatments and surgeries that necessitate a maneuverability.

Bending section of the endoscope is steered by rotating two knobs on the control body. This type of steering is not intuitive because the bending section bends in two perpendicular directions while the knobs are arranged in the same axis. Additionally, the size and structure of the knobs make it difficult to manipulate the control body with one hand. Some physicians remarked that their hands are too small to manipulate the endoscope.

Unnatural body movements are frequently generated when rotating the endoscope and this causes injury to the shoulders and wrists of physicians. Additionally, communication errors often occur in therapeutic endoscopy when more than two people collaborate on the procedure.

Due to these problems, long learning curve is required to perform the endoscopy. Approximately 100 to 200 procedures are required to operate the colonoscopy safely and within a reasonable timeframe.

Robotics is expected to overcome these limitations, and several studies are underway. The Invendoscope is actuated by an insertion module equipped with gearwheels. Steering and translation of the endoscope are actuated, but rotation of the endoscope was not actuated. Ruiter et al developed a robotic add-on steering system for the endoscopy. The system consists of 3 modules to control the commercial endoscope, instruments, and robotic instruments. [1]

In this study, a robotic handler of a conventional endoscope and an instrument is proposed by attaching several parts to the control body of the endoscope for solo-endoscopy. Also, two intuitive input devices, namely one for endoscope manipulation and the other for instrument manipulation are proposed.
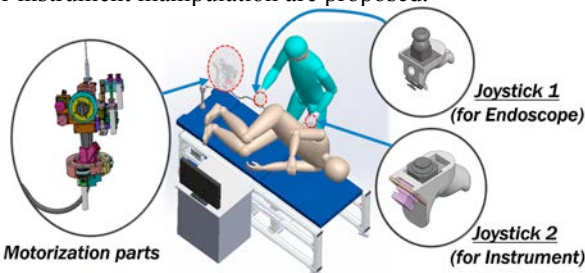

Fig. 1 System Overview

MATERIALS AND METHODS

A. Design of Input Devices

Intuitive input devices are required to improve maneuverability. A method of increasing intuitiveness includes the use of force feedback. Force feedback is particularly important when introducing the endoscope into a patient body. It helps the physicians to estimate the shape of the endoscope and the interaction force between the endoscope and tissue. However, it is technically challenging to implement the force feedback perfectly. [2] Alternatively, we suggest a way to obtain force feedback from the endoscope itself by holding the insertion tube of the endoscope directly with an input device.

Another method to increase intuitiveness is to design the input device kinematically same with the endoscope. However, it is difficult to make up/down and left/right motions by holding the insertion tube when introducing the endoscope into the body. Alternatively, a joystick is used, which is not exactly same as the endoscope but could be similarly movable. Spring force based on the relative position and angle difference in a joystick enhances intuitiveness.
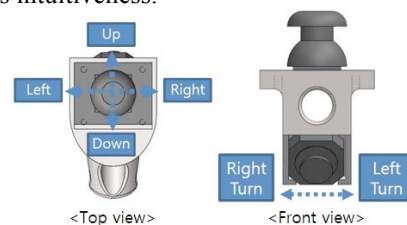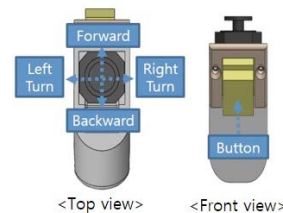

Fig. 2 Input Device for the Endoscope

Fig. 3 Input Device for the Instrument

In case of the endoscope, the up/down and left/right bendings are matched with those of the joystick and rotation of the endoscope also is matched with the left/right movement of joystick. Translation is manually controlled by holding the endoscope and the input device together.

In case of the instrument, translation and rotation are matched with up/down and left/right movements of joystick. With respect to the grasping, the on/off type button is used to manipulate the forceps. The forceps

close when the button is pressed. The forceps open in other instances.

B. Motorization of Endoscope and Instrument

The endoscope and instrument are motorized by attaching several parts. A positioning arm with a hinged door was fixed to the operating bed to free the control body of the endoscope from a physician.

The two knobs on the control body are driven with pulleys and belts. The knobs are converted into pulleys by attaching a few parts. Rotation of the endoscope is driven by a gear mechanism. The control body is converted into a gear by attaching parts on the lower part of the control body, which is attachable to the positioning arm. There are three small gears in the positioning arm, one of them was driven by a motor.

The instrument is motorized by attaching a few parts to the motorization parts of the endoscope. A collect chuck is used to hold the various instruments. The instrument is rotated by rotating the collet chuck.

A linear guide and a ball screw is used for the translation of the instrument. When the motor actuated the ball screw, the collect chuck performs a rectilinear motion. With respect to the grasping, tension springs and a wire are used. When the button is pressed, the motor winds the wire and the forceps close.
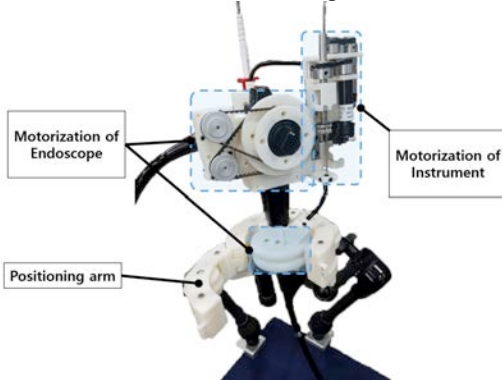

Fig. 4 Motorization of endoscope and instrument

RESULTS

Two experiments were conducted to assess the usability of the proposed system. The first task was to introduce the endoscope from the anus to the cecum where colon starts. The second task involved transferring two yellow rubber rings from two poles with red marks to a pole with a black mark and guiding a blue rubber ring from an end of a tortuous wire loop to the other end. The proposed manipulation method was compared with the conventional manual manipulation method. The variables were measured, time required for tasks, Workload based on a NASA Task Load Index.

Five subjects (age 21-30, 5 men) were participated in the experiments. The subjects who are engineers did not possess any prior experience in endoscope handling. Subjects were asked to perform each task six times with both manipulation methods. In the second task, an assistant controlled the instrument when the subject operated in the conventional method.
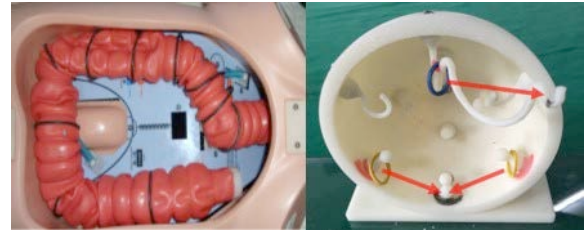

[Task 1]   **[Task 2]**
Fig. 5 Experiment environment

Table 1. Experiment results

Setup	1. Conventional method	2. Proposed Method
Time for task 1(sec)	197.77 ± 15.23	117.40 ± 9.34
Time for task 2(sec)	220.53 ± 16.54	104.41 6.71
Workload for task1 (on scale of 0-20)	10.80	6.43
Workload for task2 (on scale of 0-20)	14.83	4.53

Table 1 shows the results of the experiments. As indicated in the table, the proposed method involved the less amount of time with respect to conventional method in both tasks. To determine if the difference in mean time is significant, ANOVAs were conducted the level of significance corresponded to $p=0.05$. As a result, it was confirmed that both p-values were $0.000(<0.05)$.

The Task Load Index involved measuring different variables such as mental and physical demands and effort. The results showed that the workload of the proposed method was the lower than conventional method in both tasks. This indicated that the proposed method was more intuitive and ergonomic.

DISCUSSION

In this paper, the attachable robotic handler to the endoscope and instrument was developed for Solo-Endoscopy. Experiments conducted for novices showed that the proposed method was more intuitive and convenient than the conventional method and the feasibility of single operation was verified.

Since people who actually use this system will be doctors, additional experiments such as ex-vivo, in-vivo with doctors are being planned to evaluate this system.

Through the proposed system, it is expected that physicians who have difficulty in the endoscope manipulation can manipulate more comfortably and intuitively, thereby it can reduce the stress. In addition, it is expected to decrease medical expenses since the number of assistants and procedure time can be reduced.

REFERENCES

[1] J. G. Ruiter, G. M. Bonnema, M. C. van der Voort, I. A. M. J. Broeders, "Robotic control of a traditional flexible endoscope for therapy" J. Robotic Surgery, vol. 7, issue 3, pp. 227-234, 2013
[2] Franken M.C.J, "Control of Haptic Interaction: An Energy-Based Approach", PhD Thesis, University of Twente, the Netherlands, 2011.

Vision Based Shape Reconstruction of Tendon Driven Snake-Like Surgical Robots

P. Berthet-Rayne, G.-Z. Yang

Hamlyn Centre for Robotic Surgery, Imperial College London, UK

ptb14@imperial.ac.uk

INTRODUCTION

Tendon driven flexible snake-like surgical robots are bio-inspired devices that are capable of bending and navigating inside the human body. These devices have the potential to significantly improve existing surgical procedures by providing access to deep seated lesions through natural pathways [1]. For snake robot control, the use of tendons for actuation is a popular choice [2]. However, tendon driven robots are subject to backlash and tendon elongation which can result in inaccurate shape reconstruction particularly when exposed to external forces exerted on the device. Existing sensing method for shape reconstruction include fiber bragg grating [3], piezoelectric sensors [4] or external vision tracking [5]. This paper introduces preliminary results of a real-time vision based in-situ shape reconstruction framework for tendon driven snake-like surgical robots as shown in fig. 1.

MATERIALS AND METHODS

The concept of the presented framework is to visually track tendon pairs as they are being pulled or loosened and to use this information to reconstruct the shape of the controlled robot. The materials used include a tendon driven back driveable snake-like robot: the i^{2}Snake (Hamlyn Centre, UK), a C920 HD webcam (Logitech, Switzerland) and a computer running the tracking and reconstruction software.

Mechanical Setup: For the snake robot considered in this study: the i^{2}Snake, the tendons are exposed and arranged linearly on a flat fixture as shown in fig. 2. The tendons are made of SUS316 WHT stainless steel (Ø=0.45 mm; 7x18). With the current i^{2}Snake version, 24 tendons need to be tracked for the shape reconstruction. Each tendon was equipped with a 3D printed mechanical fuse made of Polyjet VeroBlack material (Stratasys, USA), calibrated to rupture if the applied forces are greater than 40 N, hence avoiding damage to the robot. This mechanical fuse interconnects two sections of tendons and therefore moves linearly with the tendons. One of the key features of the mechanical fuse is that it facilitates the image processing and tracking of each tendon as it is plain black and wider than the tendons (Ø=3.5 mm). The next step consists of tracking the mechanical fuse as external forces are applied to the body of the snake robot.

Image Processing: The image processing algorithm is constrained to a region of interest (ROI) from the camera image where the tendons are exposed as depicted in fig. 2. This ROI is converted in grayscale and a Gaussian blur filter is applied to reduce the camera's pixel noise. The following step consists of applying a threshold to obtain a black and white image
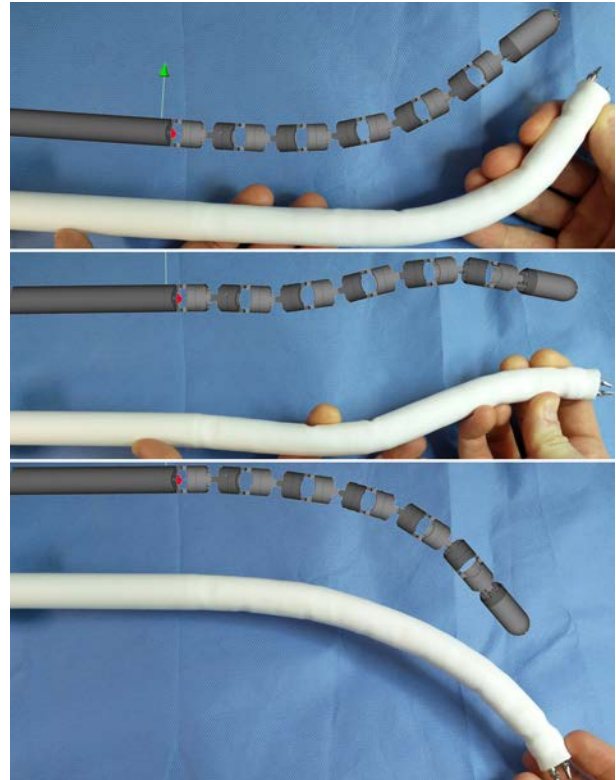

Figure 1: Shape reconstruction of a tendon driven snake-like surgical robot. As the physical device (in white) is bent, the shape is reconstructed by visually tracking the tendons.

that reveals only the mechanical fuses as shown in fig. 2. To track its position, the distance from the top of the image to the fuse, and from the bottom to the fuse is measured in pixels. As the fuses move along a single line, the linear motion centre is known and fully determined and the fuse search can be constrained to the vertical black lines represented in fig. 2. A for loop explores all the pixel along the four lines and if a pixel value is 0 (black), the fuse's intersection with the line is found. Four search lines are used for each tendon (top and bottom) to filter the pixel noise. The central position of the fuse is calculated by averaging the four intersection points. This process is repeated for each tendon and runs at the maximum frame rate of the camera: 30 fps.

Shape Reconstruction: Once the position of each fuse is known, the corresponding tendon position in mm is calculated. Since the tendons are moving in a single plane, parallel to the image plane, a linear mapping can be used to convert the tendon variation from pixel to mm. The transformation constant was calibrated using a ruler placed in the same plane as the tendon and by measuring the amount of pixel within a known
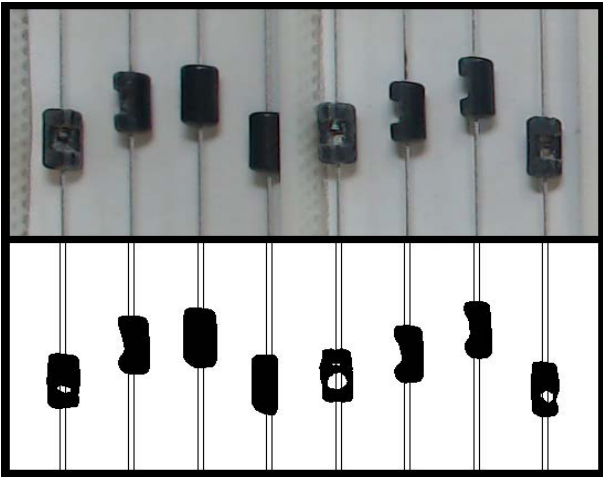
Figure 2: Visual tracking of the tendons. The top image shows the tendon arranged linearly and moving in a single plane and the mechanical fuse in black. The bottom presents the image processing result to track the position of each tendon.

dimension. The tendon variation is then converted into joint angle using the mathematical model of the joint being used: in this case a rolling joint. This process is repeated for all tendons allowing to accurately measure the variation induced by external movement of the snake robot and to reconstruct its shape in 3D.

RESULTS

The shape reconstruction results are presented in fig. 1 & 3. The tendon tracking was performed in real-time across the 24 tendons at 30 fps. Each tendon variation was converted into joint variation to reconstruct the shape of the snake robot. The current setup allowed for a tendon measurement precision of 0.15 mm/pixel with a measurement noise of ± 1 pixel, resulting in an overall measurement accuracy of 0.45 mm. In the case of the joint model being used, this resulted in a joint measurement accuracy of 1.14°. During the experiment, multiple shapes were reconstructed and the result is plotted in fig. 3. The average error is 2.3° with a standard deviation of 6° allowing to approximately reconstruct the overall shape of the robot. During the experiments, the camera noise at the pixel level and the measurement inaccuracies induced some jitter in the snake robot simulator. An important step of the reconstruction is to align the tracking with the initial shape of the robot. This was done by inserting the snake in a tubular shape to enforce a straight position of all the joint combined with a home position setting in the tendon tracking.

DISCUSSION

The presented framework allows for an efficient and inexpensive real time method for shape reconstruction of tendon driven mechanism in 3D. The use of a camera rather than mechanical sensors has the advantage of avoiding physical contacts and does not require mechanical fixtures that would introduce backlash and friction. The method also returns absolute position values that only requires a single calibration, removing the need for further homing or initialization sequences
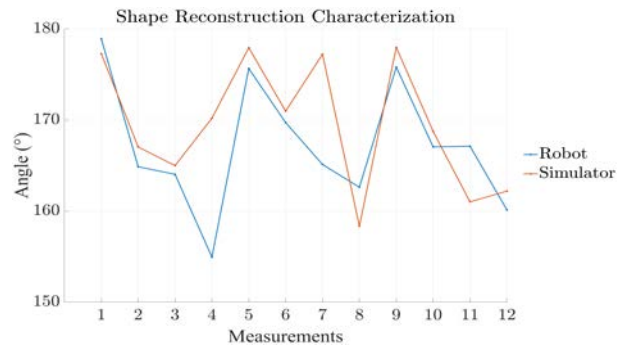

Figure 3: Characterization of the reconstruction method. The joint angles of the robot are plotted in blue and the one estimated from the tendon tracking in red.

even after a power loss. Existing video based shape reconstruction typically monitor the device itself to estimate its shape. As a result, they are not suitable for in-situ surgical application as a camera showing the entire device is required. The presented method only uses the tendons for reconstruction and could therefore be used during surgeries.

The current framework is limited in terms of frame rate and resolution. Noisy pixel measurements result in undesired oscillations. The use of multiple cameras, tracking sub-sections of all the tendons would increase the tracking accuracy. Moreover, high frame rate cameras would allow to filter the measurement noise by averaging the values without altering the real-time capabilities. Finally, this method is limited by the amplitude of the mechanical tendon backlash. If the backlash is too large, it will result in no tendon motion visible by the camera. Customized mechanical design to ensure a minimal tension using springs could improve the method accuracy.

Future work will investigate real-time backlash compensation and closed-loop control for increased accuracy. Force estimation will also be investigated by considering the asymmetrical variation of tendons pairs.

REFERENCES

[1] Vitiello, V., Lee, S.L., Cundy, T.P., and Yang, G.Z.: 'Emerging robotic platforms for minimally invasive surgery', IEEE Rev Biomed Eng, 2013, 6, pp. 111-126

[2] Burgner-Kahrs, J., Rucker, D.C., and Choset, H.: 'Continuum Robots for Medical Applications: A Survey', Ieee T Robot, 2015, 31, (6), pp. 1261-1280

[3] Abayazid, M., Kemp, M., and Misra, S.: '3D flexible needle steering in soft-tissue phantoms using fiber bragg grating sensors'. Proc. IEEE Conf. on Robot. and Autom. 2013 Year pp. 5843-5849

[4] Leleu, S., Abou-Kandil, H., and Bonnassieux, Y.: 'Piezoelectric actuators and sensors location for active control of flexible structures'. Proc. Proc. IEEE Instrument. and Measur. Techno. Conf., 2000, Year pp. 818-823

[5] Camarillo, D.B., Loewke, K.E., Carlson, C.R., and Salisbury, J.K.: 'Vision based 3-D shape sensing of flexible manipulators'. Proc. IEEE Conf. on Robot. and Autom., 2008, Year pp. 2940-2947

Recovering Dense Tissue Multispectral Signal from *in vivo* RGB Images

J. Lin[1,2], N.T. Clancy[1,3], D.S. Elson[1,3]

[1]The Hamlyn Centre for Robotic Surgery, Imperial College London, London, UK

[2]Department of Computing, Imperial College London, London, UK

[3]Department of Surgery and Cancer, Imperial College London, London, UK

j.lin12@imperial.ac.uk

INTRODUCTION

Hyperspectral/multispectral imaging (HSI/MSI) contains rich information clinical appliations, such as 1) narrow band imaging for vascular visualisation, 2) oxygen saturation for intraoperative perfusion monitoring and clinical decision making [1]; 3) tissue classification and identification of pathology [2]. The current systems which provide pixel-level HSI/MSI signal can be generally divided into two types: spatial scanning and spectral scanning. However, the trade-off between spatial/spectral resolution, the acquisition time, and the hardware complexity hampers implementation in real-world applications, especially intra-operatively. Acquiring high resolution images in real-time is important for HSI/MSI in intra-operative imaging, to alleviate the side effect caused by breathing, heartbeat, and other sources of motion. Therefore, we developed an algorithm to recover a pixel-level MSI stack using only the captured snapshot RGB images from a normal camera. We refer to this technique as "super-spectral-resolution". The proposed method enables recovery of pixel-level-dense MSI signals with 24 spectral bands at ~11 frames per second (FPS) on a GPU. Multispectral data captured from porcine bowel and sheep/rabbit uteri *in vivo* has been used for training, and the algorithm has been validated using unseen *in vivo* animal experiments.

MATERIALS AND METHODS

Super-resolution, which estimates high resolution (HR) images from low resolution (LR) counterparts, is a highly ill-posed problem, since one LR image could be matched to many possible HR images. This problem is solvable only under certain constraints. In this work, we made the following assumptions: 1) optimised matching can be found by learning the training set which contains similar information to the unseen test set; 2) the HR information from the HR images could be recovered from its LR correspondences; 3) there is no correlation between adjacent pixels.

Recently, deep learning techniques including convolutional neural networks (CNNs) has been applied on image super-resolution, and proved to provide promising results [3, 4]. In this work, similar strategies were adopted to upscale an RGB image which contains 3 channels ($M{\times}N{\times}3$ matrix), to an MSI stack with 24 channels ($M{\times}N{\times}24$ matrix).

The proposed model consists of two phases (Fig. 1):

- **The upscaling phase:** Three 3D deconvolutional layers followed by one convolutional layer were piled together to transform the input from $M{\times}N{\times}3$ to $M{\times}N{\times}24$
- **The high resolution extraction (HRE) phase:** A residual network block was used to extract and combine the high frequency (HF) with low frequency information from the upscaling phase's output.
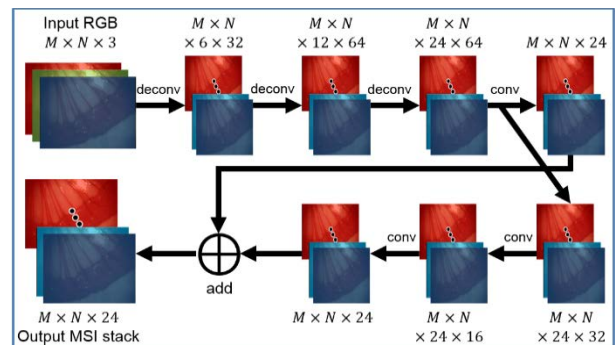

Fig. 1 The prediction model. The input is a RGB image with a user-defined dimension ($M{\times}N$); the output is an MSI stack with the same spatial dimension and 24 channels.

MSI stacks collected from porcine bowel and sheep/rabbit uteri *in vivo* with a liquid crystal tunable filter (LCTF) endoscopic imager were used for training and validation [2]. The MSI stacks were collected at 10 nm spectral interval, in the range of 460-720 nm. A non-rigid registration method was used to eliminate the small displacement between MSI slices at different spectral bands [5], generating the MSI stacks as the ground truth for training. Synthetic RGB images were simulated from these MSI stacks, with the transmission spectrum measured from a normal RGB camera (Thorlabs DCU223C). The training set contains the 243 MSI stacks (augmented from 50 porcine bowel, 21 rabbit uterus, and 10 sheep uterus). During training, based on assumption no. 3, every pixel was trained independently, with convolutional kernels expanding along the spectral dimension only. Then the learnt weights were used to predict a whole MSI stack from input RGB images, by only changing the input data dimension from ($1{\times}1{\times}3$) in the training network to ($256{\times}192{\times}3$) in the prediction counterpart. Both the training and prediction were applied with Tensorflow [6]. Predicting the MSI stack from an RGB image ($256{\times}192$) cost ~90 ms on a PC (CPU: i7-3770; GPU: NVIDIA GTX TITAN X).

RESULTS

The proposed algorithm was evaluated for two outputs: the overall and inter-class prediction. The peak signal-to-noise ratio (PSNR) was used to quantify the MSI stack prediction accuracy.

Firstly, all the *in vivo* data from different sources were mixed and underwent a 5-fold cross validation. The PSNR value for different spectral bands were evaluated by comparing the calculation results and the ground truth. The average and standard deviation of PSNR were plotted alongside the RGB camera transmission spectra in Fig. 2 (upper). It can be found that PSNR is relatively high (>28) for most spectral bands, but drops in the blue/green/red spectra overlapping areas. We also demonstrates the accuracy of MSI estimation intuitively, by comparing the estimated MSI signal with the ground truth, at different locations on a rabbit uterus (Fig. 2 (lower)). As is known, HSI/MSI signal can be used to calculate the oxygen saturation, by fitting it using a linear combination of absorption spectra of oxy/deoxy-haemoglobian, as is shown in Fig. 2 (upper).
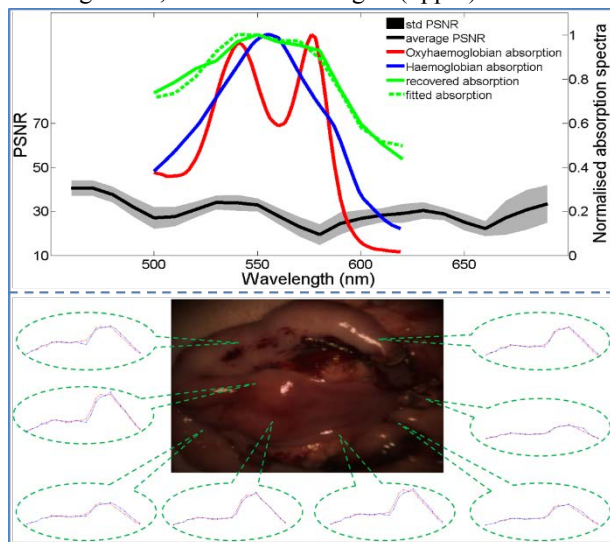
Fig. 2 Upper: average (black line) and stadard deviation (yellow shadow) of the PSNR values for all wavelengths; the normalised absorption spectra for oxy/deoxy-haemoglobian (red and blue line), together with the estimated and fitted MSI signal (grean and grean dash line); Lower: comparision between the estimated (blue line) and ground truth (red line) MSI signal at different locations on a rabbit uterus.

The inter-class prediction was also validated. The models trained on individual classes were used to predict the MSI stacks on other classes, and peak signal-to-noise ratio (PSNR) was adopted to evaluate the results (Table 1). Promising results (PSNR > 30) were achieved on sheep and rabbit uteri, while the training using pig bowel led to the worst outcome (PSNR $\approx$ 26). This is mainly due to the more frequent presence of specular reflections, and larger error in generating the MSI ground truth due to imperfect registration. This result shows the potential of transfer learning to use this technique to estimate MSI of tissues with limited available samples by training on other similar datasets, e.g., prediction of human tissue MSI using the training result from *in vivo* animal data.

Table. 1 PSNR for inter-class MSI prediction. Data from three sources were used for the validation: 1) pig bowel (PB); 2) sheep uterus (SU); 3) rabbit uterus (RU).

Test / Train	PB	SU	RU
PB	**25.75**	27.47	28.80
SU	24.80	**32.49**	32.34
RU	25.08	31.83	**32.96**

DISCUSSION

In this work, we developed a CNN based model to recover dense pixel level MSI signals from RGB images, in real-time. As the HSI/MSI signal is important for many applications such as narrow-band imaging, tissue classification, and tumor detection, we believe that this technique can benefit these applications. It overcomes the problem of long acquisition time for normal HSI scanning systems and the need for separate specialized imaging equipment, providing promising MSI estimation with only slight accuracy loss in most spectral bands. In future work the research will focus on: 1) the validation of the current algorithm on more *in vivo* data, especially human tissue; 2) the extension of both the algorithm and the hardware to achieve higher accuracy.

REFERENCES

[1] Clancy, N.T., Arya, S., Stoyanov, D., Singh, M., Hanna, G.B., and Elson, D.S. Intraoperative measurement of bowel oxygen saturation using a multispectral imaging laparoscope. Biomedical Optics Express, 2015, 6, (10), pp. 4179-4190.

[2] Lu, G., and Fei, B. Medical hyperspectral imaging: a review. Journal of Biomedical Optics. 2014, 19, pp. 010901.

[3] Shi, W., Caballero, J., Huszár, F., Totz, J., Aitken, A.P., Bishop, R., Rueckert, D., and Wang, Z. Real-Time Single Image and Video Super-Resolution Using an Efficient Sub-Pixel Convolutional Neural Network. 2016 IEEE Conference on Computer Vision and Pattern Recognition (CVPR), 2016, pp. 1874-1883.

[4] Oktay, O., Bai, W., Lee, M., Guerrero, R., Kamnitsas, K., Caballero, J., de Marvao, A., Cook, S., O'Regan, D., and Rueckert, D. Multi-input Cardiac Image Super-Resolution Using Convolutional Neural Networks. Medical Image Computing and Computer-Assisted Intervention (MICCAI) 2016, Proceedings, Part III, pp. 246-254

[5] Du, X., Clancy, N., Arya, S., Hanna, G.B., Kelly, J., Elson, D.S., and Stoyanov, D. Robust surface tracking combining features, intensity and illumination compensation. International Journal of Computer Assisted Radiology and Surgery, 2015, 10, (12), pp. 1915-1926.

[6] Abadi, M., Barham, P., Chen, J., Chen, Z., Davis, A., Dean, J., Devin, M., Ghemawat, S., Irving, G., Isard, M., Kudlur, M., Levenberg, J., Monga, R., Moore, S., Murray, D.G., Steiner, B., Tucker, P., Vasudevan, V., Warden, P., Wicke, M., Yu, Y., and Zheng, X. TensorFlow: A system for large-scale machine learning, ArXiv e-prints, 2016, 1605.

A Magnetic Laser Scanner for Non-Contact Endoscopic Ablations

A. Acemoglu, N. Deshpande, L.S. Mattos

Department of Advanced Robotics, Istituto Italiano di Tecnologia, Genova, Italia.
(alperen.acemoglu, nikhil.deshpande, leonardo.demattos)@iit.it

INTRODUCTION

Lasers are commonly used for high-precision microsurgeries on delicate organs, such as transoral laryngeal microsurgeries. In these soft tissue surgeries, the benefits of lasers include improved post-operative function, decreased morbidity [1], better hemostasis, and minimal peripheral tissue injury [2]. Furthermore, scanning lasers increase the quality of the tissue ablations enabling the fast and continuous motion of the laser. The scanning feature provides clean incisions with less thermal damage to surrounding healthy tissue. The state-of-the-art laser systems have scanning capabilities as a standard feature, usually implemented with fast steering mirrors [3].

It is highly desirable to adapt this laser-based surgical technology to endoscopic tools for enabling endoscopic laser microsurgeries. Endoscopic microsurgeries can potentially increase the precision of the incision enabling the operations close to the surgical sites [4]. In addition to this, also enable access to surgical sites which are not reachable with conventional techniques. As these advantages of endoscopic microsurgeries are considered, investigating novel actuation mechanisms is crucial in order to incorporate precise laser positioning and high speed scanning in endoscopic tools.

In literature, researches proposed magnetic actuation for the miniaturization of the surgical catheters [5-7]. In these systems, position control of a cantilevered structure with a permanent magnet is performed using external magnetic fields. A similar concept can be used for actuating the laser light carrying optical fibers in order to micromanipulate the surgical laser beam using the fiber as a cantilever beam.

In this paper we propose the use of a magnetically actuated optical fiber to create a novel endoscopic laser scanning device. This actuation method provides many advantages such as precise positioning, high scanning speed, high resolution, and simple control. Here we propose the use of two pairs of orthogonally placed coils to create an electromagnetic scanning tool with two degrees-of-freedom (DOFs). This is achieved by attaching a permanent magnet to a cantilevered optical fiber and by controlling the electromagnetic field produced by the coils. Laser focusing at a distal ablation target is achieved using two plano-convex lenses appropriately placed to collimate and focus the laser light. As the electromagnetic field changes, the fiber cantilever is deflected and the laser spot moves on the target, allowing the execution of precise laser scanning motions.

MATERIALS AND METHODS

Fig. 1a depicts the conceptual design of the magnetic laser scanner device. It includes an optical fiber, electromagnetic coils, a permanent magnet, collimating and focusing lenses. The optical fiber is fixed in the center of the tool wall and a permanent magnet is attached to it. Four electromagnetic coils are placed around the optical fiber. Fig. 1b shows the actuation mechanism for one degree-of-freedom and optical design for focusing the laser on the target. The system's working principle is based on the interaction between electromagnetic fields created by the coils and the permanent magnet. As current flows through two orthogonal coil pairs placed around a cylindrical tool, a magnetic field is produced in the workspace. This generates a magnetic torque on the permanent magnet, which deflects the tip of the optical fiber. The two plano-convex lenses are included in the design to collimate and focus the laser to account for divergence of the laser light as it exits the optical fiber. Thus, bending of the optical fiber using two electromagnetic coil pairs in y- and z- axes provides 2D position control of the laser spot on the target.
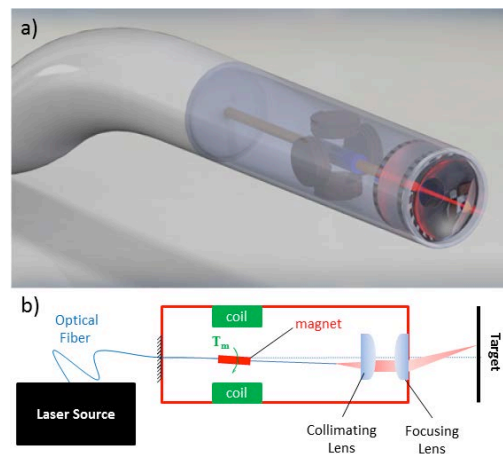

Fig. 1 a) Conceptual design of the magnetic laser scanner with an optical fiber, four electromagnetic coils, a cylindrical permanent magnet, and optical lenses. b) Schematic presentation of the magnetic interaction between coil pair and permanent magnet.

Fig. 2 presents the experimental setup with the magnetic laser scanner prototype. A visible red (625 nm) laser light was used to characterize the system and develop its control system. A multimode optical fiber with 300 μm core diameter and 0.39 NA (Thorlabs - FT300EMT) was used to carry the laser light. A plano-convex lens with 6 mm diameter and 10 mm focal distance was used for collimation, whereas another plano-convex lens with 6 mm diameter and 30 mm focal

distance was used to focus the laser light. A high speed camera is used to record the laser spot trajectories on the target. Then, recorded videos are post-processed in order to extract the laser positions in each frame.

For trajectory execution, an open-loop control is used where predefined current values are fed to the coils to observe the laser trajectory. Current values are calculated with the equations: $I_x = \alpha_1 d_x$ and $I_y = \alpha_2 d_y$, where I_x and I_y are currents, and d_x and d_y desired positions, α_1 and α_2 are free coefficients.
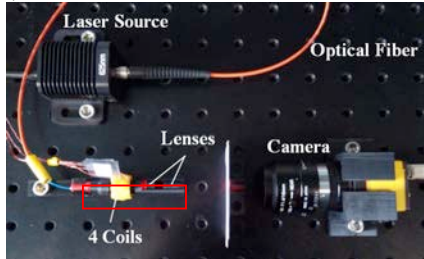
Fig. 2 Experimental setup with magnetic laser scanner prototype, laser source, and a recording camera.

RESULTS

In order to assess the repeatability of the high speed laser scan trajectories, an 'M' shaped trajectory was chosen because it is challenging for fast scanning. Then, set of current values are defined to execute this trajectory. These current values defined excitation patterns, which were fed to the coils 10 times, i.e., number of passes, N, was 10. All executed trajectories were recorded. The first pass was accepted as the reference trajectory, allowing the computation of the root mean square error (RMSE) for the subsequent consecutive passes of the laser spot over the desired trajectories.

Results from the repeatability assessment considering the 'M' shaped trajectory are presented in Fig. 3. The RMSE calculated for each axis resulted in: $RMSE_y = 48 \pm 16$ µm and $RMSE_z = 75 \pm 35$ µm.
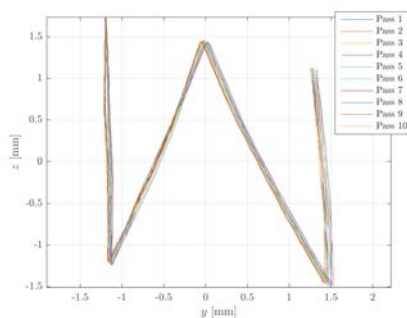
Fig. 3 Repeatability results with a 'M'-shaped trajectory for 10 repetitions (Number of pass, n = 10).

DISCUSSION AND CONCLUSION

During surgeries, surgeons generally define an incision path and execute this trajectory with repetitive manual passes. During these repetitions, keeping the laser spot exactly on the same path is highly important to avoid unexpected incisions in the vicinity of the desired path. Repeatability is therefore an important criteria for microsurgeries where high precision is

needed. The results of the repeatability experiment indicate that the magnetic laser scanner shows high repeatability.

The magnetic laser scanner is an alternative to the piezoelectric drive systems which are used for endoscopic imaging applications [8]. These systems have an illuminating fiber and light collecting fiber bundle. Although these systems generally have very small diameter (~1mm), the fiber can only be actuated at resonant frequency for scanning purposes. The proposed system with electromagnetic actuation provides 2D position control along with high speed scanning for endoscopic laser microsurgeries enabling non-contact incisions. Furthermore, the system can also be teleoperated by using a tablet device for intuitive laser position control. This allows surgeons to perform intra-operative incision planning and the system can repeat automatically these customized trajectories for precise incisions.

The proposed magnetic laser scanner has been designed as an end-effector module for precise laser ablations close to surgical site. As it can be coupled to manual or robotic devices, and to rigid or flexible holding structures (e.g. flexible endoscopes or continuum robots). In addition, the same system actuation and control structures can be used to create an scanning fiber imaging system.

REFERENCES

[1] C. A. Solares and M. Strome, "Transoral robot-assisted co2 laser supraglottic laryngectomy: Experimental and clinical data," The laryngoscope, vol. 117, no. 5, pp. 817–820, 2007.

[2] S. C. Desai, C.-K. Sung, D. W. Jang, and E. M. Genden, "Transoral robotic surgery using a carbon dioxide flexible laser for tumors of the upper aerodigestive tract," The Laryngoscope, vol. 118, no. 12, pp. 2187–2189, 2008.

[3] Digital Acublade System. Lumenis Inc. Israel. [Online] Available:http://www.lumenis.com/Surgical, Accessed on 14-03-2017.

[4] Mattos, L., Andreff, N., "The µRALP Project: New Technologies and Systems for Robot-Assisted Laser Phonomicrosurgery," 3rd Joint Workshop on New Technologies for Computer/Robot Assisted Surgery, DOI: 10.13140/RG.2.1.1346.9284, Verona, Italy, September, 2013

[5] M. N. Faddis and B. D. Lindsay, Magnetic catheter manipulation, Coronary artery disease 14(1) (2003) 25–27.

[6] I. Tunay, Position control of catheters using magnetic fields, Mechatronics, 2004. ICM'04. Proceedings of the IEEE International Conference on, IEEE (2004), pp. 392–397.

[7] K. J. Boskma, S. Scheggi and S. Misra, Closed-loop control of a magnetically-actuated catheter using twodimensional ultrasound images, Biomedical Robotics and Biomechatronics (BioRob), 2016 6th IEEE International Conference on, IEEE (2016), pp. 61–66.

[8] E. J. Seibel, R. S. Johnston, and C. D. Melville, "A full-color scanning fiber endoscope," Optical Fibers and Sensors for Medical Diagnostics and Treatment Applications VI. Proceedings of the SPIE, vol. 6083, pp. 9-16, 2006.

Low Coherence Interferometry based Proximity Sensors for Medical Robotics

A. Bradu[1], M. Hughes[1], G.Z. Yang[2], A. Podoleanu[1]

[1]Applied Optics Group, School of Physical Sciences, University of Kent, Canterbury, UK

[2] Hamlyn Centre for Robotic Surgery, Imperial College London, UK

a.bradu@kent.ac.uk

INTRODUCTION

We report progress in the development of fast, real-time, miniaturised low coherence interferometry based proximity sensors for navigation and collision avoidance in medical robotic systems. As well as providing accurate quantitative distance measurements, the systems provide an auditory cue to the user by generating a sound with a frequency proportional to the tissue distance. The sensors are intended for guidance of robotically steered endobronchial catheters for access to remote lung nodules, but could also be used for other applications [1].

METHODS

Two configurations have been investigated:

1. Camera based interferometer (CBI). This sensor uses a super-luminescent diode emitting in the near infrared as optical source (central wavelength 800 nm, spectral bandwidth 20 nm) and a fast line-scan camera for detection (acquisition rate 27 kHz.) Thus, the sensor can deliver distance information with a theoretical accuracy of around 15 μm every 37 μs.

2. Swept source based interferometer (SSBI). For this configuration, a swept laser optical source emitting light over a spectral range of 100 nm, centred on 1300 nm, has been employed, providing a theoretical accuracy of around 15 μm. The sweep rate of the SS, and hence the update rate of the distance measurement, is 100 kHz.

The two interferometer configurations are non-common path (the arms of the interferometer are independently controlled). This ensures: (i) full control of the reference power, allowing optimisation of sensitivity when various sensing probes are used; (ii) better sensitivity in general, as the interferometer optical path difference can be easily adjusted to place the sample in the region of maximum sensitivity; (iii) simpler, lower cost sensing probe in comparison with common-path configurations which require a partial reflector placed close to the sample to be investigated, and hence incorporated within the sensing probe.

For both interferometer configurations, the sensors consist of an optical fibre of 250 μm diameter, terminated with a gradient index (GRIN) lens of 1 mm diameter to focus the light onto the tissue (Fig. 1). The optical fibre and lens can be customised for the requirements of different applications. In our case, the length of the sensor probe (fibre + lens) was 1 m. The GRIN lens has a rigid length, L = 5 mm, a diameter of 1 mm and a working distance, WD = 2 mm, as shown in Fig. 1a. The distances are inferred using the (complex)

master slave interferometry ((C)MS) method [2-3]. The conventional Fourier transform (FT) approach, for both implementations (CBI and SSBI), could limit the achievable resolution and cost. Since the instruments are built using optical fibres, matching their lengths in the arms of the interferometer with high accuracy to avoid dispersion effects would be challenging. To compensate for unbalanced dispersion, hardware and/or numerical methods would then need to be implemented, leading to an increase in the complexity of the system and requiring heavy computation. In comparison, when using MS, the intrinsic dispersion compensation provided by the calibration procedure means that variations in the length of the optical fibre or lens are tolerated without compromising the accuracy.
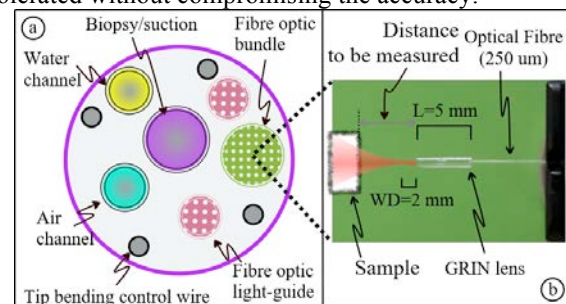

Fig. 1 Schematic diagram of a generic flexible bronchoscope (a). Inset photo of the sensor used for the present study (b)
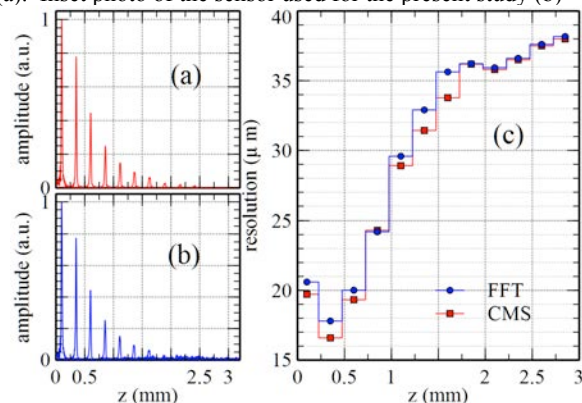

Fig. 2 CBI instrument: Sensitivity drop-off using the MS (a) and FT method (b) and the variation of axial resolution (c).

RESULTS

CBI instrument: Both MS and FT based instruments produce similar results in terms of sensitivity (Fig. 2(a-b) and resolution (Fig. 2c). The sensor has a resolution ranging from 15.8 to 38 μm within a limited axial range (up to around 2 mm). The reflectivity profiles (Fig. 2(a-b)) were obtained by altering the length of the reference arm in the interferometer.
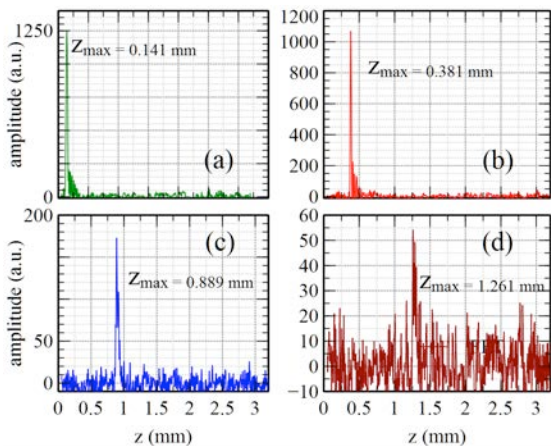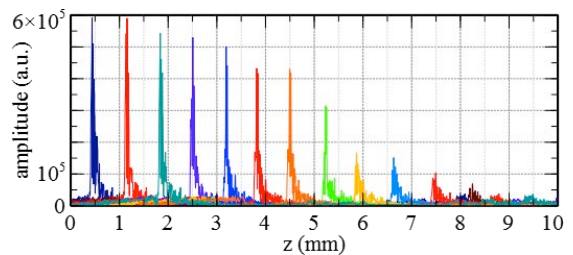
Fig. 3 CBI: axial reflectivity profiles obtained for different axial positions of the probe with respect to the sample (paper).

The axial reflectivity profiles depicted in Fig. 3 were generated using a sheet of paper as a sample. To produce them, the sample was kept stationary while the sensing probe, placed on a micrometre-resolution translation stage (TS) was moved away from it. The peak of the reflectivity profile (z_{max}) is assumed to be the position of the sample. We consider that the maximum axial range is achieved when the amplitude of the signal decreases to a level that is twice the noise level. For our particular CBI instrument, the maximum achievable depth is measured as $z_{max} = 1.261$ mm.

SSBI instrument: In comparison to the CBI case, the SSBI instrument provides a much longer axial range and better sensitivity. When implemented via MS, it also offers flexibility in the choice of axial range to be used which is dictated by the maximum sampling rate of the digitizer employed.
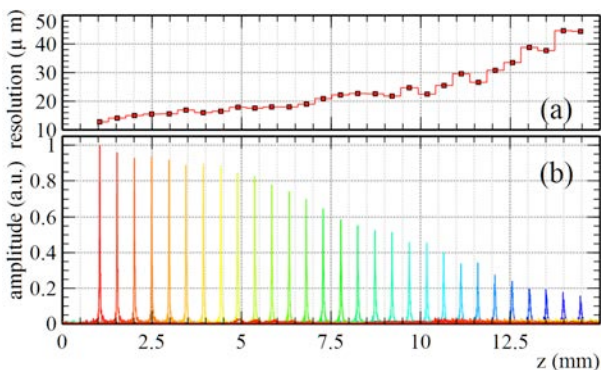
Fig. 4 For a SSBI instrument: Axial resolution at different depth positions (a) and sensitivity drop-off vs depth obtained using the MS method (b).

The SSBI instrument uses a digitizer able to sample data at high speed (500 MS/s), providing a very long axial range of over 12 mm. As illustrated in Fig. 4b, the sensitivity drops by a factor of 2 over 6 mm depth range, while the axial resolution varies from 15 to 40 μm over 15 mm. When using paper, the position of the sample can be determined correctly even when the sample is as far as 9.5 mm from z = 0 (Fig. 5). To evaluate the accuracy of the sensor, the position of the sample was determined using the MS method as well as by using the digital position sensor of a TS (Fig. 6). The accuracy of MS is that given by the axial resolution.

Fig. 5 SSBI: axial reflectivity profiles obtained for different axial positions of the probe with respect to the sample (paper).
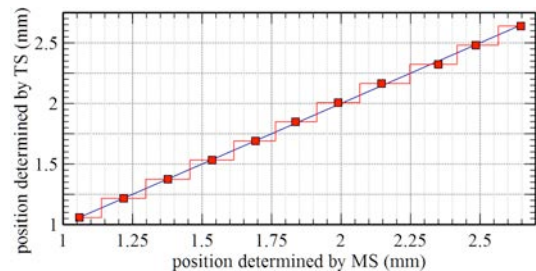

Fig. 6 SSBI: position of the sample measured by MS vs position measured using the digital sensor of the TS.

Figure 7 shows temporal monitoring of a tissue sample (human thumb) over 5 s, while the sensor is kept stationary. The MS system can perform a measurement every 10 μs over a range from 0 up to nearly 10 mm. However, in Fig. 7, to distinguish between successive points, only 500 points are displayed, which corresponds to measurements performed every 100 ms.
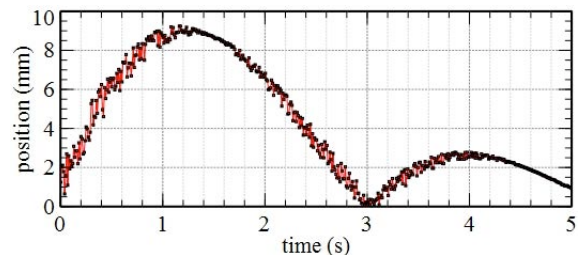

Fig. 7 Temporal monitoring of sample's position.

CONCLUSION

Both instruments, CBI and SSBI, can easily be interfaced with distance sensor probes, and provide high accuracy distance measurements only limited by the inverse of the bandwidth of the source (CBI) or the tuning bandwidth (SSBI). Although the CBI presented here cannot provide a long axial range, it may be assembled for a lower cost than the SSBI. However, progress in the development of SS sources together with the use of technologies such as MS can reduce the cost of the SSBI instrument tremendously so it becomes acceptable for medical use. SSBI is the technique of choice if a large axial range is needed, taking advantage of the progress in the coherence length of swept sources.

REFERENCES

[1] A. Lucesoli et al. Optical Ranging in Endoscopy: Towards Quantitative Imaging. Advances in Biomedical Sensing, Measurements, Instrumentation and Systems 2010 74-92.
[2] A. Podoleanu and A. Bradu. Master–slave interferometry for parallel spectral domain interferometry sensing and versatile 3D OCT. Opt. Express 2013 21:19324-38.
[3] S. Rivet et al., Complex master slave interferometry. Opt. Express 2016 24(3): 2885-904.

Effect of Path History on Concentric Tube Robot Model Calibration

J. Ha, G. Fagogenis, P.E. Dupont

*Department of Cardiovascular Surgery, Boston Children's Hospital,
Harvard Medical School, Boston*

INTRODUCTION

A variety of models have been developed to describe the kinematics of concentric tube robots [1,2]. While some of these are based on mechanics-based modeling [1], others employ parametric [1] and nonparametric [2] models. Almost all modeling attempts neglect history-dependent effects, i.e., the dependence of robot shape and tip location on prior motion. Physically, these effects can arise from phenomena such as friction and hysteretic stress-strain. Furthermore, such state dependency has been observed experimentally.

While the neglect of these effects may be justifiable in order to simplify and speed kinematic computations for real-time control, it is worthwhile to understand the effect of unmodeled state dependency on the accuracy of state-independent models.

Consider the three-tube robot in Fig. 1 that consists of a proximal pair of tubes that rotate, but do not translate with respect to each other and a distal tube that can rotate and translate with respect to the proximal pair. The robot configuration (neglecting rigid body displacements) can be defined by two relative rotation angles and one translation. Considering only the two rotations, a specific configuration can be approached from four angular "directions," which actually result in four robot tip positions for the same configuration.
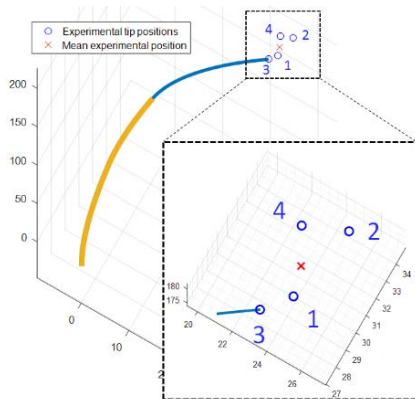
Fig. 1. Four experimentally measeured robot tip positions corresponding to same relative rotation angles, but different directions of approach. Tube parameters in Table 1.

To calibrate a state-independent model of this robot, one could collect data in a number of ways. For example, one could sequentially increment each of the two relative angles through complete revolutions. Depending on the selected directions of rotation, that would correspond in Fig. 1 to collecting all data points in, e.g., configuration 1. Since for arbitrary robot motions, all four configurations are equally likely, this would introduce a systematic bias in the calibrated

model and likely increase model error when tested against a verification data set – unless, of course, the verification data was collected with the same bias.

Alternately, one could design a data collection algorithm to select a random direction of approach for each sample configuration. This is an appropriate technique for acquiring a verification data set and, if also used to acquire training data, it would eliminate the dirctional bias and could reduce modeling error.

As a final alternative, consider the mean position of the four directional configurations, which is also shown in Fig. 1. A model trained on the set of mean positions for all configurations is likely to produce the smallest error when validated against data collected with random directions of approach. Such a calibration method is time consuming, however, since actual robot position must be measured 2^n times, where n is the number of rotational joints.

One can speculate, however, that the mean position corresponds to the position the robot tip would take if there were no state-dependency in the robot's behavior. This suggests that if there was a technique to shake a robot free of its history dependence as it approached a configuration, one could reduce collection of the calibration data set to one point per configuration while still reducing modeling error to what could be achieved using the mean of all potential configurations.

Dithering has long been used to reduce the effect of friction and we have also used a type of dithering to drive elastically unstable tube sets to configurations inside the major hysteresis loop created by the instability [3]. In this case, dithering refers to driving the tubes to the desired relative angles following an oscillatory path of decreasing amplitude in joint space.

MATERIALS AND METHODS

A three-tube robot, with parameters given in Table 1, was used with an electro-magnetic (EM) sensor to capture the tip position. This robot design is chosen as it possesses a large workspace relative to other designs [1]. Two kinematic models were used for calibration – the mechanics-based model of [1] and the truncated Fourier series model of [1].

To validate the calibration concepts proposed above, we collected and compared two different calibration data sets of robot tip positions. One dataset was acquired using dithering to minimize path history effects, while the other dataset included four measurements of tip position for each joint space configuration, corresponding to the four angular directions of approach. Each dataset included 512 joint

space configurations (base rotations and translations) evenly distributed over the joint space.

In the data set acquired without dithering, the four measurements corresponded to the following rotation directions of the second and third tubes relative to tube 1: (1) CCW,CCW, (2) CCW,CW, (3) CW,CCW and (4) CW,CW. A third data set was collected for verification of the calibrated models that consisted of 500 random configurations. To reflect real-world conditions, the directions of approach for each configuration in this set were selected using a random number generator.

Table 1. Tube Parameters**.**

	Tube 1	Tube 2	Tube 3	
	Section 1	Section 1	Section 2	Section 1
Length (mm)	150	150	150	86.4
Radius of curvature (mm)	265	265	∞ (straight)	55
Relative stiffness	1	1	0.2857	0.2857

RESULTS

To verify if the dithered data set is equivalent to the data set that includes all four approach directions, we first computed the mean positions of the latter and compared them with the former. The dithering consists of a sequence of 20 angular offsets: $\{+40^o, -38^o, +36^o, \ldots, -2^o, 0^o\}$. The dithered positions are good approximations to the mean of the 4 undithered positions, with average and maximum distances between them of 0.5025mm and 1.4716mm, respectively. This provides some support for our hypothesis that dithering can average out path-dependent phenomena.

Next we calibrated the mechanics-based and truncated Fourier series models using four different subsets of our calibration data sets and compared them all using the verification data set. The first two training sets correspond to the complete dithered and undithered training data sets. We anticipate that these two sets will produce comparable errors. The third training set was the subset of undithered data associated with directions (1) CCW,CCW. This set corresponds to the typical approach one would use to collect data when neglecting path-dependent effects. The fourth training set was a subset of the undithered data set in which one of the four directions was selected randomly for each configuration.

The mean and maximum errors for the four training data sets and two models are given in Tables 2 and 3. As anticipated, the dithered data set and the full undithered data set give comparable results. The biased subset of the undithered data produces the largest errors. The use of a directionally-random subset of the undithered data produces smaller errors, but not as small as those provided by the dithered and full undithered data sets.

The choice of training data set also affects the comparison of the two kinematic models. Based on the biased undithered sets, which likely have been used in many prior papers, the accuracy of both models is comparable. When compared using the dithered and full

undithered data sets, however, the truncated Fourier model significantly outperforms the mechanics-based model. The difference in modeling error is likely related to the relative expressive power of the two models as determined by the number of parameters (9, mechanics-based; 343, truncated Fourier series). A representative robot configuration is given in Fig. 3.

Table 2. Prediction errors of mechanics model on 500 random evaluation configurations.

Calibration data set (number of measurements)	Mean error (mm)	Max error (mm)
Dithered set (512)	3.3 (±1.6)	9.4
Full undithered set (2048)	3.3 (±1.6)	9.5
Biased undithered set (512)	4.5 (±2.4)	14.5
Random undithered set (512)	3.3 (±1.6)	9.0

Table 3. Prediction errors of truncated Fourier model on 500 random evaluation configurations.

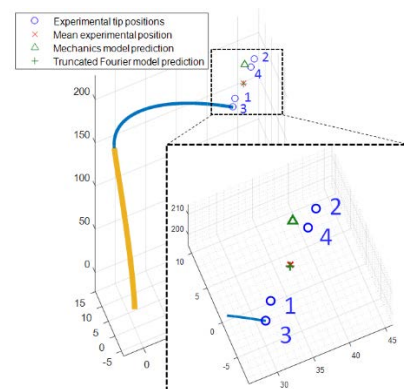| Calibration data set (number of measurements)	Mean error (mm)	Max error (mm)
Dithered set (512)	2.3 (±1.3)	7.2
Full undithered set (2048)	2.3 (±1.3)	7.1
Biased undithered set (512)	4.1 (±2.5)	14.5
Random undithered set (512)	3.5 (±2.2)	12.8

Fig. 3. Representative configuration illustrating large model errors. (Calibrations using dithered data set.)

DISCUSSION

We have demonstrated that standard approaches to calibration data collection introduce bias and increase modeling errors owing to the dependence of concentric tube robot configuration of path history. We have also introduced a dithering technique that can be used to avoid bias while also dodging the collection of multiple data points for each configuration. While we have only considered the path dependency of tube rotation here, tube translation should also be considered.

REFERENCES

[1] P. E. Dupont, J. Lock, B. Itkowitz, E. Butler, "Design and control of concentric tube robots", IEEE Trans. Robotics, vol. 26, no. 2, pp. 209-225, 2010.

[2] G. Fagogenis, C. Bergeles, P.E. Dupont, "Adaptive Nonparametric Kinematic Modeling of Concentric Tube Robots", IEEE/RSJ Int. Conf. Intelligent Robots and Systems, 2016.

[3] J. Ha, Park F.C., P.E. Dupont, "Optimizing Tube Precurvature to Enhance Elastic Stability of Concentric Tube Robots", IEEE Trans. on Robotics, vol. 33, no. 1, pp. 22-37, 2017.

Towards Biocompatible Conducting Polymer Actuated Tubes for Intracorporeal Laser Steering

M. T. Chikhaoui[2], A. Cot[1], K. Rabenorosoa[1], P. Rougeot[1], N. Andreff[1]

[1]AS2M Department, FEMTO-ST Institute, Univ. Bourgogne Franche-Comté/CNRS/ENSMM, Besançon, France

[2]Laboratory for Continuum Robotics, Leibniz Universität Hannover, Hanover, Germany
chikhaoui@lkr.uni-hannover.de

INTRODUCTION

Actuation of an endomicroscope tip is a major technological challenge. In the realm of gastro-intestinal endoscopy, this possibility brings tremendous potential to accurate navigation and diagnosis as closely as possible to the tissue. In order to reduce invasiveness of medical/surgical operations and to improve standard endoscope's accuracy, this paper introduces a novel biocompatible micro-actuation technique of tubes able to house diagnosis tools to perform fiber-based optical biopsy or laser surgery. After comparison of different techniques of micro-actuation, ElectroActive Polymers (EAP), and particularly Conducting Polymers (CP) are selected for several reasons. Indeed, they require low operating voltages (< 2 V) while providing large deformations, biocompatibility, softness, and high miniaturization potential [1]. These actuators can undergo volume change by applying a potential of reduction or oxidation onto the component electrodes, which results in the expansion or contraction of the polymer by absorption or expulsion of ions. The latter are provided by a surrounding electrolyte in aqueous form or as gel to allow for encapsulation. One of the less energy consuming CP, PolyPyrrole (PPy) is studied hereby. The challenge is to bend tubes with diameters smaller than 1.5 mm with PPy-based micro-actuators of approximately 10 µm in thickness for use in active endomicroscopy. The kinematic benefits of such an actuation were studied in combination with concentric tube paradigm [2] and the first integration of such actuators in a soft robot was introduced [3]. The general concept is depicted in Fig. 1. In the following, the technological development is detailed and the first experimental results are reported.

MATERIALS AND METHODS

All micro-actuator samples are constructed by electrochemical polymerization process using a PGP 201 potentiostat (Radiometer Analytical, Loveland CO, USA) controlled by VoltaMaster 4 software. A standard three-electrode system is linked to the potentiostat and composed by Ag/AgCl electrode as reference electrode and a platinum sheet as counter-electrode. The working electrode is a PolyVinylidene DiFluoride (PVDF) membrane Immobilon-P (Merck Millipore Corp., Darmstadt, Germany) of 110 µm in thickness. The

interest in using this membrane relies on the 0.45 µm diameter pores, thus it can absorb and permits transport of electrolyte during actuation. Prior to its introduction in the polymerization setup, conductance of the membrane is supplied by vacuum plasma sputtering of 40 nm chromium/gold layer on both sides. Further, the electrochemical deposit is performed based on Yamaura *et al.* protocol [4] and Gairhe *et al.* process [5]. Thus, low oxidation potential (< 1 V) and current density (0.1 mA/cm²) are applied, while operating at low temperature ($\sim$ -25°C). In order to provide better adherence and compactness to the polymer layer, organic solvent is selected, namely Bis(TriFluoromethane) SulfonImide Lithium salt (LiTFSI) at 0.05 M and 99% pure pyrrole at 0.06 M (Sigma Aldrich, Saint Louis, MO, USA).
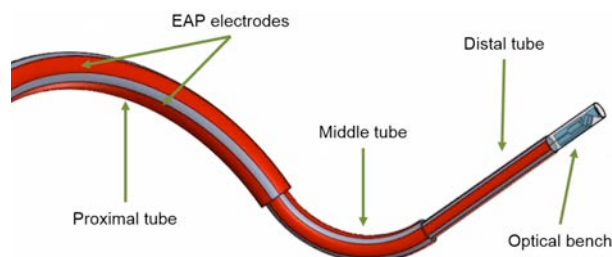

Fig. 1 Concept of a continuum robot founded on concentric tube paradigm with variable curvatures using soft micro-actuators based on EAP. An optical bench is embedded in the robot's end-effector as an example.

EXPERIMENTAL RESULTS

After synthesis, a micro-actuator of $35 \times 2 \times 0.15$ mm^3 is patterned. For actuation, the sample is immersed in the actuating solution composed by 0.05 M of LiTFSI diluted in propylene carbonate.

a. PPy thickness impact on generated force

Force measurements are performed using the experimental setup depicted in Fig. 2. The micro-actuator is fixed to a conductive gripper ensuring both mechanical fixation and power supply. A FT-S-1000 force sensor (FemtoTools AG, Buchs, Switzerland), shown in Fig. 2b, provides up to 1000 mN measurement range with a resolution of 0.05 µN at 10 Hz. Further, a camera is set in order to monitor the experiments and to align the actuator movement with the sensor's probe sensitive direction (Fig. 2b). The latter works in compression and traction and has a width of 50 µm,

consistent with the actuator's width of 2 mm to ensure full contact during motion. Control power and data acquisition are performed via a Matlab/Simulink program. Measurements are ensured to start at the closest possible position to the probe to prevent disturbances due to dynamics effects.
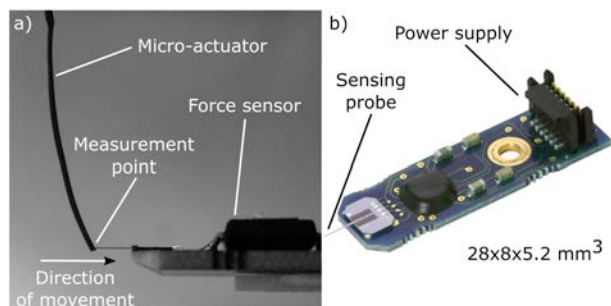

Fig. 2 Experimental setup to measure generated forces of the PPy based micro-actuator. a) Actuator at a measurement configuration and b) force sensor.

Over incremental actuation voltages ranging from 0.2 to 2.2 V, the maximum generated force at the tip is considered. Results of force sensing are depicted in Fig. 3 for polymerization durations from 2 to 14 hours. Maximum forces range from 175 to 425 μN.
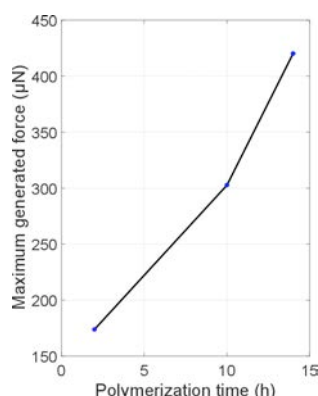
Fig. 3 Impact of polymerization time on maximum generated forces at the micro-actuator tip.

b. PPy actuated tube for laser steering

As an application example, the planar micro-actuator is fixed to a silicone tube of 1 mm diameter using a heat-shrinkable sleeve at the lower end, as depicted in Fig. 4. Optical fiber linked to a laser generator is placed inside the tube. The system is then actuated and the laser is steered to a maximum displacement of 5 mm. This proves motion capabilities of PPy-based micro-actuator notwithstanding its softness. Thus, using a soft actuator while generating sufficient output force provides medical/surgical applications with operational yet safe approach. The range of displacement is satisfactory to operate B-scans with optical coherence tomography (OCT) compared to MEMS based probes [6], and mosaicking with confocal laser endomicroscopy [7].

DISCUSSION

This paper presents first prototype integrating a PPy-based micro-actuator in a laser sweeping scheme. Further, the actuator's maximum force is assessed with respect to its polymerization time. Overall, the forces were sufficient to perform 5 mm displacement.
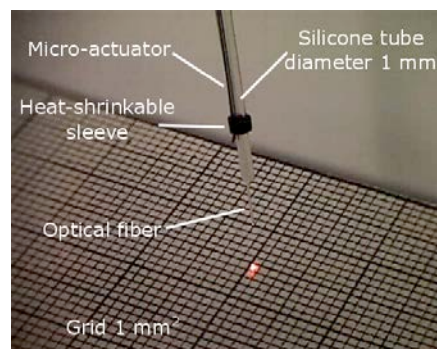
Fig. 4 Proof of concept of a PPy-based micro-actuator fixed with a tube embedding optical fiber linked to a laser generator. Video can be found at https://youtu.be/fwIC-UY1s38

In order to increase the movement amplitude, longer polymerization time is required. Conversely, saturation of thickness growth during the fabrication process could prevent enhancing motion performances and reduce the dynamics. Using Interpenetrating Polymer Networks (IPN) is a promising technique to combine benefits of high-force polymers (i. e. PPy) and high-speed ones (i.e. Polyethylene oxide–polytetrahydrofurane, PEDOT).

ACKNOWLEDGMENT

REFERENCES

[1] Carpi F, Smela E. Biomedical Applications of Electroactive Polymer Actuators, Wiley On. Lib., 2009.

[2] Chikhaoui MT, Rabenorosoa K, Andreff N. Kinematics and Performance Analysis of a Novel Concentric Tube Robotic Structure with Embedded Soft Micro-actuation, Mech. Mach. Theory, 2016, 104, 234-254.

[3] Chikhaoui MT, Cot A, Rabenorosoa K, Rougeot P, Andreff N. Design and Closed-loop Control of a Tri-layer Polypyrrole based Telescopic Soft Robot, IEEE/RSJ IROS, 2016, 1145-1150.

[4] Yamaura M, Hagiwara T, Iwata K. Enhancement of Electrical Conductivity of Polypyrrole Film by Stretching: Counter-ion Effect. Synth. Met., 1988, 26(3), 209-224.

[5] Gairhe B, Alici G, Spinks GM, Cairney JM. Synthesis and Performance Evaluation of Thin Film PPy-PVDF Multilayer Electroactive Polymer Actuators. Sens. & Act. A: Physical, 2001, 165(2), 321-328.

[6] Sun J, Xie H. MEMS-based Endoscopic Optical Coherence Tomography. Int. J. Opt., 2011.

[7] Rosa B, Erden MS, Vercauteren T, Herman B, Szewczyk, J, Morel G. Building Large Mosaics of Confocal Endomicroscopic Images using Visual Servoing. IEEE T. Bio-Med. Eng., 2013, 60(4), 1041-1049.

Discussion of Link Designs for Fibre-optic Shape-Sensing in a Snake-like Robot

A. Schmitz, A.J. Thompson, P. Berthet-Rayne, G.-Z. Yang

Hamlyn Centre for Robotic Surgery, Imperial College London,

a.schmitz16@ic.ac.uk

INTRODUCTION

Snake-like robots [1] have a great potential for minimally invasive surgery, but one of the drawbacks is their open loop control architecture and lack of shape sensing capabilities. Moreover, this drawback is even more important when considering tendon driven small diameter robotic surgical instruments for snake-like robots. This leads to control issues caused by factors such as tendons backlash, elongation and crosstalk. Thus, it is desirable to close the control loop by incorporating shape sensing capabilities into the robotic tools. Fibre Bragg Gratings (FBGs) [2], magnetic sensors [3] and optical reflectance sensors [4] have been reported for this purpose. Although FBGs provide high fidelity shape sensing, they are limited by their cost, size and complexity. As an alternative to FBGs and other shape sensors, we designed a fibre-optic shape sensor to measure the bend angle in a single robot joint. A two-joint proof-of-concept prototype with an outer diameter of 4 mm was built to demonstrate real time shape sensing. We achieved a mean measurement error of only 0.7°. Several joint designs were investigated to find the best trade-off between accuracy, joint range and amount of required fibres. This paper discusses the different designs.

METHOD – THE PRINCIPLE

The angle measurement is done with a single joint as a proof of concept. This joint robot is controlled by in-house software running on a PC. This software receives all inputs from the user interface and calculates the motor motion to move the joints. It communicates with 2 motor controllers (Maxon Motors AG), which controls motors that alter the tensions in the tendons. A super continuum laser source (Fianium WL-SC-400-4, NKT Photonics A/S, Birkerød, Denmark) is coupled into a central optical fibre of 3 to 5 fibres that are secured within the base part of the robot. The light is reflected from the polished lower surface of the upper part of the joint and collected by the remaining 2-4 fibres. The collected light is delivered to proximal phototransistors (Kingbright) for detection, and the signals are converted by a PSOC micro-controller and then received by the PC. The bend angle of the joint can then be calculated based on the light intensity detected at each phototransistor and the control software can then take that measured angle into account.
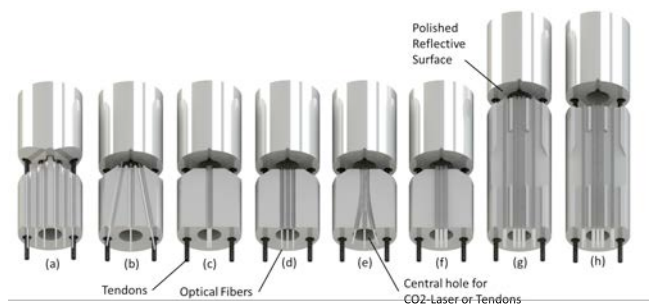

Fig. 1 The evolution of link designs. (h) is the final link design which is used to measure angels

DISCUSSION OF EVOLVED DESIGNS

We designed and tested multiple joints to find an optimal solution. In this paper we present the evolution of these designs and discuss the relative merits of each. Figure 1 shows the different design steps. All the proposed designs share some required key features. In the centre of the link is a core channel through the full length of the instrument that is used to deliver a CO_2-laser fibre for soft tissue ablation or to contain tendons for the control of further joints/tools. On the sides of the core are two channels for tendons to actuate the joint. The design phase presented in Figure 1 showing a section view is described below:

(a) Three optical fibres were positioned on either side with each fibre placed in a separate hole. The middle fibre on each side acted as the light source. The opposite link of the joint had the same V-shape shown in the figure. We were able to detect light for a small range of angles and had the following flows: Due to the angle of the opposite site the light was reflected away from the joint at quite sharp angles and was not efficiently collected by the fibres. Further, the height of the fibres were different in this design, which also acted to limit the range of angles over which light was collected. So only a reduced joint angle range was measurable.

(b) This design had a flat surface on both sides of the joint. The flat surface on the opposite link improved the range of detection of the reflected light. The design had three fibre channels which were located on the flat part. Because the fibres had a specific angle range in which they were able to collect light, the collecting fibre channels were angled to enhance the level of the received light signal, using light

pathway simulation. However, experimentally this design did not improve the collection efficiency due to manufacturing limitations. When placing all three fibres in the central channel we observed an improvement in the light collection. The biggest improvement was reached by having a flat surface on both sides and all fibres are at the same height.

(c) In this design a single hole was used for all three fibres. This leads to further assembling difficulties such as fibre alignment and twisting fibres. If the fibres cross, they come out with an undefined angle. We required all fibres to be parallel and for the emitting fibre to be positioned in the centre.

(d) In this design three smaller holes were used to better align the fibres. This resulted in the need to change the manufacturing process to obtain smaller tolerances. The printing process was switched from a metal selective laser melting technology printer, Mlab cusing (ConceptLaser, Germany), to a scan spin and selectively photocure technology printer, Ultra HD (EnvisionTEC, USA). However, the resulting smallest feasible holes were still too large to ensure a tight fit and a good alignment of the fibres.

(e) Design (e) aimed to tackle the same problem as (d). One large hole was divided into three smaller holes. The idea was to first insert the central fibre and then insert the left and right fibres using the additional outer channels. These were guided along the central fiber. Unfortunately, the minimum achievable channel size was too large and led to fibre overlap.

(f) In design (f) we exchanged the fibre from a multimode fibre with 50μm core diameter (Thorlabs Inc, USA) to a multimode fibre with 200μm core diameter (Thorlabs), which provided considerable advantages. It has a stronger jacket and thus was more robust while bending. The hole size had to be increased to fit the new fibre. These fibres had no overlap problems and ideally fit into the minimum sized holes. This simplified the assembly. The fibre aligned at the same height, protruding from the surface slightly. With this design a good distinctive coverage of a small angle range was achieved.

(g) To improve the the angle range measurement we added one fibre at each side (two fibres in total). This increased the measurable range. We added an opening to the side of the joint, which provided access to the fibres and enabled us to align the fibres more accurately and and fix them in position.

(h) We discovered that positioning the upper part of the robot joint slightly further from the optical fibers increased the range of measurable angles. Thus, in the final design the distance between the optical fibres and the upper reflective surface was increased.

RESULTS AND DISCUSSION

Using the final design (h) we were able accurately measure angles. This optimised setup contained five optical fibres: one emitting fibre and four receiving fibres. We used a multimode fibre with 200μm core diameter (Thorlabs Inc, USA) because of its wide emission/collection angle as well as its robustness. The emitting fibre together with two receiving fibre were located in the middle hole. These three fibres fit tightly into this hole with no overlap. Two further fibres (one on each side) were placed in the outer channels. These extended the range of the angle measurement significantly. All fibres were levelled at the same height, protruding slightly from a flat surface. The joint containing the fibres had a flat surface for the fibres as well as a flat opposite reflecting surface. The distance from the fibres to the reflective surface had a strong effect on the collection efficiency and was optimised to allow effective angle measurements. We tested several different heights to reach the optimal distance. The reflective surface had to be flat and smoothly polished. The degree of polishing is important for the measurement, although a manual polishing was sufficient in our case. The alignment of the fibres is crucial: we found that they have to sit at exactly the same height (protruding slightly) and must be parallel to one another. If they were positioned within the joint, their range of collection angles were severely limited.

Using the final design (h) we built a prototype with an outer diameter of 4 mm. This design allowed us to receive specific light distributions through the fibers in the whole angle range of -20 to +20 degree. The prototype was implemented and trained with a multilayered perceptron. It was able to measure the joint angle with a mean error of 0.7°these are promising results for joint angle measurement.

This design has to be tested in realistic environments before use. We believe it is possible to control the environment with a sheath covering the tool to seal it from outside influences. This is a demonstration of the principle based on the assumption of a controlled environment. Future work will investigate the influence of the environment on a sheath covered instrument (water condensation, smoke, etc.) on a multi joint system.

REFERENCES

[1] J. Shang et al., "A single-port robotic system for transanal micro-surgery – design and validation," 2017.

[2] R. Younge et al., "Optical fiber shape sensing systems," Nov. 20 2008. US Patent App. 12/106,254.

[3] S. Tully et al., "A filtering approach for image-guided surgery with a highly articulated surgical snake robot," IEEE Transactions on Biomedical Engineering, vol. 63, no. 2, pp. 392–402, 2016.

[4] J. Peirs et al., "A micro optical force sensor for force feedback during minimally invasive robotic surgery," Sensors and Actuators A: Physical, vol. 115, no. 2, pp. 447–455, 2004.

Design of an Ultrasonic Bone Cutting Tool for the da Vinci Platform

A. Gordon, P. Francis, R. Saab, T. Looi, J. Drake, C.R. Forrest

Center for Image Guided Innovation and Therapeutic Intervention (CIGITI), The Hospital for Sick Children, Toronto, Canada
alex.gordon@mail.utoronto.ca

INTRODUCTION

The da Vinci® Surgical System (dVSS) is the most widely used robotic surgical system, providing improved precision, control, and intraoperative visibility, with a range of interchangeable tools available for performing various surgical tasks [1]. However, no bone cutting tool exists commercially for the dVSS. The lack of a dVSS bone cutting tool is a drawback when using the system to perform surgeries where bone cutting is required. The surgeon must undock the robot to manually perform the bone cutting, interrupting surgical workflow [2]. Additionally, traditional handheld cutting tools are limited in precision and control, posing a risk to soft tissues in delicate procedures. For the proposed tool, ultrasonic cutting was selected over traditional saws/burrs due to reduced risk to soft tissue structures, reduced blood loss, improved visibility, and increased cutting precision [3]. The novel tool aims to combine the benefits of the da Vinci system and ultrasonic cutting, and is designed for surgeries with the da Vinci system where bone cutting is required, including craniofacial and neurosurgical operations. This paper will explore the finite element analysis (FEA) results of the initial design.

MATERIALS AND METHODS

Ultrasonic bone cutting tools employ high frequency mechanical vibrations of a metallic cutting tip to impact and cut bone. The cutting blade vibrates at a frequency in the range of 20-30 kHz, with displacements of 15-350 microns [4]. The ultrasonic vibrations are created by a piezoelectric transducer. Vibrational motion is created by applying alternating current of a certain frequency to the piezoelectric material, which expands and contracts at the same frequency. The transducer is designed to operate at longitudinal resonance, where larger output amplitudes are possible for lower input electrical energy. To accelerate the design of the tool, a suitable transducer was selected off-the-shelf: a 150W bolt clamped langevin type transducer operating at 28 kHz +/- 0.5 kHz.

The output amplitude of piezoelectric langevin transducers is small, typically around 10-20 microns. This amplitude must be increased at the cutting tip to effectively cut bone [4], and so mechanical gain is incorporated into the rest of the ultrasonic system, which consists of a sonotrode/horn, a transmission rod, and the cutting blade (Fig. 1). Each component of the system must operate at the same longitudinal frequency. As well, the system must have sufficient frequency separation between the longitudinal vibrational mode
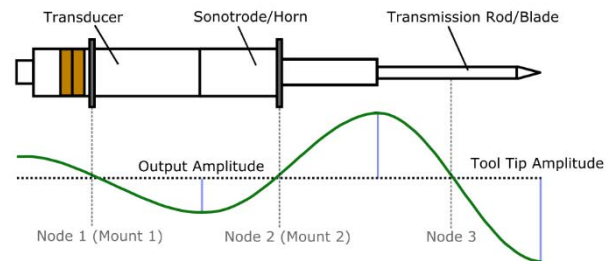

Fig. 1 Ultrasonic cutting system showing amplitude output (green) corresponding to the length of the tool. Nodes are points of zero vibrational motion, where the tool is mounted.

and undesirable modes, such as bending and torsional modes.

If these modes are too close to the longitudinal mode, the power supply may 'jump' to a nearby mode, causing undesirable behaviour. Previous work suggests that 10% is a sufficient amount of frequency separation [5]. Additionally, large stresses in the system due to the vibrational motion can result in fatigue failure of the device; stress must be minimized while still maximizing mechanical gain. The device must also be long enough such that it passes the remote center of motion (RCM) of the dVSS, however, increasing length results in reduced bending and torsional stiffness, leading to the rise of undesirable modes. SolidWorks CAD and ANSYS FEA software were used to design the tool. Modal analysis was performed on the entire ultrasonic system to determine frequencies and shapes. Following modal analysis, harmonic analysis was performed by applying 15 microns of longitudinal displacement at the transducer output. The piezoelectric elements were modelled as transverse isotropic material, defined by a total of nine elastic material constants. All analyses are linear elastic, and contact was defined as either bonded or no separation (Fig. 2). Parametric studies were run in ANSYS DesignXplorer to optimize the geometry of the sonotrode, transmission rod, and blade. Key geometric features of the system were parameterized and assigned ranges. For the initial design process a screening
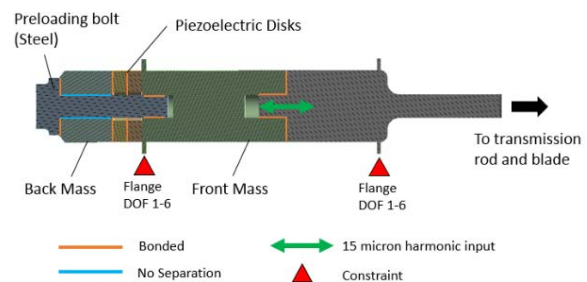

Fig. 2 FEA setup showing contact, boundary conditions, materials, and location of harmonic input
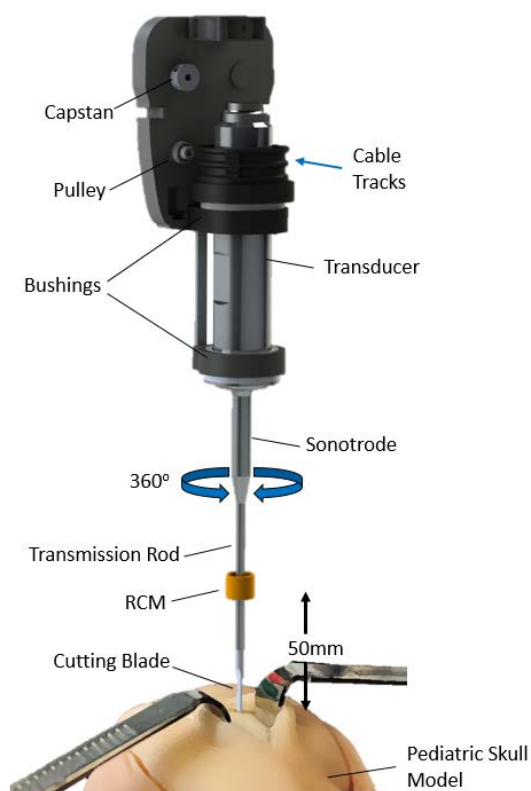
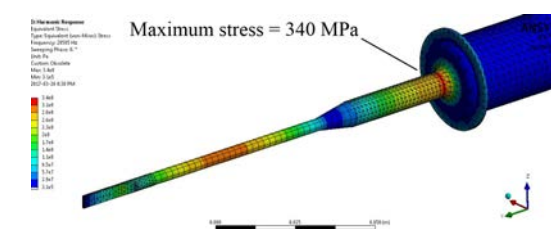Fig. 3 Render showing the tool above a pediatric skull model

Fig. 4 von Mises stresses for 141.4 microns output at 28,501 Hz; max stress is 340 MPa
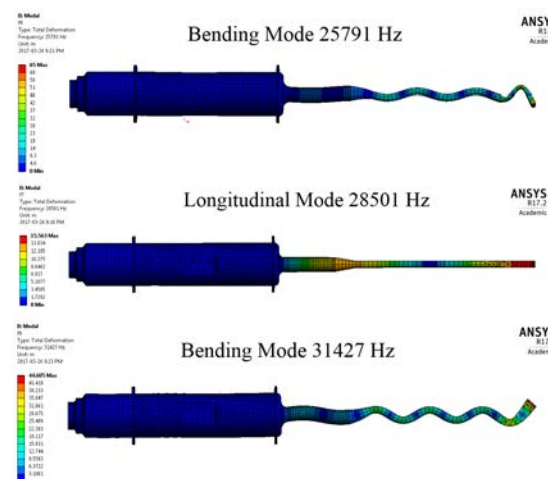

Fig. 5 Modal analysis showing sufficient frequency separation between modes. Images show scaled modal shapes only and do not represent actual displacements.

method was implemented, where a user-defined number of quasi-random designs were generated from the parameterized geometry. Each design was analyzed with the goal of maximizing gain, maximizing frequency separation, and minimizing stress. The best candidates were determined based on the defined objectives, and the final design was selected by the user. Multiple iterations of this process were performed, and in total thousands of designs were assessed. The proposed design was chosen by maximizing the product of gain and frequency separation. Aluminum alloy (7075-T651) was selected due to its low acoustic impedance and high strength-to-weight ratio.

RESULTS

Figure 3 shows a render of the proposed tool attached to the disk-driven adapter for the da Vinci platform, above a pediatric skull model. The tool will be mounted on two bushings; a cable driven system enables roll. Analysis of initial designs showed that a second mounting location was required to reduce the proximity of bending modes to the desired longitudinal mode. When the tool is fully extended along the Patient Side Manipulator (PSM), the transmission rod and cutting blade extend approximately 50 mm past the remote center of motion. For the proposed design, longitudinal resonance is predicted to occur at 28,501 Hz, with the next closest modes at 25,791 Hz (bending, 9.5% separation) and 31,427 Hz (bending, 10.3% separation). For the expected input of 15 microns, output amplitude of the cutting blade is predicted to be 141.4 microns, a gain of 9.63. The maximum stress is predicted to be 340 MPa (Fig. 4). At its thinnest section of 4.0 mm in

diameter, the transmission rod has a length of 93.4 mm. The cutting blade measures 17.3 mm long with a width of 1.1 mm.

DISCUSSION

This paper presents the idea of a novel ultrasonic bone cutting tool for the da Vinci platform, and initial FEA results. As there are multiple conflicting design objectives, a more robust optimization algorithm will be implemented for future iterations. Due to high stresses, fatigue analysis will be incorporated in future analyses. Following finalization of the design, the components of the ultrasonic system will be machined and the system will be assembled. Experimental modal analysis will be performed to validate the FEA results. The device will then be mounted to the da Vinci Research Kit and the cutting effectiveness will be tested on artificial bone.

REFERENCES

[1] Freschi C, Ferrari V, Melfi F, Al E. Technical review of the da Vinci surgical telemanipulator. Int J Med Robot. 2011; 7(April):375-392

[2] Chauvet D, Missistrano A, Hivelin M, Carpentier A, Cornu P, Hans S. Transoral robotic-assisted skull base surgery to approach the sella turcica: Cadaveric study. Neurosurg Rev. 2014; 37(4):609-17

[3] Pavlíková G, Foltán R, Horká M, Hanzelka T, Borunská Šedý J. Piezosurgery in oral and maxillofacial surgery. Int J Oral Maxillofac Surg. 2011;

[4] MacBeath A., Ultrasonic Bone Cutting, University of Glasgow, Ph.D. Thesis, 2006.

[5] Al-Budairi H.D, Design and Analysis of Ultrasonic Horns Operating in Longitudinal and Torsional Vibration, University of Glasgow, Ph.D. Thesis, 2012

A Multiscale Airway Descriptor for Peripheral Bronchoscopic Navigation

M. Shen[1], S. Giannarou[1], P. Shah[2], G.-Z. Yang[1]

[1]The Hamlyn Centre for Robotic Surgery, Imperial College London,

[2]National Heart & Lung Institute, Imperial College London
mali.shen09@imperial.ac.uk

INTRODUCTION

Interventional bronchoscopy provides a less invasive way of nodule biopsy for lung cancer patients. However, it is a challenging task to steer the scope towards peripheral airways due to the complexity of narrow distal branches. Thus far, several interventional tracking techniques have been investigated to assist bronchoscopic navigation including Electromagnetic (EM) tracking and 2D/3D image registration [1]. The major limitations of EM based navigation approaches are field distortion and airway deformation caused by breathing. On the other hand, image-based methods are more tolerant to airway deformation, but the lack of reliable salient features that can be detected on the airway surface restricts its performance. It has been shown that image registration based on geometrical information such as pq-space [2] or depth [3] can be more robust than direct registration methods based on image intensity.

In this paper, we present an image-based navigation approach tailored for robot assisted navigation in the distal airways with smaller lumen sizes, an increasing number of bifurcations, and larger respiratory motion. Airway bifurcations are detected by applying the Maximally Stable Extremal Region (MSER) detector on the depth maps recovered from either bronchoscopic videos or virtual views generated from the 3D CT airway model. An airway descriptor based on shape context [4] that encodes both local structural characteristics and global spatial relationships of airway bifurcations is proposed. Continuous camera tracking is achieved by registering video images to CT airway model using optimal airway feature matching. The proposed tracking method has been validated on both phantom data and in-vivo data and the results obtained show improved accuracy compared with the depth-based registration approach [3].

MATERIALS AND METHODS
Detection of airway bifurcations

Depth maps are generated and used to compute airway bifurcation features due to their robustness to illumination artefacts and surface texture [2]. The depth maps of the bronchoscopic video data z_V are recovered using a Shape from Shading (SFS) method tailored for the endoscopic environment [5]. A virtual camera with the same intrinsic parameters as the bronchoscope is simulated and moved along the centreline of a patient-specific CT airway model from the trachea to the bronchioles. A CT reference depth map z_{CT} is generated at each point along the centreline with the camera

direction being tangential to the centreline. The MSER detector is applied to the depth maps to extract a set of salient regions $R_{i,\ i=1\dots n}$. Only those single detections of distinct airway bifurcations are kept. Non-circular regions ($f_{circ}(R_i) < thr_{circ}$), wall regions ($min(z(R_i)) < z_{wall}$) and multiple detections of the same salient region R_j ($R_j \cap R_j = R_i$ and $(R_j - R_i) \cap \forall R_k = \{\}$ where $k \neq i, j$) are removed. The detection of anatomically meaningful MSER regions on the depth maps of a video frame and its corresponding CT virtual view is illustrated in **Fig. 1**.
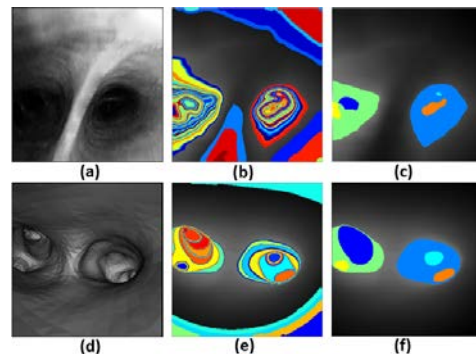

Fig. 1 The detection and filtering of the salient airway regions (colour labelled) on the depth maps of (a)-(c) a video image and (d)-(f) its corresponding 3D view reconstructed from CT.

Local and global airway representation

Our aim is to represent each part of the airway along the centreline based on the number of bifurcations, their shape, size and spatial association. For this purpose, an airway descriptor is proposed to capture the local structural characteristics of each bifurcation region R_i while incorporating the global distribution of the boundary points of the detected bifurcations. The local shape context of region R_i is represented by a 4D coarse histogram H_i^L which describes the relative radial and angular distribution of the boundary points of R_i, as well as their maximum principle curvature and depth values.

$$H_i^L(k) = \#\{q \in B(R_i): (q - C(R_i), z(q), P_{\max}(q)) \in bin(k)\} \quad (1)$$

where, $B(R_i)$ and $C(R_i)$ are the boundary points and centroid of region R_i, respectively. $P_{max}(q)$ and $z(q)$ are the maximum principle curvature and depth value at point q, respectively. The block feature around the centroid of the region on the depth map is also extracted.

A global shape context is computed to describe the spatial distribution of the other detected bifurcations relative to region R_i. It is represented by a 2D coarse histogram H_i^G of the relative radial and angular distribution of the boundary points of all the remaining regions.

$$H_i^G(k) = \#\{q \in B(R_t), t \neq i: (q - C(R_i)) \in bin(k)\} \quad (2)$$

The radial-angular bins of both $H_i^L(k)$ and $H_i^G(k)$ are centred at point $C(R_i)$. A reference radius r_{ref} is defined by the mean distance d_{mean} between the boundary points of all the detected bifurcations on the CT depth map. The reference orientation axis for the angular bins is set to the horizontal axis of the image for video data. For the CT airway descriptor, different orientations are considered in order to find the reference orientation θ_{ref} that gives the best matching to the video data.

Feature matching between the CT reference frame and a candidate video image is achieved by minimising the total cost of matching between their descriptors. The cost of matching one region R_{V_j} on the video data and one region R_{CT_i} on one of the pre-computed CT depth maps is given by Eq. (3).

$$C_{ij} \equiv C\left(R_{CT_i}, R_{V_j}\right) = C_z + C_{LH} + C_{GH} \quad (3)$$

C_z is the normalised correlation score between two patch descriptors, C_{LH} and C_{GH} are the distances of the local and global descriptors estimated using the χ^2 test. The total cost of feature matching is solved with the Hungarian method.

Camera localisation

Camera localisation is achieved by identifying the virtual camera view with the highest similarity to the examined video image. The state of the camera location is defined as $s = [d, \theta, l]$, where d is the distance of the camera location from the trachea point along the centreline, θ is the rotation around the centreline with respect to the initial orientation of the virtual camera, and l is the centreline branch where the camera is located. The estimation of the camera state is solved by minimising the total cost of matching the features in the video image to the pre-computed CT depth maps.

$$\varphi(z_{CT}, z_V) = \min_{d,\theta,l}\left\{\sum_i C\left(R_{CT_i}(d,\theta,l), R_{V_{\pi(i)}}\right)\right\} \quad (4)$$

$\pi(i)$ is the matched region index in the video image to R_{CT_i}. Particle swarm optimisation was applied to find the optimal camera state for the non-differentiable cost function. The camera state of the previous frame is used to initialise the camera state for the next frame.

RESULTS

The proposed tracking approach was validated on data from a silicon human lung phantom and three bronchoscopic examinations of the distal airways performed with an Olympus BF-260 scope. The image resolution was 313×307 pixels. CT airway models were segmented from 1mm slice-thickness CT scans. The CT airway descriptors are computed on the depth maps sampled with a distance interval of 0.01mm along the airway centreline. For MSER region detection, a step size of 0.2 and a maximum area variation of 2 are used.

Parameter	thr_{circ}	z_{wall}	b_{rad}	b_{ang}	b_{dep}	b_{cur}
value	0.4(v),0.6(c)	0.25	12	5	5	5

Table 1. Parameters for MSER filtering and local and global airway descriptors. b is the number of bins.

The values of parameters used for MSER region filtering and construction of airway descriptors are set to values as listed in **Table 1**. The relatively lower thr_{circ} for video data is to include deformed airway bifurcation regions with lower circularity. A patch size of 5×5 pixels is used for the local patch descriptor. A log scale was used for binning the angular distances in the range of $[1/8, 2] \times d_{mean}$. The continuously tracked camera location on airway centreline with the proposed method has been compared to the state-of-the-art depth-based localisation approach in [3]. Manually registered camera locations along the centreline are used as ground truth. Quantitative analysis of the distance error on the validated datasets is summarised in **Table 2**.

Dataset (frames)	Airway Ø	$\mu(\delta_D)$	$\sigma(\delta_D)$	$\mu(\delta_S)$	$\sigma(\delta_S)$
Phantom (271)	8.3 - 12.2	17.28	12.83	10.63	9.13
In-vivo 1 (393)	5.6 - 8.3	41.33	16.05	15.33	13.02
In-vivo 2 (260)	8.3 - 12.2	27.42	14.52	9.26	9.45
In-vivo 3 (190)	5.6	15.39	4.35	9.79	7.47

Table 2. Mean µ and SD σ of the distance error of the proposed method δ_S and depth-based registration δ_D in mm.

DISCUSSION

Reliable intra-operative tracking is a prerequisite of robot assisted endobronchial navigation. Our results show that the proposed airway descriptor outperforms the depth-based registration approach with significantly higher accuracy at distal airway locations for both phantom and in-vivo validation. The method is robust to large tissue deformation because the airway description is based on shape context which allows a certain degree of variation in the local bifurcation structure and also it incorporates the global spatial relationship of the bifurcations which is not significantly affected by the tissue deformation.

Camera tracking can be temporarily affected if the airway features detected on the video images are affected by noise and structural artefacts. However, correct tracking resumes when bifurcations reappear in the video. To conclude, the validation results verify the improved performance of the proposed method in dealing with tissue deformation, fast camera motion and image artefacts at distal airways compared to the depth-based bronchoscope localisation method, indicating its potential value for clinical use.

REFERENCES

[1] Reynisson PJ, et al. Navigated bronchoscopy: a technical review. J Bronchology Interv Pulmonol. 2014;21(3):242-64.

[2] Deligianni F, Chung A, Yang GZ. pq-space based 2D/3D registration for endoscope tracking. MICCAI. 2003(pp. 311-318).

[3] Shen M, Giannarou S, Yang GZ. Robust camera localisation with depth reconstruction for bronchoscopic navigation. IJCARS. 2015;10(6):801-13.

[4] Belongie S, Malik J, Puzicha J. Shape matching and object recognition using shape contexts. PAMI. 2002;24(4):509-22.

[5] Visentini-Scarzanella M, Stoyanov D, Yang GZ. Metric depth recovery from monocular images using shape-from-shading and specularities. ICIP. 2012(pp. 25-28).

3D Gaze Tracking based on Eye and Head Pose Tracking

D. García-Mato[1,3], A. Lasso[1], A. Szulewski[2], J. Pascau[3], G. Fichtinger[1]

[1] *Laboratory for Percutaneous Surgery, School of Computing, Queen's University, Canada*

[2] *Department of Emergency Medicine, Kingston General Hospital, Canada*

[3] *Departamento de Bioingeniería e Ingeniería Aeroespacial, Universidad Carlos III de Madrid, Instituto de Investigación Sanitaria Gregorio Marañón, Spain*

dgmato@hggm.es

INTRODUCTION

Psychological studies on eye movements have documented a temporal and spatial relation of gaze direction with the requirements of performed motor tasks. The oculomotor system directs the gaze towards the spot of greatest interest in the scene, the point providing the most information for the task at hand [1].

Eye tracking has been used in radiology for the evaluation of the visual search process to determine the effectiveness of displays in radiology workstations [2]. More recently eye tracking technology has started being used in surgeries, mainly for the quantitative assessment of surgical skills during minimally invasive surgeries. Significant differences have been found in the eye movements of novices and experts during the performance of surgical tasks [3] and it has been demonstrated that skill assessment is improved when eye-gaze data is added to surgical tool motion data [4].

The eye tracking data used in the previously mentioned studies is two-dimensional, since most applications are based on 2D images or videos. However, the increased importance of 3D imaging and image-guided surgical procedures in the operating room demands the analysis of gaze data in 3D space. The purpose of this work is to assess the feasibility of combining both eye tracking and head positioning to estimate gaze in the 3D space.

MATERIALS AND METHODS

The proposed framework (Fig.1) combines the use of a wearable eye tracker device (Tobii Pro Glasses 2, Tobii Technology, Danderyd, Sweden), an optical tracking system (Polaris®, NDI, Waterloo, Canada) for the real-time positioning of the user's head and a 3D scanner (Artec Eva™, Artec 3D, Luxembourg) for the tridimensional modeling of the objects in the workspace.

In addition, an application was developed in 3D Slicer [5], a free open-source platform for the analysis and visualization of medical images, which receives the gaze data from the eye tracking glasses through a wireless Ethernet connection and the head positioning data from the optical tracking system through OpenIGTLink communication protocol [6] using PLUS open-source software [7].

The proposed methodology consists of four steps:
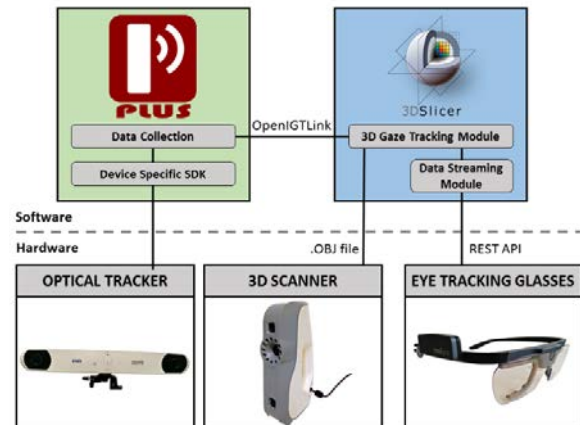
Fig. 1 System overview

1) **3D modeling:** A model of the workspace is generated using the 3D scanner. Several visual markers must be attached to the scene before scanning for calibration and registration purposes.

2) **User preparation:** The wearable eye tracker and a set of three reflective spheres, visible by the optical tracking system, are attached to the user's head using elastic and adjustable straps. Gaze tracking is also possible for those users with eye vision problems, either using glasses or contact lenses.

3) **Calibration:** A calibration procedure is required to compute the relationship between the eye tracker and the optical tracker coordinate systems. During this process the user is asked to focus on 6 visual markers attached to the workspace while gaze data and head position are recorded. A minimization of the shortest distance between each gaze line and corresponding marker 3D position is performed using L- BFGS -B algorithm [8].

4) **Navigation:** Once calibrated, the system is able to display the 3D gaze line in real-time and it is possible to visualize which region of the 3D workspace (generated model) the user is looking at.

The experimental setup for the performance evaluation of the proposed system consists of a room simulating a simple surgical scenario (Fig. 2). A set of 16 visual markers were attached to the scene: 6 of these markers are used for the calibration of the system (calibration markers) and the remaining 10 for accuracy evaluation purposes (evaluation markers).
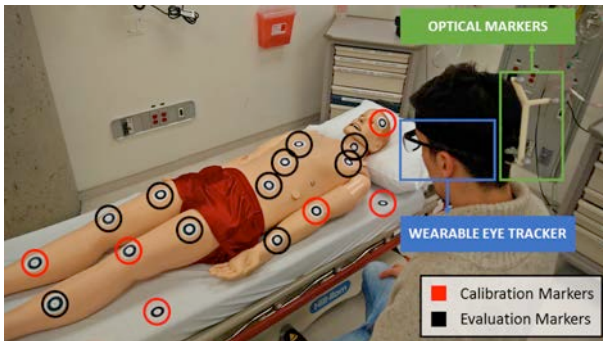
Fig. 2 Distribution of visual markers in workspace

First, the system was calibrated asking users to focus on each of the calibration markers during 3 seconds. Then, users were asked to look at each of the 10 evaluation markers in the scene for 3 seconds in order to assess the accuracy of the 3D gaze tracking system. During this time, samples of the gaze direction and the head position were recorded and 3D gaze lines were estimated. A total of 20 repetitions of this experiment were performed. Gaze tracking error was measured as the shortest distance between gaze lines and marker positions, and as the angular deviation between real and estimated gaze lines.

RESULTS

Results for the accuracy evaluation of the 3D gaze tracking system indicate an average shortest distance between estimated gaze lines and marker positions of 6.0 ± 3.3 mm and an average angular difference between real and estimated gaze lines of $0.4° \pm 0.2°$. The mean distance between the user's eyes and the visual markers was 94.1 ± 11.7 cm. The average range of motion of the user's head was $73.7° \pm 1.8°$ rotation, $37.8° \pm 4.7°$ flexion-extension, and $23.5° \pm 2.9°$ lateral flexion. 3D head and gaze tracking information can be visualized in real-time together with the generated models of the objects in the scene (Fig. 3).
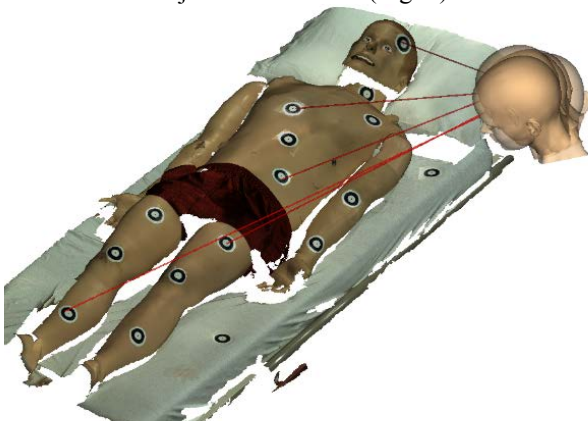
Fig. 3 Visualization of 3D gaze line intersections with model

DISCUSSION

Gaze tracking accuracy is affected by the devices intrinsic errors, the calibration procedure and the attachment of the optical markers to the user's head. The system requires a 6-point calibration procedure which takes less than 30 seconds and assumes the relative position of the eye tracker with respect to the optical markers is maintained. Therefore, during the described experiment the eye tracker was not removed or repositioned after the calibration. However, errors could be reduced by fixing the optical markers directly to the wearable eye tracking glasses.

Although this study was done in a static environment, some applications could involve movable objects in the workspace. For those cases, optical markers could be attached to those objects to know their relative position with respect to the user's head. As a future work, we will study the feasibility of using RGB-D cameras for periodic updates of the 3D scene.

For this work, a 2-camera optical tracking system with limited field-of-view was used, restricting the movement of the user's head. Using multi-camera optical tracking systems would remove this limitation.

The results of this study demonstrate the feasibility of this novel system to provide tridimensional gaze tracking with an average localization error of 6 mm and average angular error in the estimated gaze line of 0.4°. The reported accuracy will enable this system to be used for the analysis and visualization of gaze data in the 3D space for applications requiring the identification of which objects in the scene a person is focusing on.

REFERENCES

[1] M. Land, N. Mennie, and J. Rusted, "The roles of vision and eye movements in the control of activities of daily living," *Perception*, vol. 28, no. 11, pp. 1311–1328, 1999.

[2] M. S. Atkins, A. Moise, and R. Rohling, "An application of eye gaze tracking for designing radiologists' workstations: Insights for comparative visual search tasks," *ACM Trans. Appl. Percept.*, vol. 3, no. 2, pp. 136–151, 2006.

[3] B. Law, M. S. Atkins, A. J. Lomax, and C. L. Mackenzie, "Eye Gaze Patterns Differentiate Novice and Experts in a Virtual Laparoscopic Surgery Training Environment," *ETRA '04 Proc. 2004 Symp. Eye Track. Res. Appl.*, vol. 1, no. 212, pp. 41–48, 2004.

[4] N. Ahmidi, G. D. Hager, L. Ishii, G. Fichtinger, G. L. Gallia, and M. Ishii, "Surgical Task and Skill Classification from Eye Tracking and Tool Motion in Minimally Invasive Surgery," *Lect. notes Comput. Sci.*, vol. 63, no. 63, pp. 295–302, 2010.

[5] S. Pieper, M. Halle, and R. Kikinis, "3D Slicer," in *2004 2nd IEEE International Symposium on Biomedical Imaging: Macro to Nano (IEEE Cat No. 04EX821)*, 2004, vol. 2, pp. 632–635.

[6] J. Tokuda *et al.*, "OpenIGTLink: an open network protocol for image-guided therapy environment," *Int. J. Med. Robot. Comput. Assist. Surg.*, vol. 5, no. 4, pp. 423–434, Dec. 2009.

[7] A. Lasso, T. Heffter, A. Rankin, C. Pinter, T. Ungi, and G. Fichtinger, "PLUS: Open-source toolkit for ultrasound-guided intervention systems," *IEEE Trans. Biomed. Eng.*, vol. 61, no. 10, pp. 2527–2537, 2014.

[8] R. H. Byrd, P. Lu, J. Nocedal, and C. Zhu, "A Limited Memory Algorithm For Bound Constrained Optimization," *SIAM J. Sci. Comput.*, vol. 16, no. 5, pp. 1190–1208, 1995.

Deep-Learning for Motion Compensation in Robotic Surgery

P. Triantafyllou, J. Liu, G.-Z. Yang, S. Giannarou

The Hamlyn Centre for Robotic Surgery, Imperial College London
p.triantafyllou16@imperial.ac.uk

INTRODUCTION

Biophotonics techniques, such as probe-based Confocal Laser Endomicroscopy (pCLE), have enabled in vivo, in situ tissue characterisation without changing the surgical settings. Recently, robotically controlled endomicro-scopy probes have been developed to provide motion stabilization using either force sensing [1] or visual servoing [2]. The latter has the advantage of allowing seamless integration with the existing surgical flow since it employs the existing laparoscopic camera and does not introduce any additional equipment to the surgical scene. Visual servoing requires recovery of the 3D structure as well as of the motion of the tissue to automatically plan and control the motion of the imaging probe on the tissue surface. Conventional 3D reconstruction and optical flow estimation methods might struggle in the case of pCLE applications, where the slightest probe-positioning error can lead to severe image-quality deterioration.

For this reason, in this paper, a vision-based framework is proposed based on deep learning for stereo reconstruction and optical flow, which can be used for the stabilization of imaging probes on the tissue surface.

MATERIALS AND METHODS

Vision-based motion stabilization in a surgical environment requires accurate and real-time recovery of the dense 3D structure of the tissue surface and the dense optical flow of the surgical scene. Although a plethora of 3D reconstruction and optical flow estimation methods have been proposed in the literature, these tasks remain challenging tasks for medical data, mainly because of poor texture, specular reflections and occlusions due to the presence of instruments.

In this work, the use of deep learning techniques for 3D reconstruction and optical flow estimation is explored. Convolutional Neural Networks (CNNs) have recently proven very successful in both tasks [3], [4], [5]. However, their suitability for medical data is not at all obvious, as they are usually trained on natural or even synthetic images. In what follows, the reconstruction accuracy of two state-of-the-art CNN-based stereo reconstruction methods and a dense CNN-based optical flow approach is investigated.

As far as CNN-based stereo reconstruction is concerned, the *MC-CNN* [3] and *DispNet* [4] approaches are examined. *MC-CNN* entails training a Siamese network to compute a matching distance between two rectified image patches. A series of post-processing steps, such as cross-based cost aggregation and Semi-Global Matching [6], are required to generate the final disparity map. The authors proposed two

network architectures: one focusing on speed and the other on accuracy. In this paper, the real-time version, trained on the KITTI 2012 dataset, is investigated.

DispNet involves end-to-end training of a CNN for disparity estimation. The network consists of a contracting part, which reduces computational time and aggregates information over large areas of the input images, and an expanding part, that efficiently upsamples the disparity to high resolution. Two network variants were proposed. According to the *DispNetCorr* architecture, the network processes the two images separately for the first few layers and the resulting features are then correlated using a 1D correlation layer, whereas in the *DispNetSimple* architecture both input images are stacked together and fed through the network. The former variant is used here, as it proved to be more accurate than the latter in all cases.

The aforementioned approaches are two of the best real-time disparity estimation methods according to online leaderboards, such as KITTI and Middlebury, but to the best of the authors' knowledge, they have not been extensively tested on medical data.

As for optical flow estimation, the only real-time CNN-based approach is the *FlowNet* [5]. There are two variants, which are directly equivalent to those of the *DispNet*. The *FlowNetCorr* architecture, which in the case of optical flow estimation uses a 2D correlation layer, has been proved to be better than *FlowNetSimple* and is used in this work. In [5], the *FlowNet* is shown to outperform the popular *LDOF* [7] method. Therefore, in this paper, their comparative performance on medical data will be explored.

RESULTS

The *MC-CNN* and *DispNet* methods are compared to state-of-the-art stereo reconstruction techniques on two medical datasets with ground truth disparity maps. The *FlowNet* method is examined alongside LDOF.

The first dataset on which the above methods will be evaluated on, is that of [8] as shown in Fig. 1. It consists of 35 stereo pairs of ex-vivo porcine liver, kidney and heart data as well as fatty tissue taken under various relative endoscope-tissue poses. Disparity ground truth is available from CT data. To enable comparison with the performance evaluation results proposed in [8], the same two stereo reconstruction algorithms are used for validation. The first one, namely *Stereo-KIT*, is a modified version of the Hybrid Recursive Matching algorithm [9] which employs spatiotemporal information to produce a dense disparity map with subpixel precision. The second one, namely *Stereo-UCL*, uses seed propagation to generate a semi-dense disparity map [10].
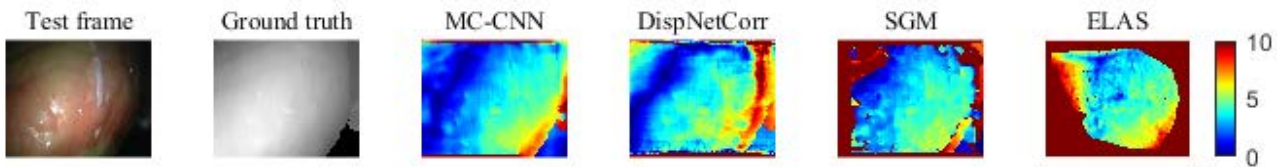
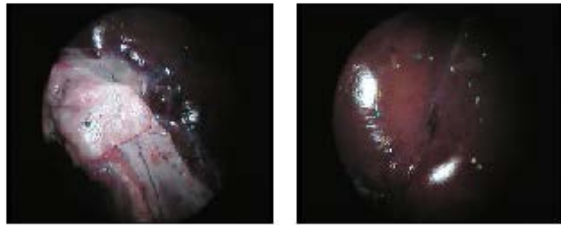**Fig. 3** Disparity estimation errors (in pixels) on the Heart dataset.

Fig. 1 Sample frames from the dataset of **[8]**.

Fig. 1 Optical flow estimation on the Heart dataset.

The second dataset [11] is a sequence of 2426 image pairs of a silicone heart phantom. Ground truth point clouds have been generated with manual registration of CT data. For validation on this dataset, an implementation of the popular Semi-Global Matching (*SGM*) approach [6] and the top-performing real-time stereo reconstruction method *ELAS* [12] are used for comparison.

The median reconstruction error for the first dataset, measured as the Root Mean Square (RMS) distance to CT reference data, ranged from 0.9 mm (*MC-CNN*) to 1.7 mm (*Stereo-UCL*). A box plot for the different methods is shown in Fig. 2. *MC-CNN* outperformed all other methods, whilst *DispNet* performed as well as *Stereo-UCL*.

Fig. 2 Box plot of the RMS surface reconstruction error for all techniques applied on the dataset of **[8]**.

As far as the second dataset is concerned, the median reconstruction error after excluding outliers, ranged from 1.4 mm (*DispNet* and *MC-CNN*) to 1.9 mm (*ELAS*). In this case, the CNN-based methods performed almost equally well, outperforming *SGM* and *ELAS*, as it is illustrated in Fig. 3.

Due to the lack of a medical dataset with ground truth dense optical flow maps, a qualitative comparison between *FlowNet* and *LDOF* was conducted for pairs of the heart dataset. As it can be concluded by Fig. 4, both methods yield similar results despite *LDOF* being about 100 times slower. Finally, *FlowNet* produces smoother flows than *LDOF*.

DISCUSSION

In this paper, CNN-based techniques were shown to outperform conventional 3D reconstruction and optical flow estimation methods in the case of medical data. Hence, they can be employed for accurate and real-time soft-tissue reconstruction and tracking. Future work will focus on applying the proposed framework for motion compensation during robotic tissue scanning.

REFERENCES

[1] Giataganas, P., et al., "Force adaptive robotically assisted endomicroscopy for intraoperative tumour identification," *Int. J. Comput. Assist. Radiol. Surg,,* pp. 1-8, 2015.

[2] Zhang, L., et al., "Autonomous Scanning for Endomicroscopic Mosaicing and 3D Fusion," in *ICRA*, 2017.

[3] J. Zbontar and Y. LeCun, "Stereo matching by training a convolutional neural network to compare image patches," *J. Mach. Learn. Res.,* vol. 17, pp. 1-32, 2016.

[4] Mayer, N., et al., "A Large Dataset to Train Convolutional Networks for Disparity, Optical Flow, and Scene Flow Estimation," in *CVPR*, 2016.

[5] Dosovitskiy, A., et al., "FlowNet: Learning Optical Flow with Convolutional Networks," in *ICCV*, 2015.

[6] H. Hirschmuller, "Stereo Processing by Semiglobal Matching and Mutual Information," *IEEE Trans. Pattern Anal. Mach. Intell.,* vol. 30, no. 2, pp. 328-341, 2008.

[7] T. Brox and J. Malik, "Large Displacement Optical Flow: Descriptor Matching in Variational Motion Estimation," *IEEE Trans. Pattern Anal. Mach. Intell.,* vol. 33, no. 3, pp. 500-513, 2011.

[8] Maier-Hein, L., et al., "Comparative Validation of Single-shot Optical Techniques for Laparoscopic 3D Surface Reconstruction," *IEEE Trans. Med. Imag.,* vol. 33, no. 10, pp. 1913-1930, 2014.

[9] Röhl, S., et al., "Dense GPU-enhanced surface reconstruction from stereo endoscopic images for intraoperative registration," *Med. Phys.,* vol. 39, pp. 1632-1645, 2012.

[10] Stoyanov, D., et al., "Real-time stereo reconstruction in robotically assisted minimally invasive surgery," in *MICCAI*, 2010.

[11] "http://hamlyn.doc.ic.ac.uk/vision/," [Online].

[12] Geiger, A., et al., "Efficient large-scale stereo matching," *ACCV,* pp. 25-38, 2010.

First Results on a Flexible Variable Stiffness Endoport for Single-Site Partial Nephrectomy

E.Amanov[1], T.-D. Nguyen[1], F. Imkamp[2], J. Burgner-Kahrs[1]

[1]*Laboratory for Continuum Robotics, Leibniz Universität Hannover, Hanover, Germany*

[2]*Clinic for Urology and Urologic Oncology, Hannover Medical School, Hanover, Germany*
burgner-kahrs@lkr.uni-hannover.de

INTRODUCTION

Minimally invasive surgery gains increasing importance in treating localized renal tumours. Improvements in diagnosis of earlier stages, of haemostats, clips, and barbed sutures lead to an increasing number of organ-preserving partial nephrectomies. While laparo-endoscopic single-site surgery (LESS) is the preferable approach, today's instruments still require mobilisation of the kidney to ensure visualisation and accessibility of many tumours. This increases invasiveness, stress for the patient, and prolongs surgery. It would thus be desirable to have a dexterous and flexible port system, which allows single site access and reconfiguration such that a tumour can be visualised from various orientations. Adjustable stiffness of the port can further enhance manipulability of the tumour with various instruments through working channels.

Thakkar *et al.* proposed a snake-like flexible single port platform for distal pancreatectomy enabling deployment of several instruments [1]. Dynamic motion of this platform for reorientation is challenging and working channels for instrumentation are limited to 2.34 mm. Ranzani *et al.* introduced a multi-segment robotic soft manipulator with variable stiffness for single port surgery [2]. However, the design does not include working channels for varying instrumentation. Comparable approaches to variable stiffness manipulators with granular jamming were proposed (e.g. [3]), yet instrumentation was not considered.

In this paper, we extend our initial investigations toward a flexible variable stiffness endoport for partial nephrectomy [4]. We introduce our first prototype robotic endoport with 2 tendon-actuated segments and 3 working channels, which is flexible and can stiffen reversibly by granular jamming. We further present qualitative results on the accessibility to the kidney and renal tumours in an *in vitro* human abdomen.

MATERIALS AND METHODS

Our endoport concept foresees a flexible manipulator realised as a two-segment tendon-actuated continuum robot equipped with a stiffening method and an actuation unit controlling the tendon tension. The concept of the endoport system is illustrated in Fig. 2. The system allows teleoperation of the manipulator's tip pose with an input device. For visualization, a camera and a light source are integrated into the manipulator's

Fig. 1 Concept and application scenario of the endoport system in an in vitro human abdomen. A potential renal tumour location is marked in green on a silicone kidney.

tip. Three working channels offer insertion and quick exchange of conventional flexible surgical tools, further cameras, or miniaturised continuum robots [5].

In the prototype described in this paper, we disregard the visualization and teleoperation in order to focus on the general feasibility of the concept. Fig. 2 illustrates the proposed design. The manipulator consists of a 1 mm central spring steel backbone, equipped with 8 spacer disks per segment allowing for channel and tendon routing. The endoport prototype is encapsulated in an air-proof latex membrane and has an outer diameter of 26 mm. Two of the three working channels have a dimeter of 8 mm and the third one has a diameter of 4 mm. They consist of tension springs moulded into silicone to ensure the air-proof design. Each segment has a length of 100 mm such that reachability of the kidney through the navel can be achieved under insufflation. We use antagonistic tendon actuation and Dyneema braided tendons. Thus, each segment can bend with 2 degrees of freedom. The actuation unit is designed such that one motor actuates one antagonistic tendon pair. For two segments, we use 4 DC motors (Maxon Motor AG, Switzerland) interfaced by a DCM-4040 motion control board and an AMP-43040 amplifiers (Galil Motion Control, Rocklin, CA, USA).
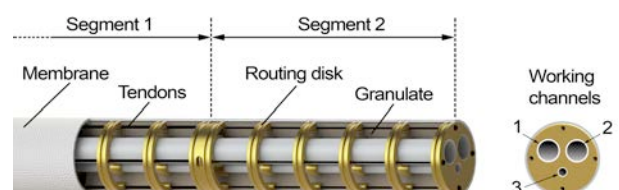

Fig. 2 CAD rendering of the principle design of the endoport (side and front view).

The reversible stiffening method to be used within our endoport system is required to be patient-safe. Stiffening methods based on electro-rheology, magneto-rheology, thermoactive or electroactive polymers, or shape memory alloys do either not provide the required dynamics, or are considered as non-patient-safe due to high currents, voltages, or temperatures (see overview in [2]). Granular jamming provides sufficient stiffening, is cost-effective, and granulate easily adjusts to the shape of the endoport in its non-stiff mode. Various granular matters were proposed in previous research [2][3]. Most prototypes utilize coffee granulate. However, for surgical applications, biocompatible and bioabsorbale granulate materials are required such that in case of leakages of the endoport safety of the patient can be assured. Thus, we propose saccharose as granulate and use refined retail sugar in our prototype. The granulate fills up the free space of the endoport (see Fig. 2, brown area in front view).

To validate the principal concept, qualitative evaluation is conducted in a custom made anatomical in vitro model of a human abdomen with a kidney and typical renal tumour locations marked with modelling clay. The kidney is 3D-printed from silicone (Agilista-3000, Keyence Corp., Japan), vertebras from PLA, and further anatomical structures manually moulded from silicone. The abdominal wall is represented by a transparent hemisphere from acrylic glass (neglecting elasticity). The insertion site reflects the ventral approach for standard laparoscopic partial nephrectomy through the navel. After manual insertion, the actuation unit is fixed on a mounting arm and the reachability of typical renal tumour locations is evaluated. In each configuration relevant in renal surgery, the endoport is stiffened, flexible disposable instruments (EndoJaw, Olympus) are inserted through the working channels, and the endoport reversed to its flexible state after instrument removal.

RESULTS

Fig. 3 shows an overlay photograph of configurations of the manipulator approaching two renal tumour locations. Fig. 4 shows an overlay photograph illustrating two view angles of a renal tumour achieved with the endoport. We were able to access the tumour locations from the insertion site with comparable quality. Deploying instruments through the stiffened endoport was possible at all times.

DISCUSSION

In comparison to using straight laparoscopic instruments through a single site, our endoport prototype allows for increased accessibility of renal tumours. This can potentially reduce invasiveness of the procedure, as mobilization of the kidney may not be required if visualization and accessibility are guaranteed.

In this paper, we presented our initial prototype system for minimally invasive single-site partial nephrectomy and proved feasibility in an initial in vitro setup. While our achieved qualitative results are promising, the development is at an early stage. Future work includes quantitative evaluations of achievable stiffness and pose maintaining accuracy of the endoport. With a flexible endoport at hand, research on dedicated surgical instruments is required. We envision concentric tube or tendon-driven continuum manipulators as promising technologies for instrumentation.
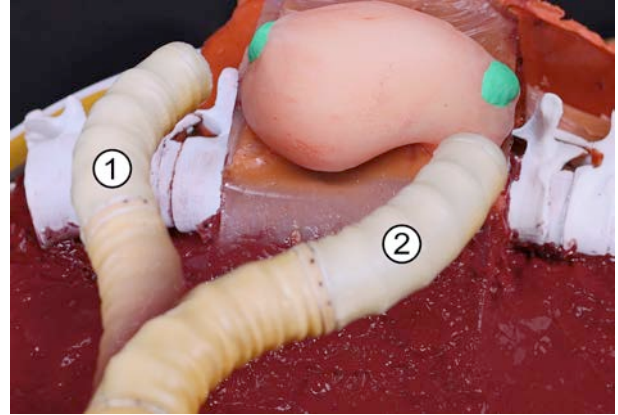
Fig. 3 Reachability of the kidney for 2 renal tumour locations (green) by two endoport configurations (overlay photographs).
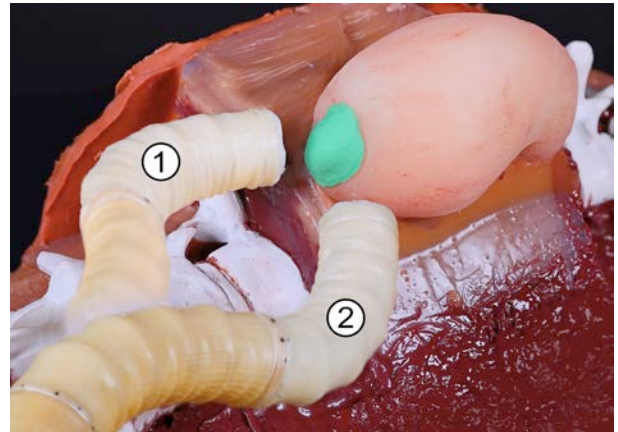
Fig. 4 Approaching a renal tumour (green) with two robot configuration (overlay photographs).

REFERENCES

[1] S. Thakkar, M. Awad, K.C. Gurram, S. Tully, C. Wright, S. Sanan, and H. Choset. A Novel New Robotic Platform for Natural Orifice Distal Pancreatectomy. Surgical Innovation. 2015; 22: 274-282.

[2] M. Cianchetti, T. Ranzani, G. Gerboni, T. Nanayakkara, K. Althoefer, P. Dasgupta, A. Menciassi. Soft Robotics Technologies to Address Shortcomings in Today's Minimally Invasive Surgery: The STIFF-FLOP Approach. Soft Robotics. 2014; 1(2):122-131.

[3] N.G. Cheng, M.B. Lobovsky, S.J. Keating, A.M. Setapen, K.I. Gero, A.E. Hosoi, K.D. Iagnemm. Design and analysis of a robust, low-cost, highly articulated manipulator enabled by jamming of granular media. IEEE International Conference on Robotics and Automation, 2012; 4328-4333.

[4] E. Amanov, F. Imkamp, and J. Burgner-Kahrs. Initial Investigations toward a Flexible Variable Stiffness Single Port System for Partial Nephrectomy. Annual Meeting of the German Society for Computer- and Robot Assisted Surgery (CURAC), 2016; 93-98.

[5] J. Burgner-Kahrs, D.C. Rucker, and H. Choset. Continuum Robots for Medical Applications: A Survey. IEEE Transactions on Robotics, 2015; 31(6):1261-1280.

Author Index

The Hamlyn Symposium on Medical Robotics
25 - 28 June, 2017
Imperial College London and
the Royal Geographical Society, London